The role of merozoite surface protein 1 in Plasmodium falciparum egress from erythrocytes

The role of Merozoite Surface Protein 1 in *Plasmodium falciparum* egress from erythrocytes

Rebecca Anne Lees

Thesis submitted for the degree of Doctor of Philosophy

Birkbeck College, University of London

Declaration of Originality

I, Rebecca Anne Lees confirm that the work presented in this thesis is my own. Where information has been derived from other sources, or experiments have been performed in collaboration or by others, all effort has been made to indicate this.

Abstract

During the erythrocytic lifecycle of the malaria parasite *P. falciparum*, merozoites invade red blood cells (RBC) in which they replicate asexually. Daughter merozoites are eventually produced by a process called segmentation, then released in a lytic process known as egress to invade new RBCs. Merozoite Surface Protein 1 (MSP1) is an abundant GPI-anchored protein that decorates the merozoite surface membrane. Just before egress, MSP1 undergoes proteolytic maturation by a parasite serine protease called SUB1; the processing products remain associated at the merozoite surface where they form a complex with other partner proteins. Both MSP1 processing and complex formation are thought to be important for egress, and MSP1 has also been implicated in RBC invasion. However, the composition, structure and function of the MSP1 complex, and the precise role of SUB1 processing, are poorly understood. We report that conditional depletion of MSP1 results in defective egress but has no effect on rupture of the RBC and parasitophorous vacuole membrane or invasion of new RBCs by those merozoites that are released. Electron microscopic examination revealed that defective egress of the MSP1-null mutant could be due to a 'bystander' effect on parasite segmentation, perhaps due to loss of GPI from the outer leaflet of the parasite plasma membrane. To address MSP1 function in a more nuanced manner, we generated parasites conditionally expressing a mutant MSP1 refractory to SUB1 processing. These parasites also display abnormal egress, suggesting that SUB1-mediated cleavage is important for MSP1 function. To glean further insights into MSP1 function, we have purified the native protein complex in both SUB1 processed and unprocessed forms for analysis by single particle cryo-EM. Models of this structure in comparison to the published recombinant structure indicate the presence of partner

proteins and the regions of MSP1 with which the partners interact. The N and C termini of SERA5 (p47p18), which remain associated after SUB1 processing, appear to bind cleaved MSP1 in proximity of the 38/42 cleavage site. Localisation of SERA5 p47p18 to the merozoite surface appears to aid merozoite dispersal at egress.

Acknowledgements

There are many people to thank for helping me reach this milestone. First and foremost, my supervisors Helen Saibil and Mike Blackman. Both have been generous with their time and patiently guided me through this process. Without their sharing of knowledge and our discussions, I would not have learnt everything I know about science today. Additional thanks is owed to Helen for intuitively recognising the support I needed and tirelessly (although I'm sure she is exasperated by now) correcting my spelling of *P. falciparum*. I couldn't have asked for better supervision.

I am extremely grateful to the lab members, past and present, of the Saibil and Blackman groups, whom I've had the pleasure of working alongside. A special thanks to Christine (Chris) Collins, Fiona Hackett, Konstantinos Kousis, Abigail Perrin, Erin Johnson, Jim Monistrol and Scott Gardner for teaching me the techniques I needed to complete this work and answering my questions without judgement. Chris, in particular, has been a great friend and always given thoughtful advice. Thank you also to Chrislaine Withers-Martinez, Abhinay Ramaprasad, Theo Sanderson and Benedict Davies for your helpful comments and jokes over the four years. I must also extend my gratitude to Claudine Bisson for her hard work before the onset of my PhD and for helping me hit the ground running when starting this project. David Holdershaw, Shu Chen and Natasha Lukoyanova more than deserve a special mention for all the help they have given me at Birkbeck with all things EM, from sample preparation to data collection and processing.

I must thank my friends, family and partner for the support they have given me during my PhD. Thank you to Alex, Helena, Emile, Naomi, Max, Hannah and Molly for your patience

and understanding, particularly on the occasions I turned up an hour late because my parasites weren't behaving. Thank you to my family, Tim, Carol and Kirsty Lees, for being on the other end of the phone and making impromptu trips to London just to buy me lunch (or check I was alive).

Finally, Owain, thank you for sharing the highs and lows of this process; it can't have been easy! I promise to return the favour when you start your own research journey, although I'm sure you won't be quite as over-dramatic.

Table of Contents

Abbreviations

2D	two-dimensional
3D	three-dimensional
ACT	artemisinin combination therapy
AMA1	Apical membrane antigen 1
BiP	Glucose-regulated protein GPR78, ER resident chaperone protein
C1	Compound 1: 4-[2-(4-fluorophenyl)-5-(1-methylpiperidine-4-yl)-1H-pyrrol-3-yl] pyridine
C2	Compound 2: (4-[7-[(dimethylamino)methyl]-2-(4-fluorphenyl)imidazo[1,2-α]pyridi 3-yl]pyrimidin-2-amine
Cas9	CRISPR-associated protein 9
CCD	charged coupled device
CDPK1	calcium-dependent protein kinase 1
CDPK5	calcium-dependent protein kinase 5
cGMP	cyclic guanosine monophosphate
CMOS	complementary metal-oxide semiconductor
CRISPR	clustered regularly interspaced short palindromic repeats
Cryo-EM	Cryogenic electron microscopy
Cryo-ET	Cryogenic electron tomography
CTF	Contrast transfer function
DBL	Duffy binding like domain
DDM	n-dodecyl β-D-maltoside

DDT	dichlorodiphenyltrichloroethane
DED	direct electron detectors
DHFR	dihydrofolate reductase
DIC	differential inference contrast
DiCre	dimerisable Cre recombinase
DMSO	dimethyl sulfoxide
DNA	deoxyribonucleic acid
DQE	detective quantum efficiency
DV	digestive vacuole (also known as the food vacuole)
E64	epoxysuccinyl-Lleucylamido(4-guanidino)butane
EBA	Erythrocyte binding antigen
EDTA	ethylenediaminetetraacetic acid
EDVs	electron dense vesicles
EGF	epidermal growth factor
EM	electron microscopy
ER	endoplasmic reticulum
EXP2	exported protein 2
FEG	field emission gun
FSC	fourier shell correlation
GA	glutaraldehyde
GC-α	guanylyl-cyclase-alpha
GO	graphene oxide
GPA	glycophorin A

GPI	glycosylphosphatidylinositol
HPF/FS	high pressure freezing/ freeze substitution
HRP	horse radish peroxidase
IFA	immunofluorescence assay
IMC	inner membrane complex
LB	lysogeny broth
mAb	monoclonal antibody
MACPF	membrane attack complex pore forming
MSA180	Merozoite surface antigen 180
MSP	merozoite surface protein
NMR	Nuclear magnetic resonance spectroscopy
PAM	protospacer-adjacent motif
Pf	*Plasmodium falciparum*
PfEMP1	*Plasmodium falciparum* erythrocyte membrane protein 1
PfMOP1	*Plasmodium falciparum* Merozoite Organizing Protein
PhIP	PhIL1 (Photosensitized INA-labelled protein 1) interacting protein
PKG	cGMP-dependent protein kinase
PLP	perforin-like protein
PM	plasma membrane
PTEX	*Plasmodium* Translocon of Exported Proteins
PV	parasitophorous vacuole
PVM	parasitophorous vacuole membrane
RAP	rapamycin

RBC	red blood cell
RBCM	red blood cell membrane
RELION	Regularised Likelihood OptimisatioN (program developed by S.Scheres)
Rhs	reticulocyte- binding proteins
RON2	rhoptry neck protein 2
RP-HPLC	reversed phase high performance liquid chromatography
RPMI	Roswell Park Memorial Institute
SDS PAGE	sodium dodecyl sulfate - polyacrylamide gel electrophoresis
SEA1	schizont egress antigen 1
SEM	scanning electron microscopy
SERA	serine repeat antigen
SPA	single particle analysis
SUB1	subtilisin-like protease 1
TEM	transmission electron microscopy
TGX	Tris/glycine
WHO	World Health Organisation
WT	wild type

List of Figures

List of Tables

Chapter 1: Introduction

1.1 The Global Threat of Malaria

Malaria affected around 228 million people and caused approximately 619,000 deaths in 2022 alone (WHO, 2022). Malaria devastates continents in which the mosquito species *Anopheles gambiae* and *stephensi*, the primary vectors, thrive. The disease manifests as fever, vomiting, anaemia, respiratory problems, difficulty breathing and, in cerebral cases, coma (Moxon et al. 2020). Africa, particularly in sub-Saharan regions, is still heavily burdened by malaria; 95% of cases and 96% of deaths occurred on the continent. Pregnant women and children under the age of 5 are at particular risk of contraction and severe disease (WHO, 2022).

Although 6 species of *Plasmodium*, *P. falciparum, P. vivax, P. malariae*, *P .knowlesi, P. ovale wallikeri* and *P. ovale curtisi*, can cause malaria in the humans, the most dangerous is *Plasmodium falciparum*. *Plasmodium vivax,* though less virulent, is the most common causative agent of malaria outside Africa and infection can result in recurrent malaria. Most of the cases involving this species occur in the Asian Pacific region (Cowman et al., 2016).

1.1.1 Current approaches to eliminate malaria

Initiatives to slow the spread and prevent pathology of malaria revolve around vector control, drug and vaccine development. Despite the significant decline in disease prevalence

since 2010, the reduction in cases has plateaued (2014-2019 in comparison to 2010-2015), with increased deaths in recent years (2019-2021), likely due disruptions caused by the COVID-19 pandemic (WHO, 2022). The occurrence of new mechanisms of resistance in both the parasite, against anti-malarial drugs, and the vector, against insecticides, continues to challenge efforts to eradicate the disease.

1.1.1.1 Vector control

Distribution of insecticide impregnated bed nets, the application of insecticide on the interior and exterior of houses, zooprophylaxis and use of sprays for skin are some examples of basic vector control (Karunamoorthi, 2011). Current insecticides target the mosquito nervous system. Organophosphates and carbamates inhibit acetylcholinesterase, disrupting acetylcholine neuronal junctions, and pyrethroids prevent closure of sodium ion channels to interfere with nerve impulse transduction. Resistance in *Anopheles* continues to grow as result of behavioural, excretive and metabolic adaptations in response to widespread application of these compounds (Liu, 2015). The introduction and spread of *Anopheles stephensi*, a malaria vector from Asia, into Africa has also made vector control more challenging. *A. stephensi* flourishes in urban areas whereas the native *A. gambaei* vector is found primarily in rural regions; *A. stephensi* has also proven to be resistant to insecticides (Mnzava et al., 2022). Interestingly, blood meals containing Ivermectin have been shown to reduce *Anopheles* life span significantly. Ivermectin is used for treatment against a variety of parasitic worms including those which cause lymphatic filariasis and river blindness. This phenomenon could repurpose the drug, if taken by those at risk of bites, as a method of vector control (Chaccour et al., 2010).

Genetic engineering of Anopheles may be the future of vector control with the release of modified mosquitos having been trailed over the past few years. Current approaches in use include the release of sterile male or female mosquitos to eradicate species that transmit disease. This technology, currently implemented by Target Malaria and Oxitec, requires regular release of modified mosquitos; genetic modifications are either not inherited or exist in the population for only a short period (G. H. Wang et al., 2021). Gene drive offers an alternative; this technique could introduce mosquitos with genetic traits that have near 100% chance of inheritance across a population. Traits which result in non-viable progeny or prevent *Plasmodium* infection of mosquitos, for example. This can be done by insertion of modified genes into the genome in association with homing endonuclease genes or alongside a CRISPR-Cas 9 cassette resulting in the modified gene being copied onto both homologous chromosomes (Bier, 2022). In a recent study, CRISPR-Cas9 gene drive has been used to introduce genes that cause secretion of anti-microbials in the mosquito midgut to the create a colony of *P. falciparum* resistant *Anopheles gambiae* (Hoermann et al., 2022). Gene drive for species modification rather than eradication could prevent unforeseen and unwanted effects on the ecosystem caused by leaving a niche vacant. Some argue that, given there are over 3,500 species of mosquito worldwide, the effects of vector elimination would be negligible. Conversely, species modification comes with a different set of questions and possible complications: How will interaction with greater genetic diversity effect stability and what will be the impact of genetic changes on pathogen evolution or virulence? Though existing methods of vector control are essential and new developments

in gene drive exciting, vector control alone cannot currently stop disease spread (G. H. Wang et al., 2021).

1.1.1.2 Antimalarial drug development

The majority of therapeutics and vaccines in development target the erythrocyte stages of malaria as these are responsible for most of pathology. Artemisinin based combination therapies (ACTs) are currently the first-line treatment for infection. All modes of action of artemisinins have yet to be determined but are thought to involve breakdown of the drug within erythrocytes, resulting in the production of free radicals that cause widespread protein damage, proteasome disruption and parasite destruction. Artemisinins may be activated by binding heme in the parasite digestive vacuole (DV, also known as the food vacuole). Heme (Bridgford et al., 2018; Ouji et al., 2018) is the toxic by-product of haemoglobin25 digestion that is deposited and gradually polymerises in the DV (J. Wang et al., 2015). Due to a short plasma half-life, artemisinin is usually combined with other longer acting drugs, with different targets, hence the name 'combination therapy'. Partner drugs include lumefantrine, amodiaquine and piperaquine that prevent detoxification of the product of haemoglobin breakdown; mefloquine which inhibits merozoite invasion of RBCs, possibly by affecting lipid transport and nutrient uptake; sulfadoxine, pyrimethamine, chlorproguanil and dapsone which interfere with parasite folic acid metabolism (Ouji et al., 2018).

There appears to be growing resistance to ACTs in *P. falciparum*. Cases of delayed parasite clearance were first recorded in patients treated in Cambodia in 2009. This appears to have

spread to other countries in Southeast Asia and East Africa (Rosenthal, 2021). Delayed clearance has been linked to mutations in PfKelch13, a propeller domain protein important for early stage intraerthrocytic development such as ring stage survival and transition to trophozoite stage (*P. falciparum* life cycle is detailed below, 1.2) . Suggested roles of mutant PfKelch13 in artemisinin resistance are varied (Zhu et al., 2022). PfKelch13- containing vesicles have been shown to regulate uptake of haemoglobin; mutation of PfKelch13 may therefore prevent Artemisinin activation by reducing heme availability (Birnbaum et al., 2020). This can result in a prolonged ring stage and some fitness cost, which could explain why ACT resistance did not originate in Africa, where individuals are more frequently exposed to a variety of strains (Hanboonkunupakarn et al., 2022). However, artemisinin resistance has also been seen in parasites lacking any PfKelch13 mutations, suggesting alternative mechanisms (Das et al., 2021; Mukherjee et al., 2017); *in vitro* selection studies have also identified other genes that confer reduced artemisinin susceptibility (Demas et al., 2018). Given developments in ACT resistance and occurrence of multidrug resistant strains of *P. falciparum*, it is clear new antimalarials are desperately needed to help disease eradication (Hanboonkunupakarn et al., 2022).

1.1.1.3 Antimalarial vaccine development

Although several are in development, two vaccines, RTS,S/AS01$_E$ (Mosquirix) and R21/Matrix-M, have been approved for distribution to children under 5. Mosquirix was the first vaccine to become widely available and is designed to block initial parasitic infection in the human liver (malaria life-cycle is described below, 1.1.2). The efficacy of Mosquirix in children has been shown to be between 60 and 30%, dependant on child age, for 12 months

after 4 doses. Seasonal boosters in combination with the administration of antimalarials are recommended to maintain and ensure protection (Dicko et al., 2023). Demand for Mosquirix has far out-weighed supply; recent approval of a second malaria vaccine, R21/Matrix-M, for widespread use is anticipated to help meet the needs of endemic countries. R21/Matrix-M targets the same stage of *P. falciparum* infection as RTS,S/AS01$_E$ with similar efficacy after 4 doses, but is easier to manufacture at large scale and can be used at a lower dose meaning reduced cost ($2-4 per dose compared to $9-10) (Datoo et al., 2021).

Although both vaccines are promising, multiple doses are required for modest prevention. The genetic diversity of both parasites and the African population will also challenge and cause variability in vaccine efficacy (Tukwasibwe et al., 2023). New approaches to treatment and prevention of malaria are essential for continued decline in mortality. These could come from novel insights into the biology of *Plasmodium*, specifically the erythrocytic cycle for which there is not currently a vaccine in use.

1.1.2 *Plasmodium falciparum*

Plasmodium falciparum is a protozoan parasite of genus *Plasmodium*, which is an apicomplexan. Apicomplexans are distinguished by their mode of host cell invasion and an apical complex consisting of microtubule polar rings, secretory organelles, micronemes and rhoptries, at one end of the cell (Fig 1.1)(Cowman & Crabb, 2006).

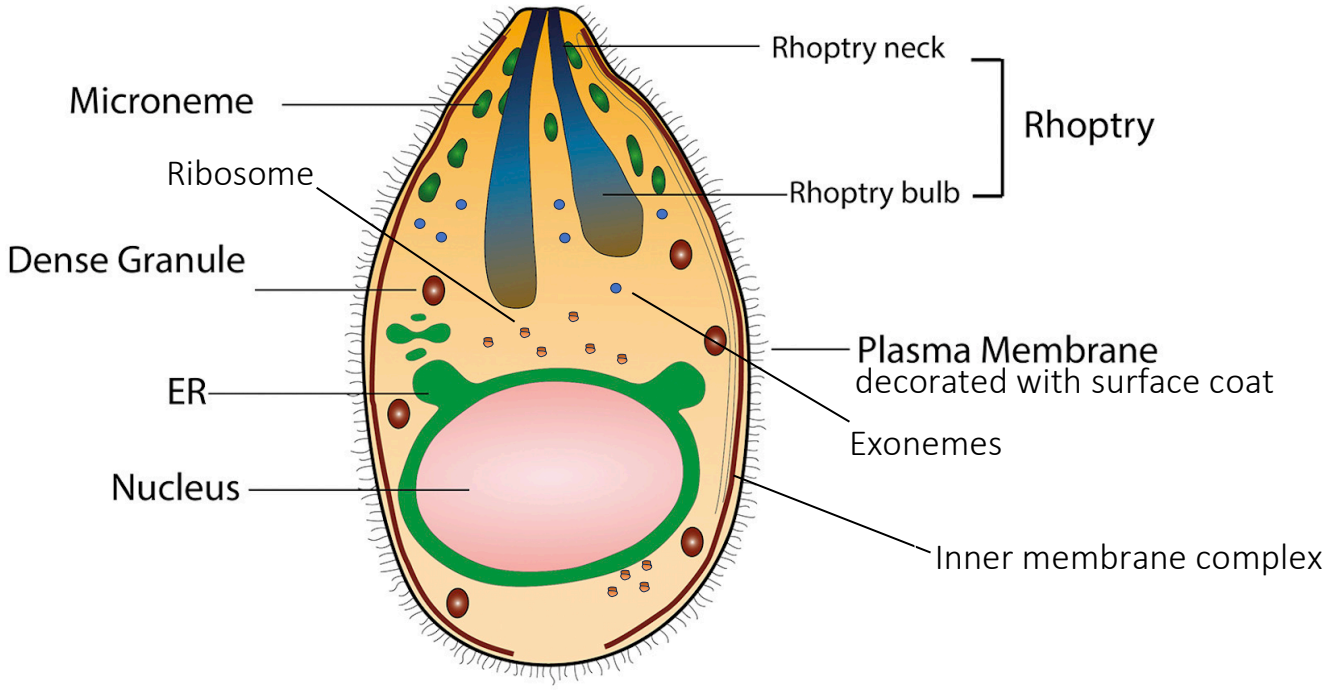

Figure 1.1 - Schematic of a Plasmodium falciparum merozoite with organelles labelled

Figure adapted (labels edited) from Cowman et al 2017, Copyright obtained from Cell Press, liscence no.: 5704410947693 . Note that recent research has suggested an alternative orientation of the organelles (Yahata et al., 2021)

The lifecycle of *P. falciparum* is well documented (Fig 1.2). A mosquito vector introduces sporozoites into human hosts, and these migrate to the liver and the parasite replicates in hepatocytes within a parasitophorous vacuole (PV) (Cowman et al., 2016). This produces liver stage schizonts, which segment to form merozoites then rupture by a parasite mediated process known as egress, releasing merozoites. These enter the blood stream and

invade erythrocytes, in which they asexually replicate, again in a PV. Merozoites then egress to invade fresh erythrocytes. Replication is by schizogony, meaning a multinucleated schizont forms before budding and segmentation into individual merozoites. In *Plasmodium falciparum* the intraerythrocytic replication cycle takes ~48 hr and produces 16-32 daughter merozoites; repetition of this cycle results in malarial pathology (Collins et al., 2017; Hale et al., 2017).

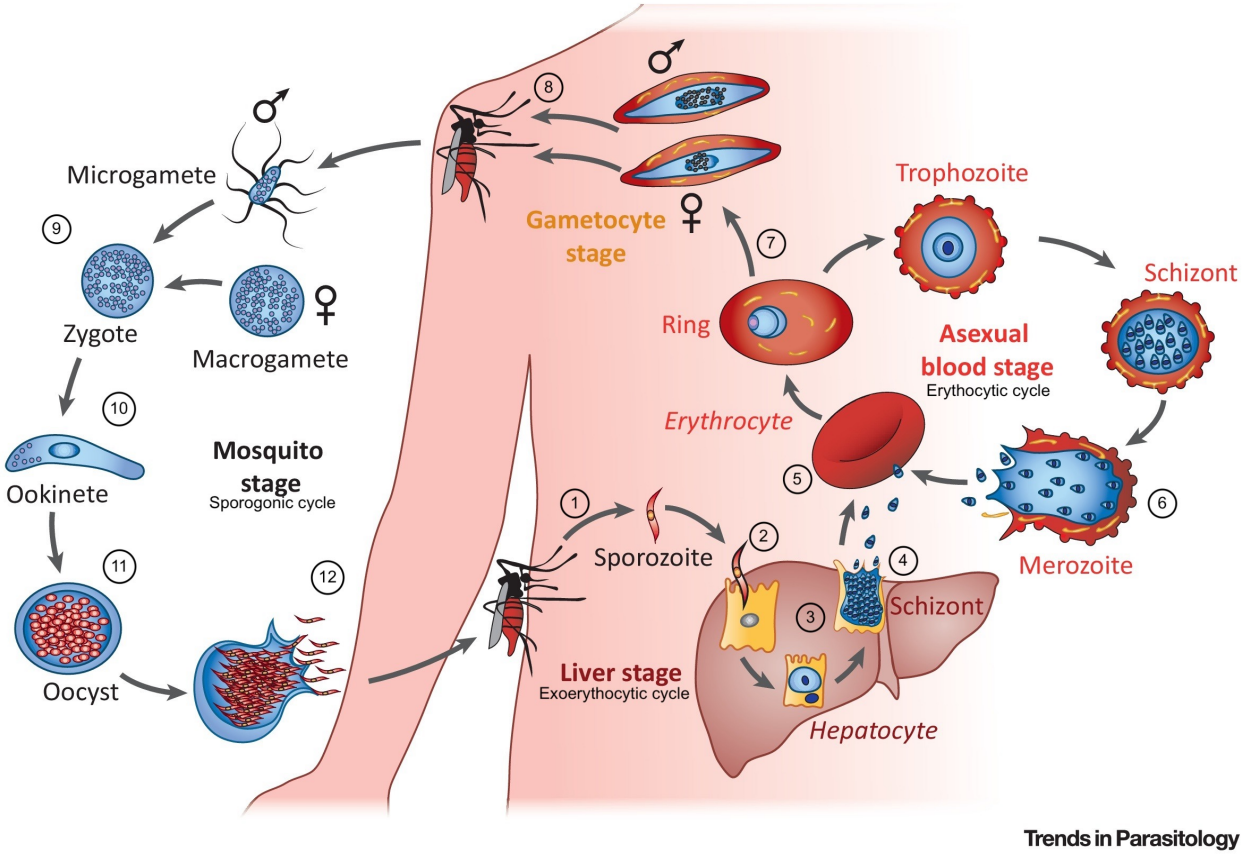

Figure 1.2 - Schematic representing the Plasmodium life cycle

During a blood meal, a malaria-infected female Anopheles mosquito transfers sporozoites into the human host ***(1)****, which infect hepatocytes* ***(2)****. This is the exoerythrocytic cycle. Sporozoites mature into schizonts* ***(3)****. The schizonts rupture and release merozoites* ***(4).*** *Merozoites enter the circulation and invade RBCs (the erythrocytic cycle). The merozoites*

develop from ring-stage trophozoites to late trophozoites and finally schizonts by synthesis and replication. ***(5).*** *The schizonts rupture, releasing merozoites in a process known as egress. Released merozoites then go on to re-infect new RBCs* ***(6).*** *A small subset of rings differentiate into gametocytes in the bone marrow or spleen* ***(7)****. During a blood meal, an Anopheles mosquito ingests the male (microgametocytes) and female (macrogametocytes) gametocytes, beginning the sporogonic cycle* ***(8).*** *In the mosquito's midgut, gametocytes mature into gametes and the microgametes fertilize the macrogametes, producing zygotes* ***(9).*** *The zygotes become motile and elongated, developing into ookinetes* ***(10).*** *The ookinetes invade the midgut wall of the mosquito where they develop into oocysts* ***(11).*** *The oocysts grow, rupture, and release sporozoites, which travel to the mosquito's salivary glands. Inoculation of the sporozoites into a new human host propagates the malaria life cycle* ***(12)****. Figure taken from A.G Maier et al, 2019, Copyright permission obtained from Cell Press, license no.: 5705561190051.*

Some merozoites commit to sexual development; infected RBC leave the peripheral circulation and enter the bone marrow where they differentiate from stage 1-V gametocytes. Environmental stress, such as high parasitaemia or exposure to antimalarials, can result in increased gametocytogenesis, which takes around 11 days. Development in the bone marrow avoids spleen clearance. Stage V gametocytes then enter the peripheral circulation, are ingested by female mosquitos feeding on the infected blood and enter the mosquito life stages or sporogonic cycle(Cowman et al., 2016). In the mosquito stomach gametocytes mature into either eight flagellated micro-(male) gametes or one macro-(female) gamete; a macrogamete is fertilised by a microgamete to form zygotes in the

stomach. Zygotes then develop into ookinetes and invade the midgut wall where they form oocysts. Oocysts rupture to release sporozoites, which move to the salivary glands to allow infection of alternative hosts and hence, disease spread (A.G Maier et al., 2019). Despite cellular understanding, there are gaps in our understanding of malaria molecular biology. It is necessary to understand this fully for treatment and vaccine development.

1.2 The intraerythrocytic cycle: invasion of host red blood cell by merozoites

Erythrocyte invasion occurs once merozoites are released into the hepatic circulation. Invasion is a multi-step process, beginning with pre-invasion: initial interactions between the parasite and erythrocyte; erythrocyte membrane deformation; merozoite re-orientation and the discharge of proteins from secretory organelles (Figure 1.3). Active invasion follows, in which a tight junction forms between the host cell membrane and the apical end of the merozoite, through which the merozoite enters the red blood cell in an actin-myosin driven process. The formation of the parasitophorous vacuole (PV) occurs simultaneously. Finally, there is a brief shrinking and deformation of the RBC by spiky protrusions occurs, a process known as enchinocytosis (Cowman et al., 2017).

The macromolecules mediating the initial contact with the RBC remain largely undetermined, but merozoite surface proteins are thought to play a role (see section 5). Once contact is made, a tighter interaction between the host cell and merozoite is formed as a result of the association of parasite adhesins, Erythrocyte binding antigen proteins (EBAs, also known as Duffy binding-like) and reticulocyte- binding proteins (Rhs) bind to

receptors on the erythrocyte cell membrane (Cowman et al. 2016). These adhesins are likely released from micronemes and discharged onto the merozoite surface in response to increased cytosolic calcium levels. This may be due to low K^+ ion concentration in the blood plasma leading to downstream protein kinase A or phospholipase C activation, causing release of Ca^{2+} from parasite internal stores (Dawn et al., 2014). The binding of EBAs to glycophorins on the RBCM, such as EBA-175 to glycophorin A, triggers secretion of proteins from rhoptries (Cowman et al. 2017).

Another increase in cytosolic Ca^{2+} concentration accompanies adhesin-mediated interactions. This activates the parasite serine/threonine phosphatase Pf Calcineurin, which acts to strengthen adhesin – host receptor interaction. This may cause adhesin dimerization, which may trigger downstream signalling events that aid invasion(Paul et al., 2015). The erythrocyte membrane warps upon initial merozoite contact, allowing further EBA and Rh binding to erythrocyte receptors. This leads to RBCM deformation and wrapping around the merozoite. After the erythrocyte membrane is deformed, the merozoite orientates so that the apical end is in contact with the erythrocyte membrane (Dasgupta et al., 2014). This is facilitated by RBCM deformation and involves PfRh5 binding to the basigin receptor on the RBCM(Weiss et al., 2015). This interaction results in Ca^{2+} influx into the host cell and activates invasion. A tight junction between the merozoite and the erythrocyte is formed; AMA1-RON2 interaction is essential for this. Rhoptry neck protein 2 (RON2) is secreted from rhoptries, deposited into the erythrocyte membrane and binds micronemal AMA1 on the merozoite surface (Srinivasan et al., 2013).

Lipid-rich rhoptry contents, as well as host lipids from the RBC membrane, form the parasitophorous vacuole membrane (PVM) as the merozoite enters the erythrocyte (Matz et al., 2020). The tight junction moves from the merozoite apical to posterior pole, powered by the parasite's actinomyosin motor(Perrin et al., 2018). The actinomyosin motor anchors to the inner membrane complex (IMC), a double membrane bilayer found just inside the schizont plasma membrane (Absalon et al., 2016), the merozoite plasma membrane (PM) and the merozoite surface adhesins through the glideosome. The glideosome is a multiprotein machine, consisting of glideosome associated proteins that span and are confined between the IMC and PM (Frénal et al., 2010).

Upon reaching the posterior pole, the adhesive proteins at the tight junction are also proteolytically removed by the serine protease SUB2, a sheddase, in a process that facilitates resealing of membranes. The parasite invades in a manner that creates a parasitophorous vacuole and the RBCM is fused (Collins et al., 2020). Echinocytosis follows; the RBC returns to its normal shape within ~10 min (Cowman et al., 2012).

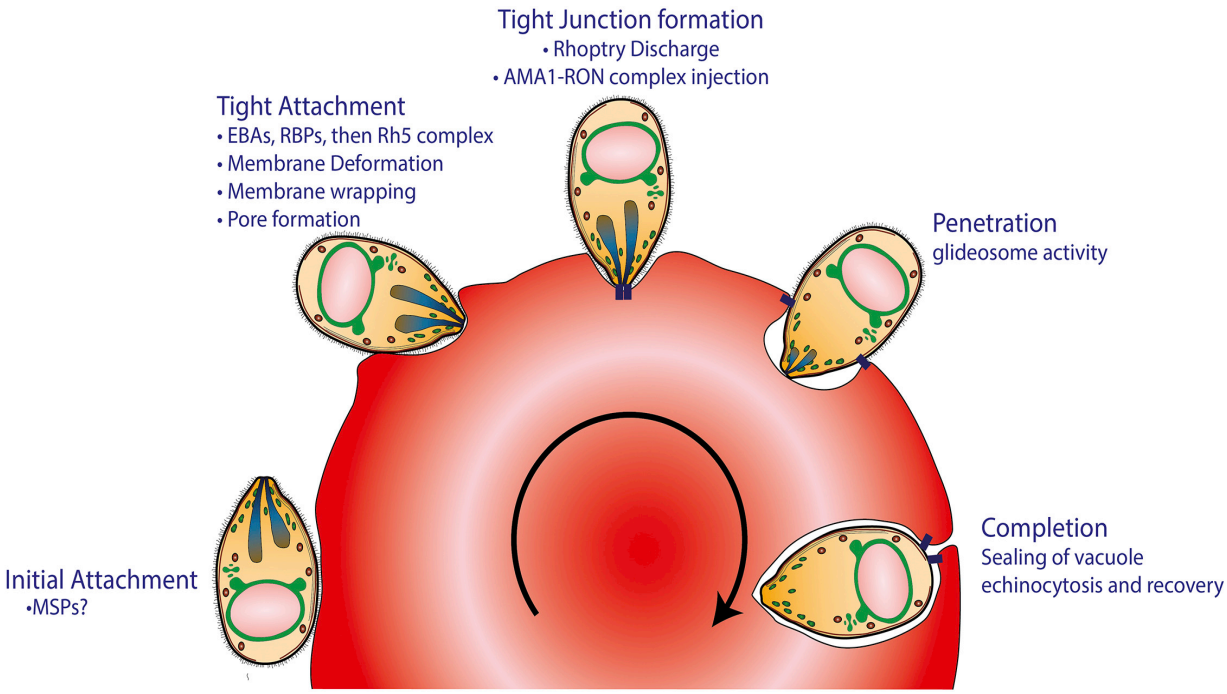

Figure 1.3 - The stages of invasion of the erythrocyte by the merozoite.

Figure taken from Cowman et al. 2017, Copyright permission obtained from Cell Host and Microbe.

1.3 The intraerythrocytic cycle: remodelling of the host cell and parasite replication

Post invasion, the parasite develops into an early trophozoite ring which matures into a late trophozoite as it consumes haemoglobin and replicates both DNA and organelles (Rudlaff et al., 2020). There is restructuring of the host cell and parasite replication. The parasite exports proteins (around 10% of the proteome) beyond the PVM to different locations within the erythrocyte, to change rigidity, permeability and cytoadherence of RBCs. Proteins are exported via a vesicle mediated pathway from the ER across the PM to the PVM. Protein translocon complex PTEX, that spans the PVM, mediates export into the host cell. Proteins

are threaded through a seven-fold symmetric channel, formed between interlocking proteins that make up PTEX core complex (Ho et al., 2018).

A trafficking network allows the sorting and moving of proteins to the erythrocyte cytosol, cytoskeleton or membrane(Cowman et al., 2016). Maurer's clefts, flattened disc shaped membrane structures that bud from the PV, are key features of this network that tether to the underside of the RBCM post invasion. Maurer's clefts, known to be involved in transport of PfEMP1 to the RBCM for parasite adhesion to the vascular endothelium, contain resident proteins that may aid protein loading for export (McHugh et al., 2020). Other vesicular structures, such as J dots and EDVs (electron dense vesicles), are also involved in mediating protein export. Exported parasite proteins cause remodelling of the erythrocyte cytoskeleton to withstand high temperatures and shear stress. Permeability pathways established at the RBCM allow the parasite to obtain nutrients and expel waste. Toxic heme accumulates as a result of parasite haemoglobin digestion and is stored in an insoluble, crystalline form known as hemozoin within the food vacuole of the parasite (Boddey & Cowman, 2013).

Over the 48 h post invasion, malaria parasites develop into schizonts, in which nuclear and organelle replication occurs rapidly, in an asynchronous manner. Daughter merozoites are then produced by budding and cytokinesis, which involves invagination of the single plasma membrane of the schizont around individual nuclei to produce 16-32 merozoites. The organisation of nuclei and apical organelles for packaging into merozoites is largely governed by interaction between by microtubules, that form the mitotic apparatus, and

kinetochore proteins. Interestingly, this is regulated independently from cytokinesis (Perrin et al., 2021; Tilley et al., 2023).

The mechanisms of segmentation are largely unknown. A study following this process using focused-ion beam scanning electron microscopy showed that, after PVM rupture, some daughter merozoites remain associated with the food vacuole, suggesting final membrane fission may occur late in segmentation, at the beginning of egress from the host cell. However, the authors admit this may have been an artefact of schizont preparation (Rudlaff et al., 2020). The IMC is thought to act as a scaffold for segmentation, defining the adjacent boundaries of individual daughter merozoites, with the exception of the poles (Rudlaff et al. 2019). At the apical end of daughter merozoites, the apical ring forms microtubules to stabilise the IMC. At the opposite pole, a basal complex is associated with the newly forming edge of the IMC and thought to act as a contractile ring, ensuring the IMC spans the length of daughter cells during segmentation and the completion of membrane fusion. Genetic disruption of the basal complex results in incomplete merozoite cytokinesis (Rudlaff et al., 2019). *P. falciparum* merozoite organising protein 1 (PfMOP1) is believed to aid proper formation of the IMC (Absalon et al., 2016).

1.4 The intraerythrocytic cycle: Egress of merozoites from the red blood cell

Egress is the process by which merozoites escape from the host cell. *Plasmodium* egress from RBCs occurs rapidly, after a series of tightly regulated steps, and is cytolytic. This causes tissue damage, inflammation and the release of pyrogens that activate an immune response and result in fever. Understanding of each stage, the pathways leading to egress

and the key proteins directly involved in membrane rupture, is not complete. However, there are proposed models of the mechanics of egress. There is also much evidence for a *P. falciparum* protein kinase G mediated biochemical pathway, leading to protein secretion, the activation of a cascade of parasite proteolytic enzymes and subsequent membrane rupture (Blackman, 2008; Blackman & Carruthers, 2013; Thomas et al., 2018).

There may also be a role for host cell proteases. Apicomplexans such as *Toxoplasma gondii* have been shown to facilitate egress by hijacking host cell calpain I, a Ca^{2+} dependent cysteine protease that remodel mammalian cell cytoskeleton during migration. *P. falciparum* may also do so to escape the red blood cell by a mechanism relating to RBC cytoskeleton degradation; activated calpain-1 has shown to degrade erythrocyte cytoskeletal components in vitro (Chandramohanadas et al., 2009). However, when RBCs isolated from mice with the mouse Caplain-1 isoform knocked out, were infected with *P. falciparum,* parasite replicated normally (Hanspal et al., 2002). The role of host proteases in the egress of merozoites in the intraerythrocytic cycle, if any, remains unclear and will not be discussed further.

1.4.1 The cellular stages of merozoite egress from the red blood cell

Initial theories of the mechanics of egress, largely determined via video light and electron microscopy, have been summarised into 4 schematics by Blackman et al (2008). Current work strongly supports the inside-out model: degradation of the PVM, followed by RBC membrane rupture (Figure1-4). Further investigations into egress (Hale et al., 2017) suggested that, following merozoites segmentation of the mature schizont, the PV rounds, the PVM porates, allowing mixing of residual RBC cytoplasm and the contents of the PV. The

PV then swells, the entire infected RBC transforms from what appears to be an 'irregular' shape, as a result of the visibility of remnants of the RBC bi-concave disk, to a more rounded appearance. The merozoites arrange around the food vacuole in a process known as 'flower formation' (Glushakova et al., 2018) and become more visible within the PV. The PVM then fragments into multilamellar vesicles. The RBC membrane loses tension, collapses around the merozoites and then porates (Hale et al., 2017; Matz et al., 2020) (Figure 1.5). Finally, the RBCM ruptures, which starts by breaking at a single point. The membrane curls open to allow merozoite release; RBCM spontaneous curvature is also believed to force remaining merozoites out of the host cell. Vesicles and membrane ghosts remain (Callan-Jones et al., 2012).

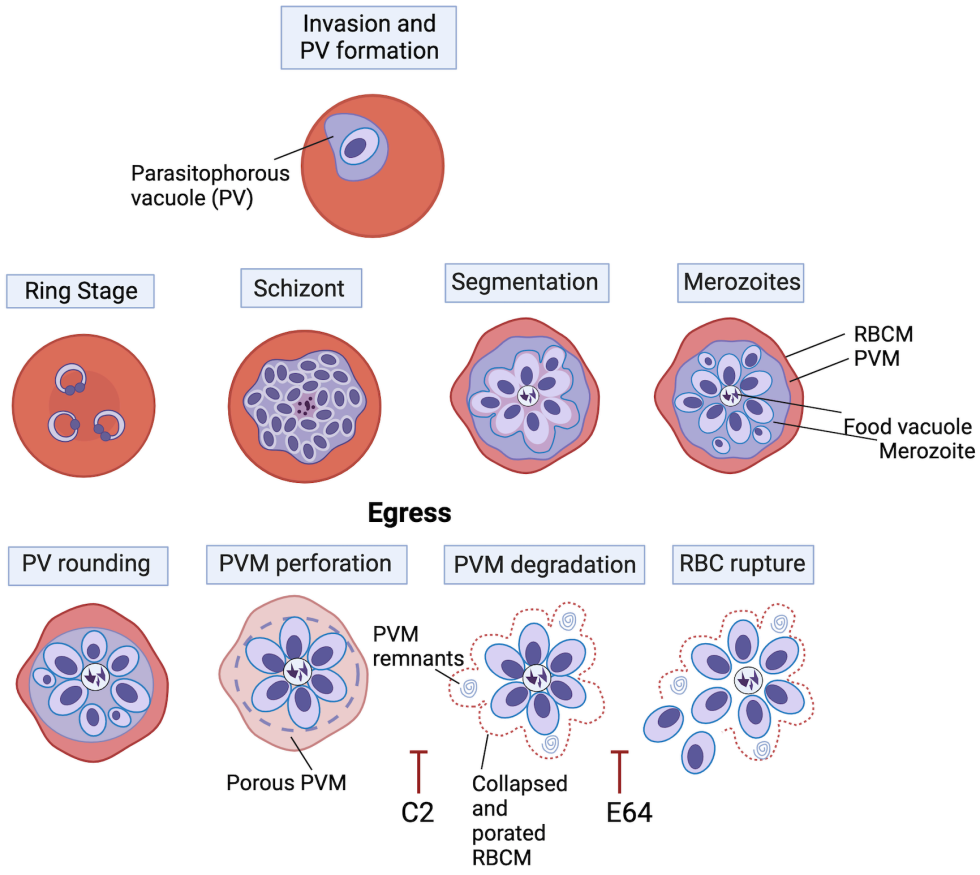

Figure 1.4 - A basic overview of progression from invasion to schizont and subsequent merozoite egress.

The multinucleated trophozoite undergoes further replication, or schizogony, followed by segmentation to form individual merozoites and the schizont. There is rounding of the parasitophorous vacuole, and the PVM porates. 'Flower formation', in which the merozoites arrange around the food vacuole, occurs; the PVM fragments and the RBC membrane collapses and porates. The contents of the RBC leak and the RBCM then ruptures at a single point, releasing merozoites, that can then go on to reinvade fresh host cells. C2 (C2) inhibits PVM degradation and E64 (cysteine protease inhibitor epoxysuccinyl-Lleucylamido(4-guanidino)butane) inhibits RBCM rupture – these are discussed in greater detail below. Figure adapted from Matz et al 2020

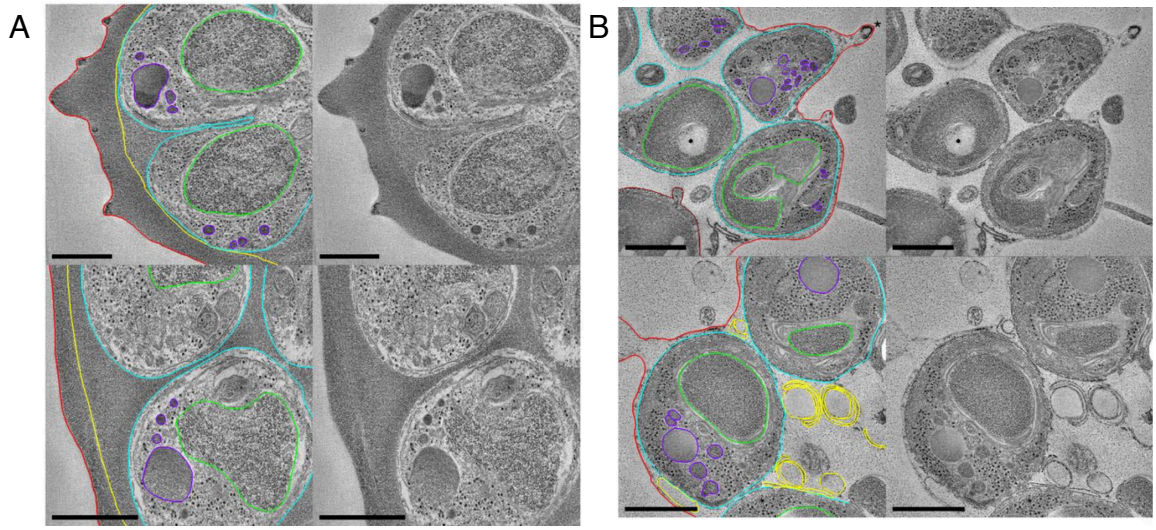

Figure 1.5 - Tomograms of Compound 1 and E64 stalled schizonts.

Micrographs taken of freeze substituted sections, showing the morphology of the PVM (yellow), RBCM (red) and the plasma membrane of the merozoite (cyan). (A) C1 treated schizonts either undergoing segmentation (top) or fully segmented (bottom). Merozoite nuclei (green) and apical organelles (purple) are also highlighted. (B) Sections of schizonts arrested by E64. The PVM has degraded to form multilamellar vesicles (yellow). The food vacuole is visible in this section (brown). For each section, the labelled and unmodified images are shown in pairs. Scale bars, 500 nm. Figure taken from Hale et al 2017, PNAS open access, reuse approved, https://creativecommons.org/licenses/by/3.0/.

1.4.2 A Protein kinase G mediated pathway has a key role in the egress of merozoites from the host cell

Gradually, through reverse genetics, chemical inhibition and proteomics, a parasite protein kinase PfPKG dependent pathway controlling egress has emerged (Blackman & Carruthers, 2013; Hale et al., 2017; Koussis et al., 2020). Parasite cGMP-dependent protein kinase PKG is localised in the merozoite cytosol and is a central mediator of merozoite egress from the RBC. PKG is essential for the initiation of this process by triggering an increase in cytosolic Ca^{2+} and hence, release of necessary proteins from secretory organelles (Collins, Hackett, et al., 2013; Koussis et al., 2020). No other roles as a scaffolding or adaptor protein in intraerythrocytic development have been found for PKG (Koussis et al., 2020). PfPKG requires cytosolic cGMP for activity, generated by guanylyl-cyclase-alpha (GC-α)(Nofal et al., 2021). Accumulation of cGMP results in premature or over activation of PKG; cGMP production is regulated by parasite phosphatase 1 suppressing GC-α (Collins, Hackett, et al., 2013; Nofal et al., 2021; Paul et al., 2020)). Other unknown triggers may activate PKG. These appear to be endogenous, although recent data also has shown that exogenous phosphatidylcholine can trigger egress (Paul et al., 2020).

Once activated, PKG stimulates an increase in cytosolic Ca^{2+} concentration by causing ion release from an intracellular Ca^{2}+ store. The location of this store and mechanism by which release occurs are currently unknown. This increase in Ca^{2+} controls PV rounding and is thought to result in the release of proteins from secretory organelles (Collins, Hackett, et al., 2013; Glushakova et al., 2013; Yeoh et al., 2007). However, there is evidence to suggest PKG may cause secretion of proteins by other means (Balestra et al., 2021).
Secretion occurs primarily from exonemes and micronemes, of which there are believed to be several subtypes (Absalon et al., 2018) . A calcium-dependent protein kinase called

CDPK5 is activated by this rise in Ca^{2+} and is also required for release of egress specific organelles, acting co-operatively with PfPKG (Absalon et al., 2018; Dvorin et al., 2010)

Work from Garg et al suggests that the increase in merozoite intracellular Ca^{2+} following PKG activation results in release of Perforin-like proteins, namely PLP1, from micronemes. The *P. falciparum* genome encodes 5 Perforin-like proteins (PLP) that work in different combinations and form pores in a multistep process(Garg et al., 2013). PLP1 monomers were shown to bind and oligomerise at the erythrocyte membrane, forming pores. This is proposed to lead to host cell membrane permeabilization (Garg et al., 2013, 2020). Furthermore, a recombinantly expressed conserved domain known as the membrane attack complex pore forming (MACPF) domain, centrally located in all PLPs, has also been shown to interact with erythrocytes to form pores in the membrane. Pore formation results in haemoglobin release and dextran uptake. Inhibitors of this MACPF domain blocks growth of *P. falciparum* in RBCs by suppressing both invasion and egress in a dose dependent manner (Garg et al., 2020). However, reverse genetic studies imply that PLP1 and 2, both individually and in combination, are not essential for the intraerythrocytic cycle (Ramaprasad et al., 2023; Yang et al., 2017). In other work, PLP1 has been shown to have a role in hepatocyte infection but was not detected in blood stage malaria (Yang et al., 2017). A role in asexual blood stage egress for PLPs, secreted due to PKG mediated cytosolic Ca^{2+} increase, is not clear.

Egress has been shown to be protease dependent and this PKG mediated pathway is believed to lead to the activation of a cascade of proteases (Figure 1.6). In early work, cysteine, serine and aspartic protease inhibitors were shown to block egress, whilst

preventing the processing and shedding of a range of parasite proteins. Serine protease inhibitor leupeptin and cysteine protease inhibitor epoxysuccinyl-Lleucylamido(4-guanidino)butane (E64) individually block egress and prevent rupture of the PV and RBC membranes respectively(Blackman, 2008). SUB1 is a parasite subtilisin that is discharged into the PV from exonemes, triggered by PKG activity; subtilisins are serine proteases that possess a Asp/Ser/His catalytic triad (Yeoh et al., 2007). SUB1 proteolytically modifies several merozoite surface and PV proteins (De Monerri et al., 2011). Many of these have themselves been released from micronemes. Direct inhibition of SUB1 with small molecules completely stalls egress (although the PVM still porates) and so PKG mediated release of this protease is essential for merozoite release (Yeoh et al., 2007). Furthermore, certain pharmacological inhibitors of PKG, termed compound 1 and C2, block SUB1 release and prevent rupture of the PVM and RBCM, demonstrating the central role of PKG in egress initiation (Collins, Hackett, et al., 2013; Hale et al., 2017; Taylor et al., 2010)

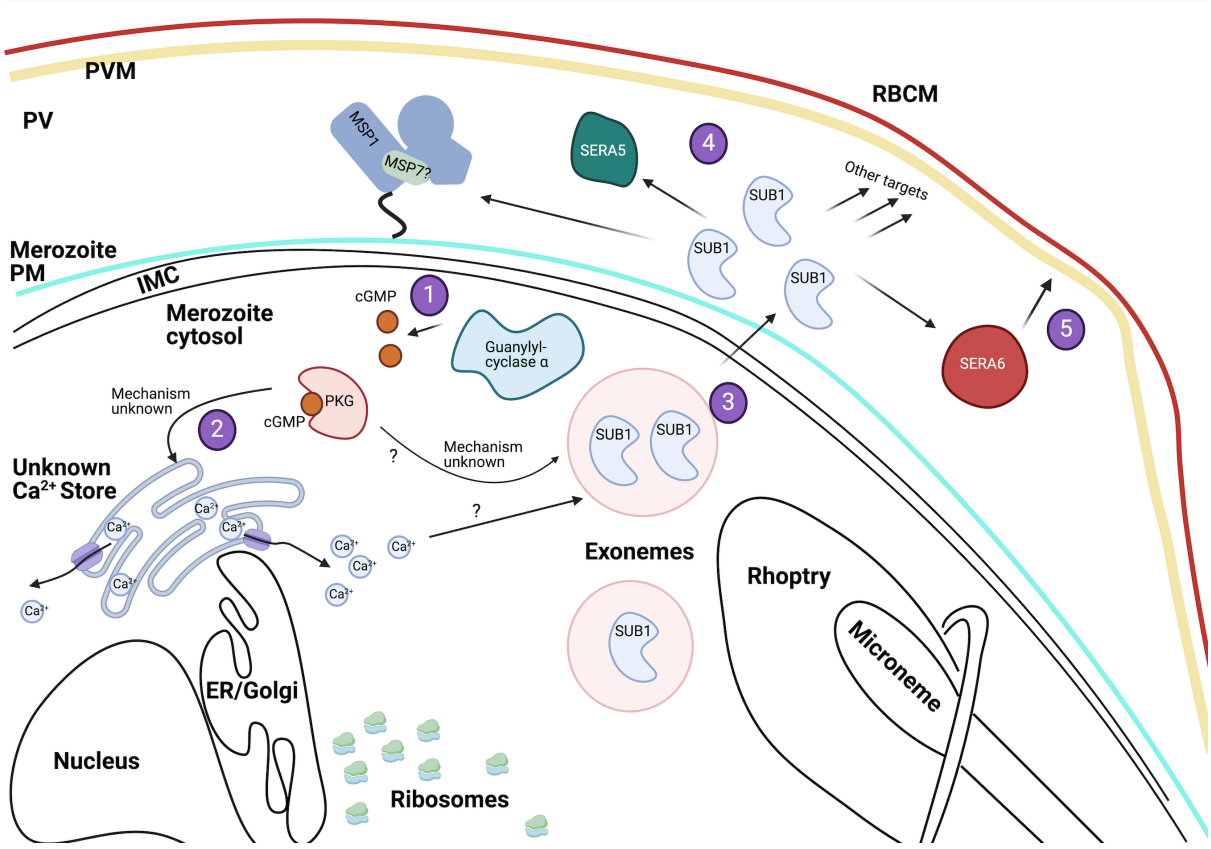

Figure 1.6 - Diagram summarising the P. falciparum cGMP dependent Protein Kinase G mediated pathway that results in merozoite egress from the RBC.

1) Protein Kinase G is activated by cGMP, produced by Pf Guanylyl cyclase. 2) PKG acts to cause release of Ca^{2+} from unknown stores. 3) This may result in trafficking of exonemes to the merozoite surface and release of SUB1 into the parasitophorous vacuole, possibly by membrane fusion, although there is evidence PKG may cause this to occur by another unknown mechanism. SUB1 is a serine protease, produced as a zymogen, which then undergoes autocatalytic processing and accumulates in exonemes. Within or during trafficking to the exonemes, SUB1 is activated by an aspartic protease called plasmepsin X. SUB1 has numerous targets, including a set of PV-located papain-like proteins SERAs 4/5 – which have a cysteine protease domain but do not all have a cysteine in the catalytic position - the merozoite surface proteins MSP1/6/7, and rhoptry proteins. 4) SERA 5 may act to regulate the progression of egress by occupying SUB1 and preventing cleavage of other proteins – KO shows egress occurring prematurely. SERA5 does not have a catalytic domain, although there is site directed mutagenesis evidence to the contrary. 5) In contrast to SERA5, SERA6 has an undisputed proteolytic domain, which is exposed as a result of SUB1 processing. SERA6 cleaves within the actin-binding domain of the RBC cytoskeletal protein β-spectrin, leading to RBCM disintegration.

1.5 The proteolytic targets of parasite subtilisin SUB1 and their suggested roles in egress

Like many proteases, SUB1 is produced as a zymogen, which then undergoes autocatalytic processing and accumulates in exonemes (Sajid et al., 2000). Within or during trafficking to the exonemes, SUB1 is activated by an aspartic protease called plasmepsin X (Nasamu et al., 2017; Pino et al., 2017). SUB1 has numerous targets, including a set of PV-located papain-like proteins SERAs 4/5/6, the merozoite surface proteins MSP1/6/7, and rhoptry proteins. Comparison of the cleavage of known substrates of SUB1 has allowed identification of a cleavage sequence consensus. This appears to comprise a polar residue at position P1 (Ile/Leu/Val/Thr), an uncharged residue (Ala/Gly) at position 2, an aliphatic residue at position P4 (Phe/Xaa) and between position P1'-5', one or more residues must be acidic. Positions are counted from the point of cleavage, between position 1 and position 1', position 1-5 and position 1'-5' move away from the site of cleavage toward the N-terminus and C-terminus respectively (Das et al., 2015; De Monerri et al., 2011) . Many targets, though confirmed by proteomics, were initially identified by location of a SUB1 cleavage sequence consensus (De Monerri et al., 2011)(Figure 1.7).

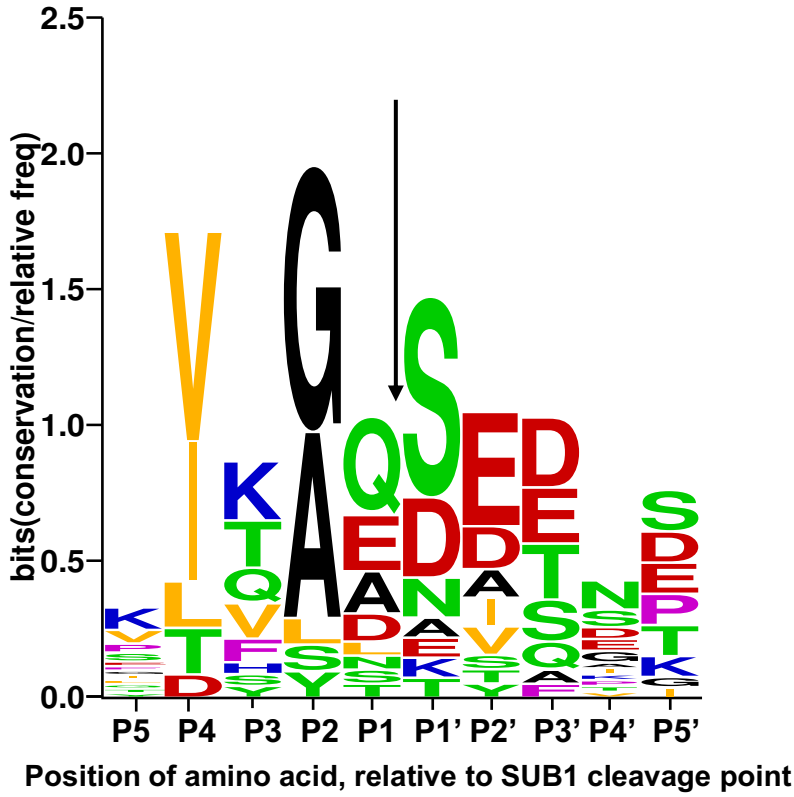

Figure 1.7 - Graphical representation in single-letter code of a multiple-sequence alignment of amino acid residues flanking known PfSUB1 cleavage sites.

Alignment of the sequences of SERA5, SERA4, SERA6, MSA180, MSRP2, RAP1, MSP1, MSP6, and MSP7, and the internal PfSUB1 autocatalytic SUB1 processing site. The y axis is in arbitrary units (bits); the overall height of each stack of residues indicates level of sequence conservation at that position and the height of each letter in a given stack indicates the relative frequency of the corresponding amino acid residue at that position. Residues are colour coded according to the nature of side chains (red, acidic; blue, basic; orange, aliphatic; black, small; green, uncharged polar; and purple, nonpolar, nonaliphatic). The scissile bond is indicated by an arrow. Residue numbering is according to the system of Schechter and Berger. Figure was adapted and recreated from De Monerri et al, using data

from De Monerri et al., 2011; Tan et al., 2021; Withers-Martinez et al., 2012 .

Weblogo.berkeley.edu was used to generate this graph.

1.5.1 PV-located SUB1 substrates involved in egress: Serine repeat antigens (SERAs)

Serine repeat antigens (SERA) 5 and 6 are soluble proteins expressed in the PV and are orthologues of proteins involved in oocyte egress in the mosquito midgut (Blackman 2008). All SERAs have a papain-like cysteine protease domain, though that of SERA5 has a Ser in place of a Cys at the key catalytic position (Blackman, 2008; Collins et al., 2017). Both PfSERA5 and PfSERA6 are targets for processing by PfSUB1 and have been shown to be involved in egress. SERA5 and 6 are secreted into the PV and cleaved by SUB1 at two sites, upstream and downstream from the papain-like domain, causing release of this domain. The remaining C and N terminal fragments remain associated by a disulphide bond (Collins et al., 2017; Stallmach et al., 2015; Tan et al., 2021; Yeoh et al., 2007).

Though extensively studied, the function of SERA5 is unclear; the expression and processing of this protein is however required for egress (Collins et al., 2017; Yeoh et al., 2007). It has been suggested that SERA5 does not act as a protease. Site-directed mutagenesis of the *P. falciparum* SERA5 gene resulting in expression of SERA5 with an Ala in place of the Ser at the pseudo- catalytic position (Ser596 –Ala596) in the papain-like domain did not cause an abnormal phenotype (Stallmach et al., 2015). Therefore, SERA5 has been proposed to kinetically regulate egress by buffering SUB1 to delay processing of other proteins that lead to PVM rupture. Parasites lacking SERA5 have accelerated but defective egress, due to improper PVM and RBCM rupture(Collins et al., 2017). However, a parasite line expressing

SERA5 processing a Ser to Arg mutation at what would be the key catalytic position site could not be established using homologous recombination, and furthermore recombinant expression of a SERA5 with a Ser-to-Cys mutation (Ser596-Cys596) produced a proteolytic enzyme. These data indicate that the pseudo-catalytic cleft is involved in protein-protein binding and interaction (Stallmach et al., 2015). Another study has shown that the increase in cytosolic levels of Ca^{2+} activates protein kinase PfCDPK1, which phosphorylates SERA5. Phosphorylated SERA5 appears to have protease activity, cleaving LLY-AMC fluorescent peptide substrate. Inhibition of SERA5 phosphorylation blocks egress, suggesting that SERA5 may not simply act as pseudo-protease buffer for SUB1 processing (Iyer et al., 2018).

In contrast to SERA5, SERA6 has an undisputable proteolytic domain, which is exposed as a result of SUB1 processing (Ruecker et al., 2012). SERA6 then undergoes autoproteolytic activation, which is facilitated by SUB1-cleaved PV resident protein MSA180. MSA180 may also act as a scaffold to localise SERA6 to the RBCM. SERA6 cleaves within the actin-binding domain of the RBC cytoskeletal protein β-spectrin, that is anchored to the RBCM; β-spectrin cleavage leads to RBCM disintegration (Tan et al., 2021; Thomas et al., 2018).

1.5.2 PM-located SUB1 substrates involved in egress: Merozoite Surface Protein 1 (MSP1)

Merozoite Surface Protein 1 (MSP1) is a 190 kDa glycosylphosphatidylinositol (GPI) anchored protein expressed on the surface of merozoites. There are 2 isoforms of MSP1 (D and F), named based on the *P.falciparum* isolates in which they were identified (3D7 and FCB1/Wellcome, respectively). MSP1 is extensively processed by SUB1 just prior to egress;

there are three SUB1 cleavage sites, named 80/30, 30/38, 38/42, named after the size of the resulting polypeptide fragments, p80, p30, p38, p42. The sequence at the 38/42 cleavage site is conserved between isoforms and has 3 adjacent cleavage points: alternative 1, alternative 2 and the canonical site (alt1, alt2, can). Once processed, MSP1 fragments remain non-covalently associated at the merozoite surface (Child et al., 2010; Das et al., 2015; Kauth et al., 2003). MSP1 associates with other surface proteins including MSP6 and 7 (Crosnier et al., 2013; Kauth et al., 2006; Lin et al., 2016); the cleavage of MSP1 is thought to allow the binding of other parasite proteins (Das et al., 2015; Kauth et al., 2006). Once merozoites have egressed and the invasion of a new RBC and tight junction formation has been initiated, the MSP1 42 kDa fragment is cleaved by the subtilisin sheddase SUB2 (Collins et al., 2020; Harris et al., 2005). This leaves a 19 kDa fragment on the surface of merozoites. The function of MSP1 is unknown but there is strong evidence that MSP1 has a role in egress (Das et al., 2015) A conditional mutant line of *P. falciparum* was generated by Das et al, in which rapamycin (RAP) triggers gene excision by DiCre recombinase (see Methods 2.2.2) . This enabled expression of a truncated form of MSP1, lacking a GPI surface anchor, to be induced. MSP1 was not bound to the merozoite surface and therefore soluble in the PV. RAP treated parasites displayed an egress defect in which the merozoites did not disperse normally after egress and the RBCM did not appear to rupture. This suggested that MSP1 is required for successful egress and must be tethered to the merozoite surface to perform this function(Das et al., 2015).

The egress defect described above is also observed when SUB1 processing of MSP1 is disrupted. Cleavage at the 38/42 site is rate limiting for complete processing of MSP1 and appears to be crucial for egress(Child et al., 2010; Das et al., 2015). A MSP1 38/42 cleavage

resistant mutant with only the canonical 38/42 SUB1 site remaining, developed using single homologous cross over, was shown to be a poor substrate for SUB1. The kinetics of processing of this mutant in comparison to wildtype was checked by western blot of lysed schizonts at different time periods after Compound 1 treatment and removal. Mutant processing was shown to be slower than in wild type. Egress of merozoites in this line is shown to be stalled as demonstrated by video microscopy (Das et al., 2015), suggesting that not only is MSP1 involved in egress, but SUB1 processing is essential for its function.

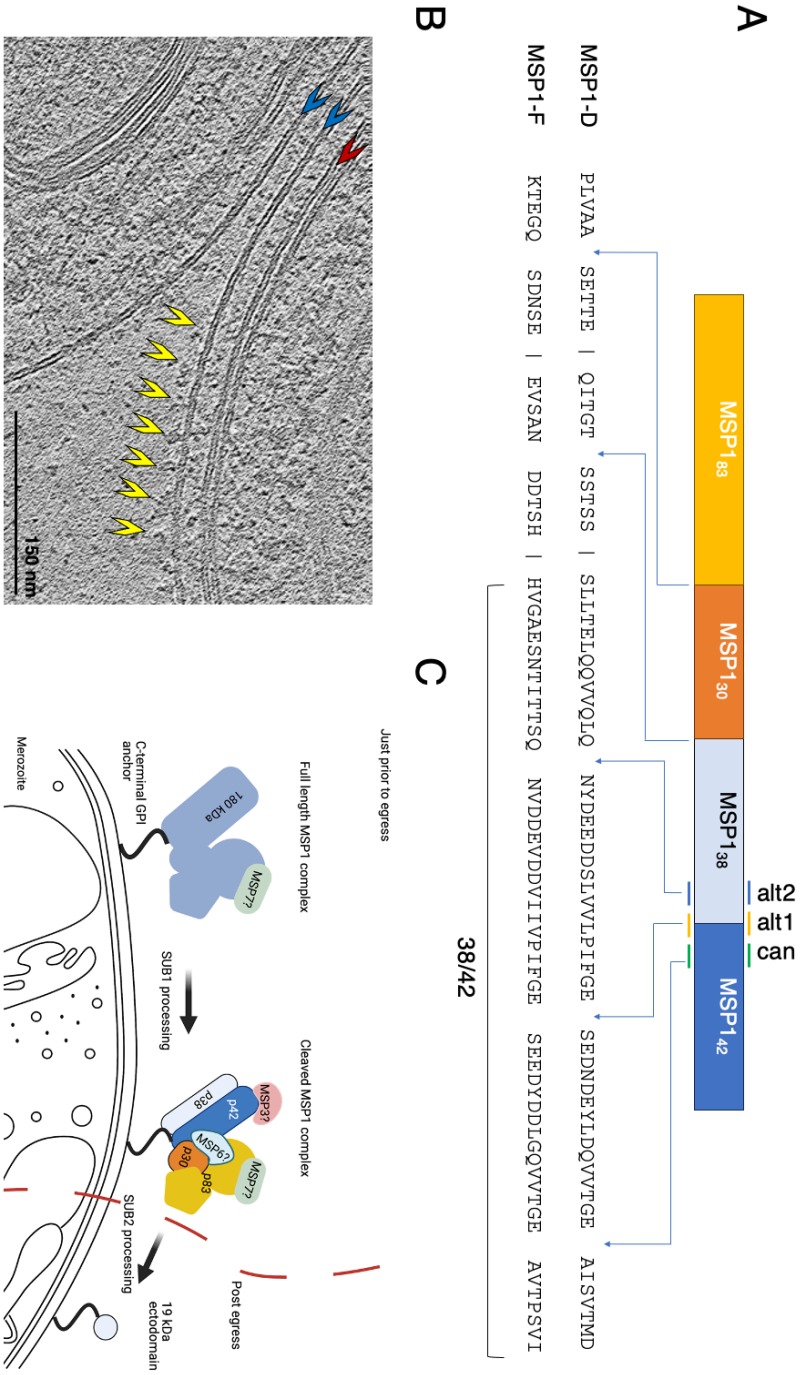

Figure 1.8 - Merozoite surface protein 1 (MSP1).

A) *A diagram showing the cleavage sites of SUB1 and the amino acid sequence of each site for the 2 isoforms of MSP1, MSP1-F and MSP1-D. Adapted from Das et al 2015*

B) *A EM-tomogram showing the merozoite plasma membrane, highlighted with the blue arrow (IMC highlighted with red arrow), which is heavily decorated with MSP1, some of the decoration is indicated with yellow arrows. Labelled Cryo-EM tomogram, produced by C.Bisson, unpublished.*

C) *A schematic showing possible arrangement of MSP1 before and after processing by SUB1 and SUB2, prior and post egress respectively. Possible interactions with some of the predicted binding partners are shown, including merozoite surface proteins 3/6/7/9 (MSP3/6/7/9) and duffy binding like proteins 1 /2 (DBL 1/ 2).*

Between PVM rupture and egress, merozoites come into contact and may interact with the inner surface of the host cell membrane to promote rupture and dispersal. Cleavage at the 38/42 site by SUB1 may induce a conformational change in MSP1 that enables MSP1 to bind and promote the rupture of the RBCM. Circular dichroism has shown that SUB1 processing of a soluble recombinant MSP1 (rMSP1-wt) expressed in HEK293E cells induces changes in the protein's secondary structure. These changes were more distinct than those seen when SUB1 was added to recombinantly expressed MSP1 lacking the 38/42 SUB1 cleavage site (rMSP1-mut) (Das et al., 2015). The capacity of SUB1 cleaved rMSP1-wt in comparison to uncleaved rMSP1 to bind a host intracellular component was investigated. Cleaved rMSP1 was shown to bind more components from permeabilised erythrocytes by far western blot than uncleaved. When inverted vesicles produced from lysed RBCM are incubated with cleaved or uncleaved rMSP1, there was greater pull down of cleaved MSP1 by western blot analysis. Finally, erythrocyte ghosts were fractionated and then run in an SDS-PAGE gel which was probed with cleaved rMSP1-wt. Cleaved rMSP1-wt bound to bands at the

positions of alpha and beta spectrin, components of the host cell cytoskeleton. No binding was observed for uncleaved rMSP1-wt. This suggests that 38/42 site cleavage is required for MSP1 spectrin binding (Das et al., 2015). Taken together, these data could suggest that conformational change resulting from SUB1 cleavage at the 38/42 site allows MSP1 to bind the host cell cytoskeleton, which may aid rupture. Das et al suggest MSP1 binding to spectrin may produce internal shear forces to disrupt the cytoskeleton; this may be aided by cysteine protease activity such as host cell caplain-1, or SERA6, since E64 inhibits host cell membrane rupture (Das et al., 2015). Despite this evidence, there is a large volume of literature suggesting a role for MSP1 in invasion and some work indicating MSP1 may be involved in intraerythrocytic development (Baldwin et al., 2015; Boyle et al., 2010; Moss et al., 2012).

1.6 A role for MSP1 in host cell invasion and intraerythrocytic development

1.6.1 Interactions between MSP1 and the host cell surface

A role for MSP1 in invasion and parasite development in the red cell is suggested by studies that show MSP1 binding to molecules localised at the erythrocyte surface (Baldwin et al., 2015; Boyle et al., 2010; Das et al., 2015) and those showing that antibodies to MSP1 prevent RBC invasion and parasite growth when bound (Moss et al., 2012). Research suggesting direct interaction between MSP1 and RBC surface molecules is disputable. Glycophorins are transmembrane sialoglycoproteins, of which human erythrocytes have 4: A, B, C and D. Interactions between glycophorins and *Plasmodium* erythrocyte binding antigens (EBA) are known to aid invasion (section 3.1). Using phage display, an interaction

between the N-terminus of MSP1 and erythrocyte glycophorin A (GPA) was detected and recombinant MSP1 was found to bind purified GPA. The carboxy terminus of MSP1 was also shown to interact with band 3, a transmembrane anion exchanger on the erythrocyte surface, via an extracellular loop that is predicted to be in proximity to GPA (Baldwin et al., 2015).

Heparin sulfate proteoglycans are found on the surfaces of erythrocytes. Heparin-like molecules have shown to block *P. falciparum* invasion, presumably by inhibiting pre-invasion interactions between merozoite and erythrocyte heparin (Boyle et al., 2010). MSP1 fragments 42 and 33 have shown to bind heparin in vitro (Boyle et al., 2010) and recombinant MSP1, cleaved by SUB1, was shown to bind immobilised heparin to greater extent than the unprocessed recombinant protein (Das et al., 2015).These data suggests that MSP1 may mediate invasion through attachment to GPA or by binding heparin sulfate proteoglycans, for which processing by SUB1 is required. However, no direct in vivo evidence was shown for MSP1 binding GPA on the RBCM, only that GPA null mice were resistant to malarial infection (Baldwin et al., 2015). This could be due to disruption of a number of pre-invasion interactions, including EBL binding. MSP1 binding to GPA was also not detected by surface plasmon resonance, adding to uncertainty around the biological significance of this interaction (Lin et al., 2014). It should additionally be noted that heparin is a relatively 'sticky' molecule, making binding assays less certain. This disputes claims of a direct involvement of MSP1 in pre-invasion interactions.

1.6.2 MSP1 as a scaffold for proteins linked with erythrocytic invasion

Despite uncertainty as to whether MSP1 interacts directly with RBCM during invasion, it could be suggested that MSP1 may enable presentation of proteins essential for invasion to the erythrocyte plasma membrane, rather than binding erythrocyte surface molecules itself. MSP1 has been shown to interact with a number of other *Plasmodium* proteins including MSP3/7/6, and MSPDBL1/2 (merozoite surface protein with a Duffy binding like domain). Complexes formed from recombinantly expressed MSP1, 6 or MSPDBL1/2 can bind the erythrocyte surface (Kauth et al., 2006; Lin et al., 2014, 2016) and surface plasmon resonance studies have suggested that recombinant MSPDBL1 and 2, but not MSP1, bound to human erythrocytes through unknown receptors (Lin et al., 2014). MSP7-null parasites have shown to have slightly impaired invasion (Kadekoppala et al., 2008). Despite being implicated in invasion, parasites lines in which these partner proteins were individually knocked out had no growth defect (Lin et al., 2016). Antibodies to MSP6/7 have shown to cause growth inhibition, possibly indicative of inhibition of invasion (Kauth et al., 2006). However, these antibodies to MSP6/7 also prevented MSP1 secondary processing, shedding and, hence, parasite maturation; steric hindrance of SUB2 cleavage may be responsible for the apparent reduced parasitaemia, as was seen in parasites in which MSP1 shedding was inhibited (Collins et al., 2020). MSP6/7 in complex with MSP1 are therefore not definitively involved in erythrocyte invasion. In addition, MSP1 antibodies targeting p83 fragment do not prevent complex formation yet still disrupt parasite growth (Lin et al., 2016). This could suggest the role for MSP1 in invasion is not to act as a scaffold for other erythrocyte binding proteins.

1.6.3 MSP1 and intraerythrocytic development

A role for MSP1 in intraerythrocytic development can be inferred from the effects of MSP1 disruption on parasite growth. After primary and secondary processing, the MSP1-19 fragment remains on the merozoite membrane and is transported with the merozoite into the host cell post invasion. This MSP1-19 fragment protein has shown to elicit an antibody response that stops parasite growth in vitro (Moss et al., 2012). Antibodies bound to this remaining fragment have shown to be internalised into the host cell, carried on the merozoite surface. These antibodies have then been located in the food vacuole and delay parasite development, potentially by interfering with food vacuole formation (Moss et al., 2012). MSP1 processing by SUB1 has also been shown to be important in parasite replication. Episomal transfection allowed a MSP1 mutant with all SUB1 cleavage sites removed to be expressed in parasites over a background of endogenous MSP1 expression. This inhibited parasite growth in due to lower replication rates. Furthermore, cleavage at the 38/42 site has shown to be essential for parasite viability. A single crossover homologous recombination approach was taken to investigate the effect of this cleavage site by removing all alternative sites in the endogenous locus. Successful integration of plasmids with 1 or 2 of the cleavage points at the 38/42 site was possible but not of plasmids with all cleavage points removed. This suggested that cleavage at the 38/42 region of at least one of the sites is needed for parasite survival (Das et al., 2015). These data and that discussed in section 5.2 demonstrate that the exact function of MSP1 remains undetermined, although the protein is evidently important in the intraerythrocytic cycle of malaria. Given that MSP1 is conserved within *Plasmodium* species and has been of interest as a potential vaccine or drug target, further work into the proteins function could aid successful therapeutic development.

1.7 Investigations into the structure of MSP1

It has been historically difficult to predict domain structures in *P. falciparum* extracellular proteins or to recombinantly express these proteins for structural study. The high A:T content and presence of long stretches of highly repetitive sequence in the *P. falciparum* genome results in low compatibility with heterologous expression systems. Signal peptides, disulphide bonds and transmembrane regions associated with many extracellular proteins also present a challenge (Crosnier et al., 2013; Kauth et al., 2003). In addition, there are no known orthologs of MSP1 found in other species, which has previously limited the capability to predict properties of this protein(Das et al., 2015). However, with the release of AlphaFold2, a number of plasmodium protein structure predictions have become available. This has great potential to aid the solving of native protein complexes (Jumper et al., 2021).

There has been success with recombinant expression of MSP1 and initially, this aided predictions of structure and has been important in uncovering functional roles (section 1.5.2, section 1.7.1) (Crosnier et al., 2013; Das et al., 2015; Kauth et al., 2003). Recently the structure of SUB1 processed and partially processed recombinant MSP1 was solved using single particle cryo-EM, a breakthrough in understanding this protein (Dijkman et al., 2021). However, as this protein was expressed in *E.coli* and processed *in vitro* with recombinant SUB1, proteins that may potentially bind MSP1 before and after cleavage are absent, and therefore the structure of the functional MSP1 complex remains undetermined.

1.7.1 Recombinant expression of truncated MSP1 or fragments

The structure of the MSP1 19kDa ectodomain was solved using NMR and subsequently, in complex with a Fab isolated from mice, by crystallography. It consists of two epidermal growth factor (EGF) domains; these are each made up of 2 beta sheets, which are in close contact (Pizarro et al., 2003) supported by hydrophobic interactions (Figure 1.9). The GPI anchored C terminus is in proximity to the N terminus SUB2 cleavage site, consistent with cleavage by the membrane bound protease (Morgan et al., 1999).

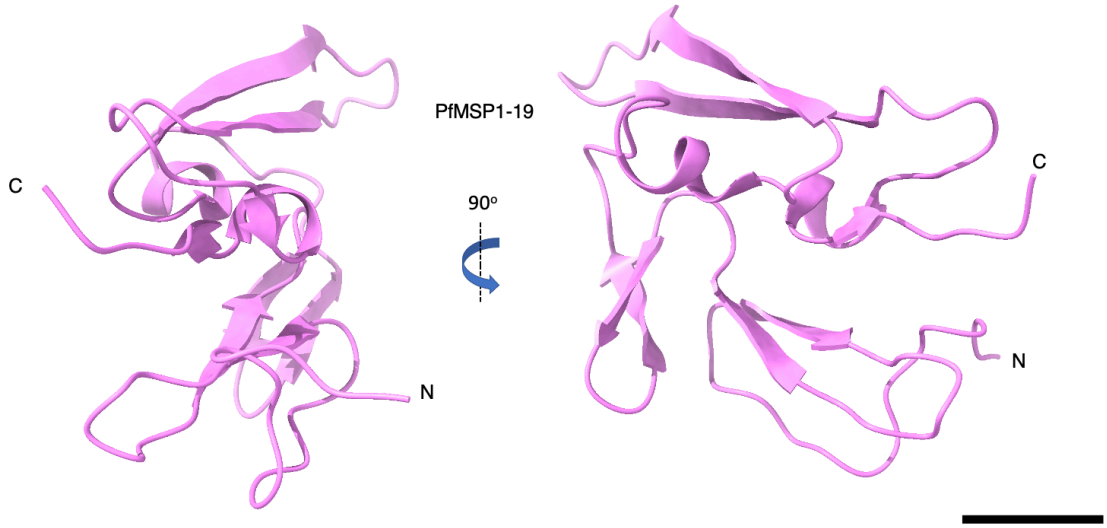

Figure 1.9 - Crystal structure of MSP1 19 kDa ectodomain.

Figure created using results from Pizarro et al. 2003, PDB:1ob1. N and C termini are indicated, scale bar 10 Å The MSP1-19 fragment was recombinantly expressed in Sf9 insect cells.

However, the rest of the complex remained unsolved until recently. HEK293 cells have been used to successfully express MSP1 by re-codonising the gene for human expression, and mutating N-glycosylation sites (NXS/T serine or threonine to alanine) to prevent

glycosylation. Recombinant proteins produced this way have been used by Das et al to determine differences in function between cleaved and unprocessed MSP1, as discussed previously (section 5), and have also been used in avidity-based-extracellular interaction screen, demonstrating MSP1 interaction with MSP7 (Crosnier et al., 2013). However, these proteins were not successfully used for structural studies.

Investigation of fragments expressed in *E. coli* and refolded in vitro allowed an initial prediction of the arrangement of MSP1 (Kauth et al. 2003). This is depicted in the figure below (Figure 1.10). The most extended conserved regions within MSP-1 are found in the N-termini of p83. The study suggested that, as p83 did not appear to be involved in formation and stabilization MSP1 and may be a flexible domain, these regions might be involved in interactions with other proteins (Kauth et al., 2003).

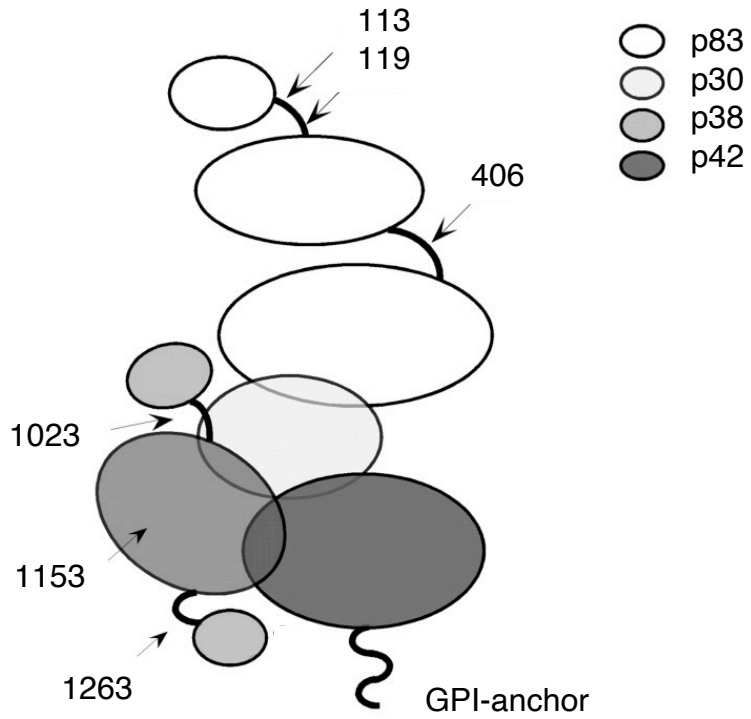

Figure 1.10 –Schematic of the suggested structure of processed MSP1.

The processed fragments are drawn to scale, shaded according to the key. Flexible linker regions determined using thrombin cleavage, these are labelled with predicted amino acid number. Figure adapted from Kauth et al. 2003.

1.7.2 Recent advances in the structure of MSP1

The structure of a recombinant MSP1 has been solved using singe particle cryo-EM (Dijkman et al., 2021) (Figure 1.11). MSP1 was expressed in *E.coli* in two halves; the p83/p30 and the p38/42 fragments were expressed individually and recovered from inclusion bodies. This method of expression of MSP1 fragments is the same used in the study described above (section 1.7.1, (Kauth et al., 2003)). MSP1 was then reconstituted using pulse renaturation and structure analysis was carried out. The reconstituted MSP1 was also subjected to cleavage by recombinant PfSUB1 and additional structure analysis of cleaved protein was done. Two dimeric structures of reconstituted MSP1 (consisting of two reconstituted MSP1 particles, 3.3-3.6 Å) and six monomeric structures (3.1-3.6 Å) of the cleaved MSP1 were determined and used to build models *de novo.* Assignment of regions of MSP1 to the densities was aided by cross linking mass spectrometry. The individual fragments of MSP1 appeared to be held together by hydrogen bonds and salt bridges. The dimerization between MSP1 protomers is facilitated by two symmetrical sites. The largest interface is between helix 14 (p83) of one protomer and helix 37 (p42) of the other. There is also interactions and between helix 37 (p42) of one protomer and helix 17 (p83) and the loop

connecting helices 27-28 (p38) on the other. This binding is true visa/versa for the symmetrical site (Figure 1.11) (Dijkman et al., 2021).

Structures showed monomeric rPfSUB1 cleaved MSP1 as an alpha helical structure with a large central cavity. The p38/p42 form a left-handed coiled coil domain thought to resemble folds associated with membrane and cytoskeletal interactions. Opposite to the central cavity, the p83 forms a flexible domain, termed the 'wing' domain. The p30 and long helices extending outward from each domain mediate connectivity between the 'wing' and coiled-coil domains. Likely due to being connected to the rest of the structure by a flexible linker, the EGF domain, constituting the C-terminus of p42, was not resolved. The original predictions of subunit arrangement were partially correct; the interaction between the p30 and p38 is the largest inter-subunit contact surface (Dijkman et al., 2021).

There were few differences between the structures of monomeric MSP1 and the individual protomers making up the dimeric MSP1 structures, apart from slight shifts in conformation, primarily of the wing domain, (Figure 1.11) and a density observed in the pocket between helix 30 and 35 in the structures of dimeric but not monomeric MSP1. This density, though unresolved, was postulated to be part of the 96 amino acid loop between Helix 34 and 35, in which the p38/42 SUB1 cleavage site of MSP1 resides. Considering previous work indicating the importance of SUB1 processing at this site, the authors suggest that cleavage may be required to release the loop from the pocket between helix 30 and 35. This may allow either exposure of the loop itself or a binding site on the coiled- coil domain for interactions that are important for MSP1 function in the erythrocytic cycle (Dijkman et al., 2021).

Dimer formation in reconstituted MSP1 occurred in a concentration dependant manner and could be due to lack of partner proteins, which are absent due to protein being from a recombinant rather than a native source. This is corroborated by reduced dimerization in the presence of β- spectrin, the RBC cytoskeletal protein thought to bind MSP1 (Das et al., 2015; Dijkman et al., 2021). This work contributes much to understanding MSP1 structure and gives some insight into function. However, given that MSP1 is known to form complexes with other malarial proteins, a native structure may shed more light on the role of MSP1 in blood stage malaria.

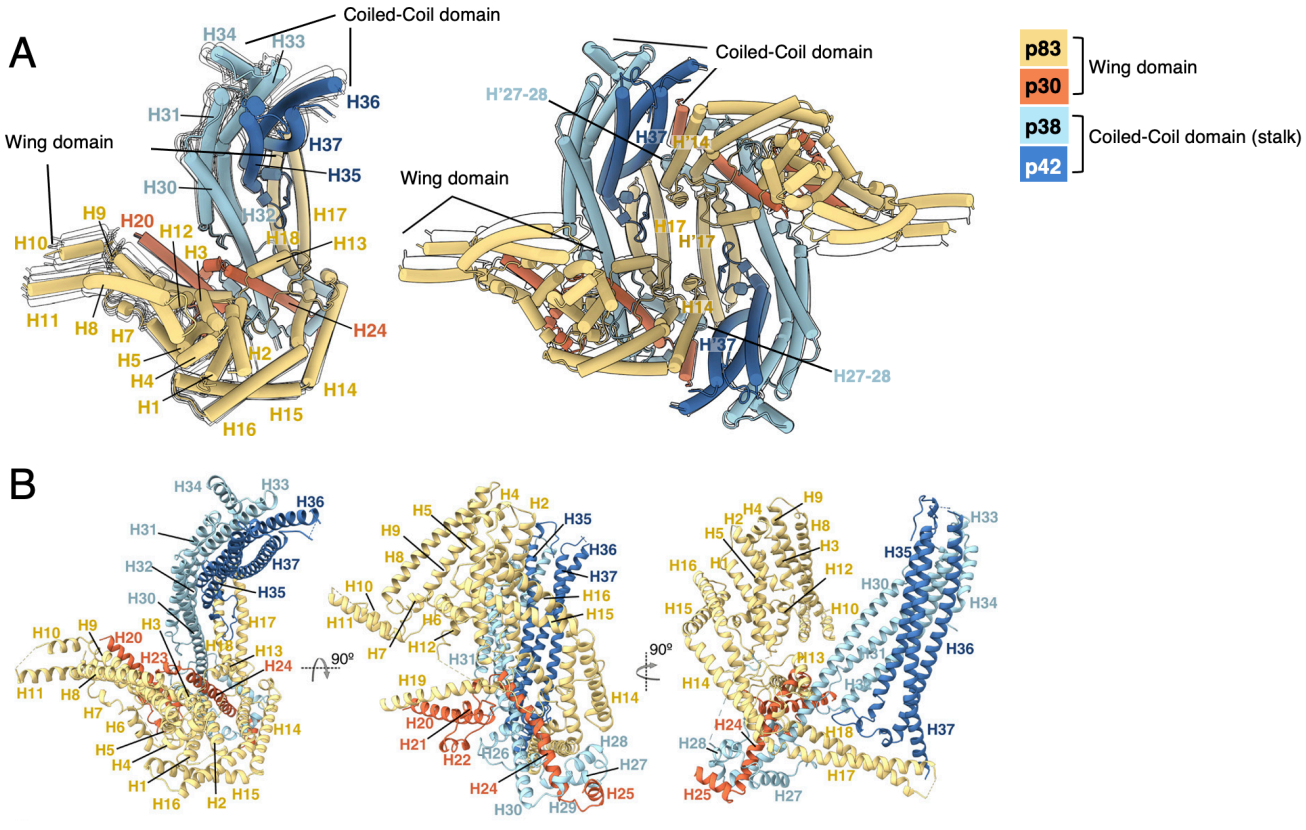

Figure 1.11 - The published atomic structures of recombinant MSP1.

A) Cartoon representation of the structures of rPfSUB1 processed monomeric MSP1 and reconstituted dimeric MSP1 (not processed by rPfSUB1). Identity of helices are shown on the monomeric structure, the faint outlines demonstrate conformational variations. Helices involved in the interactions that mediate dimer formation are indicated in the dimeric structure (that of the 'second' protomer are labelled as H').

B) The atomic structure of monomeric, rPfSUB1 processed MSP1, shown in different orientations*. Helices are labelled.*

Figure modified from (Dijkman et al., 2021) ©, open access, covered by creative commons 4.0 by NC https://creativecommons.org/licenses/by-nc/4.0/. Some rights reserved; exclusive licensee AAAS, Science Advances.

1.8 Conclusion

Malaria remains a resurgent public health threat especially for pregnant women and children under 5 in Sub-Saharan Africa and the Asian pacific. Though vector control is effective and treatments are available, there is growing levels of resistance in both mosquitos to insecticides and parasites to therapeutics. The erythrocytic cycle is responsible for most of the pathology of the malaria, however, much is unknown about *Plasmodium* biology and the biochemical mechanisms governing this cycle; there is also no vaccine in distribution that targets this cycle. Merozoite surface protein 1 has shown to be essential in *Plasmodium* parasitaemia of RBCs and has potential as a novel vaccine or drug target. Despite the breadth of literature concerning MSP1, the MSP1 function and the structure of this protein in complex with other MSPs remains unsolved. This makes targeting this protein

difficult and further research into MSP1 would benefit efforts to target this protein and identify novel therapeutics.

1.9 Aims of this study

This study looked to carry out further investigations into MSP1, with the hope of increasing understanding of the function of this protein in the asexual blood stages of malaria. This work follows on from findings that MSP1 processing by SUB1 is important for MSP1 complex formation and for MSP1 function (Das et al., 2015; Kauth et al., 2006). There is specific focus on the role of SUB1 processing at the 38/42 cleavage site of MSP1 on the basis that this site may have a role in temporal regulation of egress (Child et al., 2010; Das et al., 2015). The aims can be summarised in two main questions:

1) What is the role of SUB1 cleavage at the 38/42 site of MSP1 in the erythrocytic cycle?
2) Does SUB1 cleavage alter MSP1 complex structure and how does this inform us about protein function?

By addressing these questions and uncovering more details about the function of MSP1, it was hoped that the some of the unresolved mechanisms involved in *P. falciparum* merozoite egress from the erythrocyte would be identified.

Chapter 2 – Materials and Methods

2.1 Materials

Plasmid name:	Successful guide RNA	Purpose
MSP1null:lox66/lox71rev	(−) TAGAAAGATCATATTGAGCTTGG	Integration construct for 3D7MSP1KO:lox66/lox71rev line. DNA encoding recodonised MSP1 floxed by head-to-head lox sites. Allowing gene inversion upon addition of RAP and MSP1 knock-out.
MSP1-3842KO:loxP/loxPint	(+) TCCATCTCCATTATCTGTAAGG	Integration construct for 3D7MSP1mut38/42:loxP. DNA encoding floxed recodonised chimeric MSP1 (MSP1-D and p19 from MSP1-F fused) and, downstream, MSP1 with 38/42 SUB1 processing site mutations. Allowing gene excision and expression of MSP1 with altered 38/42 processing site upon addition of RAP.
MSP1-FLFL:lox66/lox71	(−) GTGACGGAGGTGTTGTTGGTGG	Integration construct for 3D7MSP1-FLAG:loxP. DNA encoding floxed MSP1 C-terminus and FLAG tagged MSP1 C-terminus downstream. Allowing gene excision, moving into frame the alternative FLAG tagged termini.

Table 2.1 - Integration constructs used in this study and associated guides (PAM sequence highlighted, not included in encoded guide sequence)

Primer identifier	Name	Sequence	Use
1.1	HA1_F2	GGTACAAGTCCATCATCTCGTTCAAACAC	Forward primer, integration PCR, 3D7MSP1KO:lox66/lox71rev.
1.2	3D7 Endo R1	GGTGGTGATGGTTGTGTTGGTGG	Reverse primer, integration and inversion PCR, 3D7MSP1KO:lox66/lox71rev.
1.3	MSP1 recodR2	CACTAATAAGATTATGGGCCTCCTC	Forward primer, inversion PCR, 3D7MSP1KO:lox66/lox71rev.
2.1	F1	GATGATATCAAACAATTCGTAAAATCTAATTC	Forward integration/excision PCR for 3D7MSP1mut38/42:loxP and 3D7MSP1-FLAG:loxP.
2.2	REV-DS-3HOM_MSP1	CATGACTAAAATATCACTATTCCTGTA	Reverse integration/excision PCR for 3D7MSP1mut38/42:loxP and 3D7MSP1-FLAG:loxP.

Table 2.2 - Primers used in this study

Primary antibody name and target	Antibody source	Western Blot Dilution	Immuno-fluorescence assay dilution	Reference
89.1, α-MSP1 p83	Monoclonal, IgG-Mouse	1:1000	1:200	(Holder & Freeman, 1982)
X509, α-MSP1 p38/42	Monoclonal, IgG-Human	1:1000	1:5000	(Blackman et al., 1991)
2F10, α-MSP1-19	Monoclonal, IgG-Mouse	N/A	1:100	(Blackman et al., 1994)
VD4, α- β-Spectrin	Monoclonal, IgG-Mouse	1:1000	N/A	Santa Cruz Biotechnology
α-GAP45	Monoclonal, IgG-Rabbit	N/A	1:200	Provided by Ellen Knuepfer
111.4, α-MSP1-19F (Wellcome type)	Monoclonal, IgG-Mouse	1:1000	1:100	(Holder et al., 1985)
α-FLAG, FLAG tag	Monoclonal, IgG-Rabbit	1:2000	1:200	Sigma Aldrich
α-MSP3	Monoclonal, IgG-Rabbit	1:2000	N/A	Provided by Ellen Knuepfer
α-MSP6	Monoclonal, IgG-Rat	1:500	N/A	Provided by Ellen Knuepfer
α -MSP7	Monoclonal, IgG-Rabbit	1:1000	N/A	(Kadekoppala et al., 2010)
α-SERA5	Polyclonal, IgG-Rabbit	1:2000	N/A	Stallmach et al. (2015)

Table 2.3 - Primary antibodies used in this study

Secondary antibody	Western blot dilution	Immuno-fluorescence assay dilution	Source
Goat- anti-mouse	1:3000	N/A	Abcam
Goat-anti-mouse-alexoflour594	N/A	1:2000	Life Technologies
Goat-anti-mouse-alexofloru647	N/A	1:2000	Life Technologies
Goat-anti-mouse-alexoflour547	N/A	1:2000	Life Technologies
Goat-anti-human	1:5000	N/A	Abcam
Goat-anti-human-alexoflor647	N/A	1:2000	Life Technologies
Goat-anti-rabbit	1:3000	N/A	Abcam
Goat-anti-rabbit-alexoflour488	N/A	1:2000	Life Technologies
Goat-anti-rabbit-alexoflor594	N/A	1:2000	Life Technologies
Goat-anti-rat	1:10,000	N/A	Abcam
Goat-anti-rat-alexoflor594	N/A	1:2000	Life Technologies

Table 2.4 - Secondary antibodies used in this study

2.2 Methods

2.2.1 Molecular Biology

2.2.1.1 Transformation

Competent bacterial cells were mixed with ~50-100 ng of plasmid to be transformed by gentle agitation and incubated for 10-15 min on ice (4°C). Cells were then heat shocked for 30 s, 42°C, and then returned to ice for a further 2 mins. If the resistance cassette used for

selection of successful transformants was ampicillin, cells were then directly transferred to an LB agar plate (100 μg/mL Ampicillin, Sigma Aldrich). If the resistance cassette used for selection was kanamycin, cells were incubated for 1 hr at 37°C in SOC (Super Optimal broth with Catabolite repression) solution, 200 rpm. Cells were then pelleted and transferred to an LB agar plate (50 μg/mL Kanamycin, Sigma Aldrich). Plates were incubated o/n at 37°C and colonies picked for grow up and further analysis. Competent cells used were either XL10 Gold® Ultracompetent *E. coli* cells (Strategene) or Sub cloning efficiency DH5α™ *E.coli* cells (Invitrogen). In cases where ligation products were transformed, colonies were tested for correct plasmid prior to DNA extraction by colony PCR using GoTaq green (Promega) and appropriate primers listed (See Materials).

2.2.1.2 Plasmid preparation

To amplify plasmids, 5 mL of lysogeny broth (LB) (treated with either kanamycin or ampicillin accordingly) was inoculated with a single colony (previously grown on LB agar) and grown o/n at 37°C, whilst shaking (200 rpm). Resultant culture was either pelleted (6000 x g, 5 mins) and DNA extracted using Qiagen Spin Miniprep kit, as per manufacture instruction, or 1 mL of culture was used to inoculate 200 mL of LB broth (treated with either kanamycin or ampicillin accordingly) for preparation of larger volumes of plasmid. For plasmid preparation from 200 mL cultures, cells are pelleted at 4,500 x g for 20 mins and DNA extracted using Qiagen HiSpeed® Maxi Kit, as per manufacturer instructions. Concentration of DNA obtained was measured using a Nanodrop.

2.2.1.3 Restriction digest

Restriction digest of DNA was carried out using restriction endonucleases supplied by New England Biolabs (NEB). This was done as per manufacturer instructions, using CutSmart buffer (NEB) and incubation at 37°C for 4 hrs or o/n, dependent on volume of DNA to be digested. Enzymes in reaction solutions were heat inactivated as per manufacturer instructions.

2.2.1.4 Gel Extraction

Specific products of DNA restriction digest to be used in ligation reactions were purified by Gel extraction. This involved separation of digestion products using gel electrophoresis in 0.7-2% agarose gel (Thermo Scientific), run at 100 V in 1X TAE buffer (40 mM Tris-acetate and 1 mM EDTA, pH 8.3). DNA of interest was excised from agarose gels under low UV and extracted using Qiagen QIAquick® Gel Extraction kit.

2.2.1.5 DNA Ligation

DNA fragments were ligated using the Rapid DNA Ligation Kit (Roche), as per manufacturer's instructions. In cases in which vector relegation was possible, such as in blunt end ligation, vectors were treated with Antarctic Phosphatase (NEB) prior to ligation as per manufacturer's instructions, to dephosphorylate the 5' and 3' ends of DNA.

2.2.1.6 Plasmid construction

2.2.1.6.1 Integration construct for 3D7MSP1mut38/42:loxP

Synthetic DNA encoding the 5' and 3' homology regions, floxed recodonised chimeric MSP1 (MSP1-D and p19 from MSP1-F fused) and MSP1 recodonised for Leishmania in a plasmid was ordered from IDT (pGB004). This was then modified to include a PbDT3' UTR, placed in a pCR blunt II vector and the desired mutations at the 38/42 site incorporated. PbDT3' UTR was extracted from plasmid CRC7-11-25 (Collins, unpublished) using XhoI and NotI-HF restriction enzymes and gel extraction (Section 2.2.1.3-4). This was cloned into the synthetic plasmid by restriction digest of the plasmid using Xho1 and Not1-HF restriction enzymes and ligation (see 2.2.1.3 and 2.2.1.5). The 5' and 3' homology regions, floxed recodonised chimeric MSP1 (MSP1-D and p19 from MSP1-F fused) and MSP1 recodonised for Leishmania and the PbDT3' UTR were cloned into pCR blunt II by extracting this fragment using restriction enzyme BsrBI (NEB) and ligating into cut PCR blunt-Mel-SS_S5-5' (restriction digest with NotI-HF and SpeI-HF (both NEB), gel purification and blunt ending of the fragment of interest using T4 DNA polymerase (NEB)). This plasmid was named RAL21-1-1.

Synthetic DNA encoding the mutations to the 38/42 site was ordered from IDT and cloned into pCR blunt II plasmid using Zero Blunt PCR cloning kit (Thermofisher). This was amplified and then the fragment extracted using restriction digest, with AhdI and AflII restriction enzymes, and gel purification. RAL21-1-1 was also cut with AhdI and AflII restriction enzymes and gel purified. Synthetic DNA encoding the mutations to the 38/42 site was then ligated into RAL21-1-1, producing the final plasmid, MSP1-3842KO:loxP/loxPint, the

integration construct for 3D7MSP1mut38/42:loxP. Selection of colonies in all cases was made by presence of antibiotic resistance genes in plasmids – pCR blunt II has kanamycin resistance cassette.

2.2.1.6.2 Integration construct for 3D7MSP1-FLAG:loxP

This construct was designed by Claudine Bisson and synthesised by Genewiz.

2.2.1.6.3 Cas9 Cassette preparation

Specific guide RNAs to direct Cas9 were designed using Benchling (www.benchling.com). Guide RNA sequences (see materials for guides used and corresponding clones) were annealed with reverse complementary oligonucleotides and then cloned into the plasmid pDC2-Cas9-hDHFRyFCU, containing a Cas9 expression cassette and the drug selection marker human dihydrofolate reductase (*hdhfr*), conferring resistance to WR9910 (antifolate, Sigma-Aldrich). Complementary oligonucleotides were designed that upon annealing generated sticky ends, compatible with the ends resulting from Bbs1-HF digestion of plasmid pDC2-Cas9-hDHFRyFCU.

2.2.1.7 Nucleotide sequencing

Nucleotide sequencing was outsourced to Beckman Coulter Therapeutics or, for whole plasmid sequencing, Plasmidsaurus.

2.2.2 Culture, transfection and assay of *P. falciparum* in erythrocytes

The clustered regularly interspaced short palindromic repeats (CRISPR)-CRISPR-associated protein 9 (Cas9) system was adapted for use in *P. falciparum* in 2014 (Ghorbal et al., 2014). CRISPR-Cas9 is an endonuclease that performs double stranded breaks at specific sites in the genome, guided by sgRNA. This endonuclease serves as an immune mechanism in prokaryotes but is now used as a molecular biology tool in many organisms. The sgRNA (approximately 20 nucleotides) is customizable to target any gene so long as there is a protospacer-adjacent motif (PAM – NGG/NAG, where N can be any nucleotide) sequence immediately downstream from where the sgRNA anneals, must be present for cleavage (Ghorbal et al., 2014). This has allowed reliable gene modification in *P. falciparum.*

P. falciparum is haploid during the asexual blood stages. Therefore, to study the function of essential genes, mutations must be conditional. Knock-down systems can be used, with the caveat that these techniques cause protein depletion, not deletion. To allow induction of gene mutations in *P. falciparum*, a DiCre-recombinase system can been employed. DiCre is a dimerisable phage derived Cre-recombinase; monomers are fused with rapamycin binding proteins FKBP12 and FRB. This means that upon addition of rapamycin, the dimers interact to form an active Cre-recombinase. Cre- recombinase recognises specific sequences or 'lox sites' and recombines DNA, allowing DNA excision, insertion and inversion (Figure 2.1). Genes of interest in the genome can be flanked by lox sites or 'floxed' using CRISPR-Cas9 guided homologous recombination and then, for example, excised or inverted by DiCre, allowing modification on a conditional basis (Knuepfer et al., 2017).

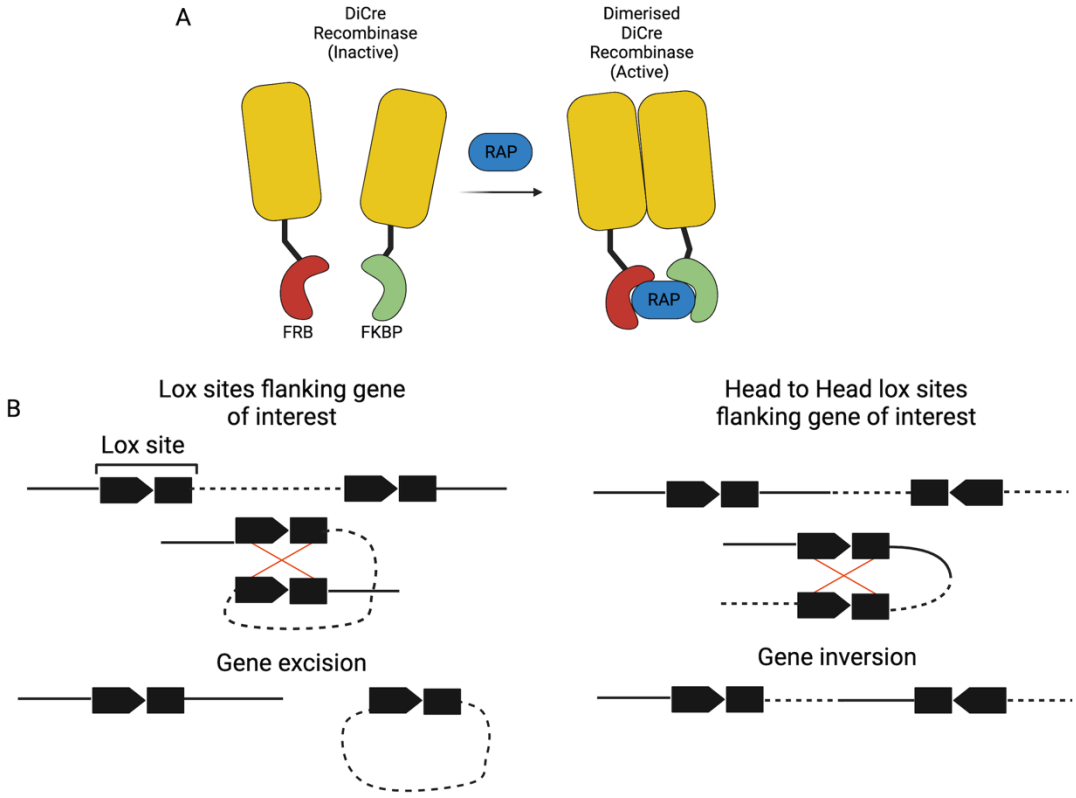

Figure 2.1 - The DiCre-recombinase system in P. falciparum allows conditional mutagenesis.

Cre-recombinase is expressed constitutively in P. falciparum as a dimer which requires rapamycin to associate and become active. In combination with CRISPR-Cas9 facilitated gene editing, this allows modification of specific target genes on a conditional basis – only if rapamycin is present. Figure adapted from Wikimedia Commons, open access, covered by creative commons copyright, https://creativecommons.org/licenses/by/3.0/

All experiments used *P. falciparum* derived from the 3D7 isolate. 3D7 parasites had been edited such that a gene encoding DiCre-recombinase was integrated at the SERA5 locus,

chromosome 2, alongside a recodonised SERA5 gene (Collins, Das, et al., 2013). Displaced endogenous SERA5, downstream of integrated DNA, was truncated by homologous recombination, mediated by the CRISPR/Cas9 system(Perrin et al., 2018). This was to ensure all SERA5 expression in the parasite was due to translation of the recodonised gene and that DiCre-recombinase was expressed in high abundance, as a result of expression being driven by the SERA5 promoter. This line is labelled B11. B11 parasites were further edited to tag the integral parasitophorous vacuole membrane protein EXP2 with fluorescent mNeonGreen at the C-terminus. This line is labelled A7 (C. Bisson, unpublished; Glushakova et al., 2018).

2.2.2.1 Culture maintenance

All culturing was carried out under sterile conditions and all reagents sterile filtered. Asexual blood cultures were maintained at 5-10% parasitaemia in 2-4% haematocrit (erythrocytes only) RPMI 1640 containing 0.5% Albumax II (Thermofisher), supplemented with L L-glutamine, gassed with CO_2. Parasites were grown at 37^{o}C. To check cultures and parasitaemia during each asexual erythrocytic cycle, blood smears of cultures were made on glass slides, fixed with 100% methanol and stained for 5 mins with 10% Giemsa (VWR International) in Giemsa buffer (8 mM KH_2PO_4, 6 mM Na_2HPO_4, pH 7). Slides were washed with water, pat dried and examined using a light microscope, 100 X oil immersion lens.

In order to ensure synchronicity, schizonts were collected by centrifugation (2,500 rpm, 8-10 mins) on a 70% Percoll® cushion (Amersham Pharmacia) and incubated with 1-2 mL fresh blood for 1-3 hrs in 100-50 mL RPMI w/ Albumax, at 37^{o}C, 100 rpm in a shaking incubator.

This was to allow schizont rupture and merozoite invasion into fresh erythrocytes. After invasion, remaining schizonts which had not egressed, were removed from culture, again using centrifugation on a 70% Percoll® cushion, and rings were treated with 5% Sorbitol (w/v) for 5 mins, 37°C, to lyse any residual schizonts. Rings were then removed from Sorbitol using centrifugation (2,800 rpm, 3 mins) and returned to culture.

2.2.2.2 Culture cryopreservation and revival

To preserve *P. falciparum* lines, asexual blood cultures in 2-4% haematocrit, ideally at 5-10% rings, were mixed 1:1 with malaria freezing solution (3.78% sorbitol, 8% NaCl, 35% glycerol) and flash frozen in liquid N_2 in 1 mL cryo-vials. These were then stored in LN_2 long term. To revive lines, solutions were defrosted quickly at 37°C, mixed 1:1 with malaria thawing solution (3.5% NaCl in ddH_2O), washed 2x 1 mL malaria thawing solution by centrifugation (1,800 rpm, 3 mins) and then transferred to culture, 2-4% haematocrit in RPMI w/Albumax. The following day, media was replaced with fresh RPMI w/Albumax and cultures scaled up for use over the course of 1-2 weeks.

2.2.2.3 Transfection and clone isolation

Transfection is done by electroporation using the AmaxaTM P3 primary cell 4D NucleofectorTM X Kit L (Lonza). To create transgenic lines, 60 μg of a given integration construct was linearised with an appropriate restriction enzyme (NEB) by o/n incubation at 37°C. The enzyme was then heat inactivated the following morning in the procedure specified by the manufacturers. 20 μg of CRISPR/Cas9 cassette with appropriate guide DNA was added to the 60 μg of linearised integration construct and DNA was co-purified by

ethanol precipitation. Pellets were dried under sterile conditions and resuspended in 10 μL of sterile TE buffer (10 mM Tris, pH 8.0, and 0.1 mM EDTA). 20-50 μL of densely packed synchronous late schizonts were mixed with resuspended DNA and 100 μL of P3 solution (Lonza). This was then placed in cuvettes provided by Lonza and delivered an electrical pulse using 4D-Nucleofector machine (Lonza), program FP158. Cells were then transferred into a flask containing 2 mL RPMI w/Albumax at 20% haematocrit (erythrocytes only) and incubated for 30 mins – 1hr at 37°C, shaking (100 rpm), to allow invasion of transfected cells. 8 mL of RPMI w/Albumax was then added and culture left o/n at 37°C. In the morning, media and debris were removed from the culture and replaced with fresh media containing 2.5 nM WR99210 (antifolate, Sigma-Aldrich). This selects for uptake of the CRISPR/Cas9 cassette and integration, as this plasmid encodes human dihydrofolate reductase, conferring resistance to WR99210. The culture was kept on WR99210 for 4 days and then returned to RPMI w/Albumax w/o WR99210. The culture was monitored, with fresh media and erythrocytes being added weekly, until signs of asexual stage *P. falciparum* were detectable.

Once 3-5% parasitaemia is reached and the culture was predominantly at ring stage, the transfectant can separated into clones by serial dilution, necessary as cultures are likely a mixed population of parasites in which integration has been successful and others in which it has not. This involves diluting the culture 10-fold in RPMI w/Albumax at 1% haematocrit and then serially diluting the culture 4-fold across a 96-well flat bottom plate in in RPMI w/Albumax at 1% haematocrit. This is in the hope of obtaining wells with only one parasite. Plates are incubated at 37°C without disturbance for 10-12 days. As the blood settles, a thin layer is formed at the base of the well and any parasite present will form a single plaque

after development and egress. Those wells which have only one identifiable plaque, therefore, contain a single parasite. Wells with single plaques were expanded for further analysis.

2.2.2.4 Genomic DNA extraction

The DNA can be isolated from infected erythrocytes by treatment with saponin (0.15% in PBS), causing membrane lysis. The insoluble material was then pelleted (13,000 rpm), supernatant removed and genomic DNA extracted using Qiagen DNeasy Blood and Tissue DNA Extraction Kit, following manufacturers guidelines. This can then be used in PCRs to check for integration or, if extracted following rapamycin treatment, excision.

2.2.2.5 PCR to identify gene integration or excision

Gene integration using PCR, either directly on blood using Blood direct Phusion (Thermo Scientific) or genomic extracts using Clone AMP (Takara), using the primer pairs listed and manufacturer guidelines. PCR products were analysed using gel electrophoresis in 0.7-2% agarose gel (Thermo Scientific), run in 1X TAE buffer (40 mM Tris-acetate and 1 mM EDTA, pH 8.3) at 110 V.

2.2.2.6 Rapamycin treatment to trigger gene excision and mutation in P. falciparum

To trigger gene excision and hence mutagenesis, parasites must be treated with rapamycin. This is done after synchronisation on newly invaded erythrocytes, with parasites in ring stage. Cultures were treated with 10 mM rapamycin (Sigma-Aldrich) o/n in RPMI w/Albumax, incubated as normal at 37^{o}C. Rapamycin was then removed the following day

by replacing culture media with fresh RPMI w/Albumax. As a control, separate replicates of cultures were treated with an equal volume of DMSO in the same manner.

2.2.2.7 Preparation of pre and post egress schizonts for analysis by EM

After synchronisation and treatment with rapamycin or DMSO (Methods 2.2.2.1, 2.2.2.6), schizonts were Percoll® enriched, washed in RPMI w/Albumax and incubated in 1 μM Compound 2 (C2) in fresh RPMI w/Albumax for 4 hrs, 37°C to allow maturation (Collins, Hackett, et al., 2013b). Schizonts were then washed by centrifugation (pelleted at 1,800 rpm, 1 min and then resuspended) by either 2X in pre warmed RPMI w/ Albumax, 50 μM E64, for pre-egress samples, or 2X in pre warmed RPMI w/ Albumax only, for post egress samples. Pre-egress samples were then resuspended in RPMI w/ Albumax, 10 μM E64 and incubated for a further 2 hours, 37°C to allow further maturation and PVM degradation. Post egress samples were resuspended in fresh media (RPMI w/ Albumax) and allowed to egress for 2 hrs by shaking (100 rpm) at 37 °C. Pre-egress schizonts were then pelleted (1,800 rpm, 1 min) and washed 2X in PBS w/10 μM E64; post egress samples were pelleted (1,800 rpm, 1 min) and washed 2X in PBS only. Samples were fixed in 2.67% formaldehyde and 1.33% glutaraldehyde in PBS for 5 mins, 37 °C and then pelleted at 5000 xg and resuspended in PBS.

2.2.2.8 Egress assay

After synchronisation and treatment with rapamycin or DMSO (Methods 2.2.2.1, 2.2.2.6), schizonts were Percoll® enriched, washed in RPMI w/Albumax and incubated in 1 μM C2 in fresh RPMI w/Albumax for 4hrs, 37° to allow maturation (Collins, Hackett, et al., 2013b). Schizonts were then washed by centrifugation (pelleted at 1,800 rpm, 1 min and then

resuspended) 2X in pre warmed RPMI w/o Albumax (Gibco RPMI 1640 media), 1 μM C2. For pre-egress samples, schizonts were resuspended in 10 fold v/v RPMI w/o Albumax, 1 μM C2 and flash frozen in LN_2. For post egress samples, schizonts were washed by centrifugation (pelleted at 1,800 rpm, 1 min and then resuspended) in 2X prewarmed RPMI w/o Albumax, resuspended in 10 fold v/v RPMI w/o Albumax, gassed with CO_2 and left to egress for 1-2 hrs at 37°C, shaking (200 rpm). Post egress samples were then spun down and schizont extract and supernatant separated; separated samples were flash frozen in LN_2. Both pre and post egress samples were stored at -80°C until analysis.

2.2.2.9 Video microscopy of egress

After synchronisation and treatment with rapamycin or DMSO (Methods 2.2.2.1, 2.2.2.6), schizonts were Percoll® enriched, washed in RPMI w/Albumax and incubated in 1 μM C2 in fresh RPMI w/Albumax for 4 hrs, 37°C to further synchronise schizonts and allow maturation, whilst preventing egress. Schizonts from both DMSO and rapamycin treated cultures were collected by pelleting (1,800 rpm, 3 mins) and one of either culture (DMSO or RAP treated) treated with 8.12 μM Hoechst nucleic acid stain (Invitrogen) in RPMI w/Albumax, 1 μM C2, for 5 mins. This was to allow differentiation during imaging. Schizonts were then washed by centrifugation (pelleted at 5000 Xg, 1 min and then resuspended) 1X RPMI w/Albumax, 1 μM C2, to remove the dye from those stained and mixed. Mixed schizonts were washed 2X by centrifugation in prewarmed and gassed (CO_2) RPMI w/ Albumax without C2. Parasites were applied by capillary flow to a prewarmed viewing chamber, made by adhesion of a 22 × 64 mm borosilicate glass coverslip to a microscope slide. Slides were then placed immediately on a 37°C heated stage on a Zeiss Axioplan 2 Imaging system, and imaged using a Plan-APOCHROMAT 100×/1.4 oil immersion objective

and an EC Plan-Neofluar 1006/1.3 oil immersion DIC objective, fitted with an AxioCam MRm camera. Images were collected at 5 s intervals for 30 mins, annotated and exported as QuickTime movies using Axiovision 3.1.

2.2.2.10 Invasion assay

After synchronisation and treatment with rapamycin or DMSO (Methods 2.2.2.1, 2.2.2.6), mature schizonts were collected using a 70% Percoll® cushion and washed in RPMI-Albumax. Schizonts were then placed in fresh erythrocytes at 5-10% parasitaemia in 2% haematocrit RPMI-Albumax, in a total volume of 2 mL. Parasites were gassed (CO_2) and incubated at 37°C. shaking (150 rpm) for 4 hrs. Rings were then collected using a 70% Percoll® cushion and treated with 5% Sorbitol (w/v) for 5 mins, 37°C, to lyse any residual schizonts. To count rings, cultures were stained with 2 x SYBR Green I nucleic acid gel stain (Life Technologies) for 30 min at 37°C. Labelling was stopped with an equal volume of PBS and samples analysed using a BD Fortessa flow cytometer (BD Biosciences) with BD FACSDiva software (BD Biosciences). Total RBC numbers were estimated from forward- and side-scatter whilst fluorescence intensity detected using the 530/30 blue detection laser was used to determine numbers of infected erythrocytes. Gates were fixed based on uninfected red blood cells, which emit low fluorescence (Appendix 1). Data was analysed using FlowJo.

2.2.2.11 Growth assay

After synchronisation (Methods 2.2.2.1), rings were collected and set up at 0.1% parasitaemia in 2% haematocrit, RPMI-Albumax, in a final volume of 2 mL per well of a 6 well plate. Parasites were treated with rapamycin or DMSO (Methods 4.7.2.6) o/n. Media

was replaced and samples of cultures were taken for t = 0 timepoint. Further samples were taken at 48 hrs (cycle 1), 96 hrs (cycle 2) and 144 hrs (cycle 3). Culture media was replaced with fresh RPMI-Albumax at 96 hrs and 120 hrs) All samples were fixed with 0.2% glutaraldehyde and stored at 4°C for flow cytometry analysis. For flow cytometry analysis, cultures were stained, fluorescence measured and data analysed as described above (Methods 2.2.2.10).

2.2.2.12 Development assay

For determining parasite development of RAP treated rings: after synchronisation (Methods 2.2.2.1), rings were collected and set up at 3-5% parasitaemia in 2% haematocrit. Rings were mock or treated with rapamycin overnight (Methods 2.2.2.6) and then DNA replication followed over a period of 48 hrs. This was done by taking samples of culture at 0 hrs, 12 hrs, 18 hrs, 24 hrs, 36 hrs, 42 hrs and 48 hrs, which were fixed with 0.2% glutaraldehyde and stored at 4°C for flow cytometry analysis (Methods 2.2.2.10).

For determining development after invasion of RAP – treated merozoites: after synchronisation (Methods 2.2.2.1), rings were collected and rapamycin or mock-treated (Methods 2.2.2.6). Resulting schizonts were collected and set up to invade fresh erythrocytes. Rings were collected (Methods 2.2.2.1) and set up to 3-5% parasitaemia in 2% haematocrit. DNA replication was followed over a period of 48 hrs as above.

2.2.3 Protein Biochemistry

2.2.3.1 Protein separation by sodium dodecyl sulphate polyacrylamide gel electrophoresis (SDS PAGE) and Coomassie or Western blot analysis

Samples to be separated were solubilised 3:1 in 4X SDS loading buffer (0.2 M Tris-HCl, 277 mM SDS (8% w/v), 6 mM Bromophenol blue, 4.3 M glycerol) and boiled at 95^{o}C for 5 mins, ensuring protein denaturation, the breakage of cysteine disulphide bonds and displacement of negative charge across proteins in a manner proportional to mass. Proteins in samples were then separated, alongside a protein standard molecular weight marker (SeeBlue® Plus2, Invitrogen), on 4-15% gradient polyacrylamide gel (Mini-Protein TGX precast protein gels, BioRad) by gel electrophoresis at a constant voltage of 200 V in SDS running buffer (25 mM Tris, 192 mM glycine, 0.1% SDS, pH 8.3).

Following separation, gels were either analysed by Coomassie Blue, allowing analysis of total protein content, or Western blot, probing for specific protein epitopes. For Coomassie staining, gels were incubated at RT in InstantBlue™ (non-colloidal Coomassie stain, Abcam) for 1 hr and then de-stained for 2 hrs and imaged using . For Western Blot, proteins separated in gels were transferred onto nitrocellulose membrane (pore size 0.2 μm, Biorad) via o/n wet transfer (Trans-Blot™ cell, Biorad) in transfer buffer (25 mM Tris, 192 mM glycine, 20% methanol (v/v), pH 8.3). Nitrocellulose was blocked for 1 hr using 5% semi-skimmed milk in PBS 0.05% Tween® 20, washed 3X in PBS 0.05% Tween® 20 and incubated at RT with primary antibody diluted in 3% w/v BSA (see Materials 4.8 for primary antibodies and dilutions used) for 1hr. Blots were then washed 3X in PBS 0.05% Tween® 20 and then incubated at RT with horseradish peroxidase conjugated secondary antibody diluted in PBS

0.05% (see Materials Table 2.4 for secondary antibodies and dilutions used) Tween® 20 for 1 hr. After incubation, blots were washed a further 3X for 5 mins in PBS 0.05% Tween® 20, horseradish peroxidase substrate (Immobulin, Millipore) applied and then immediately imaged using a Biorad ChemiDoc imaging system.

2.2.3.2 Immuno-fluorescence assay

After synchronisation and treatment with rapamycin (Sigma-Aldrich) or DMSO (Thermo Scientific), parasites were collected at schizogony or after having invaded fresh erythrocytes by using centrifugation on a 70% Percoll® cushion. Parasites were then washed in RPMI w/Albumax. If schizonts were to be assayed, parasites were placed in PKG inhibitor C2 (4-[7-[(dimethylamino)methyl]-2-(4-fluorphenyl)imidazo[1,2-α]pyridine-3-yl]pyrimidin-2-amine), LifeArc), 1 μM in fresh RPMI w/Albumax, and allowed to mature for 4 hrs. Schizonts or rings were then smeared onto glass coverslips and allowed to dry completely. If not to be used immediately, dried coverslips were wrapped in tissue paper and stored at -80^{o}C in water-tight sealed bags with silica beads (desiccant condition). Sealed containers were then warmed to 37^{o}C for 1 hr prior to use. Smears on coverslips were then fixed with 4% formaldehyde (Thermo scientific) in PBS for 1 hr and then washed with 0.1% Triton^{TM} X-100 in Phosphate buffered saline (PBS, 137 mM NaCl, 2.7 mM KCl, 10 mM Na_2HPO_4, 1.8 mM KH_2PO_4) for 10 min and then 2X in PBS for 5 min. Slides were blocked with 3% w/v BSA (Sigma Aldrich) o/n and then washed 3X in PBS. Slides were incubated with primary antibody in 3% w/v BSA (X509, 1/5000; 111.4, 1/50, see Materials) in a humidified chamber at 37^{o}C for 1 hr and then washed 3X PBS for 5 min. Incubation with secondary Alexa Fluor antibodies diluted in 3% w/v BSA (1/2000, see Materials) was carried out in a humidified chamber at 37^{o}C for 1 hr, shielded from light and then washed 3X PBS for 5 min. Slides were

mounted in Vectashield containing DAPI (Vector laboratories) and images acquired using a AxioVision 3.1 software on an Axioplan 2 microscope (Zeiss) with a Plan-APOCHROMAT 100×/1.4 oil immersion objective and processed using Fiji.

2.2.3.3 Reversed phase High Performance Liquid Chromatography (HPLC)

Large-scale preparation of egress culture supernatant was carried out following the method described in 5.7.2.7. After synchronisation and treatment with rapamycin (Methods 5.7.2.1, 5.7.2.6), schizonts were Percoll® enriched, washed in RPMI w/Albumax and incubated in 1 μM C2 in fresh RPMI w/Albumax for 4hrs, 37°C to allow maturation (Collins, Hackett, et al., 2013b). Schizonts were then washed by centrifugation (pelleted at 1,800 rpm, 1 min and then resuspended) 2X in pre warmed RPMI w/o Albumax (Gibco RPMI 1640 media), w/o C2. In this case, 200 μL of schizonts were used. After washing schizonts were then resuspended in 10 mL RPMI w/o Albumax, gassed with CO_2 and left to egress for 1-2 hrs at 37°C, shaking (200 rpm). Post egress samples were then spun down and the supernatant collected. The supernatant was filtered using a syringe and a 0.45 μm membrane syringe filter (PES, Starlab), flash frozen in LN_2 and stored at -80°C until chromatography was performed.

For separation of cleavage products culture supernatants were acidified by the addition of trifluoroacetic acid and loaded onto a Vydac 4.6 mm by 150 mm 214TP C4 RP-HPLC column. Bound proteins were eluted with an acetonitrile gradient, eluting at 1 mL/min with a 0-40% (v/v) gradient of acetonitrile in 0.1% trifluoroacetic acid over 20 min, followed by 40-55% (v/v) gradient of acetonitrile in 0.1% trifluoroacetic acid over 30 min. Collected eluate fractions (1 mL each) were dried overnight in a Speedvac. Dried fractions were each resuspended in 50 μL of 1x SDS reducing sample buffer. Fractions were analysed by SDS

PAGE and Western blot, probing with mAb X509 to determine the position of elution of the MSP1 fragments.

2.2.3.4 MSP1 purification from P. falciparum culture

P. falciparum line 3D7MSP1-FLAG:loxP was synchronised and rings rapamycin treated as previously described, resulting schizonts Percoll® enriched and C2 treated for 3-4 hrs, to further synchronise and mature parasites. At the point of full maturation schizonts are collected and washed in RPMI w/o Albumax w/ C2. For pull down of MSP1 unprocessed by SUB1, schizonts were lysed in cooled (4°C) Tris-buffered Saline (Sigma-Aldrich) w/ Protease inhibitors (w/o EDTA, Roche), 0.15% Saponin, v/v 1:5 schizonts: buffer, and kept on ice. The soluble fraction of the lysed material was obtained by centrifugation of lysed sample (20,000 xg, 4°C, 15 mins) and collection of the resulting supernatant. For harvest of SUB1 processed MSP1, after washing collected mature schizonts in RPMI w/o Albumax w/ C2, schizonts were further washed 2X in RPMI w/o Albumax w/o C2. Parasites were then allowed to egress in fresh RPMI w/o Albumax w/o C2 (1:20 v/v schizonts: media) for 1-2 hrs at 37°C, whilst shaking. Egress supernatant was collected by centrifugation (17,000 xg, RT). Lysed and egressed samples were flash frozen in LN_2 and stored at -80°C until subject to pull down.

For purification, M2 agarose anti-FLAG affinity resin (Sigma-Aldrich) was washed by centrifugation (200 xg, 1 min) 5X in pre-cooled Tris-buffered saline w/ Protease inhibitors (w/o EDTA, Roche). Lysed/egressed crude samples were clarified to remove aggregates or free merozoites, using Spin-X filter columns (Corning™, Costar™, 0.45 μM nylon filter, centrifugation at 20,000 xg, 4°C) and applied to the washed resin. Protein was allowed to bind to the resin for 1 hr at 4°C, the unbound material removed and then the resin washed

by centrifugation (200 xg 1 min) 5X in pre-cooled Tris-buffered saline w/ protease inhibitors (w/o EDTA, Roche). Protein was eluted from the resin using 1X FLAG peptide (Pierce) at 500 mg/mL (2:1 v/v peptide solution: resin, o/n at 4°C) and collected using Spin-X filter columns (Corning™, Costar™, 0.45µM nylon filter, centrifugation at 20,000 xg, 4°C). Remnant FLAG peptide removed from the purified sample using desalting columns as per manufactures guidelines (Zeba™ Spin Desalting Columns, 7 kDa MW CO, ThermoFisher). Samples of crude, unbound and purified material, as well as that of washes, were analysed by SDS PAGE (4-15% and western blot (see Materials for antibodies and dilutions) or Coomassie stain (InstaBlue, Abcam). Controls for MS analysis were prepared from mock treated 3D7MSP1-FLAG:loxP parasites using the same protocol.

2.2.3.5 Mass spectrometry

Mass spectrometry and data analysis were performed by Steve Howell and Fairouz Ibrahim, as part of the Crick Proteomics Science Technology Platform. Reduced and alkylated proteins were in-gel digested with 100ng trypsin (modified sequencing grade, Promega) overnight at 37°C. Supernatants were dried in a vacuum centrifuge and resuspended in 0.1% TriFluoroAcetic acid (TFA). On an Ultimate 3000 nanoRSLC HPLC (Thermo Scientific) 1-10ul of acidified protein digest was loaded onto a 20mm x 75um Pepmap C18 trap column (Thermo Scientific) prior to elution via a 50cm x 75um EasySpray C18 column into a Lumos Tribrid Orbitrap mass spectrometer (Thermo Scientific). A 90' binary gradient of 6%-40%B over 63' was used prior to washing and re-equilibration (A= 2%ACN, 0.1% formic acid; B= 80%ACN, 0.1% formic acid). The Orbitrap was operated in 'TopS' Data Dependent Acquisition mode with precursor ion spectra acquired at 120k resolution in the Orbitrap detector and MS/MS spectra at 32% HCD collision energy in in the ion trap. Automatic Gain

Control was set to Auto for MS1 and MS2. Maximum injection times were set to 'Standard' (MS1) and 'Dynamic' (MS2). Dynamic exclusion was set to 20s. Raw files were processed using Maxquant (maxquant.org) (Cox & Mann, 2008) and Perseus (maxquant.net/perseus) (Tyanova et al., 2016) with recent downloads of the Plasmodium falciparum 3D7 (www.plasmodb.org) and the Uniprot Homo sapiens reference proteome, together with the Maxquant common contaminants databases. A decoy database of reversed sequences was used to filter false positives at protein and peptide FDR of 1%. T-tests were performed with a permutation-based FDR of 5% to cater for multiple hypothesis testing.

2.2.4 Transmission Electron microscopy for macromolecular structure determination

The three-dimensional (3D) structures and spatial arrangement of biological molecules and complexes, both *in vivo* and *in vitro*, are essential for understanding the processes and mechanisms that underpin life (Orlova & Saibil, 2011). Electron microscopy (EM), with advances in image recording and processing, has become an essential tool for providing high-resolution images of atomic to cellular structures in near native state. Transmission EM (TEM) directs a high energy electron beam (80-300 kV) onto a specimen and records the interference between electrons that pass through and are scattered by the specimen (Figure 2-2). This methods section covers the basics of TEM, biological sample preparation, and image processing used for the imaging of cells and molecules. Following the explanation of TEM, the specific protocols used in this work are detailed.

2.2.4.1 Transmission electron microscope anatomy

2.2.4.1.1 Electron sources

An electron microscope consists of an electron source from which electrons are extracted and accelerated through the microscope column and focused into a beam by a series of lenses. The beam is directed onto the sample which scatters electrons, which are then focused to form a magnified image. Electron sources are of two major types: thermal emission source or field emission gun (FEG). Thermal emission sources include a bent metal filament made of tungsten, which is heated to extreme temperatures (2000-3000°C) to promote electron emission, or a sharpened crystals of lanthanum hexaboride (LaB_6), which require less heating for emission of electrons from the crystal vertex (5 – 10 μm in diameter). The FEG comprises of a sharpened tungsten crystal tip (10-20 nm in diameter), coated in zirconium oxide, to decrease the energy required for electron emission. An electrostatic field is used to draw electrons from the tip. FEGs can be cold or heated to increase rate of emission, and use of a FEG results in a more coherent, brighter electron beam. This increases the ratio of signal to noise and improves image resolution (Orlova & Saibil, 2011).

2.2.4.1.2 The lens system

Once emitted, electrons are accelerated to the operating voltage, typically 300 kV for cryo-EM data collection. The wavelength of an electron is determined by the accelerating voltage of the microscope; with an accelerating voltage of 300 kV, the wavelength is 2 pm. The column must be maintained under a high vacuum to prevent scattering of the electron beam by gases. The beam is directed through the electron lenses in the column; to focus electrons, lenses consist of a coiled metal wire, through which an electrical current is

passed. This creates an electromagnetic field that bends the trajectory of electrons, forcing them to spiral and move toward the focal or crossover point.

There are 3 lens systems within the column of the microscope: the condenser, objective and projector lenses (Figure 2.2). Above the lens systems are deflectors, ensuring the electron beam is directed through the lens, and below, stigmators are used to correct beam aberrations caused by lenses. Apertures are also employed after lenses, to limit electron passage. The accelerated beam first passes through the condenser lens system, of which 3 lenses are found in most high-end FEG microscopes (condenser 1-3), that allow the beam size at the sample to be adjusted while retaining parallel illumination. Condenser 1 and condenser 2 control the coherence, spread and intensity of the beam by controlling the points of beam crossover. Condenser 3 ensures the beam is parallel to the optical axis and hence, parallel illumination of the sample. The specimen sits in the middle of the objective lens system on a stage, perpendicular to the optical axis, and the beam is transmitted or scattered by the sample. The objective lens system focuses the electron scatter and magnifies the image. Tuning of the objective lens sets the image focus and the objective aperture controls the maximum angle of scatter that can be detected. The image is further magnified and electrons are focused onto a detector by intermediate lenses and the projector lens system (Orlova & Saibil, 2011).

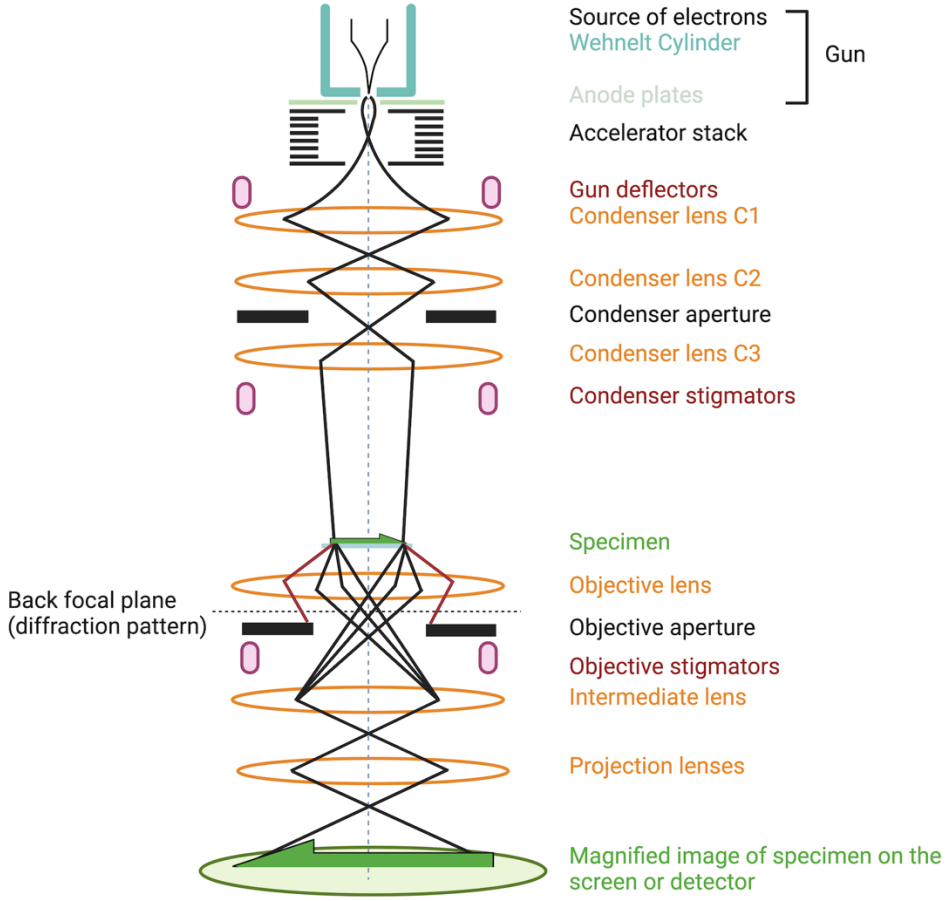

Figure 2.2 - The anatomy of a transmission electron microscope.

Figure adapted from Orlova & Saibil, 2011.

2.2.4.1.3 Electron detectors

Digital detectors are used for electron detection. Coupled charge device detectors (CCDs) are used in lower end microscopes. A scintillator is used to convert electrons into photons, photons are transferred to a cooled CCD by a fibre optic plate (Figure 2.3A). Photon energy is converted to an electrical charge by photosensitive elements that are arranged in a grid on the CCD. Charge accumulates at each pixel and is then shifted row-by row to the final

row, known as the readout register. Here pixel charge is sequentially converted to voltage. This allows image formation by the recording of a sequence of voltages, which vary depending on light intensity, each associated with a specific location on the sensor. The conversion of electrons to photons and the fact that high energy electrons can be further scattered in the scintillator introduces noise (Hell et al., 2021).

Higher end microscopes now use direct electron detectors (DEDs) (Figure2.3B), which have greatly improved signal to noise ratio and detective quantum efficiency (DQE – a measure of combined effects of signal and noise performance of an imaging system), making high resolution possible. They use a complementary metal oxide semiconductor (CMOS), in which electron charge is converted to voltage at each pixel and rows of pixels are connected to wires for a fast, simultaneous readout. Monolithic active pixel sensors (MAPS) are a type of direct electron sensor; the sensor and the CMOS are in a single chip, which is 8 μm thick, scattered electrons only deposit a fraction of their energy as a result. Pixel size is much smaller (5 μm) meaning higher resolution, but pixel saturation can occur. The fast readout is important because it allows the images to be recorded as movies that enable correction of beam-induced motion which otherwise greatly limits the resolution (Carroni & Saibil, 2016; Hell et al., 2021; Orlova & Saibil, 2011).

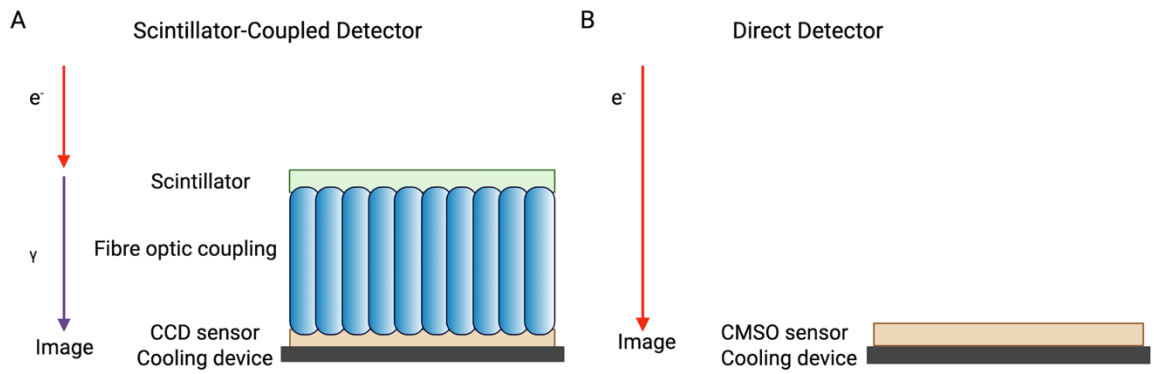

Figure 2.3 - Types of electron detector.

A) Coupled charge device detector (CCD) and B) Direct electron detector (DED). Figure adapted from Hell et al 2021.

2.2.4.2 TEM image formation

TEM images are formed due to variations in the intensity of electrons that pass through the sample (contrast) and are captured by the detector. These variations result from the interaction of the beam with the sample, and are two-dimensional (2D) projections of the 3D density of the object (Carroni & Saibil, 2016; Orlova & Saibil, 2011).

2.2.4.2.1 Electron Scatter

Electrons can be considered as both particles and waves. They interact strongly with the atoms of a given sample to give rise to two types of contrast, amplitude and phase, which will be discussed further below (Section 2.2.4.2.2). They are scattered in one of two ways: the electron interacts with the sample but does not transfer energy, known as elastic

scattering (Figure 2.4B); the electron interacts with and transfers energy to the sample, known as inelastic scattering (Figure 2.4C and D). In elastic scattering, the electron energy remains unchanged. Elastically scattered electrons are responsible for image formation in TEM and specifically provide signal for high resolution features. Elastically scattered electrons tend to be scattered at higher angles; elements with higher atomic numbers produce the greatest electron deflections.

In inelastic scattering events, the electron energy is changed. Incident electrons may collide with and transfer energy to the nucleus or an atomic electron; this can cause ejection of an atomic electron from the electron cloud or cause X-ray emission. Free radicals may also be generated and chemical bonds may be altered. Damage to the sample is sustained as a result of inelastic scatter. Most beam electrons do not interact with biological samples (Figure 2.4A) but if interaction occurs, there is a higher probability of inelastic rather than elastic scatter. Inelastically scattered electrons have longer wavelength and lower energy, so that they focus in a different plane from elastically scattered ones and contribute noise to the image. Inelastically scattered electrons can be eliminated from the image by an energy filter. Thicker samples increase the chance of inelastic and multiple scattering which degrade the image by damaging the sample and adding noise (Orlova & Saibil, 2011).

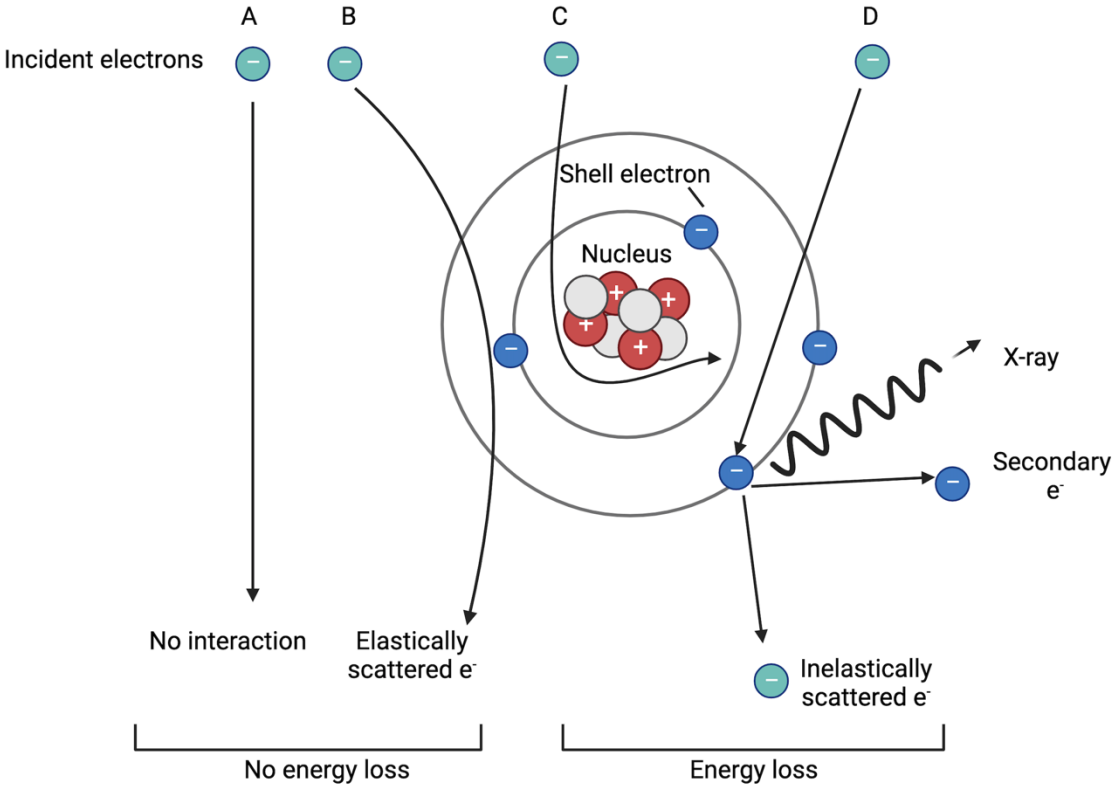

Figure 2.4 - Possible interactions of electrons with a given atom of a sample.

A) No interaction, B) elastic scattering – the electron is deflected by the atomic electron, C) and D) inelastic scattering - transfer of energy to the atomic nucleus or electrons.

2.2.4.2.2 Image Contrast

There are two types of contrast, phase and amplitude contrast. Amplitude contrast results from scattering by heavy atoms and can be thought of as absorption of part of the incident beam. For high angle scatter, scattered rays appear to be absorbed, because they are blocked by the objective aperture. This is sometimes called aperture contrast (Figure 2.5). Biological samples do not produce much amplitude contrast because they are made up of light atoms (H,O,N and C) which do not scatter electrons to high angles.

To understand phase contrast we consider the electron beam as a planar wave, which interacts and is changed by the sample (change in phase of the wave in space, Figure 2.5B) but no energy is absorbed. Phase contrast arises from interference between scattered electron waves that have altered phases and unscattered electron waves, in which the phase has not changed. This is extremely weak and does not produce visible features, but it can be greatly enhanced by selectively shifting the phase of the scattered rays relative to the unscattered beam by 90°. This produces constructive and destructive interference which can be seen as light and dark areas in the image, effectively converting phase contrast into amplitude contrast. The phase change can be created by a phase plate, but a technically much simpler approach in EM is to defocus the objective lens. The spherical aberration of the lens (described in section 2.2.4.2, Figure 2.6B) has the effect of focussing the unscattered electrons, which pass through the centre of the lens, differently from the scattered ones, which are deflected off the optical axis and pass through a more peripheral part of the lens. This means that defocus of the objective lens selectively introduces phase shift in scattered electrons (Orlova & Saibil, 2011).

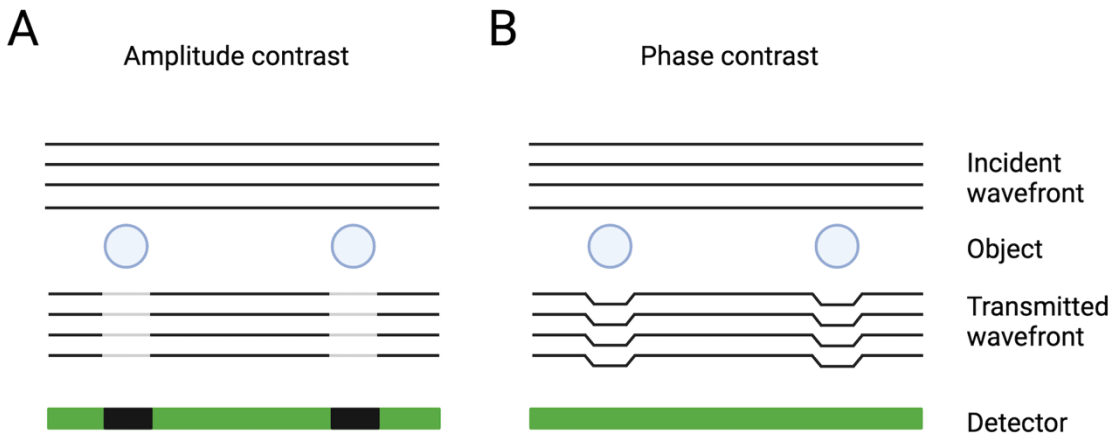

Figure 2.5 - Depiction of the types of contrast that form a TEM image.

A) Amplitude contrast appears as absorption of some of the incident beam. B) Phase contrast, change in the phase of the incident beam, converted to amplitude contrast by objective lens defocus. Figure adapted from Orlova & Saibil, 2011.

2.2.4.2.3 Electron microscope aberrations

The electromagnetic lens system in TEM has some defects that affect image formation. The most consequential of these are spherical, chromatic and astigmatic aberrations. Spherical aberration is a property of the objective lens, that focuses higher angle scattering differently from low angle or unscattered electrons (Figure 2.6B). This results in electrons not reaching a common focal point. In addition to its useful effect in enhancing phase contrast, it produces distortions in the image that are described by the contrast transfer function (CTF, described below) and can be corrected for computationally during image processing.

Chromatic aberration occurs because the lens focusses rays with different wavelengths at different points, so that parts of the image are formed in different planes (Figure 2.6C). This is a property caused by a non-monochromatic electron source but is also seen with inelastic scattering, that causes change in electron wavelength. These effects can be reduced by using an energy filter to remove electrons with altered wavelengths from the image. High end materials science microscopes are fitted with spherical and chromatic aberration correctors, but these are not currently widely used in biological cryo-EM. Astigmatism results from non-symmetrical lens field strength results in 2 image planes which causes image distortion (Figure 2.6D). This can be corrected by adjusting the lens stigmator settings or computationally as part of CTF correction (Orlova & Saibil, 2011).

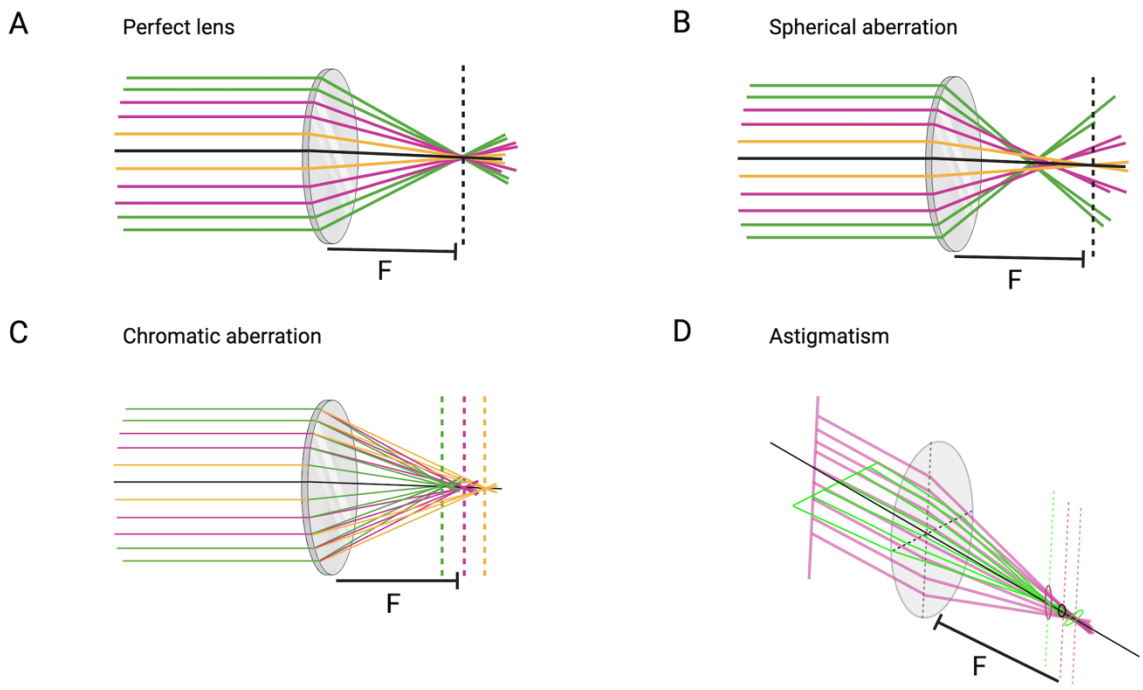

Figure 2.6 - TEM aberrations.

Figure adapted from Orlova & Saibil, 2011.

2.2.4.3 Sample preparation

The sample must be in a state that is stable within a vacuum, such that it does not evaporate, and can withstand exposure to the electron beam. Samples must also be thin enough to allow electron transmission.

2.2.4.3.1 Grids

Initially, samples are applied to grids which are circular (3 mm diameter) metal discs, typically with a square 200-300 mesh. Commonly used metals include copper and gold, although molybdenum and titanium can also be used. Metals chosen for grids are preferably non-ferromagnetic, to not distort the magnetic field of the objective lens, and conductive, to remove heat generated by the interaction of the electron beam with the sample, to prevent thermal expansion and movement. Grids are coated with an absorbent surface, typically amorphous carbon or, formvar or silicone monoxide, which acts to support the sample. Carbon supports can be either continuous, with no holes; holey, with regular spaced and sized holes, or lacy, with irregularly distributed holes of various sizes. Holes allow passage of electrons, preventing scattering by the carbon film, which adds background noise (Carroni & Saibil, 2016; Orlova & Saibil, 2011).

Other continuous thin supports can be applied such as graphene oxide, to help improve particle absorption and distribution. Before sample application, the surface charge of grids is usually altered to render them hydrophilic, ensuring particle absorption occurs and is

even across the grid. This is carried out by plasma cleaning or glow discharging grids, applying voltage to gases at low pressure, such as oxygen, in order to bombard the grid surface with ions, leading to a rearrangement of surface atoms (Carroni & Saibil, 2016; Orlova & Saibil, 2011).

2.2.4.3.2 Sample fixation

There are primarily 3 ways samples are fixed, such that they remain as close to native state as possible but are not dehydrated in the column vacuum.

2.2.4.3.2.1 Negative stain

The simplest of these is negative staining, which involves applying a heavy metal salt to samples that have typically been absorbed onto a continuous carbon supported grid, and blotting grids to ensure a thin layer of stain. Uranyl acetate is widely used, although tungsten and molybdenum salts are alternatives; stains coat the biological structures after drying, making them more visible because of exclusion of the heavy metal, which produces good contrast. Negative stain allows rapid assessment of sample properties and homogeneity, and can be used for initial data collection and generation of reference volumes for cryo-EM data processing. However, fragile protein complexes may denature during staining because of stain acidity and drying. Additionally, internal structural information is lost as a result of stain exclusion and complete coverage of the molecule surface may not be achieved by stains. This means parts of the structure may not be discerned in negative stain image processing (Carroni & Saibil, 2016; Orlova & Saibil, 2011).

2.2.4.3.2.2 Cryo-preservation

Cryo-preservation of samples allows biological samples to be studied by EM in a hydrated state, under a vacuum. Samples are applied to grids and rapidly frozen in liquid ethane (-182°C), cooled by liquid nitrogen. Rapid freezing prevents ice crystallisation which would damage the sample, and traps molecules in a hydrated state in vitrified, glass-like ice. Frozen grids must be maintained at low temperature (-170°C) during handling and imaging to prevent devitrification; the low temperature also slows the damaging effect of the electron beam. For the study of single particles by EM, the thinnest possible ice layer is essential for imaging; the atoms of the specimen to be studied scatter electrons only slightly more than the atoms of vitrified water, meaning image contrast and the signal to noise ratio are impacted by volume of water present. Hence ice should not be much thicker than particle diameter. Varying the force and time that grids are blotted after sample application, prior to freezing, and the use of holey grid supports, can help to optimise ice thickness (Carroni & Saibil, 2016; Orlova & Saibil, 2011).

In the seconds prior to vitrification of an aqueous sample, biological molecules moving around in solution by Brownian motion, interact in multiple orientations with the air-water interface. Some orientations may be more favourable than others as a result of hydrophobic and electrostatic interactions between protein and the interface. This can result in the adoption of a preferred orientation by many particles or denaturation of the particle at the interface. Graphene oxide supports can help to increase particle absorption onto the grid ideally before air-water interface interaction is possible. Small amounts of detergent can

also be applied to supported grids prior to sample application, to change the charge at the air-water interface and hence the way particles interact, with the aim of reducing preferred orientation (B. Li et al., 2021).

2.2.4.3.2.3 High-pressure freezing

Finally, for imaging of thicker regions of whole cells or tissues in a vitreous state by TEM, samples can be frozen at high pressure (2000 bar). This is to overcome slower freezing rates, due to sample thickness, that would lead to crystalline ice formation. The media surrounding cells must also be supplemented with antifreeze agents such as 20% dextran, which have better thermal conductivity than water, to prevent ice crystallisation, aid vitrification and prevent pressure induced cell shearing. Other fillers include yeast paste, which fill up air pockets in the volume being frozen and prevent inhomogeneous freezing. High pressure freezing avoids need for chemical fixation that causes cell shrinking, swelling, or redistribution of cell contents (Bullen et al., 2014).

High pressure frozen cells can be sectioned into 50-150 nm layers at -170^{o}C using a microtome and an angled diamond knife 25-45^{o} to create samples thin enough for imaging. Sections are generally imaged by tomography, so that the dose of each tilt image is very low. Therefore section contrast is low and it can be difficult to locate the object of interest (Al-Amoudi et al., 2004). In freeze substitution, the sample is gradually warmed and water substituted with acetone, the sample is stained and then embedded in resin. However some ice crystals form during the warming phase and staining is not uniform. Although the sample is no longer in the native state, resin sectioning is much easier and provides useful biological

information in many cases. High pressure freezing and freeze-substitution give much better sample preservation than room temperature fixation and embedding, which cause sample damage by fixation and by the high temperatures used to polymerise conventional resins. The resin used in freeze substitution is polymerised by UV activation at low temperature (Bullen et al., 2014; Orlova & Saibil, 2011).

2.2.4.4 Single particle analysis

Single particle analysis is used to determine the 3D structures of macromolecular complexes after purified complexes are vitrified by plunge freezing as described above.

2.2.4.4.1 Data collection

Data is collected as a series of movies, possible with the high frame rate allowed by DEDs (Zheng et al., 2017). Ideally, the particles exhibit uniformly dispersed orientations and a set of images is collected without tilting. In practice, many samples suffer from preferred orientation and numerous trials of different conditions are required to optimise data collection. Collecting data from tilted samples can be done if the preferred orientation cannot be improved by other means (Orlova & Saibil, 2011).

2.2.4.4.2 Motion correction

Beam-induced motion is inevitable in cryo samples and it is corrected by aligning sub-frames of direct detector movies to bring the whole series into register. This correction allows for local motion and can be done over small patches. The aligned frames are averaged to produce the starting image for processing (Zheng et al., 2017).

2.2.4.4.3 CTF correction

The contrast transfer function (CTF) describes how the optical system transmits the signal as a function of spatial frequency (Figure 2.7A). It is well approximated by an oscillating, sinusoidal function with a set of zero crossings whose positions are determined by the defocus used. Therefore the defocus in each image, or even subregion, can be accurately determined by matching the CTF function with the zero crossings, which are seen as minima in the power spectrum of the image (Orlova & Saibil, 2011). Once the defocus is known, the distortions it causes to the image can be corrected using CTF correction. Although the image information is lost at the zero crossings, these are at different positions for different defocuses, so the normal range of defocus in a dataset will allow all the information to be retrieved and combined in the final structure (Figure 2.7B) (Adrian et al., 1984). The importance of defocussing is that it enhances the low-resolution contrast so that the particles are visible and can be picked (Zhang, 2016).

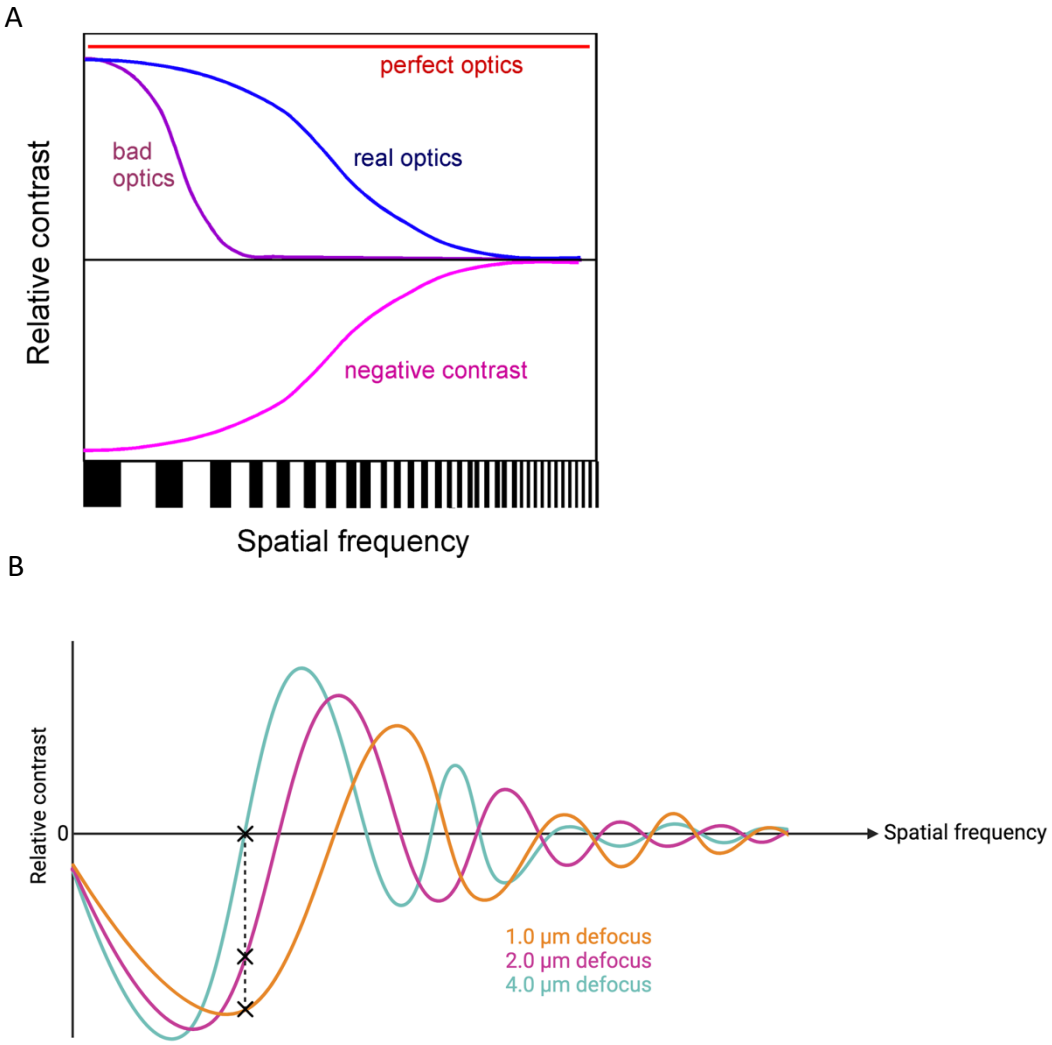

Figure 2.7 - The contrast transfer function.

A) Depiction of the overall pattern of the contrast transfer function for different optics – perfect optics gives information for all special frequencies, real optics gives less information as the spatial frequency increases. B) Demonstration of how the contrast transfer function varies for different defocus values and means that information for spatial frequencies that have zero contrast at one defocus can be collected at a different defocus. Figure adapted from Adrien et al, 1984.

2.2.4.4.4 Particle picking and 2D alignment

Selecting particles from micrographs requires them to be recognised by some variant of cross correlation/template matching. This must be done by an automated method since the data sets required for this work are in the tens and hundreds of thousands of particles. A variety of techniques are used including starting with blobs or more specific templates, or neural networks either generally or specifically trained. None of these methods are perfect and there will always be incorrectly picked particles (junk) and missed good particles. The picked particles are extracted in boxes, in which they are centred, so that they can be classified on the basis of orientation or structural differences.

2.2.4.4.5 2D classification

Classifying particles into different views allows the evaluation of the data set to see if the particles are consistent with a single structure, and then a first pass at removal of junk. If there appear to be a set of high quality views at different orientations, a first 3D reconstruction can be calculated.

2.2.4.4.5 3D classification

3D reconstruction from the 2D projections is an iterative process, in which a first set of orientation assignments is tried. Reprojections of the 3D map are compared with the input projections and the reprojections can be used as templates for improved alignment and orientation assignment. This refinement process is iterated and can incorporate more

accurate CTF corrections. Finally, structural variations can be sorted out by 3D classification into multiple data sets, so that high resolution maps can be obtained without resolution loss by averaging variable conformations.

2.2.4.5 TEM methods used for completion of this work

2.2.4.5.1 Schizont imaging

2.2.4.5.1.1 High-pressure freezing and freeze substitution

Fixed schizonts (see Methods 2.2.2.7) were pelleted for 15 s at 1,800 rpm. Pellet volume was estimated and pellet was subsequently resuspended 20% (w/v) dextran in RPMI medium (w/o phenol red) and then yeast slurry added (Bakers yeast in 20% (w/v) dextran in RPMI medium w/o phenol red) to give a cell slurry with a final ratio of 1:4:1 pellet: dextran-RPMI: yeast. Aluminium carriers were cleaned by sonication in acetone for 1 min. 1 µL of cell slurry was high-pressure frozen (Leica HPM 100, freezing rate of over 20,000 K/s) in the 100 µm recess of type A aluminium carriers (sealed with type B aluminium carriers, applied with a PAP pen). High pressure frozen samples were stored in LN_2. Freeze substitution (FS) of vitrified samples with resin was done using the EM AFS2 (Leica). FS replaced the primary solvent of the frozen samples (vitreous ice), first with 0.2% uranyl acetate (UA) dissolved in acetone (staining), followed >99% pure ethanol and finally Lowicryl HM20 resin. Each substitution step replaces the existing solvent and is associated with a gradual temperature increase. Once the final transfer of resin is complete, the samples are gradually brought to -50°C and exposed to ultraviolet light to polymerise the resin. Blocks containing embedded material were extracted from their moulds and stored at room temperature.

2.2.4.5.1.2 Sectioning and imaging of HM20 embedded samples

Aluminium carriers were removed from the plastic blocks containing embedded material by temperature shock. Excess plastic around embedded material was trimmed using a disposable surgical scalpel. The block was mounted into a UC7 ultramicrotome (Leica) for trimming and sectioning. An intact area was chosen for sectioning, and the area around it was trimmed away on the microtome using a 45° glass knife at a rate of 1 mm/s, trimming depth of 500 nm per rotation. Sample towers were trimmed to the shape of a square. Sections were cut from the trimmed block using a 45° diamond sectioning knife (Diatome) at a rate of 0.3-1.0 mm/s; 100 nm thick sections were cut and transferred onto 200 mesh copper London Finder H1 grids with a thin continuous carbon coat as a support film. Grids were plasma treated using the PELCO easiGlow Glow Discharge Cleaning System prior to application of plastic sections. Negative glow discharge with air was used to make the grids hydrophilic. Cells were then imaged using a JEM 1400 FLASH (JOEL), at 120 keV, between 8,000 – 12,000 X magnification, recorded on a sCMOS Matataki Flash camera.

2.2.4.5.2 Single particle EM of native MSP1

2.2.4.5.2.1 Negative stain

Negative stain was used to check the distribution of MSP1-FLAG. Carbon coated copper C-Flat grids (1.2/1.3 hole size, 200 mesh) (Electron Microscopy Sciences, UK) were negatively glow discharged for 60 s at 30 mA using a PELCO easiGlow Glow Discharge Cleaning System

(Pelco, USA). 3 µL of solution containing the purified protein was then applied for 1 min at room temperature to the grids and then blotted. The grid was then stained for 20 seconds by immersing the face of the grid in a 50 µL drop of 2% uranyl acetate (w/v) and the excess solution removed by blotting. This was process of staining was repeated twice more and then the grid was left to air dry for at least 15 minutes prior to imaging. Negative stain images were collected on a Tecnai T12 operated at 120 keV. Images were recorded at a nominal magnification of 50,000 on a 4k x 4k Gatan CCD camera.

2.2.4.5.2.2 Cryo-EM grid preparation and sample vitrification

Grids were supported with graphene oxide in order to improve sample concentration and reduce ice thickness since MSP1 is relatively small (~190 kDa). For grid preparation, carbon coated copper C-Flat grids (1.2/1.3 hole size, 200 mesh) were treated with graphene oxide (GO, Sigma-Aldrich) in DDM (3 mM, diluting GO 1/10) by application of 3 µL of solution to the grid. Grids were subsequently dried by blotting with filter paper and washed first in DDM (3 mM) and then in ddH_2O, before finally being blot dried again.

Samples were vitrified on grids using a Vitrobot Mark IV, with an automated blotting and plunge freeze system. The Vitrobot chamber was set to 4^{o}C, 100% humidity. The prepared grid was placed in the chamber, 3 µL of purified sample (Methods 5.7.1) was applied and blotted for 10-14 s with a blot force of -10. Longer blot times were chosen to ensure thin ice. The sample was then plunge frozen in liquid ethane, cooling the sample at ~1 x 10^4 °C/s in order to native sample preservation in vitreous ice.

2.2.4.5.2.3 Data collection

Movies of the vitrified samples were collected on a Titan Krios (300 kV), using a K3 summit camera system in super resolution mode. Data was collected over 3 sessions for the SUB1 un-cleaved MSP1 complex and 3 sessions for the SUB1 cleaved MSP1 complex. The microscope imaging parameters are shown in Tables 2.5 and 2.6.

Un-cleaved MSP1	**Dataset 1**	**Dataset 2**	**Dataset 3**
Microscope	Titan Krios	Titan Krios	Titan Krios
Acceleration Voltage (kV)	300	300	300
Spherical Aberration (mm)	2.7	2.7	2.7
Camera	K3 summit	K3 summit	K3 summit
Energy filter slit (eV)	20	20	20
Collection mode	Super-resolution	Super-resolution	Super-resolution
Magnification	105k X	105k X	105k X
Pixel size (Å)	0.8494	0.8494	0.8494
Defocus range (μm)	-3.3 to -1.5	-3.3 to -1.5	-3.3 to -1.5
Total dose (e/Å^2)	55.9	57.25	49.46
# of frames	50	50	50
# of micrograph movies	15,426	9,998	14,102

Table 2. 5 - Summary of the datasets used for cryo-EM single particle analysis of the MSP1 complex before egress and SUB1 cleavage

Cleaved MSP1	**Dataset 1**	**Dataset 2**	**Dataset 3**
Microscope	Titan Krios	Titan Krios	Titan Krios
Acceleration Voltage (kV)	300	300	300
Spherical Aberration (mm)	2.7	2.7	2.7
Camera	K3 summit	K3 summit	K3 summit
Energy filter slit(eV)	20	20	20
Collection mode	Super-resolution	Super-resolution	Super-resolution
Magnification	105k X	105k X	105k X
Pixel size(Å)	0.828	0.828	0.828
Defocus range (μm)	-3.3 to -1.5	-3.3 to -1.5	-3.3 to -1.5
Total dose (e/A^2)	53.96	56.72	56.85
# of frames	50	50	50
# of micrograph movies	19,603	12,182	31,558

Table 2. 6 - Summary of the datasets used for cryo-EM single particle analysis of the MSP1 complex after egress and SUB1 cleavage

2.2.4.5.2.4 Data processing and single particle analysis

Data was processed using a combination of RELION and cryoSPARC. Processing workflows are shown in Chapter 5. Map resolution was determined using the resolution of the corrected FSC curve at 0.143. Briefly the FSC is the correlation between two independent half-maps of the data; half-maps, as implied, are 3D reconstructions of half of a dataset. FSC

curves are calculated of the following: raw FSC between half-maps of unmasked data (both structure and solvent are included); FSC after applying a soft solvent mask to data (Signal to noise ratio (SNR) increased); FSC after applying a tight mask to data (Signal to noise ratio (SNR) increased further); finally, the corrected FSC curve is calculated using a tight mask with correction for noise, using the previous calculations. Model building was carried out using a combination of Alphafold2/3 (Abramson et al., 2024; Jumper et al., 2021), TEMPY-ReFF (Beton et al., 2024), ISOLDE (Croll, 2018), ChimeraX (Pettersen et al., 2021) and Phenix (Liebschner et al., 2019).

Chapter 3- Defective egress of MSP1-null *P. falciparum*

The 3D7MSP1KO:lox66/lox71rev *P. falciparum* line was designed by Christine Collins and generated by Trishant Umrekar. The characterisation of this mutant line was a combination of work done by Trishant Umrekar, Claudine Bisson, Abigale Perrin and myself. Trishant Umrekar carried out the characterisation of merozoite invasion in the 3D7MSP1flox42C *P. falciparum* line previously generated as described in Das et al., 2015. Where a figure presented was generated from others' data, this is indicated in the corresponding legend.

3.1 Conditional knock-out (KO) of MSP1

Though initially speculated to be involved in invasion of erythrocytes, MSP1 has more recently been suggested to play a role in parasite egress from red blood cells (RBC). As previously described, parasites conditionally expressing MSP1 in a soluble form, not tethered to the merozoite surface, displayed defective egress (Das et al., 2015). This mutant line will be referred to as 3D7MSP1flox42C throughout this chapter, as addition of rapamycin (RAP) resulted in expression of truncated MSP1 lacking the GPI-anchor (MSP1-42TRUNC). In the case of the MSP1-42TRUNC mutant, MSP1 was still present in the PV and might have been functioning in some way. Thus, in order to further investigate the role of MSP1 in the asexual erythrocytic cycle, we created a parasite line in which MSP1 expression

in any form could be conditionally disrupted using the RAP inducible DiCre recombinase system previously adapted for *P. falciparum* (Collins, Das, et al., 2013; Perrin et al., 2018).

To produce a line in which MSP1 expression could be conditionally ablated, Cas9-enhanced homologous recombination was used to integrate synthetic DNA encoding wild-type MSP1, flanked by lox66/lox71 sites in a head-to-head orientation, into the endogenous MSP1 locus (Figure 3.1A). The resulting parasite line was generated by T. Umrekar and is referred to as 3D7MSP1KO:lox66/lox71rev. Upon induction of DiCre activity by addition of RAP, the floxed sequence was predicted to undergo an inversion event, introducing premature stop codons into the downstream sequence. This should result in a severely truncated gene encoding just an ~16 kDa N-terminal fragment of MSP1. To discern whether the 3D7MSP1KO:lox66/lox71rev line could be used to conditionally ablate MSP1 expression, parasites were synchronised, treated with RAP or mock-treated and schizonts isolated. Diagnostic PCR performed on genomic extracts from both RAP and mock-treated schizonts demonstrated successful inversion of the floxed sequence (Figure 3.1 A). IFA and western blot analysis of schizonts showed that RAP-treatment resulted in efficient depletion of MSP1 expression. Figure 3.1 B,C). This validated use of the 3D7MSP1KO:lox66/lox71rev line to effectively deplete MSP1 for investigation of its function.

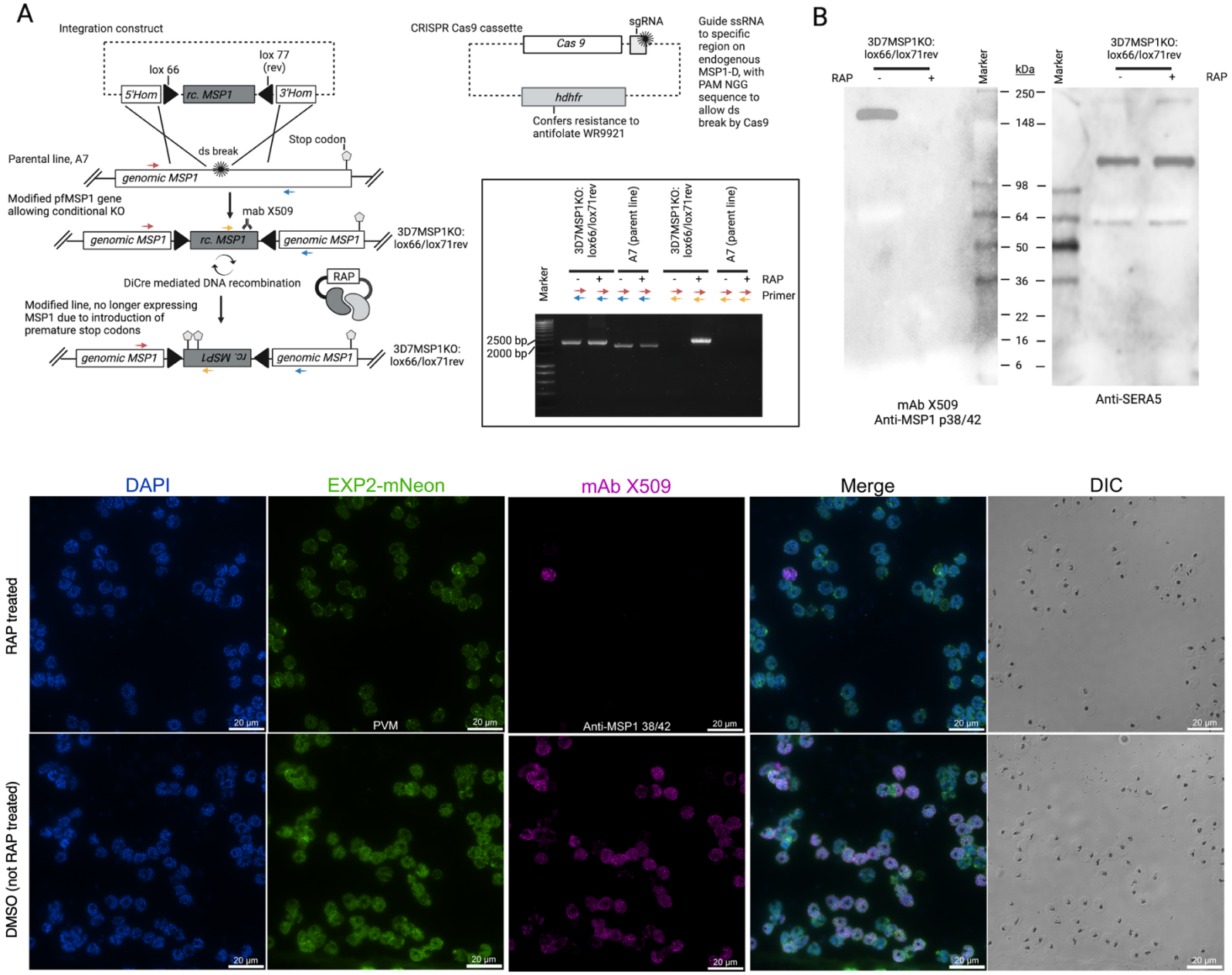
A
Integration construct
lox 66
lox 77 (rev)
5'Hom
rc. MSP1
3'Hom
ds break
Stop codon
Parental line, A7
genomic MSP1
Modified pfMSP1 gene allowing conditional KO
mab X509
genomic MSP1
rc. MSP1
genomic MSP1
3D7MSP1KO: lox66/lox71rev
DiCre mediated DNA recombination
RAP
Modified line, no longer expressing MSP1 due to introduction of premature stop codons
genomic MSP1
genomic MSP1
3D7MSP1KO: lox66/lox71rev
CRISPR Cas9 cassette
sgRNA
Cas 9
hdhfr
Confers resistance to antifolate WR9921
Guide ssRNA to specific region on endogenous MSP1-D, with PAM NGG sequence to allow ds break by Cas9
Marker
3D7MSP1KO: lox66/lox71rev
A7 (parent line)
3D7MSP1KO: lox66/lox71rev
A7 (parent line)
RAP
Primer
2500 bp
2000 bp
B
3D7MSP1KO: lox66/lox71rev
RAP
Marker
kDa
250
148
98
64
50
36
22
16
6
mAb X509
Anti-MSP1 p38/42
Anti-SERA5
C
DAPI
EXP2-mNeon
mAb X509
Merge
DIC
RAP treated
DMSO (not RAP treated)
PVM
Anti-MSP1 38/42
20 µm

Figure 3.1 - Cas 9 mediated gene editing of PF3D7_0930300 locus to allow conditional knock out of MSP1.

A) *Mutagenesis strategy. The integration construct was designed to integrate re-codonised MSP1 (rc. MSP1, dark grey) floxed with head-to-head oriented lox66/77 (black, triangles) into the endogenous msp1 locus. Integration is guided by the 5' and 3' homology sequence (white, 5'Hom and 3'Hom). The CRISPR Cas9 cassette co-transfected with the integration construct encodes Cas9 and a guide sgRNA. This ensures a targeted double stranded break in the endogenous MSP1-D sequence (PF3D7_0930300), that allows insertion of the integration construct. The hdhfr gene (light grey) confers resistance to the antifolate WR9921, allowing selection of transfected parasites. Treatment with rapamycin activates DiCre which mediates inversion of the floxed sequence, introducing premature stop codons. Only a ~16 kDa truncated form of MSP1 truncate is encoded by the modified locus, and this was not detectable in cells and likely not expressed. Oligos that prime off the endogenous MSP1-D sequence (N terminal sequence, forward primer 1.1, red arrow; C- terminal sequence, reverse primer 1.2, blue arrow) demonstrated successful integration at the expected locus (expected product for parental line A7, +/- RAP, 2000 bp; expected product after integration, 3D7MSP1KO:lox66/lox71rev +/- RAP, 2282 bp). To monitor sequence inversion, an oligo was designed to prime off the integrated inverted rc. sequence (yellow arrow, primer 1.3, rc.MSP1, dark grey) when paired with the endogenous N-terminal forward primer (red arrow). Upon addition of RAP and sequence inversion, a 2039 bp product is expected. No product is expected for DMSO treated 3D7MSP1KO:lox66/lox71rev parasites and for the parent line (A7) +/- RAP.*

B) *Evidence of loss of MSP1 expression upon addition of RAP. SDS-PAGE and Western blot analysis of mock or RAP-treated 3D7MSP1KO:lox66/lox71rev, schizonts probed with anti-MSP1 p38/42 (mAb X509). Parasites were allowed to mature in C2 before harvesting. Reduced expression of MSP1 is observed in RAP-treated parasites. Samples were also probed with anti-SERA5 as a control.*

C) *IFA of C2 arrested 3D7MSP1KO:lox66/lox71rev schizonts demonstrating loss of MSP1 expression. This line constitutively expresses EXP2 labelled with mNeon (emission 488nm), allowing visualisation of the PVM. DAPI is used as a nuclear stain. Both RAP-treated and untreated (DMSO) schizonts were probed with mAb X509 (binds MSP1 p38/42). Loss of signal for RAP-treated schizonts demonstrates loss of MSP1 expression. Scale bar 20 μm.*

To visualise the plasma membrane in parasites conditionally lacking MSP1, cryo-TEM was used. Mock and RAP-treated 3D7MSP1:lox66/lox71rev schizonts were arrested with E64-d, a cysteine protease inhibitor that prevents RBCM rupture. Cells were then plunge-frozen in liquid ethane and FIB milled to produce lamella (140 nm) for imaging of the merozoite surface by cryo-electron tomography (This work was carried out by C. Bisson, unpublished). In wild-type mature schizonts, merozoites showed a heavily decorated surface coat, with repeating protein units visible in tomograms (Figure 3.2 A,C). In RAP-treated (MSP1-null) parasites, as expected, the merozoite plasma membrane appeared to be almost completely undecorated (Figure 3.2 B,D).

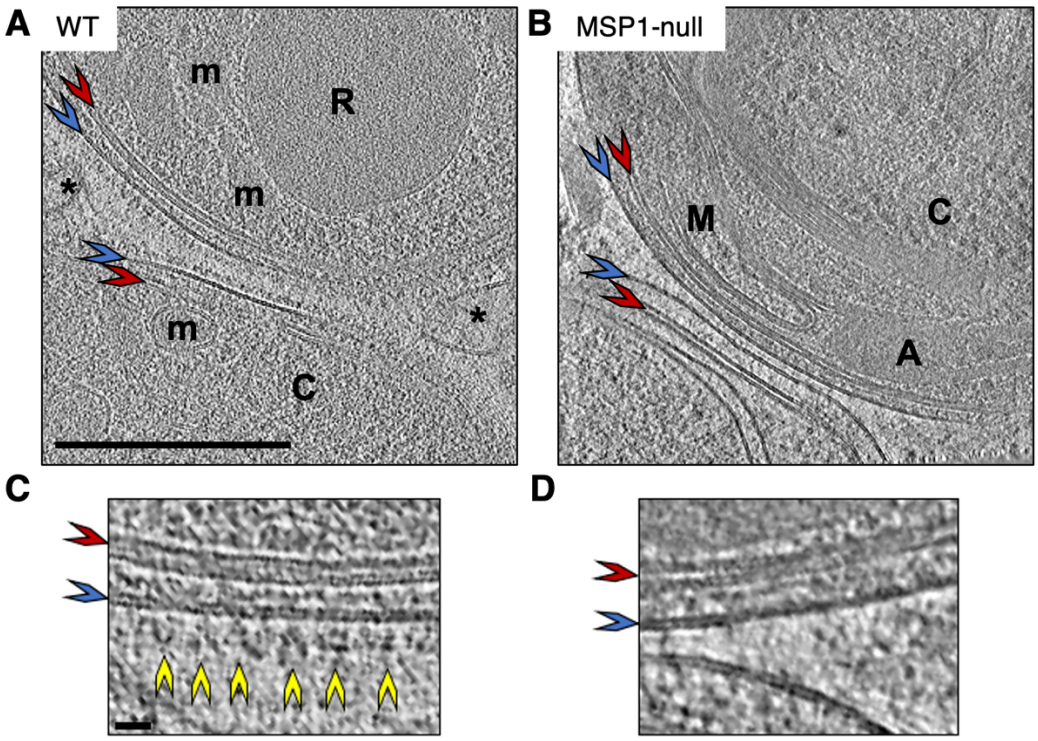

Figure 3.2 - Visualising loss of MSP1 from the merozoite surface coat by electron microscopy.

(A-B) *An average of 10 central sections from a cryo-tomogram (2.7 Å/pix) of two adjacent merozoites, from wild-type (A, DMSO treated) or MSP1-null (B, RAP treated) E64-treated schizonts. Scale bar 100 nm.*

(C-D) *A more detailed view of the merozoite surface from parts (A-B) indicating single MSP1 complexes. Scale bar, 150 Å.*

MSP1 complexes (yellow arrows) appear as V-shaped structures on the merozoite plasma membrane (blue arrow). The double membrane underlying the plasma membrane is the IMC (red arrow). R=rhoptry, m=micronemes and C=cytoplasm.

Cryo-tomogram courtesy of Claudine Bisson, unpublished.

3.2 Disruption of MSP1 expression results in reduced rates of parasite invasion and proliferation

The impact of MSP1 ablation on parasite invasion and growth was assessed by Trishant Umrekar; this was to probe the role of MSP1 in the asexual intraerythrocytic cycle of *P. falciparum*. To examine effects on invasion efficiency, synchronised RAP and mock-treated 3D7MSP1:lox66/lox71rev schizonts were added to fresh erythrocytes at low parasitaemia (5-10%), allowed to egress over a set period under both static and shaking conditions, and new ring formation quantified. As shown in Figure 3.3, rates of invasion were reduced for MSP1 null parasites under both sets of conditions (Figure 3.3A), although shaking increases merozoite dispersal; in this case, shaking increased parasitaemia ~2 fold (from static) for MSP1 null parasites and ~1.4 fold in parasites expressing MSP1 (Figure 3.3A). This suggested that the reduced invasion efficiency observed for MSP1-null parasites may be in part due to defective merozoite dispersal.

To determine the longer-term effects of loss of MSP1 expression on growth rates, cultures of synchronised 3D7MSP1:lox66/lox71rev rings were placed in fresh erythrocytes at low parasitaemia (0.1%), rapamycin or DMSO-treated o/n and then parasitaemia measured at cycle 0 – 3 (at 0 time point and then every 48 h for 3 cycles) (work done by T. Umrekar, unpublished). Wild-type cultures had significantly different parasitaemia to MSP1-null cultures by the third cycle (Figure 3.2B, $p< 0.01$). Fitting data to an exponential growth

model, as parasites grow exponentially between cycle 0 and 3, showed that wild-type and mutant parasites have significantly different growth rates ($p < 0.0001$).

Parasites expressing MSP1 in a non-membrane bound truncated form have been shown to display a growth defect (Das et al., 2015). Proliferation of the 3D7MSP1KO:lox66/lox71rev and 3D7MSP1flox42C lines was compared using the same method, to determine whether complete loss of MSP1 expression was similarly deleterious to growth. As seen in previous work, growth of MSP1 42-TRUNC parasites was significantly lower than wild-type parasites. Comparing this to growth of MSP1 null parasites showed no significant difference at the 3rd cycle (Figure 3.3C). This suggested that both complete loss of MSP1 and expression of MSP1 in a non-membrane tethered form result in a similar growth defect.

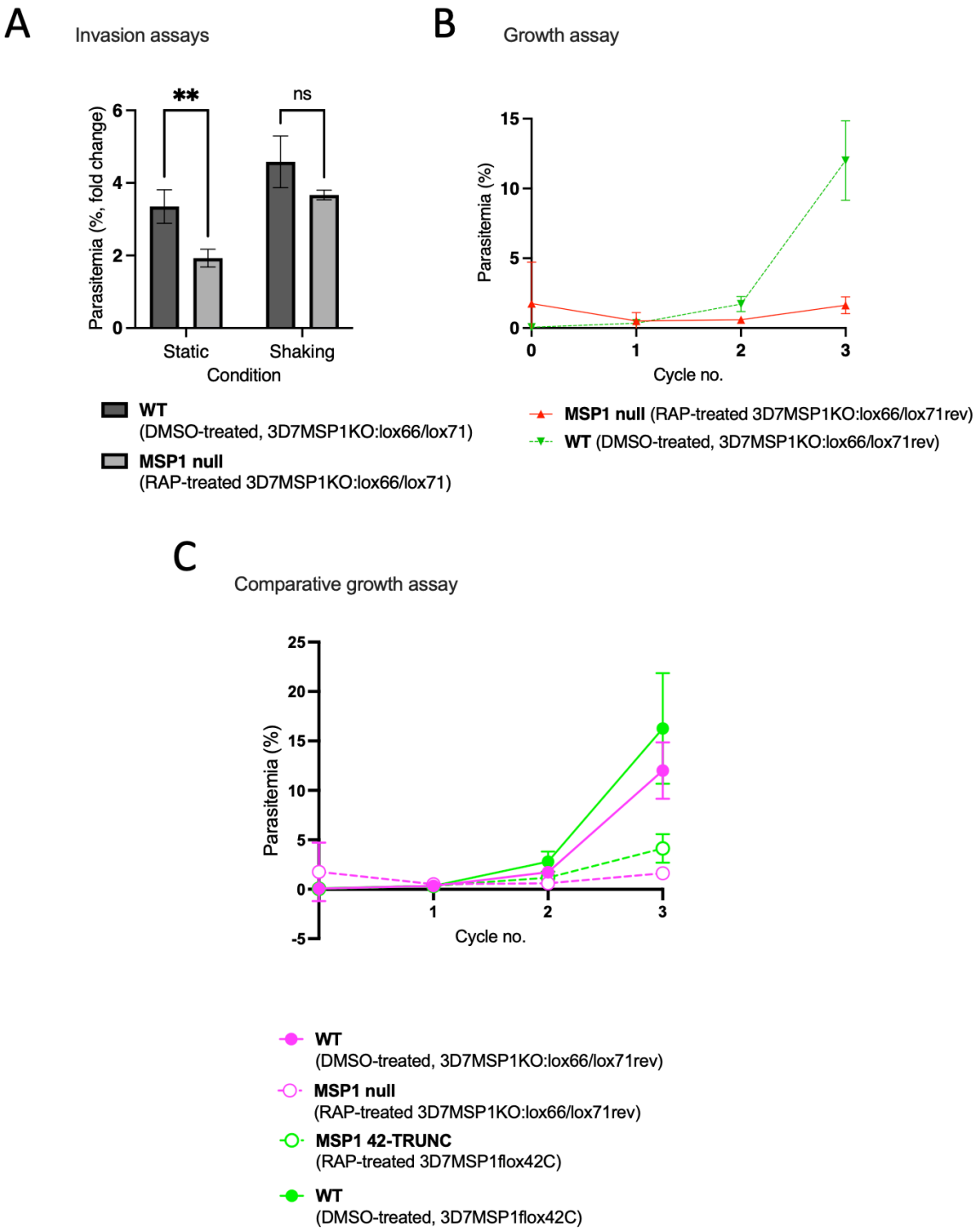

Figure 3.3 - Parasites expressing a non-membrane bound MSP1 42-truncate or MSP1-null parasites have reduced invasion and proliferation

A) *Invasion assay comparing MSP1-null and WT parasites under static or shaking conditions. Counts were corrected for starting parasitemia. There is a significant difference in parasitemia of RAP treated (MSP1-null) and DMSO treated parasites invading under static conditions (p value < 0.01, calculated by unpaired t-test) but no significant difference between RAP treated (MSP1-null) and DMSO treated parasites invading whilst shaking, n=3.*

B) *Growth assay of RAP treated (MSP1-null) and DMSO treated parasites (expressing wild-type MSP1), in which cultures at low starting parasitemia were allowed to grow over 3 cycles. Growth of mutant parasites was significantly lower at the 3rd cycle ($p<0.01$, multiple paired t-test comparison) than wild-type. Fitting data to an exponential growth model showed that wild-type and mutant have significantly different growth rates ($p<0.001$, n=3).*

C) *Comparative growth assay of mock and RAP-treated 3D7MSP1KO:lox66/lox71rev line and 3D7MSP1flox42C line. As seen previously for 3D7MSP1flox42C, growth of mutant parasites was significantly lower at the 3rd cycle ($p<0.01$, 2-way ANOVA multiple comparison) than wild-type. Fitting data to an exponential growth model showed that wild-type and mutant have significantly different growth rates ($p<0.001$, n=3). Comparing growth in RAP treated parasites from the 3D7MSP1KO:lox66/lox71rev and 3D7MSP1flox42C showed that growth of mutant parasites was not significantly different at the 3rd cycle ($p>0.05$, 2-way ANOVA multiple comparison).*

Growth and invasion assays were carried out by Trishant Umrekar.

3.3 Merozoites lacking membrane-bound MSP1 can successfully invade erythrocytes

Having seen reduced rates of invasion by MSP1-null cultures compared to wild-type under static growth conditions, and some restoration of null invasion rates when cultures were shaken, further investigations into the role of MSP1 in invasion were carried out by T.Umrekar. Using the 3D7MSP1flox42C *P. falciparum* line (Das et al., 2015), erythrocyte invasion by merozoites without MSP1 tethered to the merozoite surface membrane was observed, alongside invasion by wild-type merozoites. 3D7MSP1flox42C parasites were synchronised and either RAP or DMSO treated. Schizonts were collected, added to fresh erythrocytes at 2% parasitaemia to enrich for invasion opportunities and allowed to egress. Merozoite invasion was monitored by time-lapse video microscopy. Despite defective egress, which has been previously described for the conditional mutants of this line, invasion appeared to occur as in wild-type (Figure 3.4 A). This suggested that MSP1 is not required for merozoite invasion of erythrocytes, in turn suggesting that the reduced invasion and proliferation efficiencies of MSP1 null parasites is due to defective egress.

To confirm that MSP1-null merozoites could invade successfully mock or RAP treated 3D7MSP1KO:lox66/lox71rev schizonts were added to fresh erythrocytes and allowed to egress for 30 min. IFA was then carried out by myself on the newly invaded rings. It was expected that MSP1-19 would not be detected in rings resulting from invasion of MSP1 null merozoites. As anticipated, rings from RAP treated parasites were negative for MSP1-19, demonstrating that merozoites not expressing MSP1 are capable of invasion (Figure 3.4B).

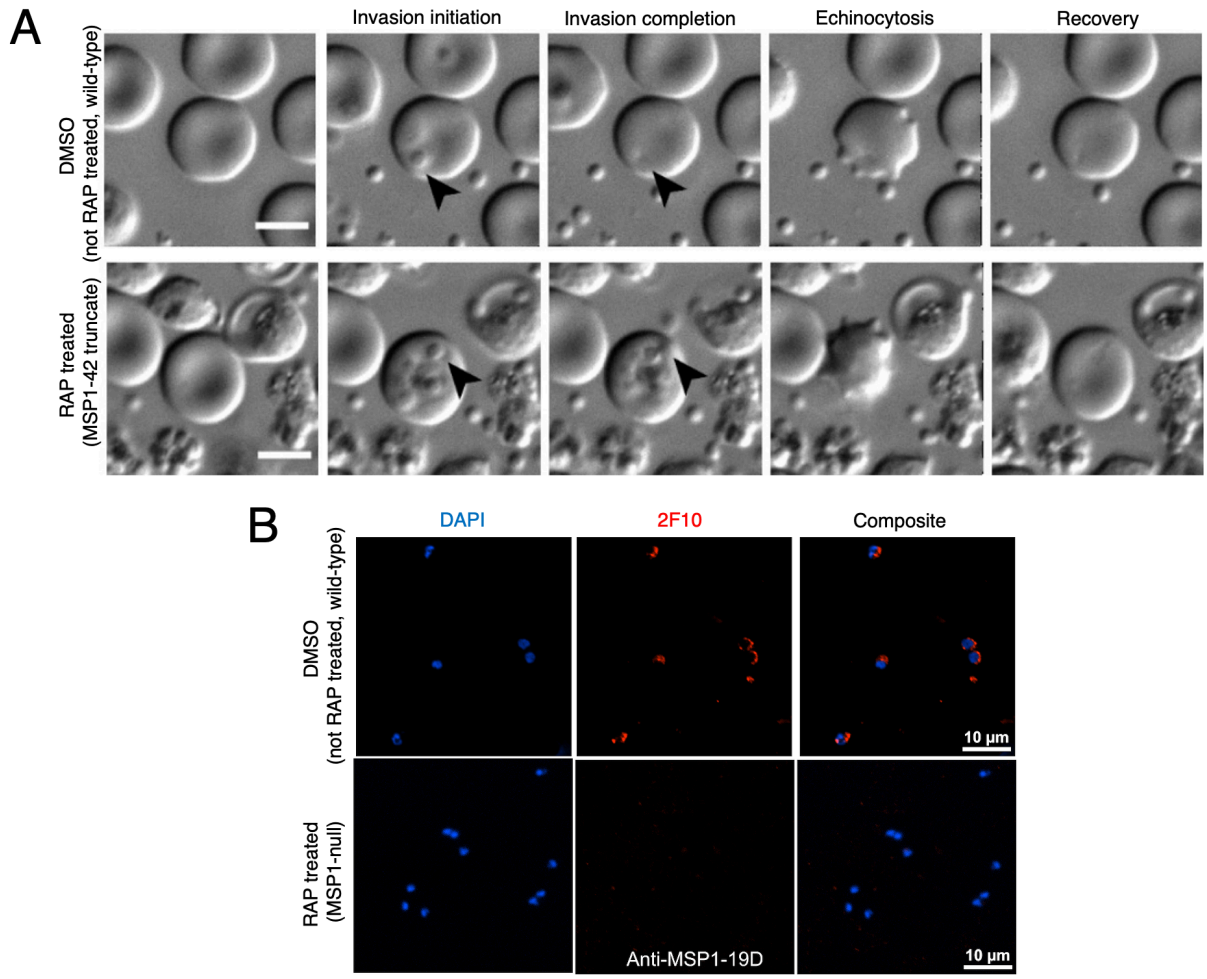

Figure 3.4 - Merozoite invasion occurs in the absence of membrane bound MSP1

A) *Stills of invasion events for parasites expressing wild-type MSP1 and RAP-treated 3D7MSP1flox42C parasites. 3D7MSP1flox42C parasites were synchronised, either RAP or DMSO treated, then the schizonts added to fresh erythrocytes at 2% parasitaemia to enrich for invasion opportunities and allowed to egress. Merozoite invasion was monitored by time-lapse video microscopy. For those merozoites that escaped egressed schizonts, normal invasion was seen in both parasite lines. It was concluded that membrane bound MSP1 is dispensable for invasion. Scale bar 5 µm. Stills courtesy of Trishant Umrekar, unpublished.*

B) *IFA confirmation of invasion by MSP1 null merozoites. 3D7MSP1KO:lox66/lox71rev parasites were synchronised and either RAP or DMSO treated. Schizonts were collected,*

added to fresh erythrocytes (10% parasitaemia) and rings collected for IFA. This line constitutively expresses EXP2 labelled with mNeon (emission 488 nm), allowing visualisation of the PVM. DAPI is used as a nuclear stain. Rings were probed with mAb 2F10 (binds MSP1 p19). Loss of signal for rings collected from RAP-treated merozoite invasion demonstrated successful invasion despite loss of MSP1 expression. Scale bar 10 μm.

3.4 Disruption of MSP1 results in defective egress

3.4.1 MSP1 null parasites show defective egress

To examine whether there is an egress phenotype associated with loss of MSP1 expression, 3D7MSP1KO:lox66/lox71rev parasites were again synchronised and either rapamycin or DMSO treated. Schizonts were treated with the PKG inhibitor Compound 2 (C2) to arrest egress but enable continued schizont maturation (Collins et al., 2013). Once maturation was complete, the schizonts were washed to remove the C2 block and allowed to egress whilst being monitored by time-lapse video microscopy. To visualise differences between parasites expressing wild-type MSP1 (untreated, DMSO) and those not expressing MSP1 (rapamycin treated), DAPI staining was used to differentiate between treated and untreated schizonts. Mutant schizonts appeared to show a similar egress phenotype to that of the MSP1 42-TRUNC (Das et al., 2015), in which egress events were less explosive and merozoites did not appear to disperse (Figure 3.5A). In confirmation of this, analysis of egress events found that 5% of mutant schizonts egressed normally, in comparison to 71.4% of wild-type schizonts

(Figure 3.5B). This indicates that MSP1 may have a role in egress, in accordance with previous work (Das et al., 2015). This work was carried out by Trishant Umrekar.

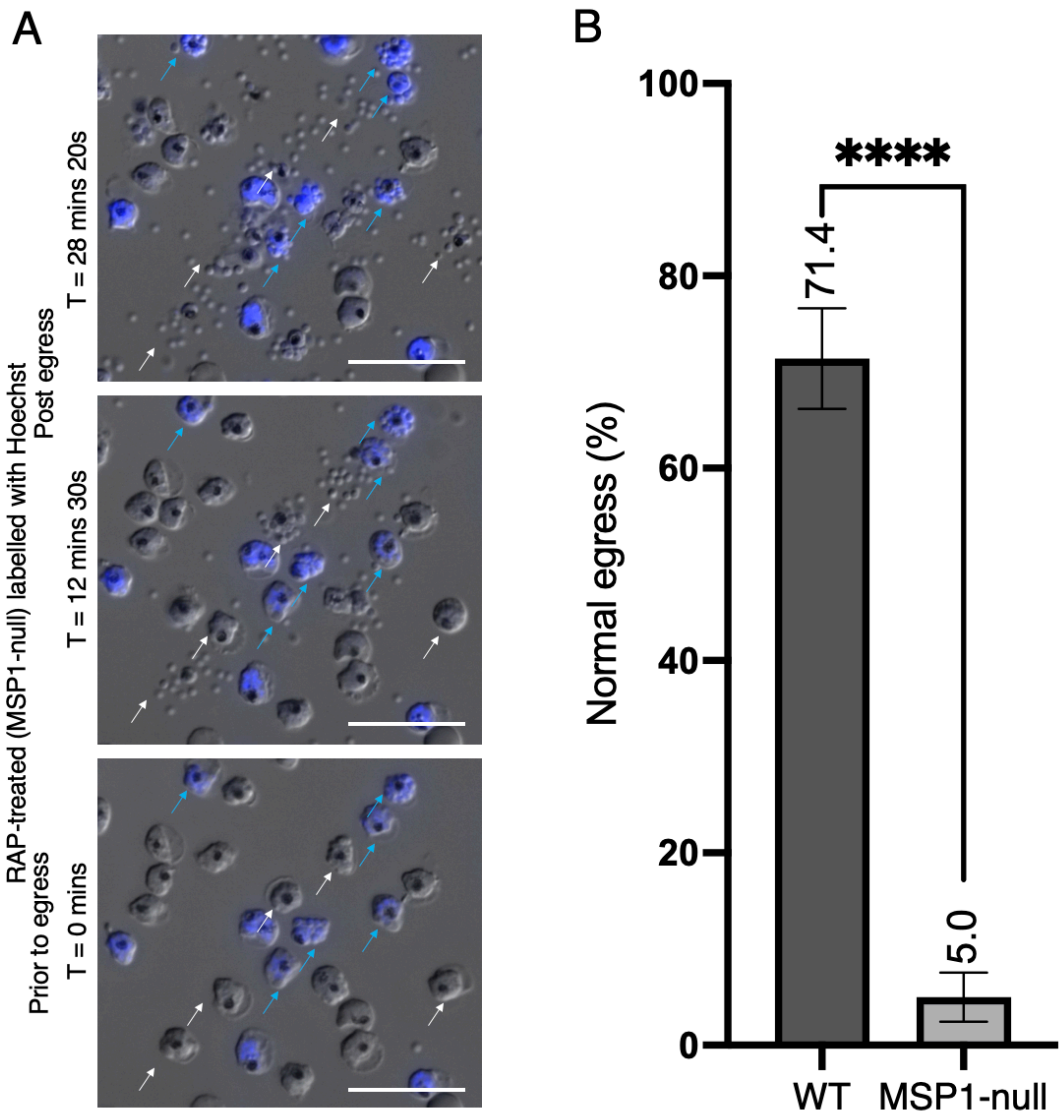

Figure 3.5 - Defective egress in MSP1-null parasites

A) *Examples of MSP- null and mock treated schizonts, just prior to, during and post egress. Stills taken from time lapse video microscopy. Synchronized schizonts were collected and allowed to mature in the presence of C2. The C2 block was removed and egress monitored by*

time lapse video microscopy. RAP-treated schizonts were labelled with Hoechst nuclear stain to distinguish between wild-type and mutant schizonts (white arrows point to wild-type (DMSO treated) schizonts and blue to mutant schizonts (RAP treated schizonts). Videos courtesy of Trishant Umrekar, unpublished. Scale bar 20 μm.

***B)** Quantification of egress events of RAP treated (MSP1-null, n =3) and mock treated (DMSO-treated, expressing wild-type MSP1, n=3) schizonts monitored by time lapse video microscopy. Normal egress was defined as explosive dispersal of merozoites after RBC membrane rupture and abnormal egress the clustering of merozoites after RBC membrane rupture. Mean values (%) of the 3 experiments is written above bars and error bars represent standard error of the mean. P value < 0.0001, calculated by unpaired, parametric t-test.*

3.4.2 PVM and RBCM rupture occur in MSP1-null parasites

Egress is a rapid and tightly regulated process in which the PVM first degrades and then the RBC membrane ruptures (Hale et al., 2017; Thomas et al., 2018). Given the apparent role for MSP1 in egress, it was considered that MSP1 might facilitate breakage of either membrane. In previous work, binding assays have suggested an interaction between MSP1 and the RBC cytoskeletal component β-spectrin (Das et al., 2015; Dijkman et al., 2021). On this basis, it was proposed that MSP1 may be involved in β-spectrin cleavage, leading to RBC membrane destabilisation and subsequent rupture. To explore whether MSP1 functions to aid SERA6 cleavage of β-spectrin (Thomas et al., 2018), the culture supernatants of egressed MSP1-null schizonts were compared to those of control schizonts. To do this, 3D7MSP1KO:lox66/lox71rev parasites were synchronised and either mock or RAP treated.

Schizonts were collected and C2 arrested to allow further maturation. Samples were taken of C2 arrested schizonts. Schizonts were then washed to remove the block and allowed to egress for 20 minutes, after which further samples were collected. Western blot analysis of wild-type and MSP1 KO schizont samples show that 20 minutes post C2 removal, during egress, β-spectrin cleavage occurs even in the absence of MSP1 (Figure 3.6). It was concluded that MSP1 is therefore not required for β-spectrin cleavage at egress.

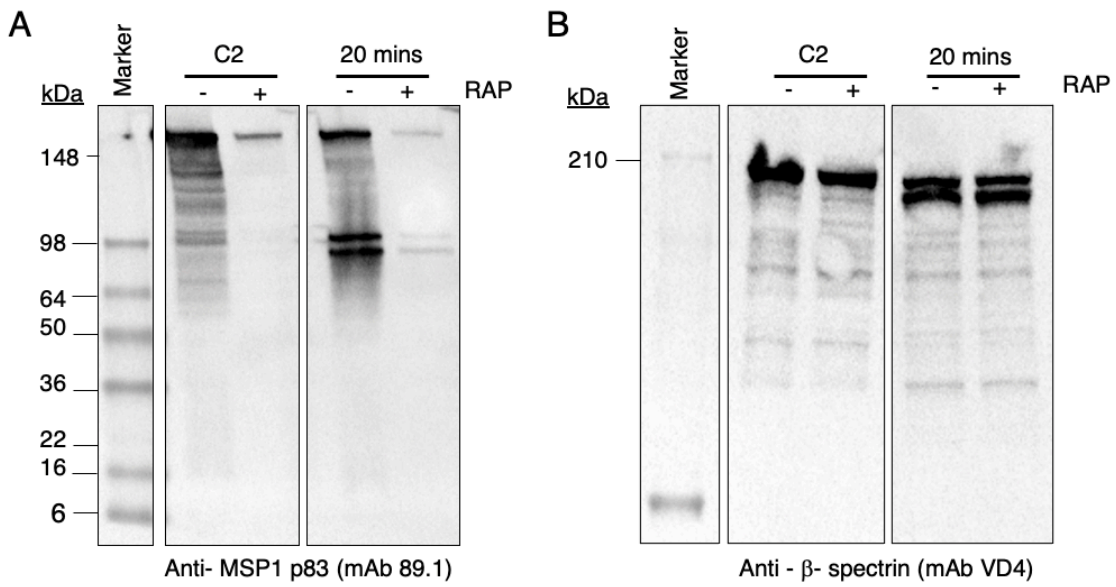

Figure 3.6 - MSP1 is not essential for β-spectrin cleavage at egress

SDS-PAGE and western blot analysis of mock (WT) and RAP (MSP1-null) treated schizonts treated with C2, allowed to mature, then either harvested straight away or the C2 block removed, cells allowed to egress for 20 min and then harvested. Blots were probed with mAb 89.1 (anti-MSP1 p83) to show loss of MSP1 expression when RAP- treated and mAb VD4 (anti-β-spectrin) to investigate cleavage of β-spectrin after egress.

To ascertain whether MSP1 is important in any way for either PVM or RBC membrane breakage during egress, both membranes were monitored using time-lapse video fluorescence microscopy of egressing MSP1-null or control schizonts; these videos were taken by A.J Perrin. The 3D7MSP1KO:lox66/lox71rev line constitutively expresses EXP2 with an mNeon tag. This effectively labels the PVM as EXP2 is an abundant PVM component (Glushakova et al., 2018). To label the RBC membrane wheat germ agglutin (WGA) was used, which selectively binds N-acetylglucosamine and N-acetylneuraminic acid (sialic acid) residues, found on all mammalian cell membranes. Video microscopy revealed that for MSP1 null schizonts, both the PV and RBC membrane rupture during egress as in wild-type, regardless of poor merozoite dispersal (Figure 3.7). It was concluded from these experiments that MSP1 is not essential for the breakage of either membrane.

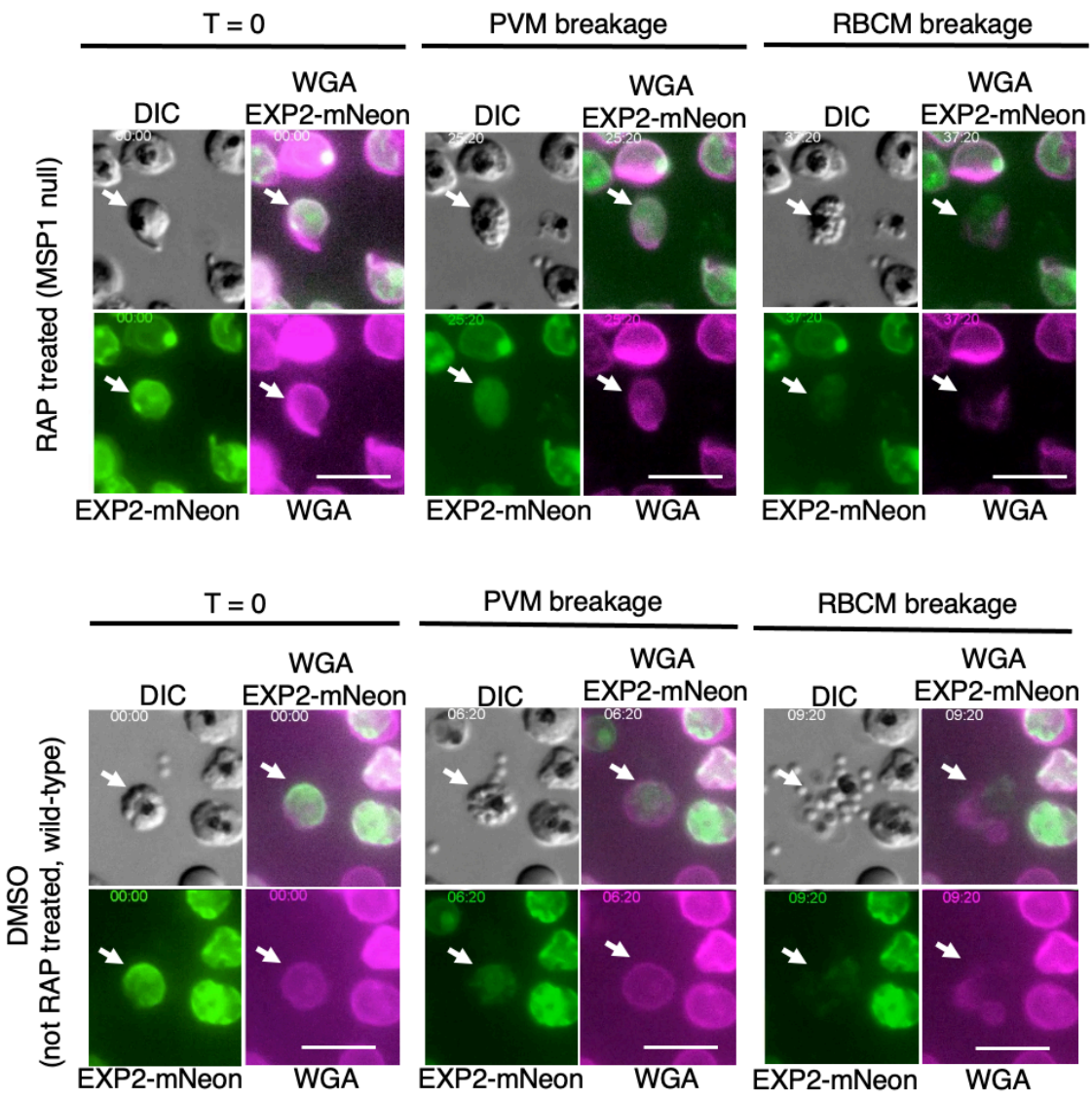

Figure 3.7 - MSP1 is not essential for RBC or PV membrane rupture

Visualization of PV and RBC membrane rupture in WT and MSP1-null schizonts by time-lapse video microscopy. Mock-treated and RAP-treated 3D7MSP1KO:lox66/lox71rev schizonts were arrested with 1 µM C2, the C2 block removed and then egress visualised using time lapse video microscopy. Cells were stained with wheat germ agglutinin-Cy5 (ex 647 nm) to allow RBCM rupture to be followed. This line constitutively expresses EXP2-mNeon, allowing PVM rupture to be followed in tandem (ex 488 nm). Figure shows an example for both

control and MSP1-null schizonts at T=0, prior to egress; PVM breakage; RBCM breakage. Scale bar 10 μm. Videos courtesy of A.J. Perrin, unpublished.

3.4.3 Loss of MSP1 may lead to a merozoite segmentation defect

To scrutinise the MSP1 null phenotype in further detail, TEM was used to examine the structural consequences of ablation of MSP1 expression. Mature control or MSP1 null schizonts were either allowed to egress (post egress cells) or treated with E64-d, a cysteine protease inhibitor, to prevent RBCM rupture (prior to egress cells). Samples were high-pressure frozen, freeze-substituted and sectioned for TEM imaging. As shown in Figure 3.8, in both WT and mutant samples the PV (97.4%, 95.2%, respectively) and RBC (94.2%, 81.9%, respectively) membranes appeared to have ruptured as expected (Figure 3.8). Interestingly, however, prior to egress (E64 treated samples) many MSP1 null merozoites had not fully segmented. 40% of mutant schizonts had not yet segmented in comparison to 8.7% of wild-type schizonts (Figure 3.8 A,B,C), with a higher overall size of the DV and associated cytoplasm (3.1 μm and 1.8 μm for mutant and WT schizonts, respectively) In all cases, merozoites appeared to contain nuclei suggesting DNA replication or segmentation was not the cause of this phenotype. Post egress, larger clusters of merozoites and membrane remnants, in addition to extended residual bodies, were seen for parasites not expressing MSP1 (Figure 3.8A,B,D). Taken at face value, this data could signify MSP1 involvement in merozoite segmentation; however, this may be a 'bystander' effect caused by loss of the major component of the plasma membrane.

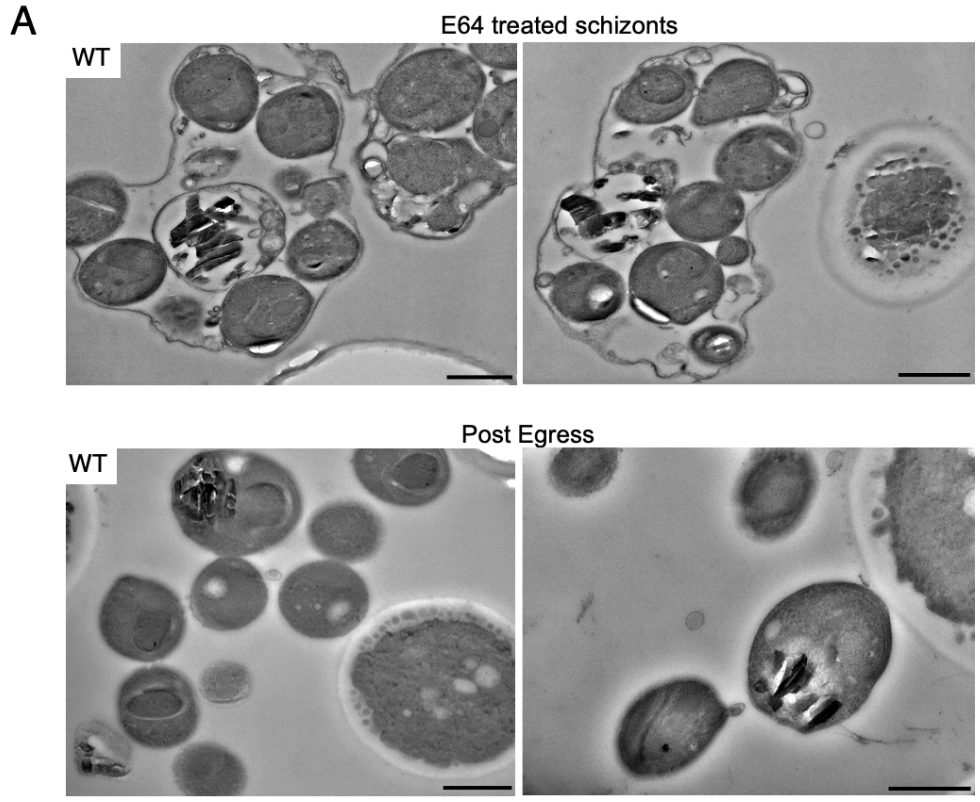
A
E64 treated schizonts
WT
Post Egress
WT
B
E64 treated schizont
MSP1 null
Post Egress
MSP1 null

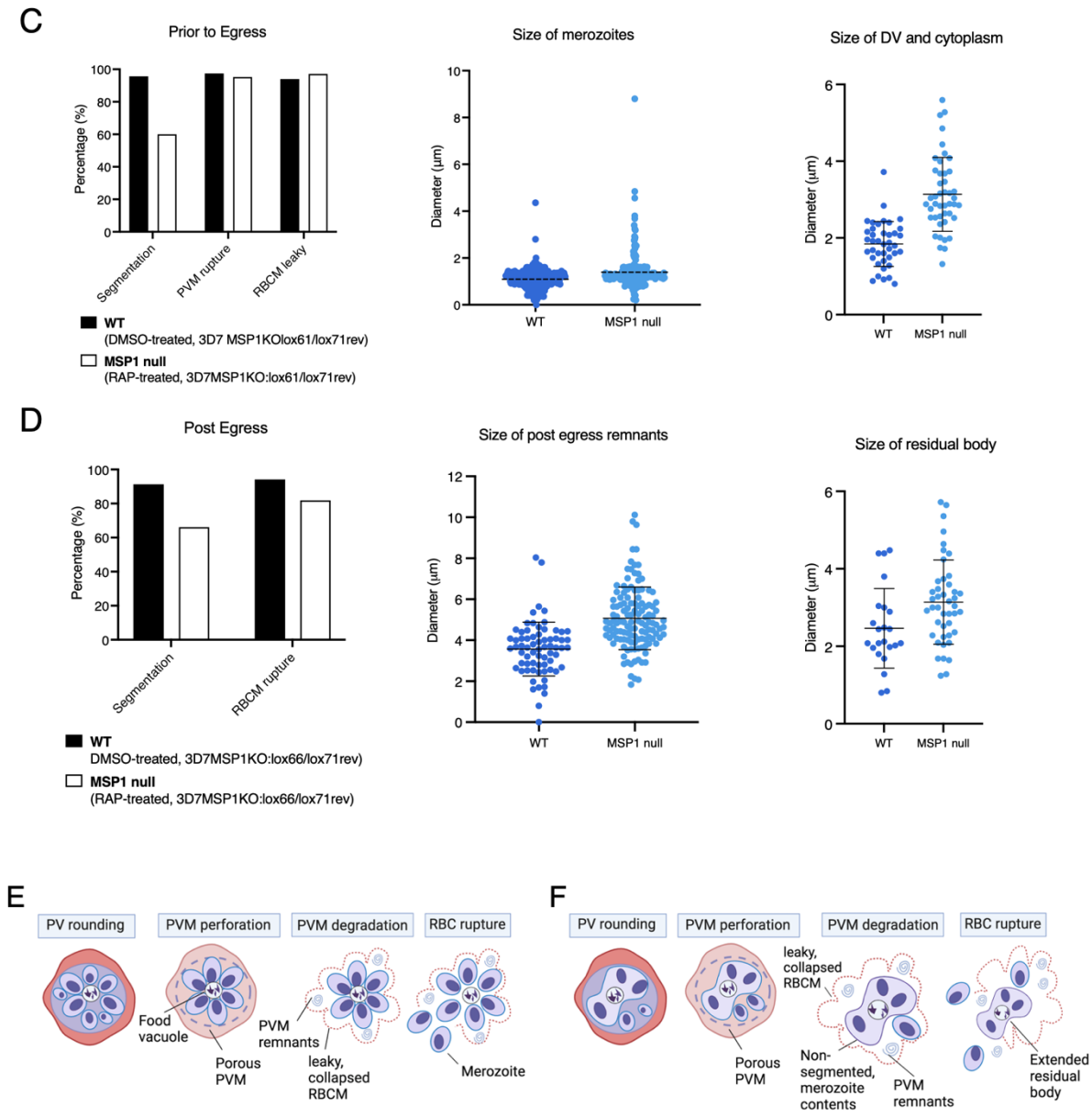

Figure 3.8 - Loss of MSP1 may affect merozoite segmentation but rupture of the PV and RBC membrane still occur.

A-B) *TEM of freeze-substituted sections of mock treated (wild-type, A) and RAP treated (MSP1 null) B) schizonts either prior to egress (RBC membrane rupture prevented by E64 cysteine protease inhibitor) or post egress (C2 arrested, C2 block removed and schizonts allowed to egress). Scale bars, 1 µm. Images of 100 cells for each E64 stalled sample, 100*

cells for RAP-treated post egress and 69 cells for mock-treated post egress. Lower cell counts for mock-treated post egress sample were due to lower cell density in sections.

C-D) *Quantification of merozoite segmentation, PV and RBC membrane rupture and RBC membrane poration seen in wild-type and MSP1-null schizonts prepared for this experiment. In effort to analyse the phenotype seen various measurements were made: the diameters of merozoites from 50 E64 stalled schizonts for both mock and RAP-treated conditions were measured (mean diameter is plot on graph, 1.39 and 1.09 μm respectively); where visible, the diameters of unsegmented cytoplasm, containing unpackaged organelles and the digestive vacuole (DV), were measured for E64 stalled schizonts for both mock and RAP-treated conditions (mean diameter is also plot: 3.1 μm, 1.8 μm respectively, error bars show standard deviation); the diameters of clusters of egress remnants (merozoites, membranes, DV) were measured for all 100 cells imaged post egress for both mock and RAP-treated conditions (mean diameter is also plot, 5.1 μm, 3.6 μm respectively, error bars show standard deviation); where visible, the diameters of the residual body (DV remnants only) post egress was measured for mock and RAP-treated conditions (mean diameter is also plot: 3.1 μm, 2.2 μm respectively, error bars show standard deviation).*

E-F) *Cartoon **s**chematic of egress that may be occurring in wild-type (E) and MSP1-null (F) schizonts, given the findings of this experiment. In the wild-type schizonts (E), merozoites segment from the cytoplasm by budding and membrane fission, assisted by the IMC; the PVM porates and then degrades; the RBCM porates, loses structural integrity and then ruptures. In the MSP1-null schizonts, segmentation of merozoites is not complete prior to the onset of egress; the PV and RBC membranes porate and rupture, as in wild-type schizonts.*

To determine whether DNA replication was normal in the MSP1-null parasites, DNA content was measured throughout parasite development within one cycle. 3D7MSP1KO:lox66/lox71rev parasites were mock or RAP-treated and followed over 48 h. As shown in Figure 3.9, this analysis revealed that the DNA content in each stage of MSP1 null parasite development was the same as in wild-type parasites expressing MSP1, confirming that the segmentation defect seen previously was not due to reduced DNA replication. Consistent with the invasion defect seen under static conditions (Figure 3.3F), fewer rings were formed in MSP1-null parasites after egress (3.9 C,D).

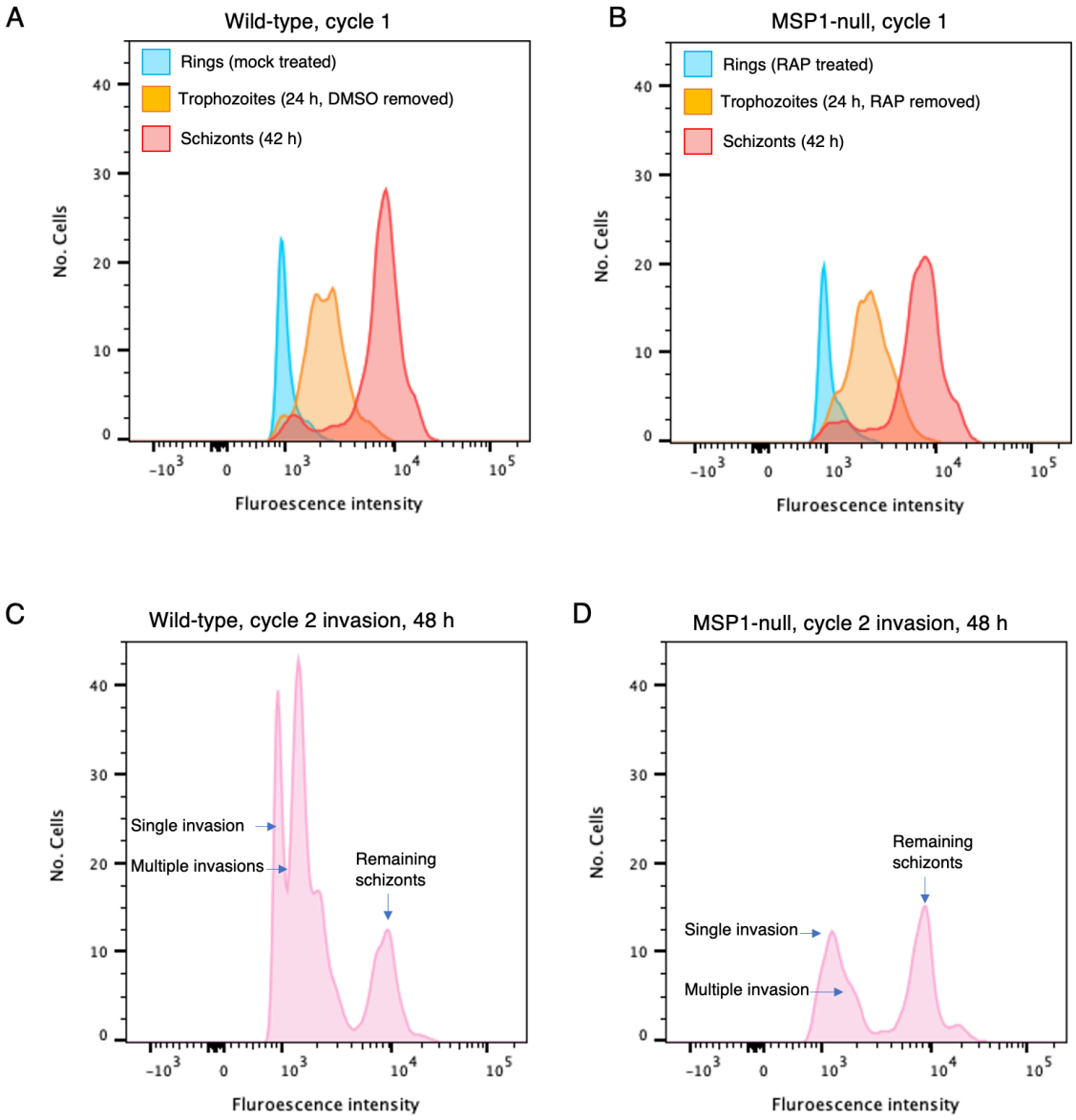

Figure 3.9 - MSP1 null parasites undergo normal DNA replication

Development assay. Schizonts (non-treated, WT) from the 3D7MSP1KO:lox66/lox71rev line were allowed to invade fresh erythrocytes (3 blood types) and rings were collected, setting up 3 biological replicates at 1-3% parasitemia each (data shown here is a representative of n=3). Rings were then either mock treated (WT) or RAP-treated (MSP1-null), treatment removed after 12 h and the DNA content of cultures was followed across one cycle (48 h total) with measurements taken at T=0, T=12 h, T=24 h, T=36 h, T=42 h and T=48 h. Data for

T=0, T=24 and T=42 h is shown for wild-type and MSP1-null parasites (A,B respectively). Data for T=48 h is shown for wild-type and MSP1-null (C, D respectively); for this graph, the life stages for that peaks account for is labelled (new rings and remaining schizonts). To follow DNA replication, samples of ~10^5 cells were collected and fixed (0.2% glutaraldehyde) then stained with 2X SYBR green and analysed using flow cytometry.

To investigate this segmentation defect further and determine whether this abnormality was specific to the previous experiment, E64 arrested schizonts from both control and MSP1-null parasites were analysed by IFA using antibodies specific for the IMC marker GAP45, and the plasma membrane marker MSP2. Additionally, nuclei were stained with DAPI to confirm that DNA segmentation was normal. The results suggested that DNA was organised in nuclei and the IMC and PM were fully segmented around individual nuclei in both wild-type and MSP1-null schizonts (Figure 3.10). It is therefore unclear, due to these conflicting results, whether MSP1-null parasites have a segmentation defect. We can conclude, however, from both the time lapse video microscopy and TEM data (Figure 3.7; Figure 3.8 C,D), that the degradation of the PVM, RBCM poration and rupture occurs in egressing schizonts that do not express MSP1, showing that MSP1 is not required for these processes.

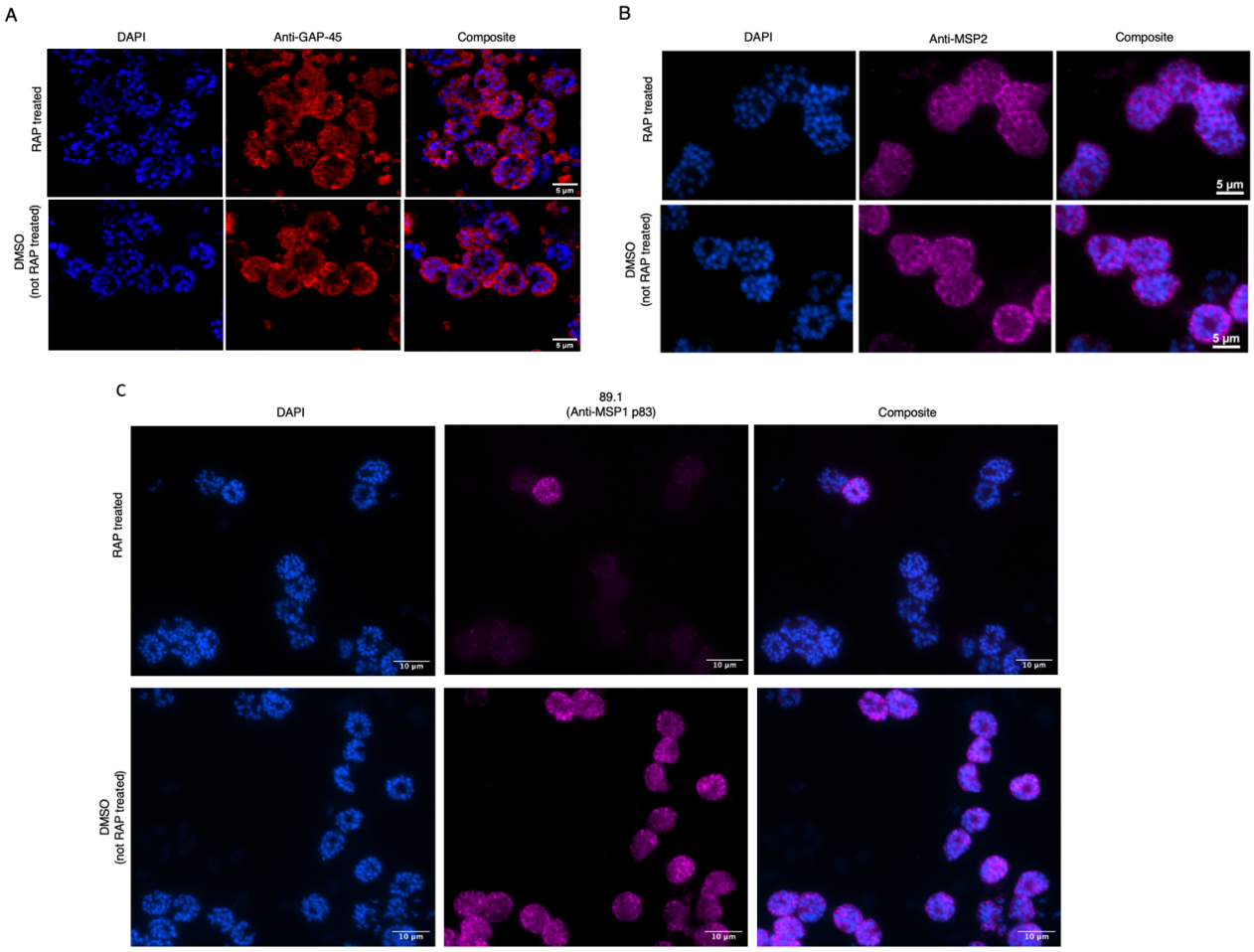

Figure 3.10 - DNA, IMC and PM segmentation occurs normally in MSP1-null parasites.

IFA of C2 arrested mock (wild-type) or RAP treated (MSP1-null) schizonts, probing for ***A)*** *GAP45, shows the IMC is segmented, scale bar 5 µm* ***B)*** *MSP2, shows the PM is segmented, scale bar 5 µm* ***C)*** *MSP1, shows gene excision and MSP1 knock out was successful, scale bar 10 µm.*

3.5 Discussion

Here MSP1 has successfully been conditionally knocked out, allowing study of function. This work has confirmed that MSP1 is not essential for invasion as merozoites without MSP1 expressed on the plasma membrane can invade and form rings.

In agreement with previous work, we have shown that in the absence of MSP1, asexual egress from erythrocytes is defective, suggesting a role for this protein in egress (Das et al., 2015). We have presented evidence that suggests MSP1 may not be involved β-spectrin cleavage, although that was previously suggested (Das et al., 2015). Through careful examination, we have ruled out a function for MSP1 in PVM degradation, RBCM poration and RBCM rupture, all of which occur during egress when cells do not express MSP1.

The actual function of MSP1 in egress remains elusive. TEM of E64 arrested and egressed schizonts suggested a possible segmentation defect upon suppression of MSP1 expression. It has been reported previously that in schizonts conditionally lacking schizont egress antigen 1 (SEA1), the cytoplasm associated with the food vacuole was extended and contained nuclei. This protein was shown to be involved in correct packaging of nuclei into merozoites and any segmented daughter merozoites were shown not to contain nuclei (Perrin et al., 2021). Our data suggests the segmentation defect seen in MSP1 null parasites is not related to nuclear division or packaging as DNA replication occurs as normal through schizont development and merozoites appear to contain nuclei, as seen by TEM and IFA.

Defective segmentation has also been described in schizonts lacking PfMOP1 and PfPhIP, with a similar agglomerate interior seen by IFA and EM in schizonts before egress as well as larger residual bodies post egress (Absalon et al., 2016; Saini et al., 2021). This is comparable to that observed for MSP1-null schizonts. Knock down of either PfMOP1 and PfPhIP showed improper formation of the IMC and PM at schizogony. PfMOP1 was concluded to be involved in IMC formation and PfPhIP part of an IMC associated complex, important for invasion (Absalon et al., 2016; Saini et al., 2021). By IFA both the IMC and PM appear to be segmented in MSP1-null schizonts, suggesting the defect observed may be experiment specific. In fact, cases of incomplete merozoite segmentation in E64 arrested wild-type schizonts has been reported. This suggests either segmentation completes late in schizogony, sometimes following PVM degradation, or that the failure of merozoites to segment in these cells is an artefact of E64 treatment (Rudlaff et al., 2020).
Further work would be needed to confirm if merozoite segmentation is affected by loss of MSP1 expression, as the lower resolution of light microscopy may limit detection of the defect in this case.

Synthesis of GPI occurs in the ER, exclusively in trophozoite stage of development (Morotti et al., 2017). If not used for tethering MSP1 to the PM this could result in excess of this phospholipid in the cell. It is possible that the fluidity and dynamics of the plasma membrane may be altered by deletion of a major surface protein and the loss of large amounts of GPI from the extracellular leaflet of the PM. This may be the reason for the segmentation defect seen. In that case, the phenotype would be a 'bystander' effect and unrelated to MSP1 function. Study of the phenotype of parasites expressing an MSP1 mutant resistant to SUB1 processing but not depleted in the merozoite membrane could

help overcome this and determine MSP1 function. The experiments described in the following chapter were carried out on this basis.

Chapter 4: The functional role of SUB1 processing of MSP1

4.1 Conditional mutagenesis of the MSP1 38/42 cleavage site disrupts cleavage by SUB1

4.1.1 Design of mutations that ablate SUB1 cleavage of the MSP1 38/42 site

As described in the previous chapter, ablation of MSP1 resulted in an egress defect. Given that the defects observed in MSP1-null parasites could be caused by the loss of major membrane surface components rather than specifically due to loss of MSP1 function, a more subtle approach to examine the role of MSP1 was devised. The importance of SUB1 cleavage at the 38/42 site has previously been highlighted in both parasite survival and temporal regulation of egress (Child et al., 2010; Das et al., 2015). The alternative mutagenesis strategy therefore focused on the disruption of processing at this site. Previous work identified mutations in the amino acid sequence flanking the 38/42 site that prevent SUB1 processing at each of the three alternative cleavage points (Das et al., 2015). Here, a new conditional mutant was designed based on the predicted substrate preference of SUB1 and characterisation of the enzyme active site (Das et al., 2015; De Monerri et al., 2011; Withers-Martinez et al., 2012, 2014)(Figure 4.1).

SUB1 substrate recognition is dependent on amino acids either side of the scissile bond (both prime and non-prime sides), with the preferred motif identified as Ile/Leu/Val/Thr-Xaa-Gly/Ala-Paa(not Leu) ↓ Xaa (where Xaa is any amino acid residue, Paa tends to be a polar residue and ↓ indicates the scissile bond). One or more acidic residues or Ser/Thr are also commonly found on the prime side of the scissile bond (De Monerri et al., 2011; Withers-Martinez et al., 2012, 2014). On this basis, the strategy chosen to disrupt recognition by SUB1 at the 38/42 site was as follows. First, at all 3 alternative cleavage points of the 38/42 site, mutation of prime site 1 (P1) to a Leu residue was planned, due to the known intolerance of SUB1 for Leu at this position. This is predicted to disrupt substrate binding in the polar S1 pocket of SUB1 (Figure 5.1B)(Koussis et al., 2009). Second, replacement of the Val, a non-polar residue, at P4 of the alt2 site with Lys, a larger and more polar residue, was planned to disrupt binding in the hydrophobic S4 pocket of SUB1 (Withers-Martinez et al., 2014). Third, the Asp residue at the P3' of alt2 was planned to be replaced with a basic Lys residue to destabilise substrate binding in the SUB1 S3' basic pockets (Withers-Martinez et al., 2014)(Figure 4.1A,C). Finally, at the alt1 and canonical (can) cleavage sites, mutation of the P2 residue from Gly to Leu was planned, substituting a residue with no side chain to that with a large side chain. This was considered unlikely to be tolerated by SUB1 because its S2 pocket is highly compact (Figure 4.1A,C)(Withers-Martinez et al., 2014). Collectively, given the predicted disruption of SUB1 recognition caused by the planned substitutions, it was anticipated that conditional incorporation of all these mutations into the MSP1 38/42 cleavage site would abolish cleavage and thus clarify the function of SUB1 processing.

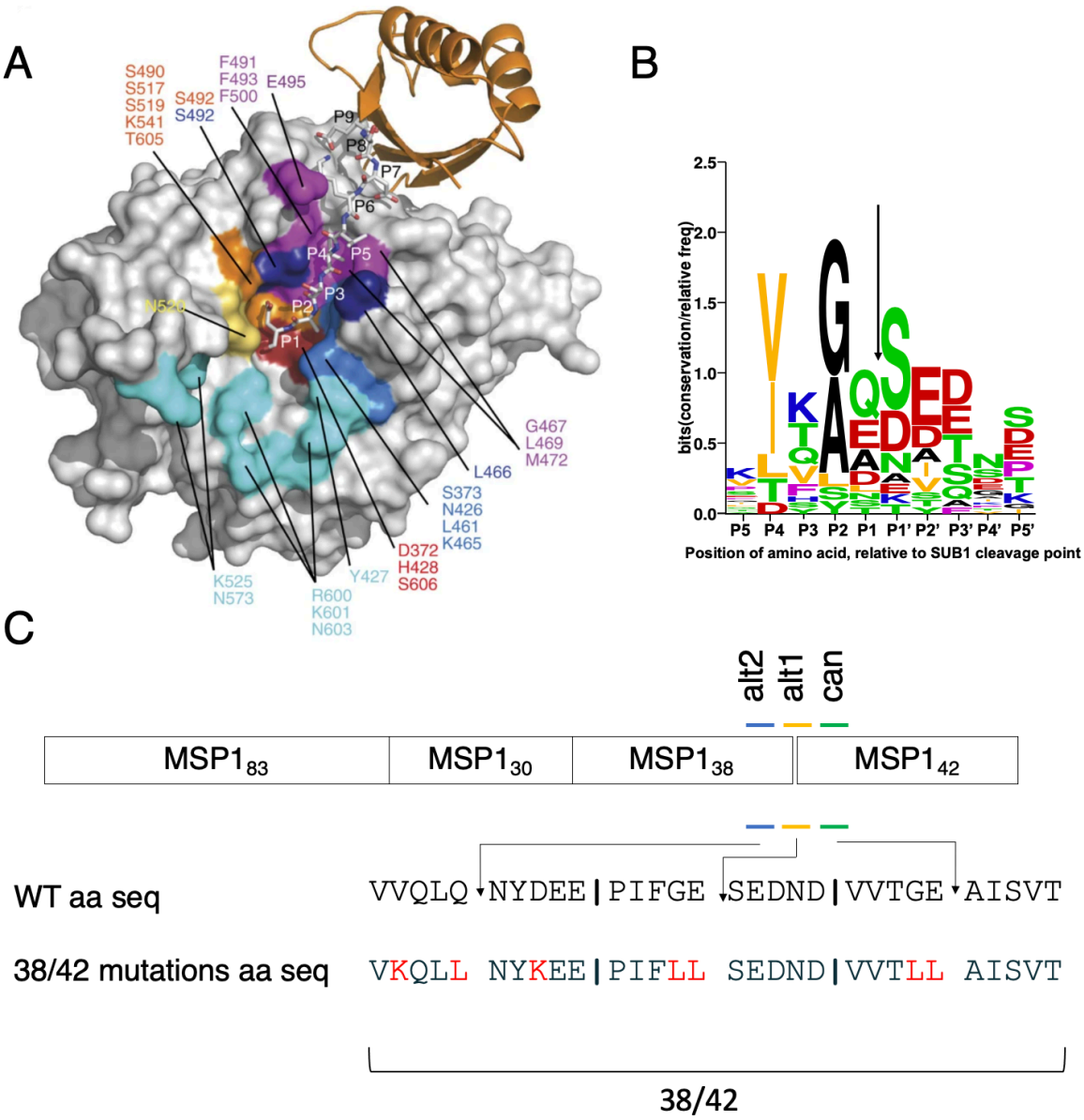

Figure 4.1 - The substrate specificity of SUB1 informed mutation of the 38/42 site of MSP1 to disrupt processing.

A) *Molecular surface representation of the crystal structure of P. falciparum SUB1. The pro-domain residues that sit in the active site pocket (p9 fragment, residues 209-217) are represented as white sticks and the rest of the pro-domain represented as an orange cartoon. The polar S1 pocket (orange), constricted S2 pocket (blue), S3 pocket (dark blue) and hydrophobic S4 pocket (magenta) are highlighted. The large basic S' surface pocket (S1'-S5') is indicated (cyan). The catalytic triad residues (Asp372, His428 and Ser606) are shown*

in red and the location of the oxyanion hole partner Asn520 in yellow. Key SUB1 active site residues are shown labelled in colours corresponding to the pocket with which they are associated. The P1 residue interacts with oxyanion hole partner Asn520 and residues Ser517, Ser519 and Ser492 at the bottom of the polar S1 pocket. The P2 space is restricted by the side chains of Lys465 and Leu461, making the S2 pocket compact. Met472, Phe491, Phe493 and Phe500 predominantly interact with substrate and form the hydrophobic S4 pocket. Important prime-side interactions likely involve P1' and P3' with Lys465 and Tyr427 by hydrogen bonding. Figure taken from Withers-Martinez et al., 2014; open access journal article covered by https://creativecommons.org/licenses/by/3.0/.

B) *Graphical representation in single-letter code of a multiple sequence alignment of amino acid residues flanking known and predicted PfSUB1 cleavage sites, with the height of each stack relating to sequence conservation and height of individual residues equal to relative frequency of amino acid at that position. Residues are colour coded according to the chemical nature of their side chains: red, acidic; blue, basic; orange, aliphatic; black, small; green, uncharged polar; and purple, nonpolar, nonaliphatic. The scissile bond is indicated by an arrow. Figure was adapted and recreated from De Monerri et al, using data from De Monerri et al., 2011; Tan et al., 2021; Withers-Martinez et al., 2012 . Weblogo.berkeley.edu was used to generate this graph.*

C) *Diagram showing the wild-type sequence of the 3 alternative cleavage points at the 38/42 SUB1 processing site of MSP1 (P5-P5', alt2 (blue), alt1 (orange) and canonical (green), as well as substitutions designed to ablate cleavage by SUB1 (red). Cleavage sites are indicated with arrows.*

4.1.2 Successful generation of a conditional MSP1 cleavage mutant

The DiCre recombinase system (Collins, Das, et al., 2013; Perrin et al., 2018) was used to create a *P. falciparum* line (3D7MSP1-38/42mut:loxP) in which the 38/42 SUB1 cleavage site of MSP1 could be conditionally mutagenised as described above. This line was additionally designed to exploit the dimorphic nature of MSP1 to allow mutagenesis to be monitored. The transgenic line was designed to express wild-type MSP1 as a chimera of the two isoforms such that the p83,30 and 42 regions of MSP1-D are fused with the p19 fragment of MSP1-F (Figure 4.2A), to allow distinction between parasites expressing WT and mutant MSP1.

To generate the conditional mutant, synthetic DNA encoding floxed, wild-type chimeric MSP1 and an altered 38/42 SUB1 cleavage site (Figure 4.2 A, integration construct) was integrated into the open reading frame of the endogenous MSP1 gene by Cas9-enhanced homologous recombination. The resulting parasite line is referred to as the 3D7MSP1-38/42mut:loxP line. Upon successful integration, addition of RAP was expected to activate the DiCre recombinase causing excision of the floxed sequence, moving the mutant 38/42 cleavage site into frame.

To determine whether the 3D7MSP1-38/42mut:loxP line could be used to conditionally mutate the 38/42 cleavage site, parasites were either mock-treated (DMSO) or RAP-treated. Diagnostic PCR of genomic DNA extracted from treated parasites showed that integration and DiCre mediated excision occurred as expected, at the correct locus (Figure 4.2A). IFA analysis confirmed that wild-type MSP1 was expressed as a chimera in mock-treated parasites. In contrast, in RAP-treated parasites MSP1 was expressed with the 3D7 C-

terminus and was therefore assumed to have a modified 38/42 SUB1 cleavage site (Figure 4.2B). Hence, conditional mutation of the MSP1 38/42 site was possible using the 3D7MSP1-38/42mut:loxP line.

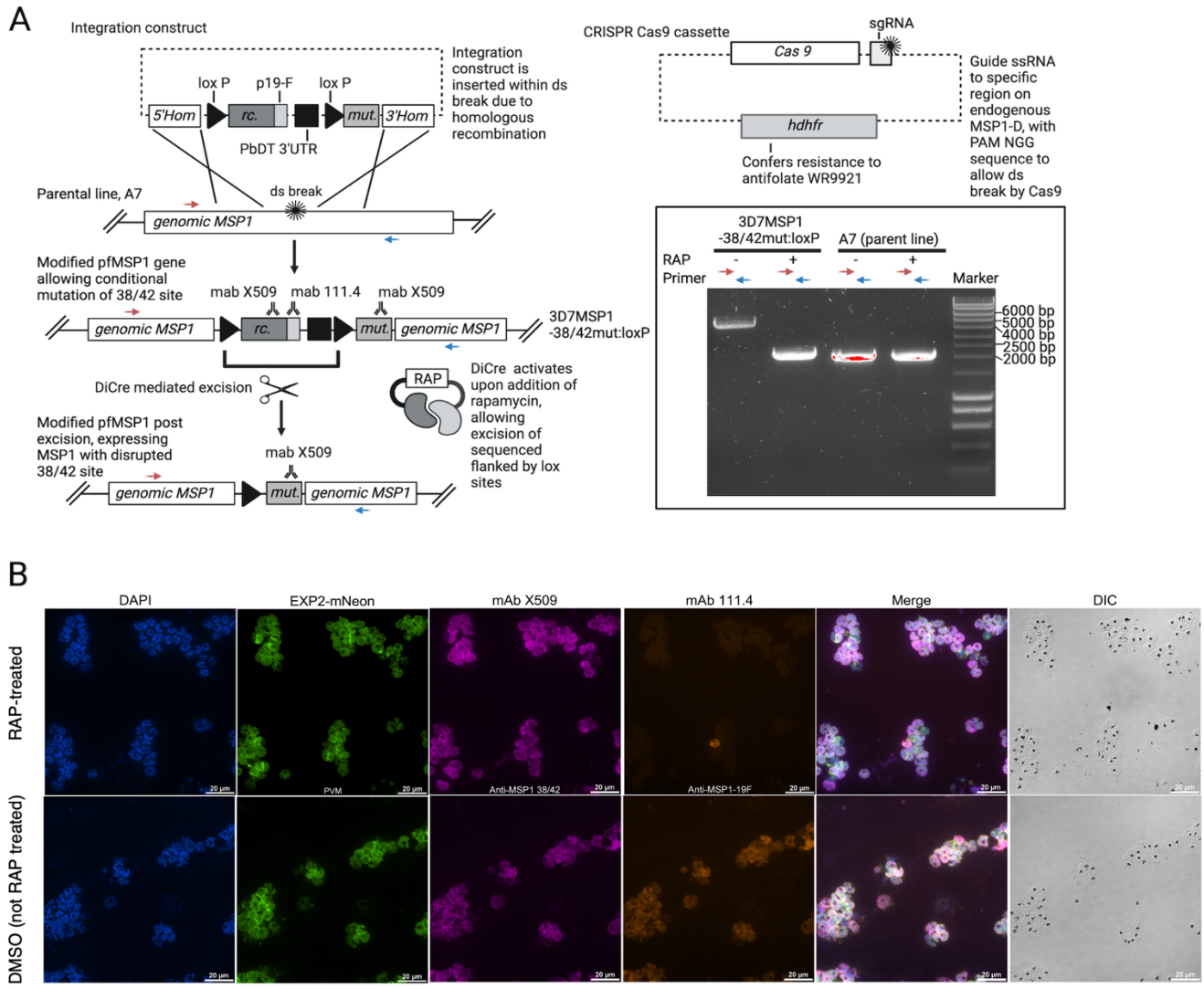

Figure 4.2 - Strategy for the ablation of SUB1 processing of MSP1 and evidence of successful mutagenesis

A) *Mutagenesis strategy. The integration construct was designed for insertion of floxed (loxP sites indicated with black arrows) recodonised wildtype chimeric MSP1 (recodonised MSP1-D*

(dark grey, rc.) fused to p19 of MSP1-F (light-grey)). Downstream of this, there is an alternative C-terminus encoding the mutations to ablate 38/42 SUB1 cleavage of MSP1 (grey, mut.). Integration is guided by the 5' and 3' homology sequence (white, 5'Hom and 3'Hom). Co-transfected with the integration construct is a separate plasmid for expression of Cas9 and a guide ssRNA. This ensures a targeted double stranded break in the endogenous MSP1-D sequence, to promote integration by homologous recombination of the repair construct. The hdhfr gene (light grey) confers resistance to the antifolate WR9921, allowing selection of parasites that have been transfected. After integration, upon treatment with RAP, DiCre is activated and excises the sequence between lox sites, moving the C-terminus encoding the 38/42 site mutations into frame. Oligos annealing to endogenous sequence were designed to check integration and excision (red arrow, forward primer 2.1; blue arrow, reverse primer 2.2). Upon successful integration, the PCR product seen for untreated parasites should be 4726 bp, as opposed to 2269 bp seen for the parent line (A7) (-RAP PCRs, 3D7MSP1-38/42mut:loxP and A7). Upon successful excision after RAP treatment of parasites, the PCR product for parasites in which synthetic DNA is integrated should be 2274bp, 2457bp smaller than untreated parasites (+RAP PCR, 3D7MSP1-38/42mut:loxP). Products observed for RAP treated parent line (A7) remain unchanged in relation to untreated parasites (+RAP PCR, A7).

***B)** Immunofluorescence assay of schizonts from the isolated clone 3D7MSP1-38/42mut:loxP, demonstrating successful integration and excision. A7 (EXP2-mNeon (em 488 nm)) was the parent line used for this work. (C. Bisson, unpublished; Glushakova et al., 2018). DAPI was used as a nuclear stain. Both RAP-treated and control untreated (DMSO) schizonts were probed with mAb x509 (binds MSP1 p38/42) and mAb 111.4 (binds MSP1-F p19). As can be*

seen in A), upon integration in untreated parasites, wild-type MSP1 is expressed as a chimera of MSP1-D and MSP1-F isoforms, reactive to mAb 111.4 and X509. However, in RAP treated parasites, MSP1 is expressed with a mutant 38/42 SUB1 cleavage site, and is not chimeric, so does not interact with 111.4, but is reactive to X509, as p38/42 is still present. Loss of the mAb 111.4 associated signal upon addition of RAP indicates successful excision.

4.1.3 Conditional mutation of the 38/42 cleavage site results in disruption of MSP1 processing

Having successfully altered the endogenous MSP1 locus to conditionally mutate the 38/42 cleavage site, it was necessary to identify whether these mutations affected SUB1 processing of MSP1. To do this, the 3D7MSP1-38/42mut:loxP line was first expanded and synchronised. Schizonts and culture supernatant were collected from mock-treated (DMSO, WT) and RAP-treated parasites (38/42 mut) and analysed by SDS PAGE and western blot both prior to and post egress. To examine the effect of mutagenesis on the processing of MSP1, blots were probed with monoclonal human antibody X509, identifying the p42 fragment of MSP1, as well as monoclonal mouse antibody 89.1, identifying the p83 fragment of MSP1. Mutagenesis of MSP1 at the 38/42 site was expected to lead to defective SUB1 processing of the C terminus of MSP1 (p42).

As described in the Introduction, following merozoite egress MSP1 undergoes cleavage by SUB2, causing complex detachment from the merozoite surface (Harris et al., 2005). SUB2 cleavage involves processing of the p42 into p33 and p19 fragments (Figure 4.4E). The bulk

of the MSP1 complex dissociates from the surface coat and the p19 fragment remains attached. SUB2 cleavage was expected to occur as normal in both mock and RAP-treated schizonts. It was predicted that this would lead to generation of a larger fragment, around ~61 kDa, corresponding to an intact p38/33 fragment, in culture supernatants from egressed RAP-treated schizonts.

As shown in Figure 4.3, the processing pattern of mutant MSP1 from RAP-treated schizonts was different from that of wildtype MSP1 in mock-treated schizonts both before and after egress (Figure 4.3B), whereas the processing pattern of MSP1 p83 remained unchanged (Figure 4.3A). Most notably, MSP1-derived fragments of higher molecular weight were observed in the post egress supernatant of RAP-treated parasites compared to the wild-type supernatants (Figure 4.3B). The most distinct of these, which migrated at ~50 kDa (Figure 4.3B, fragment e), may be the p38/33 fragment, suggesting that SUB1 cleavage at the 38/42 site had been disrupted. There appeared to be some complete processing of the 38/42 site in parasites expressing 38/42 mutant MSP1. This was inferred from the ~ 36 kDa protein species seen in blots of the egress culture supernatant of both mock (wild-type) and RAP-treated schizonts (38/42 mut) probed with X509 (MSP1 p42, Figure 4.3B). This may have been a result of incomplete gene excision.

A possible interpretation of the SUB1 cleavage for the mutant MSP1 is shown in Figure 4.3D, in which cleavage at the 38/42 site of MSP1 has been ablated. To test this interpretation, species corresponding to the predicted wild-type MSP1 p33 and mutant MSP1 p38/33 fragments were isolated from the egress culture supernatant of RAP-treated parasites using high-performance reversed-phase liquid chromatography(RP-HPLC). The purified proteins

were subjected to in-gel tryptic digestion and the resulting peptides analysed by mass spectrometry (MS) (Figure 4.4A-D).

For the MSP1 p33 species, both the N-terminal and C-terminal peptides were detected, confirming the identity of this fragment. Whether this MSP1 p33 fragment originates from some complete cleavage of the 38/42 mutant MSP1 by SUB1 or from parasites expressing wild-type MSP1 for which gene excision has not been successful is uncertain. Given that excision rate is never 100%, the latter is most likely true.

The alt2 38/42 site point mutations and the expected C-terminus were detected by MS of the isolated fragment predicted to be MSP1 p38/33 (Figure 4.4E), suggesting that mutagenesis had successfully blocked SUB1 cleavage at this site and that SUB2 cleavage had occurred. Other mutations made at the 38/42 were not detected and only a few peptides from the p38 were detected. This is likely because the products of tryptic digest in this region may be difficult to isolate or would not fly due to excessive length. Assuming that the MSP1 p33 fragment isolated from egress supernatant originates from wild-type MSP1, the difference between the N-termini of the isolated fragments suggests that SUB1 processing at the 38/42 cleavage site of MSP1 was successfully ablated by mutagenesis. Any distinct phenotype observed in further study of RAP-treated parasites can be attributed to incomplete cleavage of MSP1.

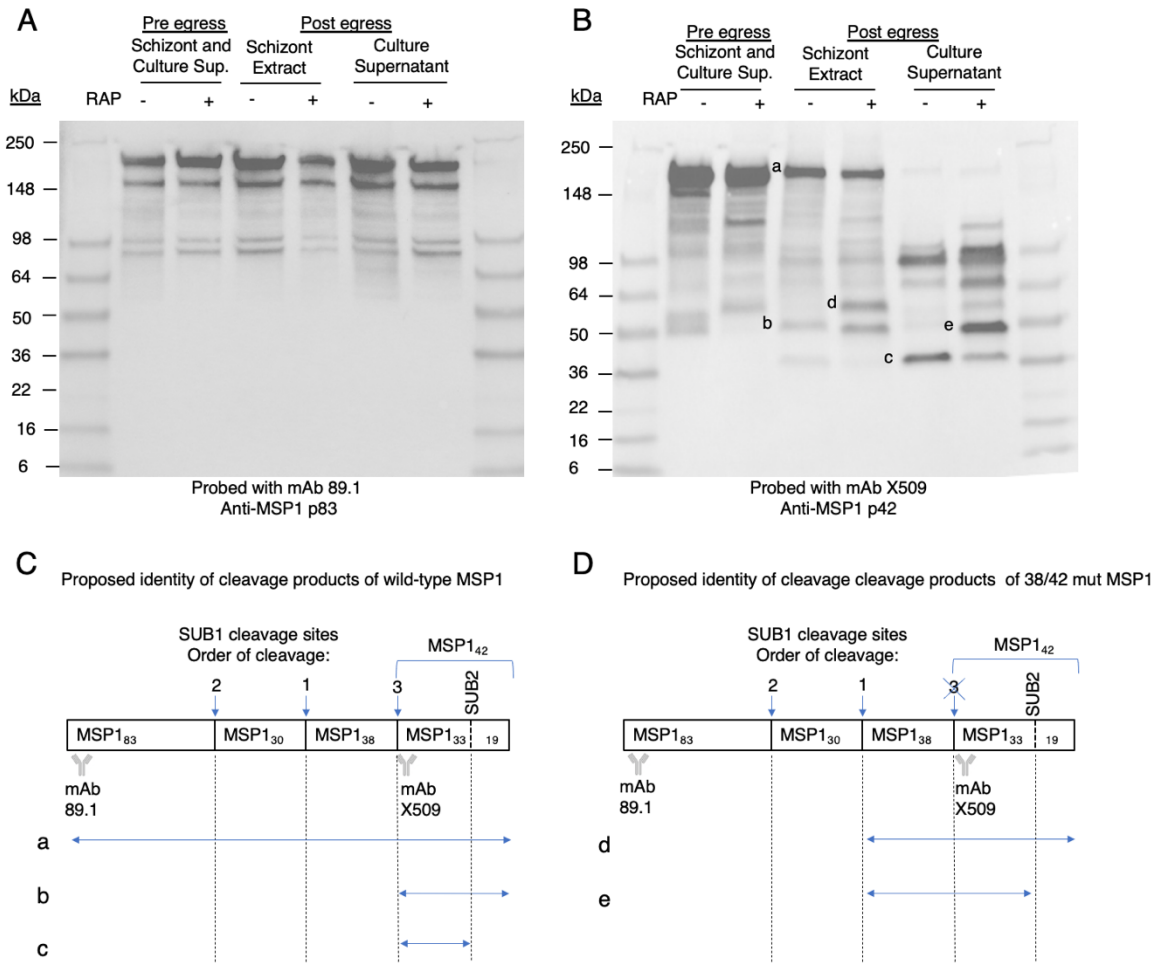

Figure 4.3 - Analysis of MSP1 cleavage patterns in wild-type and MSP1 38/42 mutant parasites.

A) *and* ***B)*** *Cleavage of MSP1 in P. falciparum expressing wild-type MSP1 and MSP1 with pre-designed 38/42 mutations was investigated by analysing schizonts and culture supernatant both prior to and post egress using SDS PAGE and western blot, probing for MSP1 p83 (A, mAb 89.1) and MSP1 p42 (B, mAb X509).*

C) *and* ***D)*** *The proposed identity of some fragments seen in post egress samples of wild-type (C) and 38/42 mutant MSP1 expressing parasites (D) probed for MSP1 p42 (labelled a-e on blot B). SUB1 cleavage sites are labelled in the order that they occur (1=30/38, 2=83/30, 3=38/42) and the SUB2 cleavage site in the MSP1 p42 is labelled, showing the resulting*

MSP1 p33 and MSP1 p19 fragments. In D, the 3rd SUB1 cleavage site (38/42) is crossed out, to indicate the mutations made at this site to ablate cleavage. The double headed arrows, labelled a)-e) are proposed fragments, and indicate how much of MSP1 a fragment spans. Dashed lines plot where the cleavage sites lie on these proposed fragments.

A

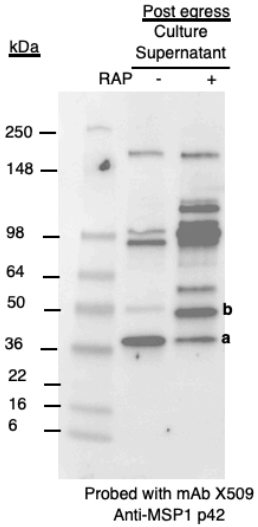
Post egress
Culture
Supernatant
kDa
RAP - +
250
148
98
64
50
36
22
16
6
b
a
Probed with mAb X509
Anti-MSP1 p42

B

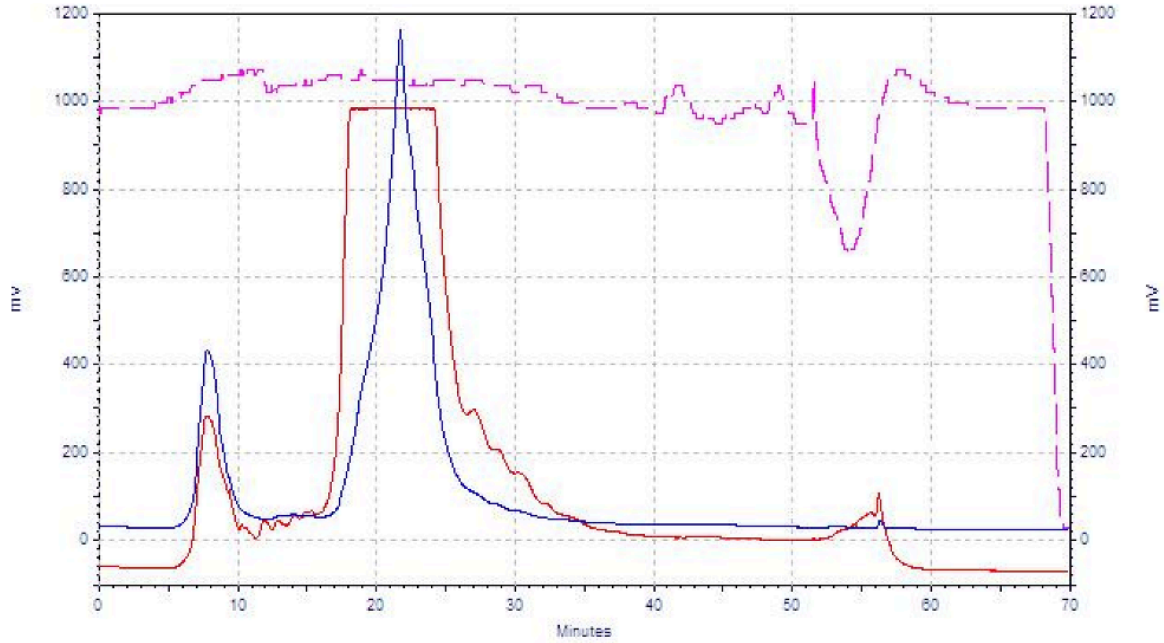
mV
Minutes
0
10
20
30
40
50
60
70
200
400
600
800
1000
1200

C

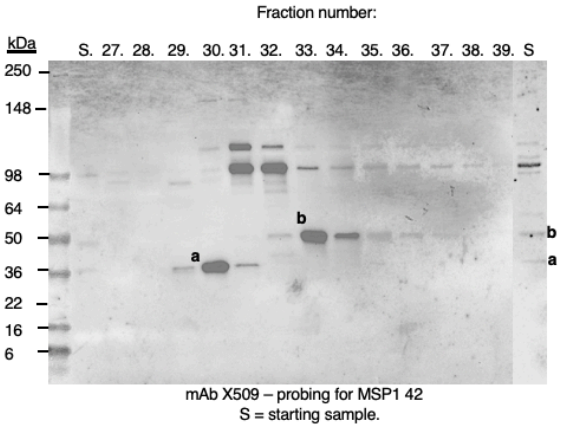
Fraction number:
kDa
S. 27. 28. 29. 30. 31. 32. 33. 34. 35. 36. 37. 38. 39. S
250
148
98
64
50
36
22
16
6
a
b
mAb X509 – probing for MSP1 42
S = starting sample.

D

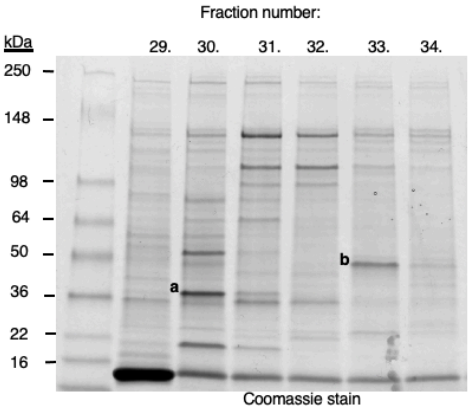
Fraction number:
kDa
29. 30. 31. 32. 33. 34.
250
148
98
64
50
36
22
16
a
b
Coomassie stain

E

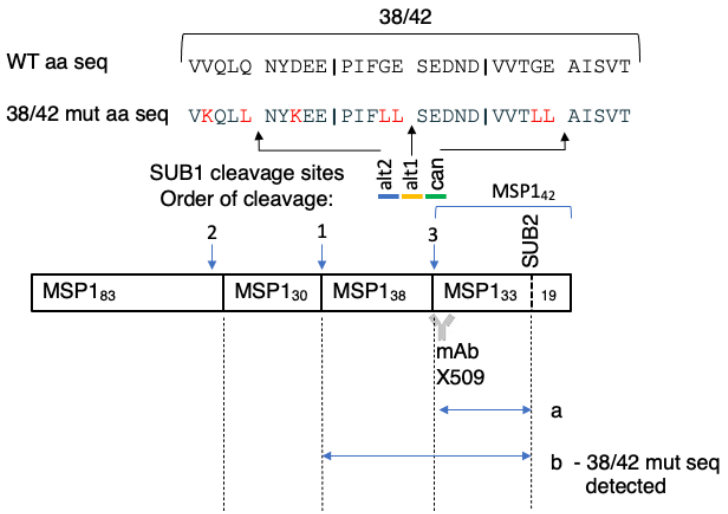
38/42
WT aa seq
VVQLQ NYDEE|PIFGE SEDND|VVTGE AISVT
38/42 mut aa seq
VKQLL NYKEE|PIFLL SEDND|VVTLL AISVT
SUB1 cleavage sites
Order of cleavage:
alt2
alt1
can
MSP1₄₂
2
1
3
SUB2
MSP1₈₃
MSP1₃₀
MSP1₃₈
MSP1₃₃
19
mAb
X509
a
b - 38/42 mut seq
detected

Figure 4.4 - Separation of post egress culture supernatant and mass spectrometry analysis

A) *SDS PAGE and western blot analysis of large-scale preps of culture supernatant of RAP treated (expressing 38/42 mut MSP1) and DMSO treated (expressing wild-type MSP1) MSP1$_{\Delta 38/42}$ parasites, probed with mAb X509 (Anti-MSP1 p42). The culture supernatant of RAP treated (38/42 mut MSP1 expressing) was subjected to RP-HPLC, in order to isolate and identify fragments labelled a) and b), predicted to be MSP1 p38-33 and MSP1 p33 respectively (see Figure 4.3C and D).*

B) *UV absorbance trace of RP-HPLC separation (elution over a gradient of acetonitrile, 0-55%, flow rate 1 mL per minute, 1 mL fractions collected) of large-scale prep of post egress culture supernatant of RAP treated parasites. Blue trace = UV 280, red trace = UV 220.*

C) *SDS PAGE and western blot analysis of fractions 27-39 from RP-HPLC separation probed with mAb X509 (Anti-MSP1 p42), demonstrating successful isolation of fragments a and b labelled in fractions 30 (a) and 33 (b), which correspond to a) and b) labelled in S, a sample of the starting material (large-scale prep of post egress supernatant of RAP treated parasites) run alongside the fractions, and a) and b) fragments labelled in A.*

D) *SDS PAGE separation and Coomassie staining of HPLC fractions 29-34, from which bands labelled a in fraction 30 and b in fraction 33, believed to correspond to fragments a and b labelled in western blots probed with mAb x509 (Anti-MSP1 p42) A and C, were extracted and sent for analysis by mass spectrometry.*

E) *Schematic showing the identities of species a and b, extracted from the SDS PAGE in D, determined by peptide mapping of mass spectrometry data. The expected sequences of the 3rd SUB1 cleavage site (38/42) are shown for 38/42 mutant and wild-type MSP1. The double*

headed arrows labelled a and b are the proposed fragment identities and indicate the span of an MSP1 fragment, based on peptide mapping. The C-terminal peptides of species a and b were seen by mass spectrometry, but the N-terminal peptide of species b was not detected. Dashed lines plot where the cleavage sites lie on these proposed fragments.

4.2 Disruption of MSP1 cleavage at the 38/42 site results in an egress defect

As previously mentioned, MSP1 cleavage at the 38/42 SUB1 processing site has been implicated in egress (Das et al., 2015). To examine whether there is an egress phenotype associated with disruption of SUB1 processing at the 38/42 cleavage site, 3D7MSP1-38/42mut:loxP parasites were again synchronised and either RAP or DMSO treated. Schizonts were treated with C2 to enable schizont maturation (Collins et al., 2013). Once maturation was complete, schizonts were washed to remove the C2 block, and allowed to egress whilst being monitored by time-lapse video microscopy. To help visualise differences between parasites expressing wild-type MSP1 (untreated, DMSO) and those expressing MSP1 38/42 mutant (RAP treated), DAPI staining was used to differentiate between treated and untreated schizonts.

The video microscopy analysis revealed that the cleavage mutant has impaired egress. The RAP-treated parasites appeared to egress abnormally, with a less explosive burst of the RBC membrane than with wild-type parasites (Figure 4.5 B). The level of normal egress was determined for parasites from 4 biological replicates (Figure 4.5 A,B). Analysis showed that egress was normal for 36.9% of mutant and 79.8% of wild-type schizonts. This result was

found to be statistically significant by paired t-test ($p < 0.01$), implying a role for SUB1 processing of MSP1 at the 38/42 site in egress.

To quantify whether merozoite dispersal was altered as a result of modification to the 38/42 SUB1 processing site of MSP1, the time taken for merozoites to disperse 5 μm from the residual body post schizont egress was recorded for mutant and wild-type schizonts across all biological replicates. The mean time taken for merozoites egressing from schizonts expressing MSP1 38/42 mutant protein to migrate 5 μm from the residual body was significantly higher (10.7 mins, Figure 4.5 C) than wild-type parasites (3.2 mins, Figure 4.5 C, $p < 0.05$). When looking at the spread of the data, there is a greater distribution of time taken for dispersal of mutant merozoites in comparison to wild-type, suggesting greater heterogeneity in mutant parasites (Figure 4.5 D).

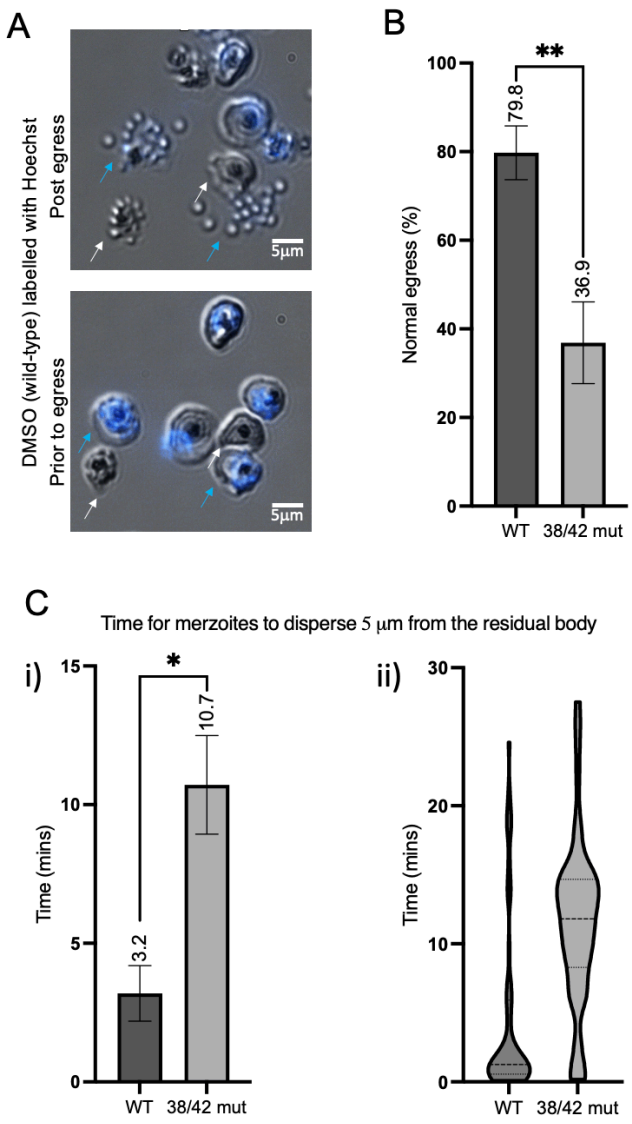

Figure 4.5 - Analysis of the phenotype seen in parasites expressing MSP1 in which the 38/42 SUB1 cleavage site has been mutated.

A) *Example of RAP treated (expressing 38/42 mut MSP1) and mock treated (DMSO-treated, expressing wild-type MSP1) schizonts, just prior to and at the post egress, stills taken from time lapse video microscopy. DMSO schizonts are labelled with Hoechst nuclear stain to allow distinguishment between wild-type and mutant schizonts (blue arrows also point to wild-type (DMSO treated) schizonts and white to mutant schizonts (RAP treated schizonts).*

B) *Result of qualitative analysis of egress in which the 'burst' for mature schizonts expressing wild type MSP1 (110 schizonts in total, over n=4 experiments) or 38/42 mutant MSP1 (139 schizonts in total, over n=4) was categorized as normal or abnormal, mean values (%) of the 4 experiments is written above bars and error bars represent standard error of the mean. P value < 0.01, calculated by unpaired, parametric t test.*

C) *Analysis of time taken for merozoites to disperse 5 μm from residual body. Both plots are of the same data, with i) showing the mean time taken (mins) of 4 experiments for wild-type MSP1 expressing and 38/42 mut MSP1 expressing schizonts, with error bars displaying the standard error of the mean, p < 0.05, calculated by unpaired, parametric t test. Plot ii) is a violin plot of all data points measured for wild-type and mutant schizonts, in attempt to visualise the distribution of times taken for merozoites to disperse 5 μm from the residual body.*

4.3 Disruption of SUB1 cleavage of MSP1 results in reduced parasite proliferation

To further examine the effects of the disruption of the 38/42 SUB1 cleavage site of MSP1, growth and invasion efficiencies of MSP1 38/42 mutant parasites were monitored and compared to those of wild-type. Again, parasites were either RAP treated (38/42 mutant) or untreated (wild-type). To calculate efficiency of invasion and growth, the same procedures were used as described previously (Chapter 3, Section 3.2). Rate of invasion of mutant parasites (5 fold increase, Figure 4.6 A) was found to be significantly reduced relative to WT parasites (7.5 fold increase, Figure 4.6 A, $p < 0.001$ by paired t-test). Rings from mutant cultures were negative for MSP1-19F. In addition to proving excision (see above), this

confirmed that merozoites expressing of 38/42 mut MSP1 can invade (Figure 4.6 B). Patterns of growth between parasites expressing wild-type MSP1 and those expressing 38/42 mutant MSP1 were compared. Growth of mutant parasites was shown to be significantly lower than wild-type at the 3rd cycle ($p<0.05$, multiple paired t-test comparison Figure 4.6 B). Fitting data to an exponential growth model showed that wild-type and mutant had significantly different growth rates ($p<0.05$).

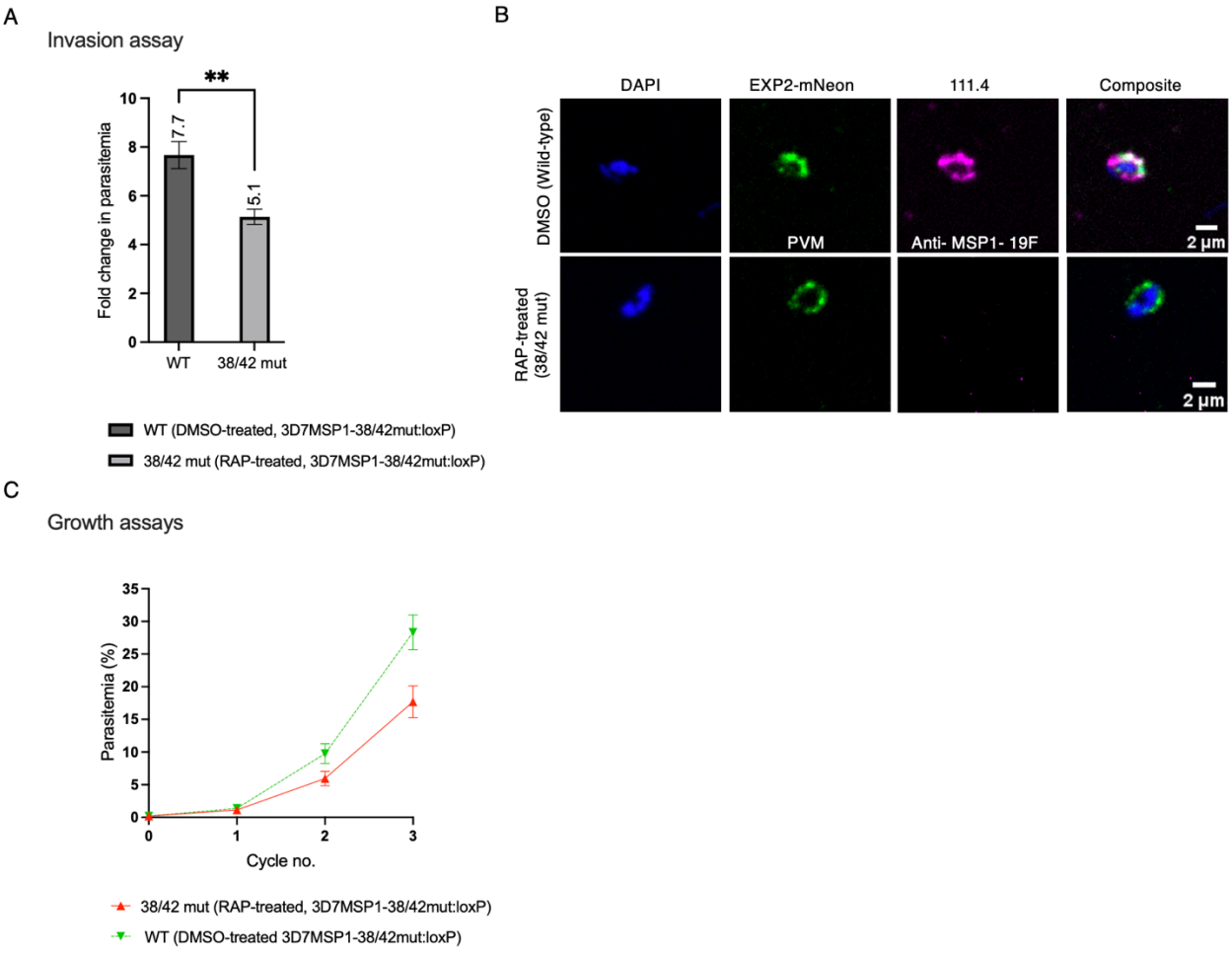

Figure 4.6 - Proliferation of 38/42 mutant parasites is impaired but merozoites can invade

A) *Invasion assay in which schizonts from both RAP treated (expressing 38/42 mutant MSP1) and DMSO treated parasites (expressing wild-type MSP1) were separately invaded into fresh*

erythrocytes and number of rings formed counted (hence, invasion events), this was corrected for starting parasitemia. p value < 0.0001, calculated by unpaired t-test.

***B)** IFA of rings from invasion of mock and RAP-treated parasites demonstrates merozoites expressing 38/42 mut MSP1 invade. Rings were probed with 111.4 (anti-MSP1-19F), marker of wild-type MSP1 expression (section 4.1.2). Scale bar 2 μm.*

***C)** Growth assay of RAP treated (expressing 38/42 mutant MSP1) and DMSO treated parasites (expressing wild-type MSP1), in which cultures at low starting parasitemia were allowed to grow across 3 cycles, with change in parasitemia being measured at each cycle. Growth of mutant parasites was significantly lower than wild-type at the 3rd cycle ($p<0.05$, multiple paired t-test comparison). Fitting data to an exponential growth model showed significantly different growth rates for wild-type and mutant ($p<0.05$).*

4.4 Disruption of SUB1 cleavage at MSP1 38/42 site does not alter merozoite segmentation

Merozoite segmentation may have been abnormal in MSP1-null parasites. This could have been an artifact of a change in the composition of the PM outer leaflet rather than a consequence of the loss of MSP1 function. It was necessary to look at MSP1 38/42 mut parasites before (E64-d stalled) and after egress by TEM. Mock and RAP treated schizonts appeared segmented (Figure 4.7: 95.8% and 88.8%, respectively). Again, although the PVM and RBCM ruptured in both mutant and WT schizonts, large clusters (definition specified in the Figure 4.7 legend) of remnants post egress were more commonly seen in MSP1 38/42

mut parasites (31.5% and 3.3% for mutant and WT respectively). This is consistent with the egress phenotype observed and implicates MSP1 in merozoite dispersion (Figure 4.5).

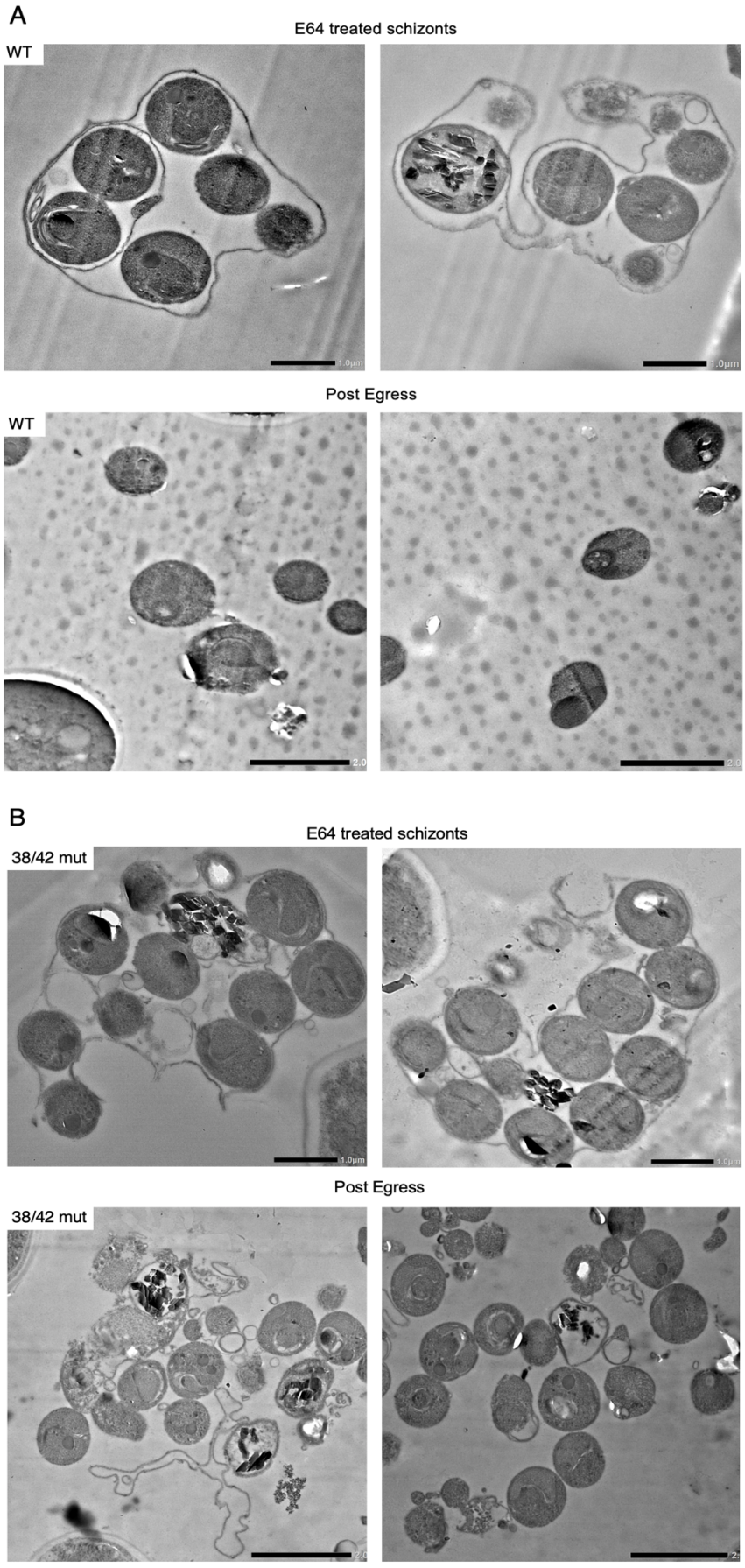
A
E64 treated schizonts
WT
Post Egress
WT
B
E64 treated schizonts
38/42 mut
Post Egress
38/42 mut

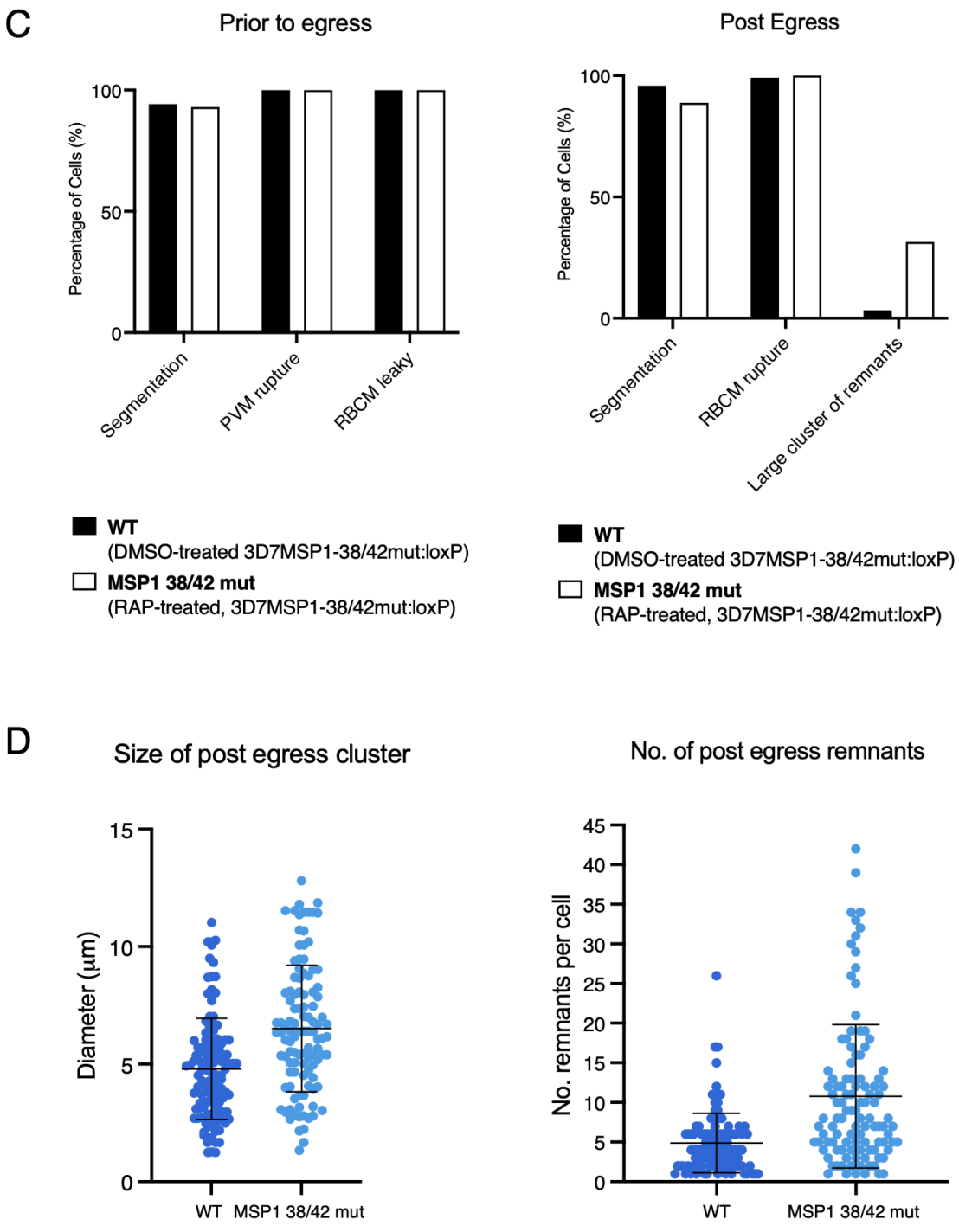

Figure 4.7 - Parasites expressing 38/42 mut MSP1 segment but egress is defective.

A-B) *TEM of freeze-substituted sections of mock treated (wild-type, **A**) and RAP treated (MSP1 38/42 mut), **B**) schizonts either prior to egress (RBC membrane rupture prevented by*

E64 cysteine protease inhibitor) or post egress (C2 arrested, C2 block removed and schizonts allowed to egress). Scale bars 1 μm for E64-d treated schizonts and. Scale bars are 2 μm for post egress schizonts. Images of 100 cells for each sample.

***C)** Quantification of merozoite segmentation, PV and RBC membrane rupture, RBC membrane poration and occurrence of larger clusters of post egress remnants for WT and MSP138/42 mut schizonts. **D)** To analyse the phenotype seen, measurements were made of: diameter of post egress cluster (largest measured distance across remnants) and number of remnants per egressed cell imaged (membrane aggregates, merozoites, residual body (egressed DV)), mean values with standard deviations are plot. Post egress clusters were defined as 'large' if greater than 6 μm in diameter and composed of more than 13 individual remnants. No statistics were calculated; this data is n=1.*

4.5 Discussion

Previous attempts to mutate all three cleavage points at the 38/42 SUB1 processing site of MSP1 simultaneously by single homologous crossover failed, leading to the suggestion that SUB1 processing at this site is essential for parasite viability (Das et al., 2015). Here, we have successfully edited the endogenous MSP1 locus, allowing all three cleavage points to be conditionally mutated. The cleavage pattern of MSP1 both prior to and post egress was altered due to mutation of the 38/42 SUB1 processing site, indicating successful interference with SUB1 processing. SUB2 cleavage occurred as expected in mutant parasites, suggesting primary processing of MSP1 is not a prerequisite for secondary processing.

There is some possibility that the cleavage site had 'slipped' as a result of mutagenesis, meaning that SUB1 cleavage may have occurred upstream of the original site, within the p38 fragment, and had not been completely blocked. The shift in the size of the species in egress supernatant predicted to be the product of SUB1 and SUB2 processing of MSP1 was not as large as anticipated between wild-type and mutant parasites (<20 kDa, as opposed to the expected 38 kDa shift, Figure 4.3B). Only a few peptides difference was seen between the predicted wild-type p33 and mutant p38/33 fragments via MS and the N-terminus of the predicted p38/33 fragment was not identified. This may account for the heterogeneity in merozoite dispersal and insignificant differences in growth of mutant parasites compared to wild-type between cycles 1 and 2 (Figure 4.6). However, this cannot be determined from these results and, in any case, SUB1 cleavage of MSP1 was definitively disrupted by conditional mutagenesis.

Parasites expressing MSP1 with an 'uncleavable' 38/42 SUB1 site were shown to have defective egress and to grow and invade at a reduced rate. This demonstrates that MSP1 processing has an important function in the erythrocytic life cycle. Mutant merozoites had segmented normally in mature schizonts, suggesting cleavage is not required for this process. The phenotype of mutant parasites suggests that SUB1 cleavage of MSP1 is important for the dispersal of merozoites from the erythrocyte, consistent with previous findings (Das et al., 2015). Defective egress could be responsible for reduced invasion and growth; ineffective dispersal of merozoites post egress may lead to fewer invasion events and lower parasitaemia of mutant cultures, in comparison to wild-type. This is corroborated by evidence that parasites expressing MSP1 38/42mut can invade.

Though this work has confirmed a role for SUB1 cleavage of MSP1 in egress of merozoites from erythrocytes, the exact function of MSP1 is still unclear. Comparing the molecular structures of a native MSP1 complex before and after SUB1 processing may help clarify this further.

Chapter 5- Structure determination of the MSP1 complex provides insight into function

5.1 Introduction

It is generally thought that SUB1-cleaved MSP1 forms a complex with other proteins at the merozoite surface. MSP7 is thought to be associated with both full-length and cleaved MSP1, with other proteins such as MSP3, MSP6 and DBL1/2 potentially binding post SUB1 cleavage (Kauth et al., 2006; Lin et al., 2016), although the composition of the complex is not precisely defined. Some hypothesize that a heterogenous population of MSP1 complexes constitute the merozoite surface coat (Lin et al., 2016). As previously described (Section 1.7), the structure of a recombinantly expressed, SUB1 cleaved MSP1 has recently been solved by cryo-EM, revealing a flexible macromolecule made up of 37 α–helices (Dijkman et al., 2021). This published structure, though a major breakthrough in understanding MSP1 function and extremely useful as a starting point for the atomic modelling of MSP1, poses important remaining questions about the composition of the *in vivo* MSP1 complex. Structures of the native MSP1 complex before and after egress would reveal changes in complex composition that define MSP1 activation and function.

5.2 Purification of the SUB1 cleaved and uncleaved native MSP1 complex

5.2.1 Conditional expression of soluble, FLAG tagged MSP1 in *P. falciparum*

In order to isolate native MSP1 complex for single particle analysis, a tagging strategy was devised to allow expression of MSP1 in *P. falciparum* as a soluble complex that could readily be isolated by affinity purification. The DiCre recombinase system (Collins et al., 2013; Perrin et al., 2018) was used to create a *P. falciparum* line in which MSP1 was conditionally expressed with a FLAG tag in place of the GPI anchor. This conditional mutant line, designed and generated by Claudine Bisson (unpublished), will be referred to as 3D7MSP1-FLAG:loxP. To achieve the desired genetic modifications, Cas9-guided homologous recombination was used to integrate a synthetic DNA construct into the open reading frame of the endogenous MSP1 (integration construct, Figure 5.1A). The construct encoded a floxed recodonised wild-type MSP1 C-terminus followed by a sequence encoding an alternative C-terminus with a 3X FLAG tag. In the 3D7MSP1-FLAG:loxP line, it was predicted that upon addition of RAP, the alternative C-terminus would move into the open reading frame, resulting in expression of soluble, FLAG-tagged MSP1 (referred to as MSP1-FLAG).

To assess whether the 3D7MSP1-FLAG:loxP line could be used for generation of a soluble, tagged form of the native MSP1 complex, parasites were either treated with RAP or mock treated with DMSO for analysis. Diagnostic PCR was then carried out on the gDNA extracted from mock and RAP treated parasites. This showed that DiCre mediated DNA excision at the modified MSP1 locus occurred as expected (Figure 5.1A). The same PCR, performed on gDNA extracted from both treated and untreated parasites of the parent line (B11), demonstrated integration and acted as a control. The efficiency of excision and the expression of MSP1-FLAG upon treatment with RAP were determined using IFA and western

blot analysis of mature schizonts cultured from the mock or RAP treated 3D7MSP1-FLAG:loxP line. In mock treated schizonts (effectively wild-type), the fluorescent signal observed for MSP1 (89.1, anti- MSP1 p83, Figure 5.1B) was localised to the merozoite surface membrane as expected, due to the expression of MSP1 with a GPI-anchor that tethers the protein to the merozoite surface coat (Kauth et al., 2003b). In contrast, in RAP treated parasites, the fluorescent signal seen for MSP1 (89.1, anti-MSP1 p83, Figure 5.1B) was diffuse and not localised to the merozoite surface membranes, suggesting that MSP1 was soluble within the PV as a result of successful gene excision and expression with a C-terminal FLAG-tag in place of the GPI-anchor. The signal observed for anti-FLAG corresponds to that seen for MSP1, confirming that MSP1 was expressed with a FLAG-tag (Figure 5.1B). SDS PAGE and western blot analysis of schizonts further confirm that RAP treated parasites express soluble MSP1-FLAG (Figure 5.2A, blot probed with anti-FLAG).

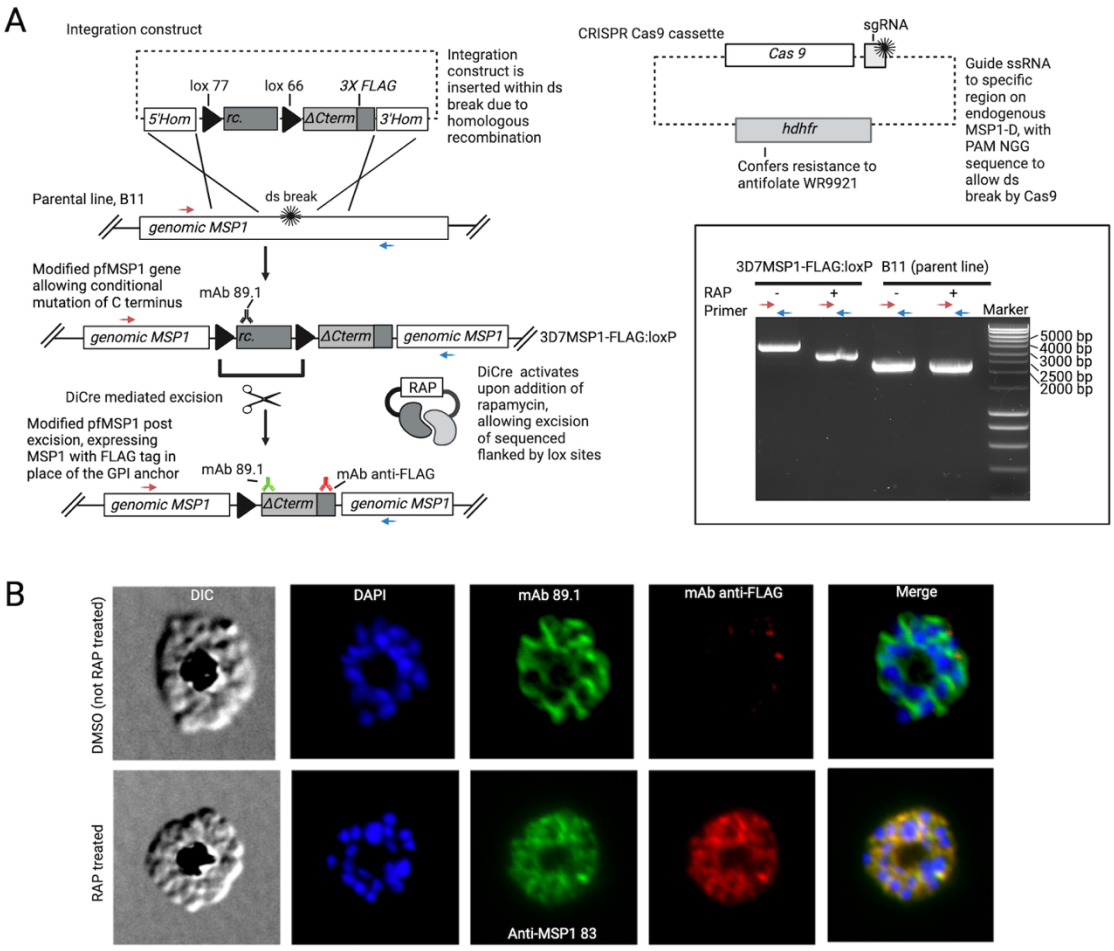

Figure 5.1 - Cas9 mediated gene editing of endogenous MSP1 to allow expression of soluble, FLAG-tagged MSP1.

A) Schematic of Cas9 mediated insertion of a FLAG-tagged C-terminus into the endogenous sequence of MSP1. The integration construct encodes a floxed (loxP indicated by black arrows) recodonised wild-type C-terminus of MSP1 (rc.) and downstream, an alternative FLAG-tagged C-terminus of MSP1 (mut). Integration is guided by the 5' and 3' homology sequence (white, 5'Hom and 3'Hom). The CRISPR Cas9 cassette that is co-transfected with the integration construct encodes Cas9 and a guide sgRNA. This ensures that a double stranded break in the endogenous MSP1 sequence occurs at the correct position for insertion of the integration construct. The hdhfr gene (light grey, CRISPR Cas 9 cassette) confers

resistance to the antifolate WR9921, allowing selection of parasites that have been transfected successfully. After integration DiCre is activated by RAP treatment and excises the sequence between lox sites, moving the alternative, FLAG-tagged C-terminus into frame. Oligos that prime off endogenous MSP1 sequence upstream and downstream from the expected site of integration, outside of the homology arms, are shown by red and blue arrows. These were designed to check integration and excision (red arrow, forward primer 2.1; blue arrow, reverse primer 2.2). In the diagnostic PCR, the correct size products are seen for gene integration (-RAP) and excision (+RAP) for gDNA isolated from the 3D7MSP1-FLAG:loxP line.

Upon successful integration, the PCR product seen for untreated parasites is 3830 bp, as opposed to 2269 bp for the parent line (B11) (-RAP PCRs, 3D7MSP1-FLAG:loxP and B11). Upon successful excision after RAP treatment of parasites, the PCR product for parasites in which synthetic DNA is integrated is 2915 bp, 915 bp smaller than untreated parasites (+RAP PCR, 3D7MSP1-FLAG:loxP). Products observed for RAP treated parent line (B11) remain unchanged in relation to untreated parasites (+/- RAP PCR, B11).

B) IFA of schizonts from the isolated clone 3D7MSP1-FLAG:loxP, demonstrating successful modification of the endogenous MSP1 locus and expression of FLAG-tagged MSP1 upon addition of RAP. Fixed, mature, C2 arrested schizonts from mock (DMSO) treated and RAP treated parasites from the isolated clone 3D7MSP1-FLAG:loxP. Schizonts are co-stained with DNA stain (DAPI), mAb 89.1 (anti-MSP1 p83) and mAb anti-FLAG. Signal for MSP1 is localised to the membranes in mock treated schizonts, as MSP1 is expressed with wild-type C-terminus with the GPI-anchor intact; there is no signal for anti-FLAG. Signal for MSP1 in RAP treated parasites is diffuse, suggesting MSP1 is localised in the PV; the signal for FLAG-tag is

colocalised to that of MSP1, suggesting MSP1-FLAG is expressed. There were few parasites for which there was no signal for anti-FLAG in the IFAs of RAP-treated schizonts, suggesting high efficiency of gene excision by DiCre.

To confirm that MSP1-FLAG expressed in RAP treated parasites was soluble, SDS PAGE and western blot analysis was also carried out on the soluble fraction of saponin lysed schizonts from the mock or RAP treated 3D7MSP1-FLAG:loxP line (Claudine Bisson, unpublished, Figure 5.2B). Saponin lyses the RBC membrane whilst leaving the merozoite surface membranes and parasitophorous vacuole membrane (PVM) intact (Cooper, 2002); therefore, the contents of the RBC are solubilised but not those of the parasite. At the point of lysis schizonts treated with PKG inhibitor Compound 2 (C2) were ensured to have matured to PVM poration, meaning that the contents of the parasitophorous vacuole (PV) and the RBC had effectively mixed. This was to prevent SUB1 discharge from exonemes and inhibit egress but enable continued schizont maturation (Collins et al., 2013). By probing the soluble fraction of saponin lysed schizonts, only proteins found in both the PV and RBC should be visible in western blot analysis. As expected, MSP1-FLAG was detected only in the soluble fraction of saponin lysed RAP treated schizonts. This corroborates that, upon RAP treatment the 3D7MSP1-FLAG:loxP line undergoes gene excision, allowing expression of soluble MSP1-FLAG which could potentially be isolated from culture (Figure 5.2B).

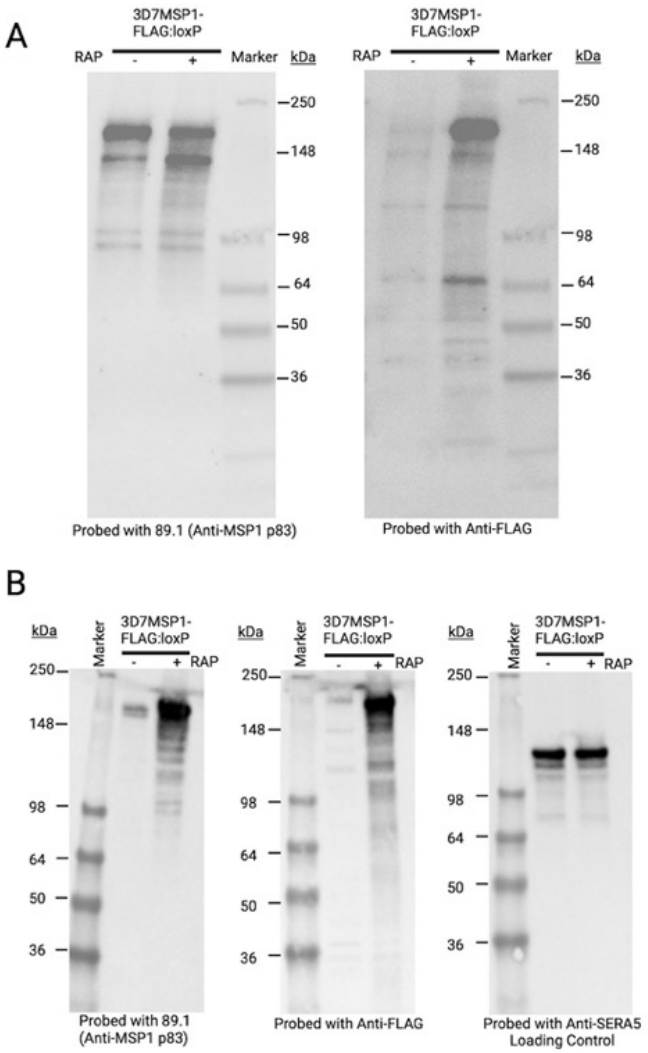

Figure 5.2 - Expression of soluble, FLAG-tagged MSP1 can be induced in 3D7MSP1-FLAG:loxP parasites

A) *SDS PAGE and western blot analysis of lysed, C2 arrested schizonts from DMSO (mock-treated) and RAP treated parasites from the 3D7MSP1-FLAG:loxP line, demonstrating that whilst MSP1 is expressed in both mock and RAP treated parasites, FLAG-tagged MSP1 is only expressed upon RAP induced gene excision. Samples were probed with mAb 89.1 (anti-MSP1 p83) and mAb anti-FLAG.*

B) *SDS PAGE and western blot analysis of the soluble fraction of saponin lysed C2 arrested schizonts DMSO (mock-treated) and RAP treated parasites from the 3D7MSP1-FLAG:loxP line. Samples were probed with mAb 89.1 (anti-MSP1 p83) and mAb anti-FLAG and blots to demonstrate that MSP1-FLAG is expressed as a soluble protein in RAP treated parasites. Saponin lyses the RBC membrane; therefore, by probing the soluble fraction of saponin lysed C2 arrested schizonts, only soluble proteins found in either the PV or RBC should be visible in western blot analysis (Cooper, 2002). These blots were carried out by Claudine Bisson.*

5.2.2 Purification of FLAG-tagged MSP1 from *P. falciparum* culture

To determine whether it was possible to purify soluble MSP1-FLAG from RAP treated 3D7MSP1-FLAG:loxP *P. falciparum* culture for single particle cryo-EM, C2 arrested schizonts from both DMSO and RAP treated cultures were saponin lysed and the supernatants applied to an affinity resin consisting of an anti-FLAG mAb conjugated to agarose beads (protocol designed by Claudine Bisson, unpublished). As predicted, the anti-FLAG resin captured the MSP1-FLAG complex from extracts of RAP treated schizonts (Figure 5.3). The complex was eluted from the resin using FLAG peptide to compete for antibody binding. No contaminants were pulled down from similar extracts of mock-treated parasites, substantiating that only FLAG-tagged protein and associated binding partners are isolated by the resin.

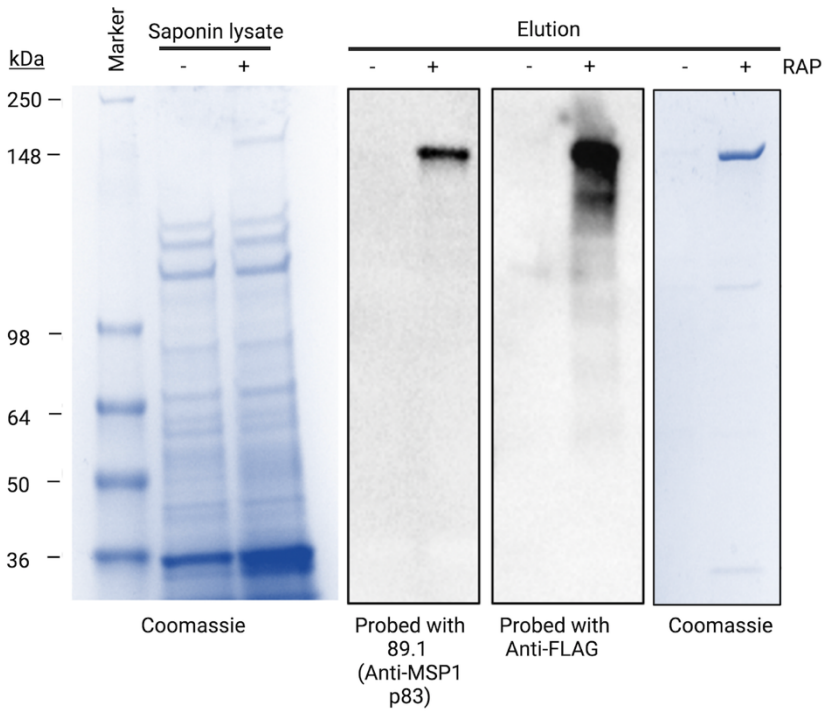

Figure 5.3 - MSP1-FLAG isolation from RAP treated 3D7MSP1-FLAG:loxP parasites

SDS PAGE, Coomassie and western blot analysis of crude sample (saponin lysate supernatant) and purified sample (eluted from anti-FLAG resin, post washing) obtained from C2 arrested DMSO (mock-treated) and RAP treated schizonts from the 3D7MSP1-FLAG:loxP line. Samples were probed with mAb 89.1 (anti-MSP1 p83) and anti-FLAG and confirm that soluble FLAG-tagged MSP1 was successfully isolated from the soluble fraction of saponin lysed RAP treated parasites, using an anti-FLAG resin. The lack of protein species in eluted material from resin incubated with the soluble fraction of saponin lysed mock treated parasites indicates that only FLAG-tagged protein and associated binding partners are isolated by the resin.

As previously mentioned, MSP1 is cleaved at 3 sites by the parasite serine protease SUB1 just prior to egress (Child et al., 2010). To investigate MSP1 function, it was necessary to obtain both SUB1 cleaved and uncleaved MSP1 for single particle cryo-EM analysis and structure comparison. By isolating MSP1 at different stages of the erythrocytic cycle of RAP treated parasites, it was possible to purify MSP1 in both SUB1 processed and unprocessed forms (Figure 5.4). Schizonts arrested prior to RBCM rupture and parasite egress using Compound 2 could be saponin lysed and MSP1, not yet cleaved by SUB1 (MSP1-$FLAG_{FL}$), purified from the soluble fraction of the lysate. Alternatively, SUB1 cleaved MSP1 (MSP1-$FLAG_{cleaved}$) could be isolated from the culture supernatant of egressed schizonts in the same fashion. SDS PAGE and western blot analysis of the starting samples, unbound material, washes and elution showed that FLAG tagged MSP1 binds the resin as expected, in both intact forms and SUB1 cleaved, is not lost during washing and effectively elutes from the resin (Figure 5.4, A and B, respectively). The eluted material was enriched for MSP1; haemoglobin and other non-interacting malarial and human proteins had been removed. As expected, due to SUB1 cleavage of MSP1, there were more protein species seen in purified SUB1 cleaved MSP1 complex than uncleaved MSP1. There were unidentifiable bands present in both purified samples that cannot be accounted for by MSP1 alone (Figure 5.4). These are predicted to be binding partners of MSP1, constituents of the MSP1 complex, and banding patterns indicate differences in complex composition prior to and post SUB1 cleavage.

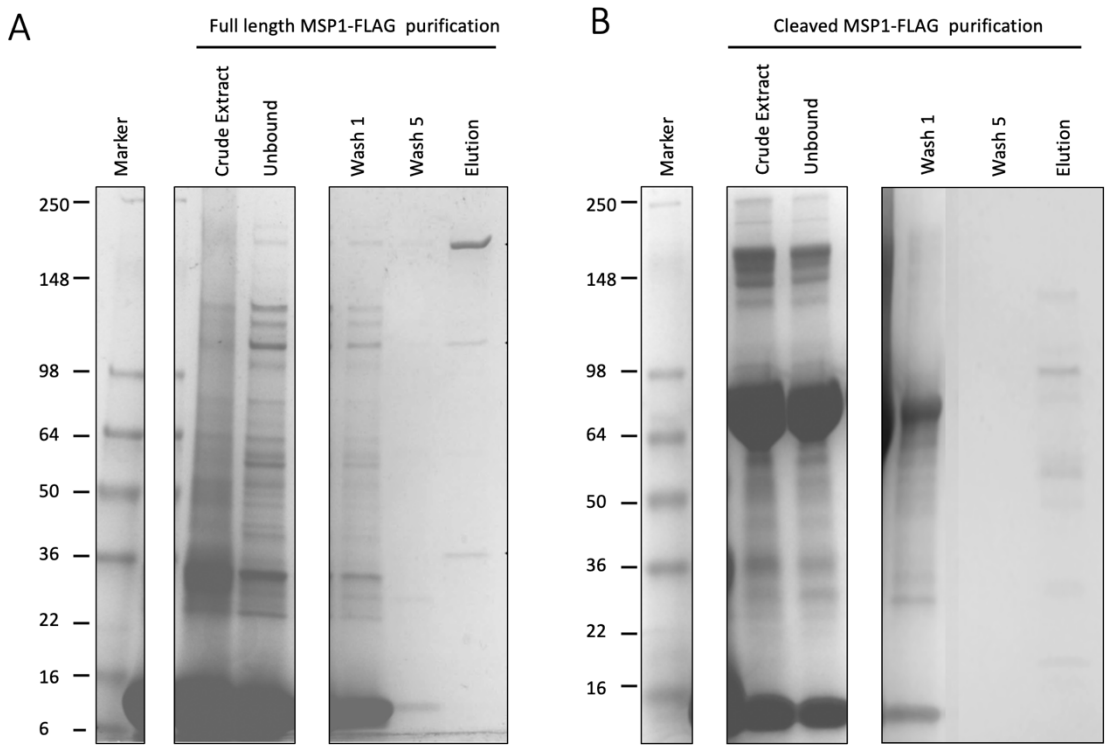

Figure 5.4 - Native MSP1 can be purified both before and after SUB1 cleavage

SDS PAGE and Coomassie analysis of ***A)*** *the purification of MSP1-FLAG$_{FL}$ complex from the soluble fraction of saponin lysed C2 arrested RAP treated 3D7MSP1-FLAG:loxP schizonts and* ***B)*** *the purification of MSP1-FLAG$_{cleaved}$ complex from the egress supernatant of RAP treated parasites from the 3D7MSP1-FLAG:loxP line, by affinity purification with an anti-FLAG resin. The crude extract, unbound fraction, first and last wash, and elution of each sample are shown and suggest that the eluted samples were enriched for intact and SUB1 cleaved MSP1 (A and B, respectively); haemoglobin and malarial proteins that do not compose the MSP1 complexes either do not bind the resin or are removed by washing.*

5.3 Full length and cleaved MSP1 complexes have different compositions

Two approaches were taken to determine the identity of the potential binding partners of MSP1, that were pulled down alongside MSP1-FLAG. First, samples were screened against antibodies specific for other merozoite surface proteins by western blot, in anticipation that this would help to correlate hits to species seen in the Coomassie stain (Figure 5.5C,D). Trace amounts of SERA5 were detected in both samples by western blot. This was presumed to be contamination rather than a specific interaction as SERA5 is highly expressed in schizonts. The pAb α-SERA5 used seems to bind SERA5 at the central papain-like domain (~56 kDa); as would be expected, SERA5 was full length in MSP1-FLAG$_{FL}$ and processed in MSP1-FLAG$_{cleaved}$. Both purified uncleaved and SUB1 cleaved MSP1 samples were found to contain MSP6 and MSP7 by western blot (Figure 5.5); the sizes of these MSP species differed between samples, likely because of SUB1 processing of these proteins has occurred in egressed schizonts. This suggested these merozoite surface proteins may form part of both the intact and cleaved MSP1 complexes, but the exact fragments of proteins involved may be differ between complexes and therefore, the make-up of the MSP1 complex prior to and at egress are distinct. MSP3 is seen in higher quantities in the purified MSP1-FLAG$_{cleaved}$ sample and β-spectrin is seen in higher quantities in the purified MSP1-FLAG$_{FL}$ sample. Again, this highlights the different compositions of the MSP1 complex before and after SUB1 cleavage and egress.

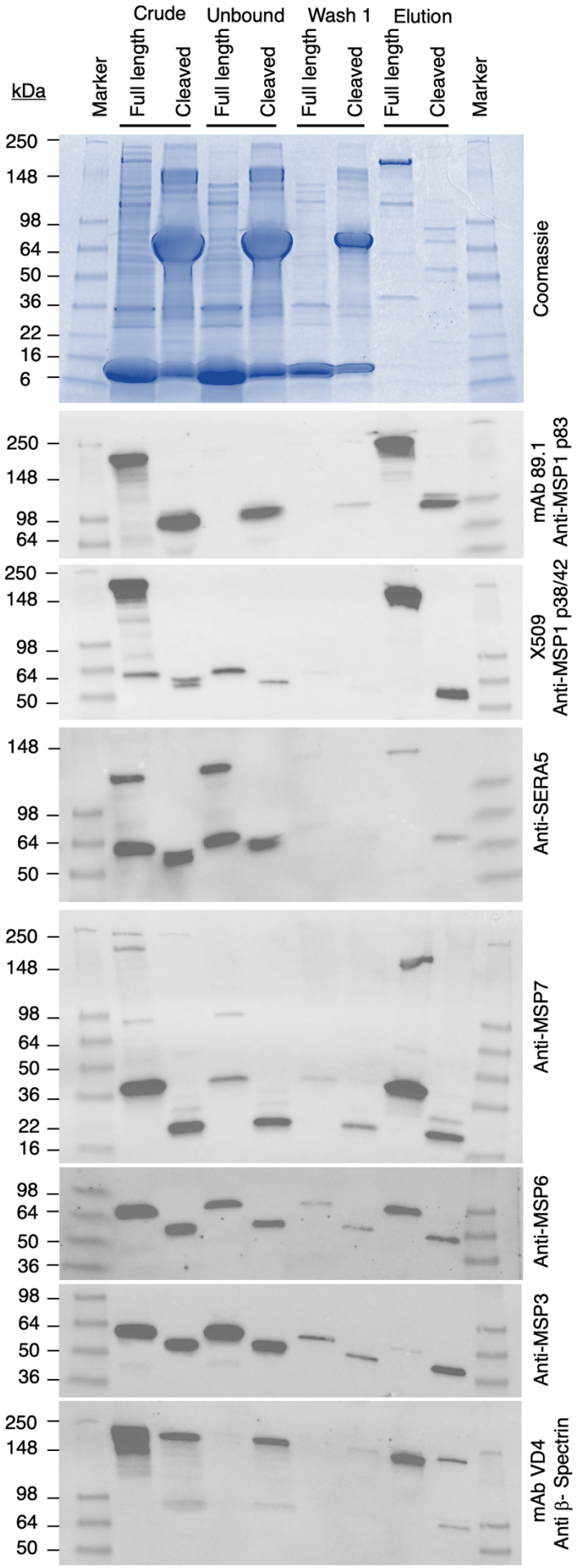
Crude
Unbound
Wash 1
Elution
Marker
Full length
Cleaved
Full length
Cleaved
Full length
Cleaved
Full length
Cleaved
Marker
kDa
250
148
98
64
50
36
22
16
6
Coomassie
mAb 89.1
Anti-MSP1 p83
X509
Anti-MSP1 p38/42
Anti-SERA5
Anti-MSP7
Anti-MSP6
Anti-MSP3
mAb VD4
Anti β- Spectrin

Figure 5.5 – The MSP1 complex composition changes after SUB1 cleavage

SDS PAGE, Coomassie and western blot analysis of the crude extract, unbound fraction, first wash and elution of the purification of un-cleaved MSP1 complex from the soluble fraction of saponin lysed C2 arrested RAP treated 3D7MSP1-FLAG:loxP schizonts and the purification of SUB1 cleaved MSP1 complex from the egress supernatant of RAP treated parasites from the 3D7MSP1-FLAG:loxP line, by anti-FLAG affinity purification. Samples were probed with mAb 89.1 (anti-MSP1 p83), mAb X509 (anti-MSP1 p38/42), pAb anti-SERA5 (thought to bind the papain domain, p5), mAb anti-MSP7, mAb anti-MSP6 mAb anti-MSP3. Blots confirm again that eluted samples were enriched for intact and SUB1 cleaved MSP1 (Full length and Cleaved elutions, respectively) and suggested that MSP7 and MSP6 are present in both intact and SUB1 cleaved MSP1 complexes, whereas MSP3 was present only in the cleaved MSP1 complex and β - spectrin was more abundant the uncleaved complex.

To identify potential constituents of the MSP1 complexes to which there were no available antibodies, mass spectrometry analysis of purified samples was carried out. Both samples had MSP6 and 7 (*PF3D7_1035500 and PF3D7_1335100 respectively)*. MSP9 (PF3D7_1228600) was detected in the MSP1-FLAG$_{FL}$ complex in high abundance. MSP1-FLAG$_{cleaved}$ had significantly higher abundances of MSP3 and SERA9 than MSP1-FLAG$_{FL.}$ In contrast to the western blot analysis, β-spectrin was found to be more abundant in purified MSP1-FLAG$_{cleaved}$.

Other SERAs were also co-purified with both forms of MSP1, including SERA4, 5, 6 and 7 (Table 5.1). In contrast to WB analysis, SERA5 was seen in high abundance in the MS analysis of both samples. However, peptide mapping showed only peptides spanning the N and C

termini, not papain-like domain, of the SERAs for MSP1-FLAG$_{cleaved}$. This could suggest that the presence of SERA5 in this sample is not just due to contamination. PfSERA4-7,9 are predicted to be processed by SUB1 in a similar manner to SERA5 and 6; the cleaved N and C termini remain associated by a disulfide bond (Yeoh et al., 2007). Possible association of SERA5 termini with cleaved MSP1 was intriguing, given that SERA5 is important for blood stage egress. These MS results confirmed differences in complex composition after SUB1 cleavage, indicative of an 'activation' of MSP1 at egress.

	Full length			Cleaved		
	Unique peptides	Seq coverage (%)	Rank	Unique peptides	Seq coverage (%)	Rank
SERA4	18	29.8	13	19	20.3	12
SERA5	50	53.9	7	31	34.2	4
SERA6	7	11.3	35	17	21.8	14
SERA7	4	7.6	21	10	14.2	13
SERA9	0	0	61	11	15.7	17

Table 5.1- Multiple SERAs detected were detected in the purified MSP1-FLAG$_{FL}$ and MSP1-FLAG$_{cleaved}$ complexes.

An overview of abundance (rank) and sequence coverage(%) of SERA4 (PF3D7_ 0207700), SERA5 (PF3D7_ 0207600), SERA6 (PF3D7_ 0207500), SERA7 (PF3D7_0207400), SERA9 (PF3D7_ 0902800) determined by MS analysis.

5.4 Single particle cryo-EM of MSP1-FLAG$_{FL}$ and MSP1-FLAG$_{cleaved}$ confirms differences in composition

5.4.1 3D reconstructions of the native MSP1-FLAG$_{FL}$ and MSP1-FLAG$_{cleaved}$ complexes

Given the differences seen in the compositions of SUB1 processed and unprocessed MSP1 complexes and the predicted conformational change of MSP1 upon SUB1 cleavage (Das et al., 2015), attempts were made to determine the structure of these complexes. Purified MSP1-FLAG$_{FL}$ and MSP1-FLAG$_{cleaved}$ were used to produce cryo-grids for single particle analysis; grid preparation was optimised and carried out by Claudine Bisson and Natasha Lukoyanova (see Methods). A series of EM movies were collected of each vitrified sample (Natasha Lukoyanova, see Methods) and the data were analysed to allow 3D reconstruction of the native MSP1 complexes. Different approaches were taken for the structure determination of the SUB1 processed and unprocessed MSP1 complexes, due to differences in behaviour of these samples (Figure 5.6). Initial 2D classification of projections collected for the un-cleaved pre-egress MSP1 complex suggested the complex had a preferred orientation (data not shown). Where necessary, datasets were rebalanced. The distribution of particles imaged for MSP1 complex post-egress and SUB1 cleavage was more even, with a larger range of projections collected; however, complexes appeared to be more heterogeneous (Figure 5.6-5.8). Final resolution for both maps was ~4 Å. Reconstructions and orientation plots are shown in Figure 5.7-5.8.

A

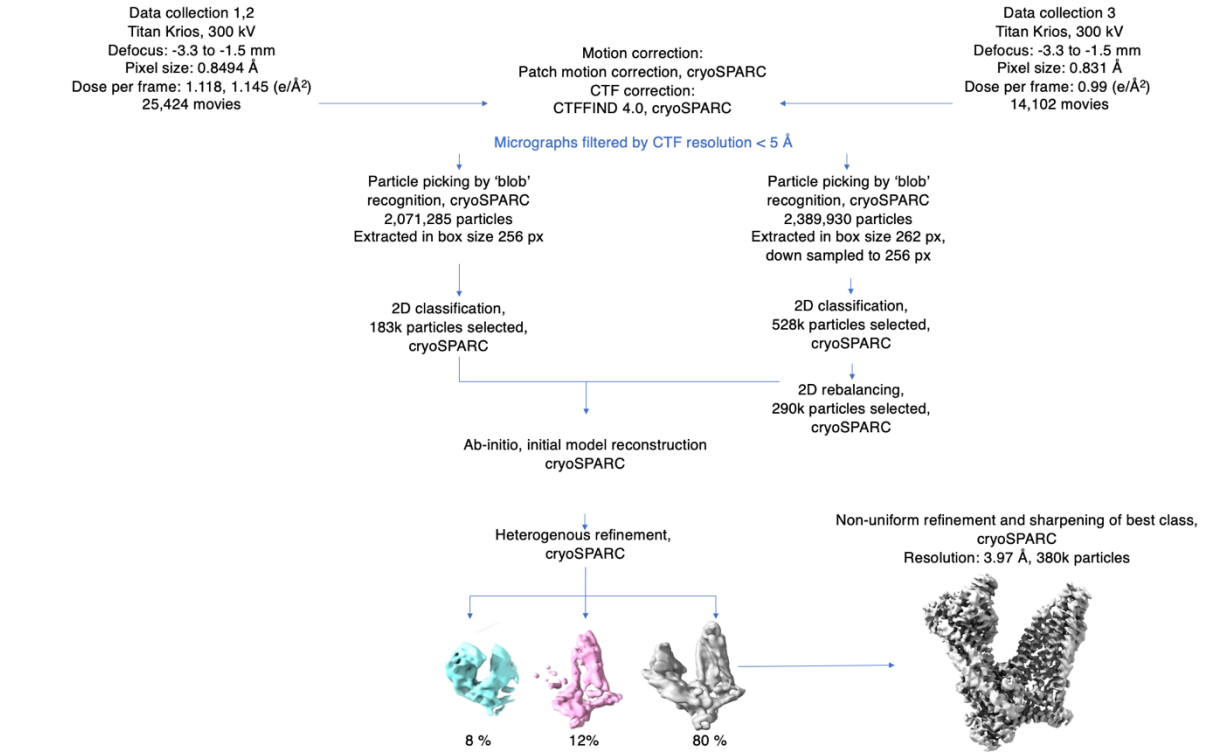
Data collection 1,2
Titan Krios, 300 kV
Defocus: -3.3 to -1.5 mm
Pixel size: 0.8494 Å
Dose per frame: 1.118, 1.145 (e/Å²)
25,424 movies
Motion correction:
Patch motion correction, cryoSPARC
CTF correction:
CTFFIND 4.0, cryoSPARC
Data collection 3
Titan Krios, 300 kV
Defocus: -3.3 to -1.5 mm
Pixel size: 0.831 Å
Dose per frame: 0.99 (e/Å²)
14,102 movies
Micrographs filtered by CTF resolution < 5 Å
Particle picking by 'blob' recognition, cryoSPARC
2,071,285 particles
Extracted in box size 256 px
Particle picking by 'blob' recognition, cryoSPARC
2,389,930 particles
Extracted in box size 262 px, down sampled to 256 px
2D classification, 183k particles selected, cryoSPARC
2D classification, 528k particles selected, cryoSPARC
2D rebalancing, 290k particles selected, cryoSPARC
Ab-initio, initial model reconstruction cryoSPARC
Heterogenous refinement, cryoSPARC
8 %
12%
80 %
Non-uniform refinement and sharpening of best class, cryoSPARC
Resolution: 3.97 Å, 380k particles

B

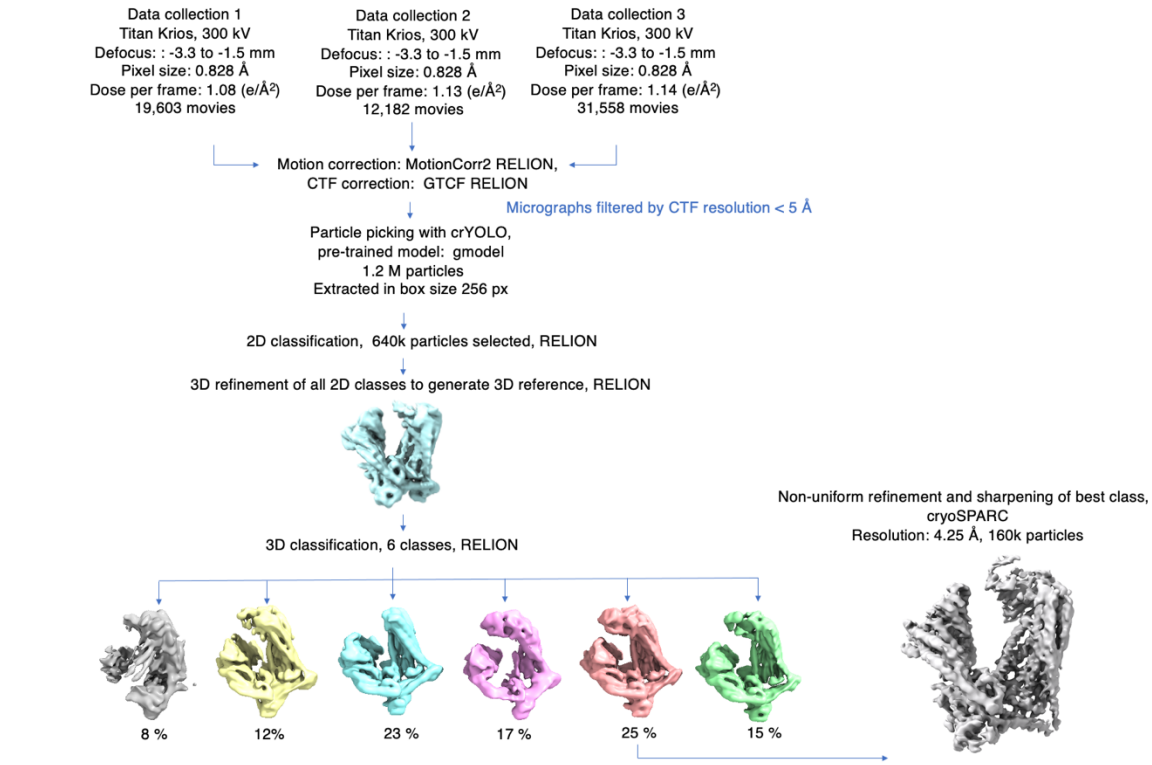
Data collection 1
Titan Krios, 300 kV
Defocus: : -3.3 to -1.5 mm
Pixel size: 0.828 Å
Dose per frame: 1.08 (e/Å²)
19,603 movies
Data collection 2
Titan Krios, 300 kV
Defocus: : -3.3 to -1.5 mm
Pixel size: 0.828 Å
Dose per frame: 1.13 (e/Å²)
12,182 movies
Data collection 3
Titan Krios, 300 kV
Defocus: : -3.3 to -1.5 mm
Pixel size: 0.828 Å
Dose per frame: 1.14 (e/Å²)
31,558 movies
Motion correction: MotionCorr2 RELION,
CTF correction: GTCF RELION
Micrographs filtered by CTF resolution < 5 Å
Particle picking with crYOLO,
pre-trained model: gmodel
1.2 M particles
Extracted in box size 256 px
2D classification, 640k particles selected, RELION
3D refinement of all 2D classes to generate 3D reference, RELION
3D classification, 6 classes, RELION
8 %
12%
23 %
17 %
25 %
15 %
Non-uniform refinement and sharpening of best class, cryoSPARC
Resolution: 4.25 Å, 160k particles

Figure 5.6 - Schematics of image processing workflow for cryo-EM single particle analysis and 3D reconstruction

Where indicated, either cryoSPARC (Punjani et al., 2017)or RELION 3.1 (Zivanov et al., 2018) were used for the image processing and 3D reconstruction of **A)** un-cleaved MSP1 complex and **B)** SUB1 cleaved MSP1 complex. Where specific methods of motion correction (MotionCor2, (Zheng et al., 2017); Patch motion correction), CTF correction (Gctf, (Zhang, 2016) or CTFFIND 4.0, (Rohou & Grigorieff, 2015)), particle picking (crYOLO, (Wagner et al., 2019)), and 3D refinement were used, this is stated in the figure. Numbers of particles picked initially and selected after 2D classification and the percentage of total particles in individual classes *of 3D reconstructions are indicated. Data collection statistics can be found in Table 2.4.*

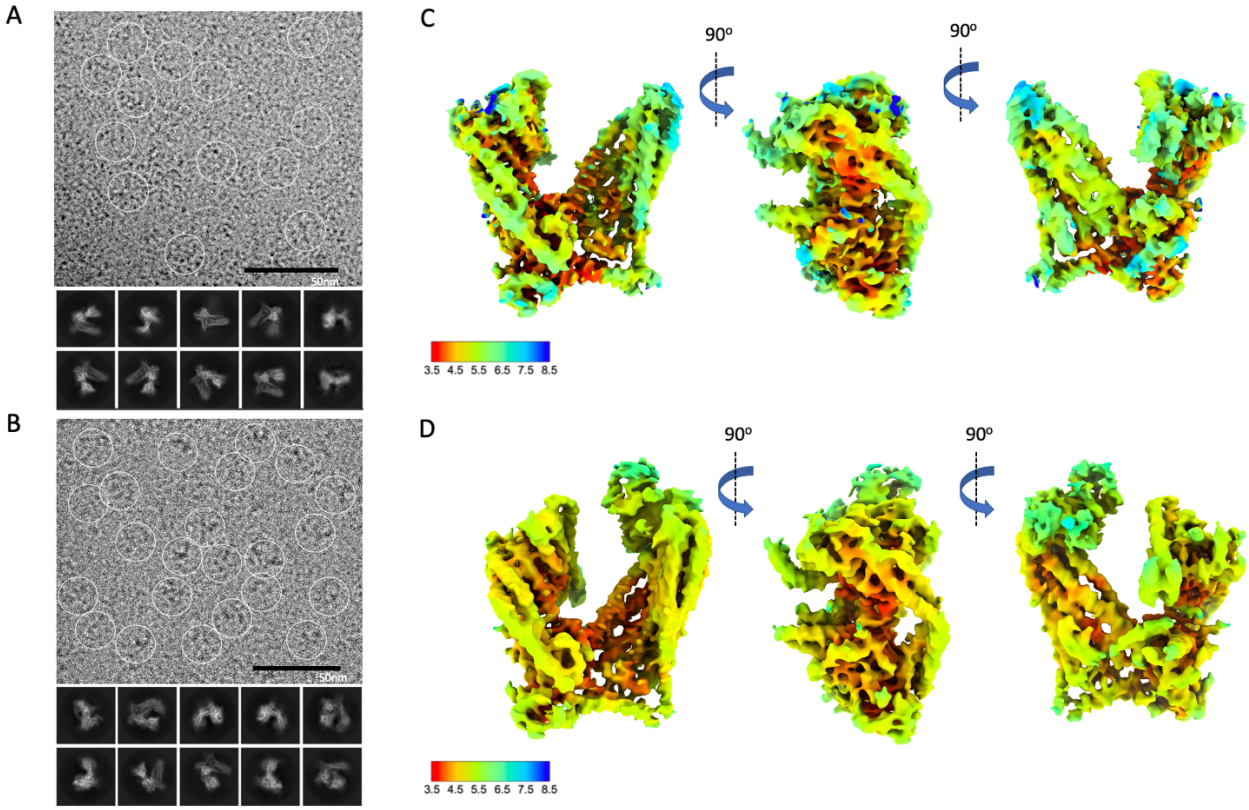

Figure 5.7- Final 3D reconstructions of uncleaved and cleaved MSP1

*Example motion corrected micrographs of vitrified samples of purified **A)** uncleaved MSP1 and **B)** SUB1 cleaved MSP1, with examples of particles highlighted by white circles on images and selected 2D classes shown below. Scale bars on micrographs are 50 nm. The final reconstructions of **C)** MSP1-FLAG$_{FL}$ and **D)** MSP1-FLAG$_{cleaved}$, in 3 different orientations, with the local resolution of the cryo-EM maps plotted on the density surfaces by colour (colour key indicates resolution in Å).*

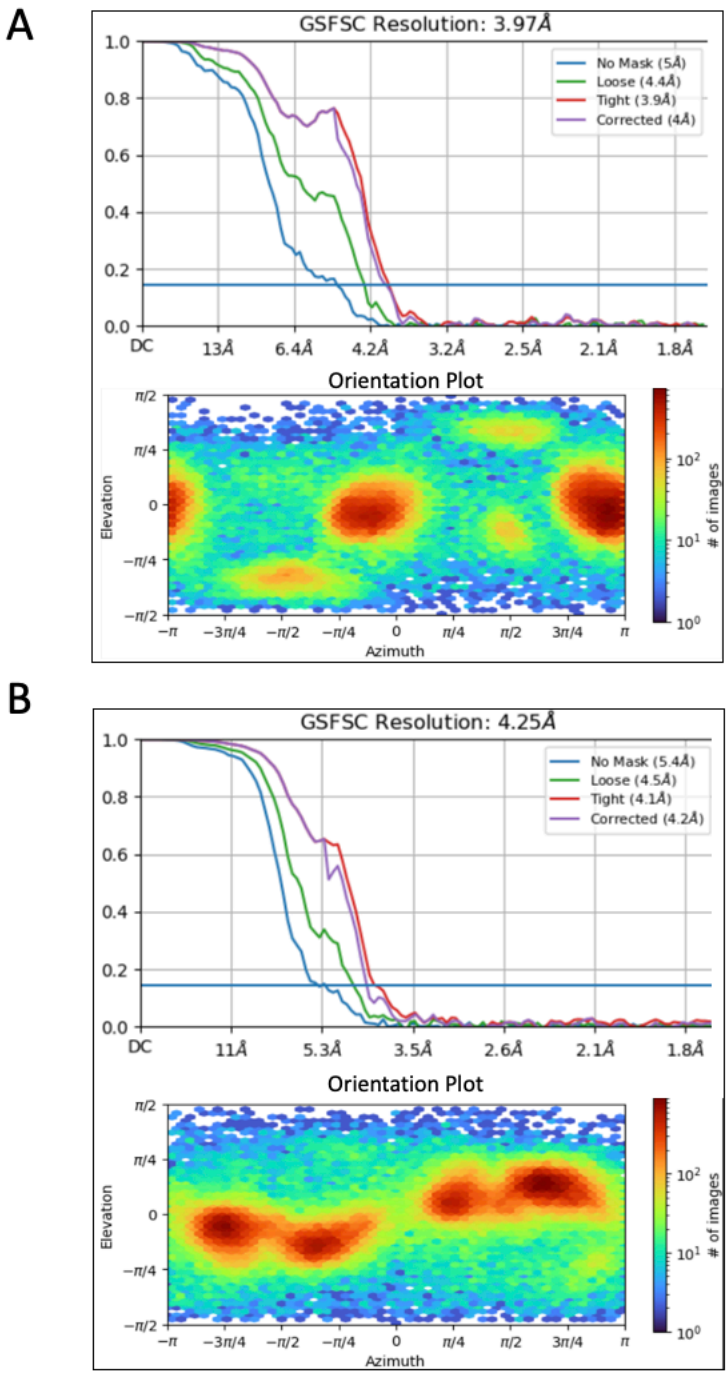

Figure 5. 8 - Estimated global resolutions and orientation plots of the final 3D reconstructions of uncleaved and cleaved MSP1

Fourier shell correlation (FSC) curves, used for global resolution estimate, and the orientation plots, showing angular distribution of particles that composite the final 3D reconstructions of

A) *uncleaved MSP1 and* ***B)*** *SUB1 cleaved MSP1. Global resolutions are 3.97 Å and 4.25 Å for uncleaved and SUB1 cleaved MSP1, respectively; these are determined by the resolution of the corrected FSC curve (purple) at 0.143. The FSC curves shown were calculated as follows: Blue - raw FSC calculated between half-maps of unmasked data; Green – FSC calculated after applying a loose solvent mask to data (Signal to noise ratio (SNR) increased); Red – FSC calculated after applying a tighter mask to data (Signal to noise ratio (SNR) increased further); Purple – FSC curve calculated using a tighter mask with correction for noise. Orientation plots show distribution of particle views, plotting the azimuth (horizontal angle) against elevation (vertical angle) in radians with number of images as a heatmap (low to high number of images via blue to red, as shown in key). Calculations were carried out and graphs generated in cryoSPARC (Punjani et al., 2017).*

5.4.2 3D reconstructions of native MSP1 complexes have additional density not accounted for by the published recombinant structure

To assess whether our structures of the native MSP1 complex contained partner proteins, the published atomic structure for SUB1 processed MSP1 was fitted into the densities (Dijkman et al., 2021)(Figure 5.9). This showed that both maps included additional densities not accounted for by the published model, suggesting that partner proteins were present in the MSP1 complexes. To aid the identification of these additional densities, Cα tracing of the density was carried out where possible. This showed that both complexes had a globular, helical domain interacting with the 'wing'-like p80 fragment of MSP1 (Figure 5.10).

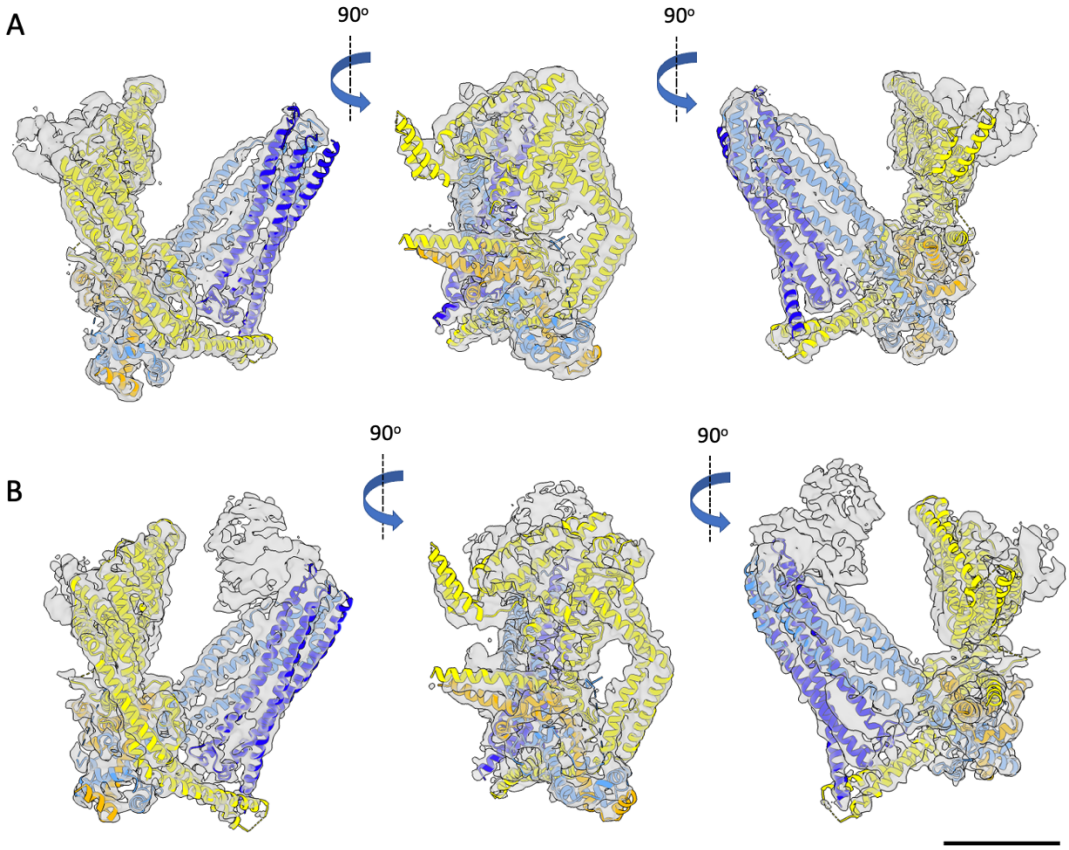

Figure 5. 9 - Docking of the published atomic structure of recombinant MSP1 into the experimental densities of native MSP1 suggest partner proteins are present

The published atomic model of recombinantly expressed, SUB1 processed MSP1 (Dijkman et al., 2021) was docked into our 3D reconstructions of native ***A)*** *uncleaved MSP1,* ***B)*** *SUB1 cleaved MSP1 using Phenix (Liebschner et al., 2019). Experimental density, unaccounted for by the published structure, present on the p83 'wing' of both complexes and on the p38/42 'stalk' of cleaved MSP1, suggests the presence of binding partners. Scale bar 50 Å.*

The release of AlphaFold2 structural predictions for malarial proteins allowed interpretation of additional densities seen in this work (Jumper et al., 2021). Comparison of the Cα trace of the additional domain associated with the p83 fragment showed that it has an almost identical fold to the Alphafold2 atomic prediction of the C-terminus of MSP7; the models

can be overlayed (Figure 5.10C). In place of the Cα trace, the predicted model of the C-terminal helical bundle of MSP7 was used for further model refinement. From the model, the MSP7 C-terminus fits into a pocket on the p83 and may interact with the positively charged surface on the wing at helix 6-8 and the negatively charged surface at helix 4,5 and 9. Hydrogen bonds are predicted between helix 6, 7, 9 and MSP7. MSP1 helicies 5 -7 and 9 have sequence conservation within *P. falciparum* strains and between *Plasmodium* species (Dijkman et al., 2021).

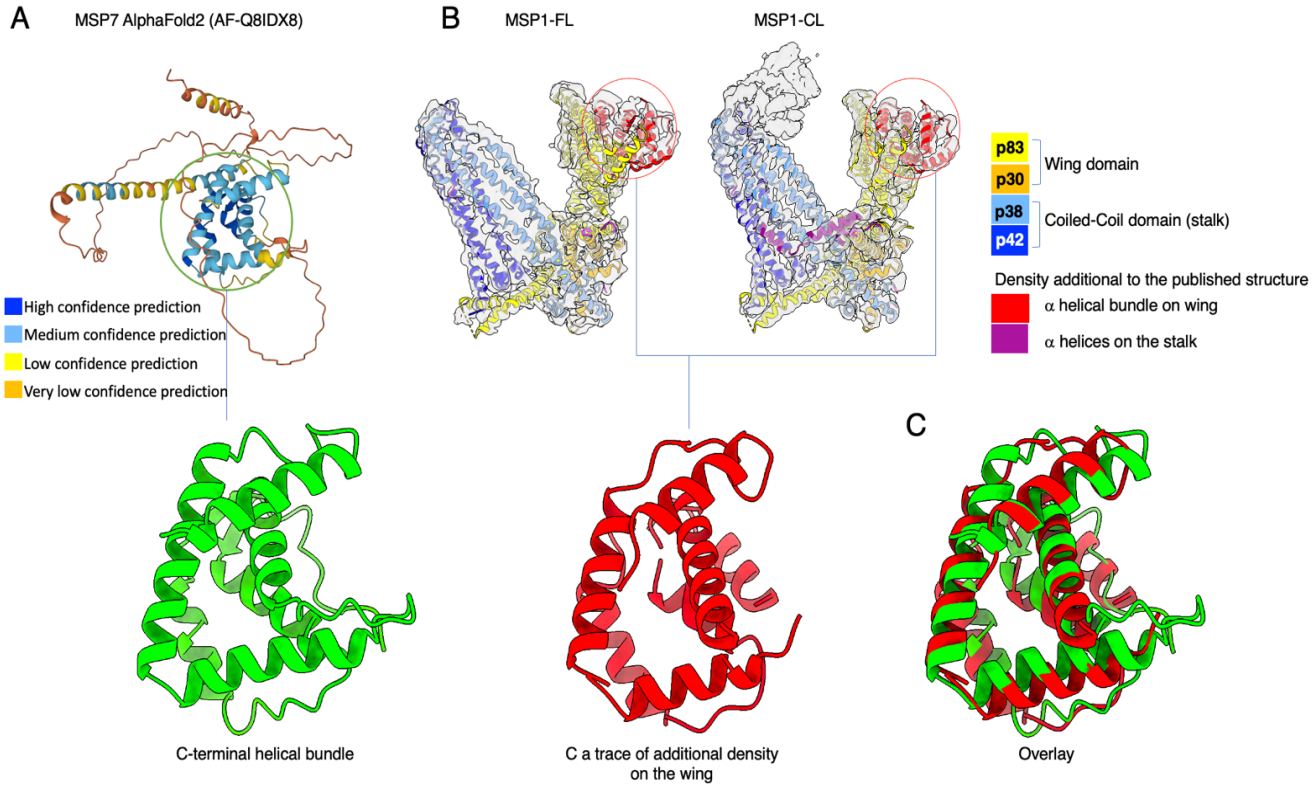

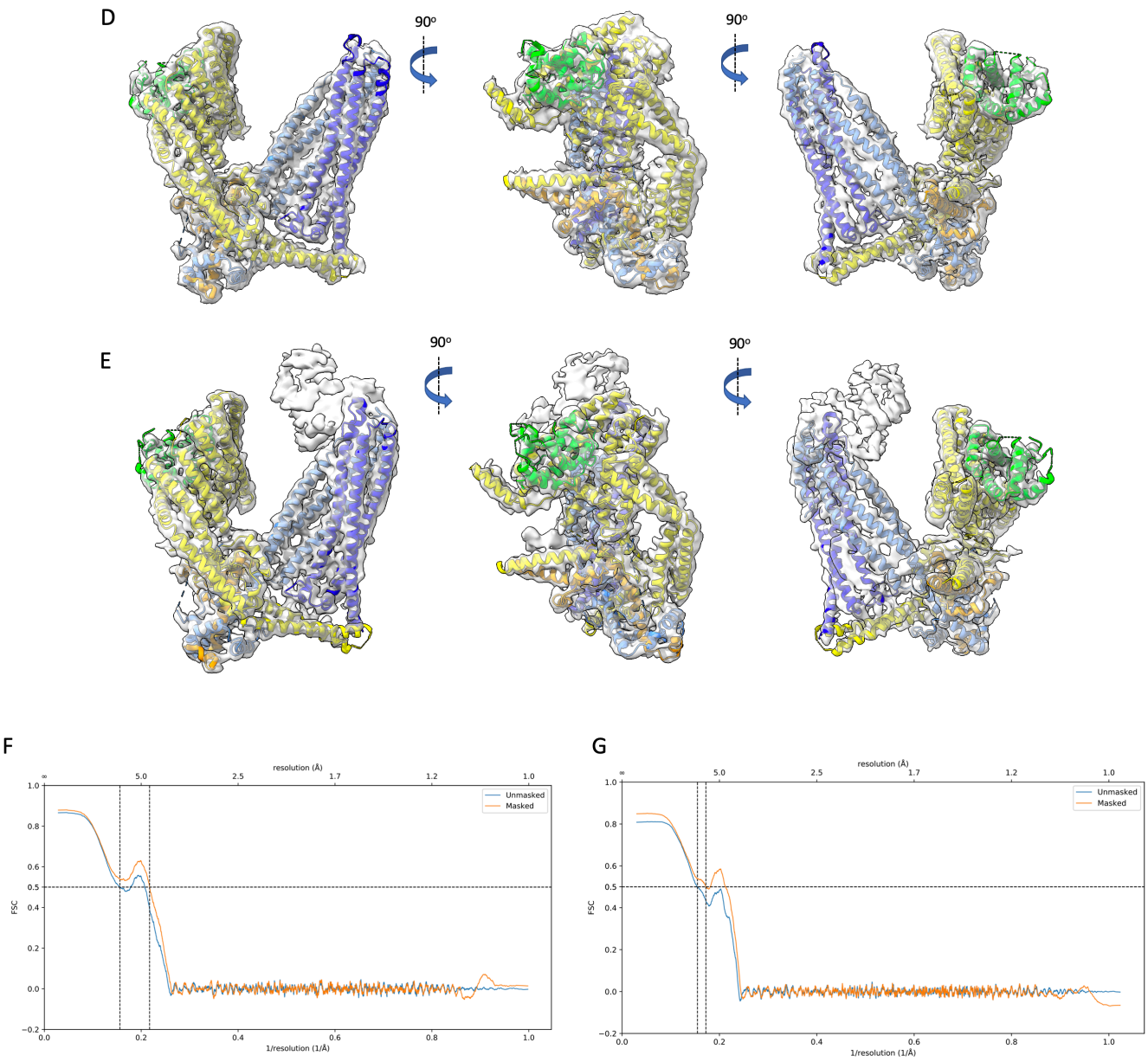

Figure 5.10 - Atomic modelling of 3D reconstructions of the MSP1 complex before and after SUB1 cleavage confirms partner proteins are present

A) *Alphafold2 prediction of the structure of MSP7 (AF-Q8IDX8) obtained from the open resource protein structure database, coloured based on model confidence, (dark blue – high, light blue – confident, yellow – low, orange- very low) and an enlarged view of the predicted MSP7 C-terminal a-helical bundle (green).*

B) *Ca tracing of the density seen on the p83 'wing' in 3D reconstructions of the MSP1 complexes, shown docked on both cryo-EM maps and in enlarged view (red), produced using COOT. An additional α-helical domain was also Ca traced in the cleaved reconstruction that flanks the posterior of the p38/p42 coiled coil domain (magenta).*

C) *Overlay of the Ca tracing of the density seen on the p83 'wing' in the 3D reconstructions and the Alphafold2 prediction of the C-terminus of MSP7, showing the high similarity of models. This suggests MSP7 is present in the MSP1 complex both before and after SUB1 cleavage.*

Modelling of the 3D reconstructions of ***D)*** *uncleaved MSP1,* ***E)*** *SUB1 cleaved MSP1 using the published atomic model of recombinant, cleaved MSP1 and the Alphafold2 prediction of the C-terminus of MSP7 with docking and refinement using ISOLDE and Phenix (Croll, 2018; Liebschner et al., 2019). Different orientations are shown. The masked (orange) and unmasked (blue) map-model FSC curves for* ***F)*** *uncleaved MSP1,* ***G)*** *SUB1 cleaved MSP1 were calculated using Phenix. FSC at 0.5 was 4.6 Å and 5.8 Å for uncleaved and cleaved MSP1 respectively (see Appendix 3 for a table of model validation statistics).*

5.4.3 SUB1 cleavage of MSP1 allows recruitment of additional binding partners

To quantify the differences between the structures of SUB1 uncleaved and cleaved MSP1, the cryo-EM maps were directly compared. No drastic conformational change of MSP1 was observed post SUB1 processing; this result was unsurprising as published work reported minimal differences between structures of MSP1 partially (cleavage only at the 30/38 site)

or fully processed by SUB1 (Dijkman et al., 2021). However, from our 3D reconstructions, the two complexes did appear to differ in composition (Figure 5.10-5.11). There were two regions of density observed in MSP1-FLAG$_{cleaved}$ that were absent in MSP1-FLAG$_{FL}$ (Figure 5.10-5.11). 3 α-helices were traced in the 3D reconstruction of SUB1 cleaved MSP1, interacting with the coiled-coil 'stalk'-like p38/p42 fragments of MSP1 at helix 32-34 (Figure 5.10, magenta). More prominently, there was an additional density at the top of the coiled-coil domain, near the 38/42 SUB1 cleavage site (the bottom of helix 33-35, Figure 5.10-11). This could not be further resolved by local or multibody refinement (data not shown) and so no trace was possible. Low resolution may be a result of flexibility of this partner protein. Regardless, this shows that the main effect of SUB1 processing on MSP1 is to change the complex composition, suggesting that SUB1 processing, at the 38/42 site in particular, 'activates' MSP1 by recruiting an additional partner protein.

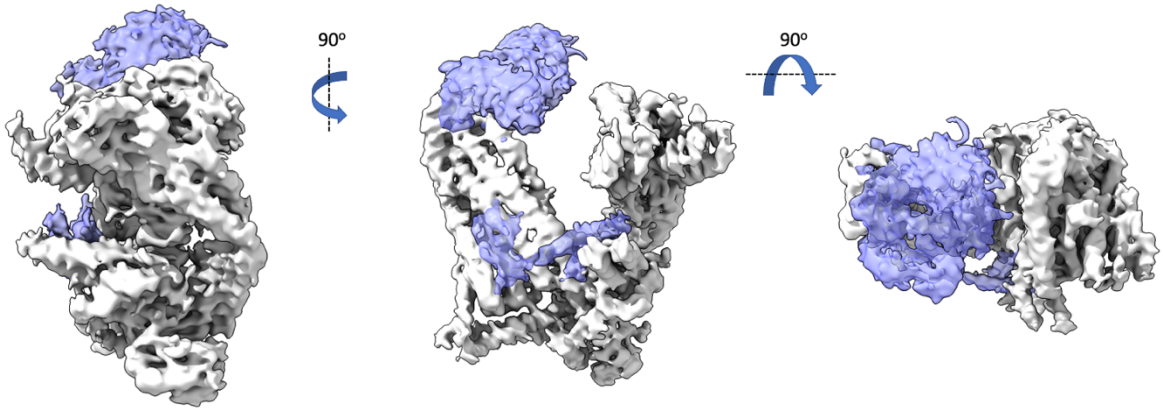

Figure 5.11 - Density subtraction of the 3D reconstructions of MSP1 confirms change in complex composition after SUB1 cleavage

Density subtraction of the 3D reconstruction of intact MSP1 complex from that of the cleaved MSP1 complex was carried out in ChimeraX. The difference density (blue) is docked onto the final cryo-EM map of the intact MSP1 complex for comparison. This provides clear evidence for the recruitment of additional proteins after MSP1 cleavage, suggesting that these components may be involved in activation of MSP1 function in egress.

5.4.4 MSP6 and a SERA protein may bind MSP1 after SUB1 cleavage

Given the differences in MSP1 composition, identification of the proteins that bind after SUB1 cleavage would give more insight into MSP1 function at egress. Work by collaborators in Hamburg (M. Maiorca) resulted in modest improvement of the MSP1-FLAG$_{cleaved}$ density (Figure 5.12). From the initial stack of particles, low-quality particles were excluded using software being developed by Maiorca et al., CSSB Hamburg. Subsequently, the selected particles underwent 3D classification using cryoSPARC. Angular parameters for each class were then re-estimated using cryoSPARC Non-Uniform Refinement. Slightly improved density in the additional domains allowed identification of a possible partner protein using an *in silico* screen of the candidates identified by MS.

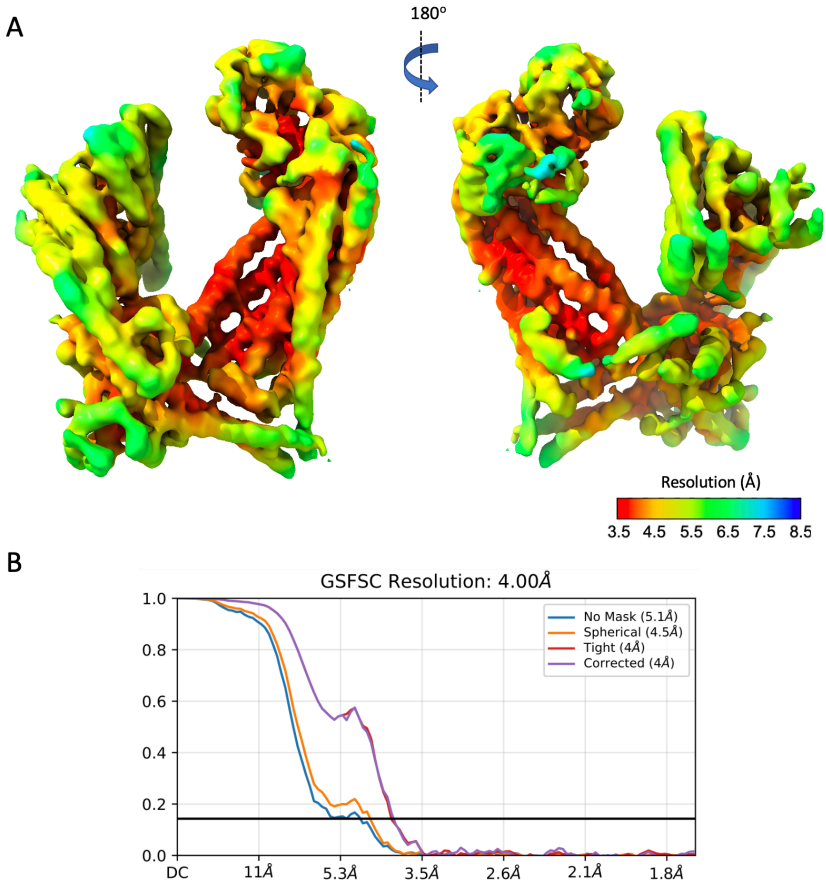

Figure 5.12 – Improved 3D reconstruction of SUB1 cleaved MSP1

A) *Improved map with local resolution plotted on the density surfaces by colour (colour key indicates resolution in Å) and* ***B)*** *FSC curve for the improved reconstruction, both calculated using cryoSPARC.*

Using AlphaFold3 multimer (Abramson et al., 2024), interactions between SUB1 cleaved fragments of MSP1, 3, 6, 7 and SERA5 were modelled. SERA5 was chosen for two reasons: because this was the most abundant SERA in the sample (Table 5.1) and because of the documented requirement for SERA5 in egress (Collins et al., 2017). The C-terminus of MSP7 (p22) was predicted to bind on the p83 fragment of MSP1 as seen in our model (Figure 5.10, 5.13). The C-terminus of MSP6 was predicted by Alphafold3 to bind at the position of the 3 α-helices traced in the density on the coiled-coil domain of MSP1- $FLAG_{cleaved}$ (Figure 5.10 B).

The N and C terminal domains of SERA5 (p47 and p18 respectively) were predicted to remain associated and bind at the position of the large unresolved additional density on the top of this domain, near the 38/42 SUB1 cleavage site (Figure 5.13). In the model, this interaction was mediated by the SERA5 p18 and MSP1 p38. Part of the loop between MSP1 helices 34 and 35 (Gln 1294 -> Glu 1311, now on referred to as the p38/42 loop) showed to contact the p38/42 coiled-coil domain, between helices 30 and 35. This may create a negatively charged surface that could allow association of a positively charged surface on SERA5 p18, (Lys 924, Arg 926); however, the structure of this loop is predicted with low confidence. Interestingly, part of MSP6 was also predicted to associate with SERA5 p47.

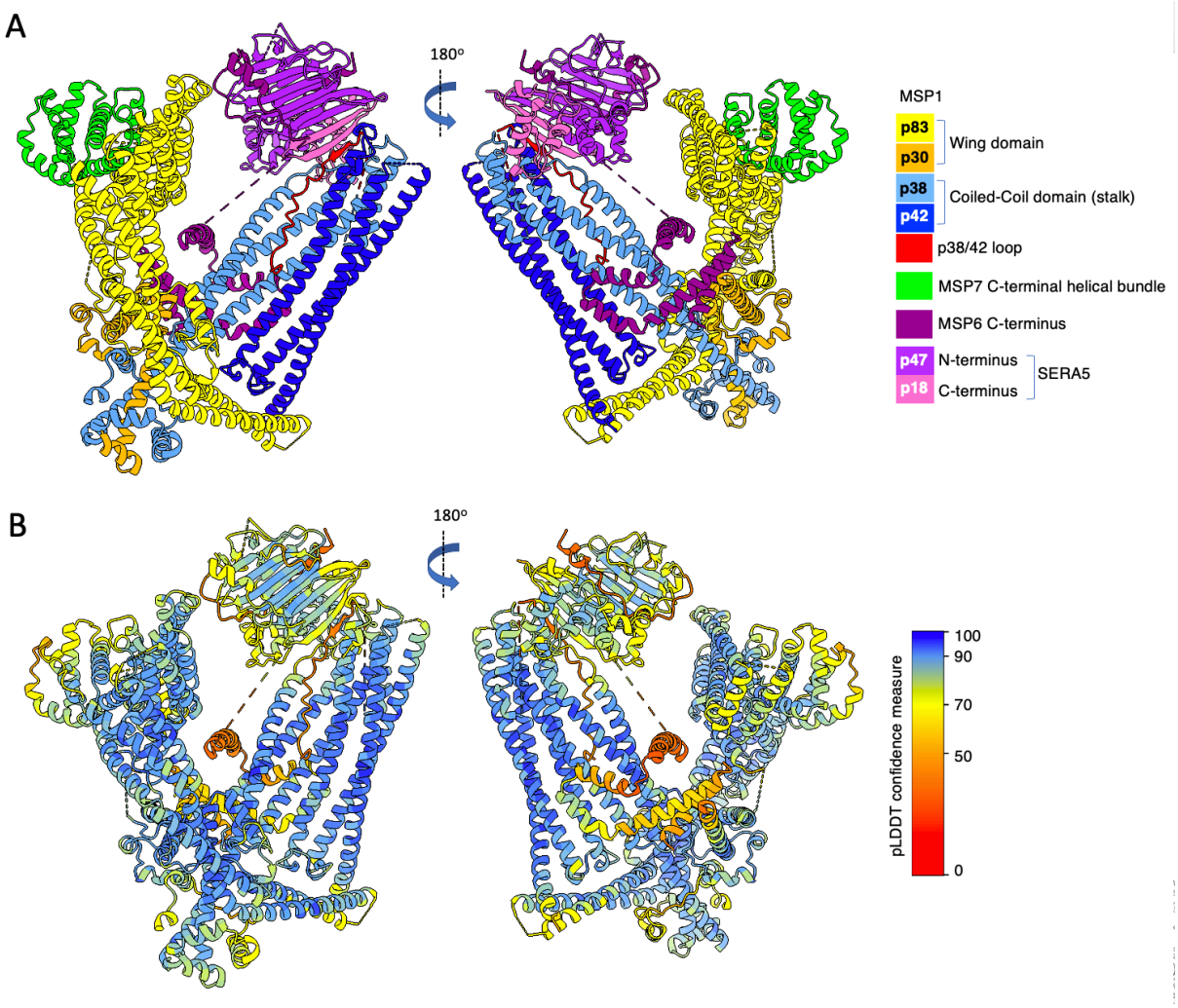

Figure 5.13 – Alphafold3 predicts the association of SERA5 to SUB1 cleaved MSP1 near the 38/42 cleavage site.

The atomic model produced by Alphafold3 multimer using the sequences for cleaved MSP1 (PF3D7_09030300), MSP6(PF3D7_1035500), MSP7 p22 (PF3D7_1335100) and SERA5 p47 p18, (PF3D7_0207600), coloured by: ***A)*** *structural elements correspond to which protein/protein fragment, indicated by key;* ***B)*** *the pLDDT score, a measure of confidence of the predicted model, indicated by colour key. Regions with pLDDT > 90 have been modelled to high accuracy. Regions with pLDDT between 70 and 90 are confident. Regions with pLDDT between 50 and 70 are low confidence. Regions with pLDDT < 50 often have a ribbon-like appearance and should not be interpreted. For the purpose of this figure, ribbon like structures have been trimmed.*

The Alphafold3 prediction was docked, regions for which there was no density were trimmed and modelled into the improved density for MSP1-FLAG$_{cleaved}$. This gives convincing evidence of MSP6 and SERA5 p47p18 in the complex (Figure 5.14). The map-model FSC for full model at 0.5 was 6.0 Å (Figure 5.14 C); when the model and density for the globular region on top of the p38/42 coiled-coil are removed from calculation, at 0.5 the map-model FSC = 4.5 Å (Figure 5.14 D). There is some density in the improved map between helices 30 and 35, not present in the MSP1-FLAG$_{FL}$ map, that may suggest the presence of part of the p38/42 loop, but it is not conclusive and this loop was not included in the model (Figure 5.14 A). Confirmation of the mode of binding proposed by Alphafold of SERA5 was therefore limited by the resolution of this region of the map. Despite this, the results of the *in silico* screen alongside the MS and EM single particle analysis provide evidence that MSP6 and

SERA5 p47p18 may bind MSP1 after SUB1 cleavage. Given that SERA5 has shown to be important for merozoite egress, this sheds new light on possible functions of both proteins. Analysis of the electrostatic surfaces of atomic models for SUB1 cleaved and full length MSP1 (ChimeraX) suggest the association of SERA5 to MSP1 may allow presentation of a negatively charged surface on the N terminus of SERA5 (p47). Association of SERA5 may also create a binding site for and allow presentation of a negatively charged loop of MSP6 at the merozoite surface (Figure 5.15A).

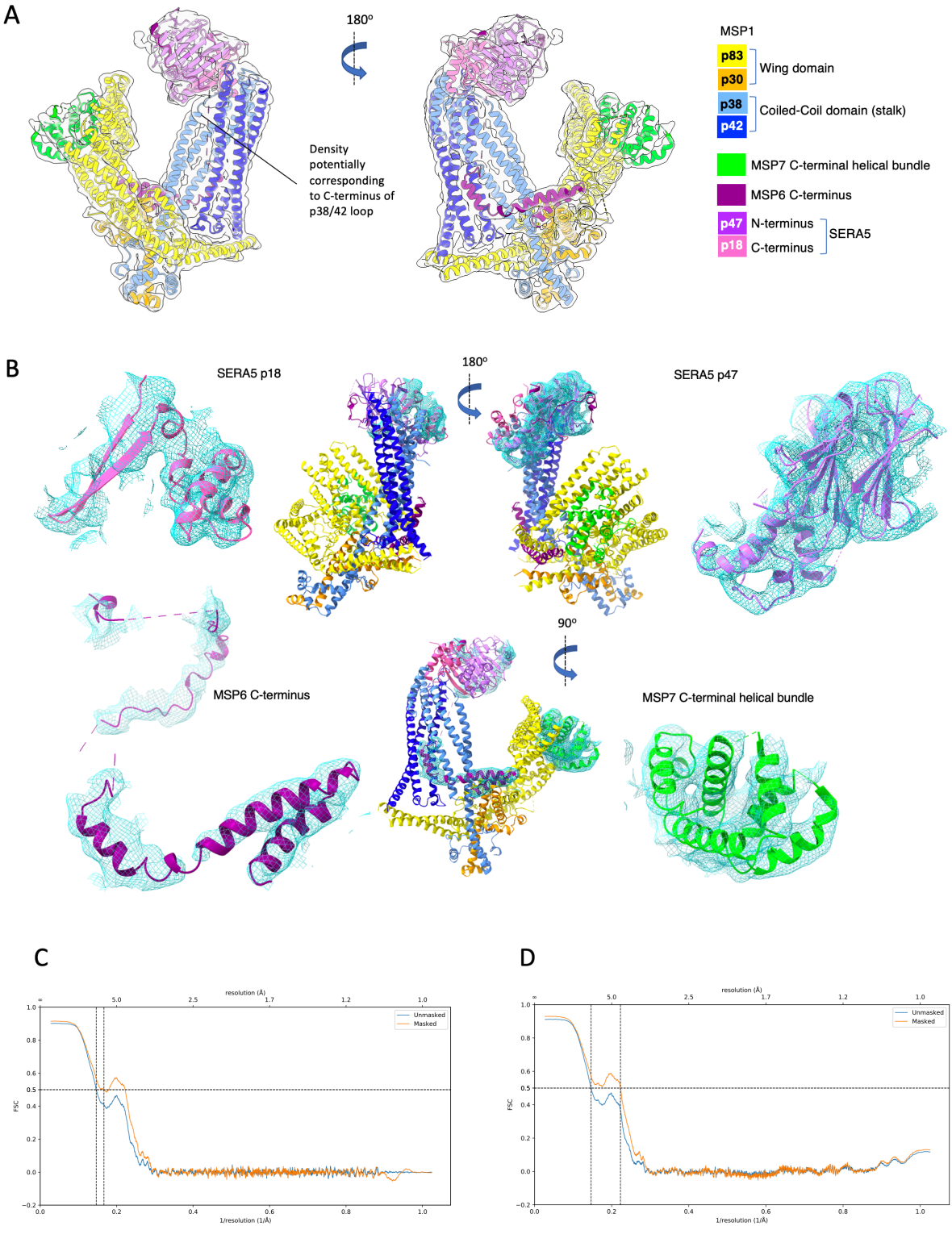

Figure 5.14 - The predicted model fits into the experimental density for MSP1-FLAG$_{cleaved}$.

A) *Views of overall fit, demonstrating MSP6 and SERA5 p47p18 are good candidates for the additional density. In the Alphafold3 prediction, SERA5 could bind through association with*

an immobilised region of the p38/42 loop and the p38. There is a region of density between helices 30 and 35 in the MSP1-FLAG$_{cleaved}$ density that may correspond to part of the disordered loop between this region, providing some indication this may be correct but this loop could not be reliably modelled. Density for MSP6, SERA5 and the p38/42 loop (H34-H35) is absent in the EM map of MSP1-FLAG$_{FL.}$

***B)** Views of fit of atomic models in the experimental density of specified partner proteins, providing evidence for the presence of MSP7, MSP6 and SERA5 in the cleaved MSP1 complex.*

*Map to model FSCs generated in Phenix for **C)** the full map and model and **D)** the map and model masked to remove the additional domain on the top of the coiled-coil of MSP1 (SERA5 p47p18 and a portion of MSP6) from the calculation. These curves give the map-model FSCs at 0.5 = 6.0 Å and 4.5 Å for **C** and **D** respectively. See Appendix 3 for model statistics.*

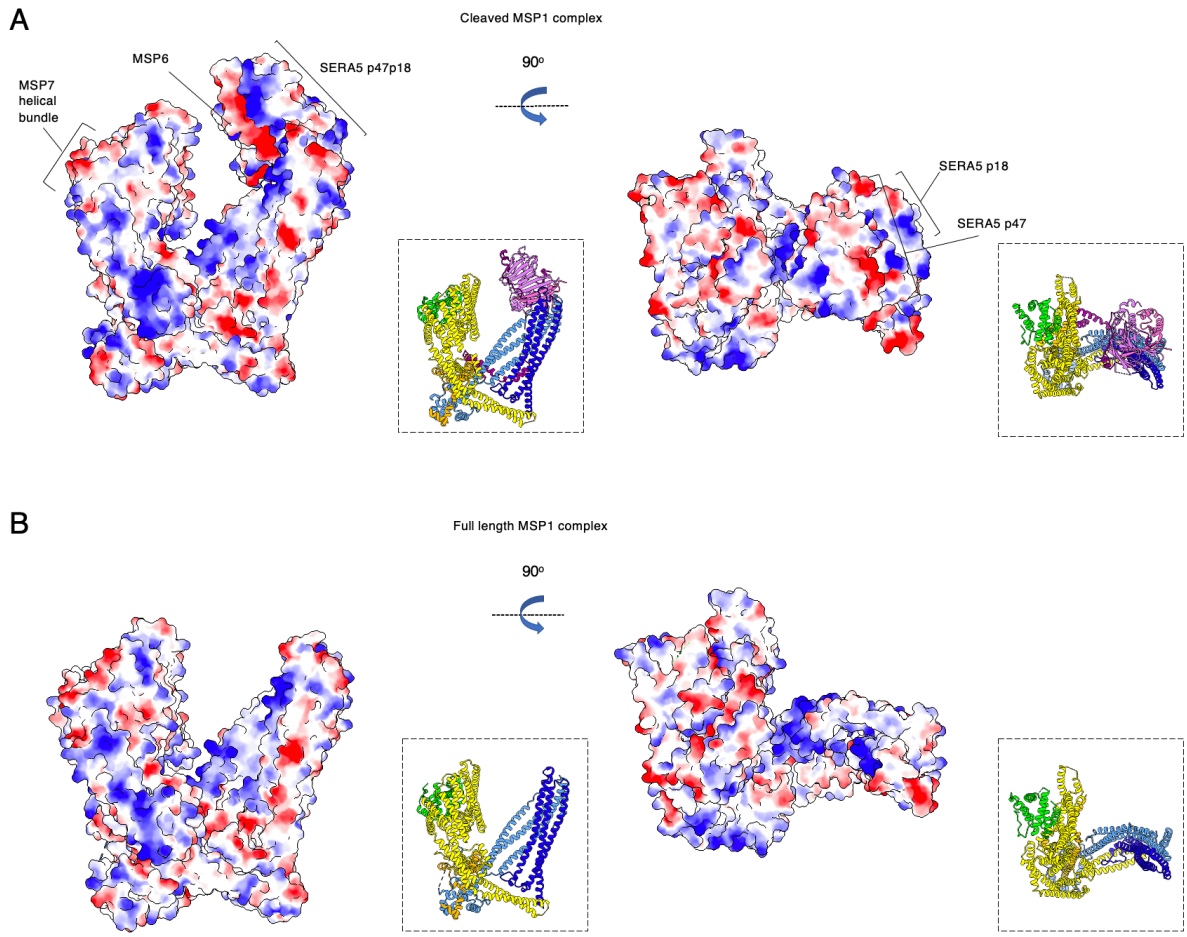

Figure 5.15 - Electrostatic surface potential of the predicted Alphafold model for cleaved MSP1-7-SERA5 and model of MSP1-FLAG$_{FL}$ complex.

*The Alphafold cleaved MSP1-7-6-SERA5 (**A**) and the MSP1-FLAG$_{FL}$ – MSP7 **(B)** models are coloured by electrostatic surface potential where red indicates negatively charged regions and blue indicates positively charged regions. Insets show the same view but in cartoon representation, to help interpretation.*

5.5 Discussion

This work presents the native structures of the MSP1 complex, both prior to and post SUB1 cleavage, purified directly from *P. falciparum* culture. As expected, MSP7 was identified in both structures using the AlphaFold2 model, at 1:1 stoichiometry. An MSP7 precursor is first processed (protease unknown) to a 33 kDa fragment in the post Golgi compartment (Pachebat et al., 2007); it is this fragment that associates with full length MSP1, possibly in the ER (Kadekoppala & Holder, 2010). At the PM, upon SUB1 processing, MSP7 is cleaved to produce a 22 kDa (p22) fragment. MSP7 p22 (C-terminus) remains bound to the cleaved MSP1 complex (Koussis et al., 2009). Only the MSP7 p22 domain was accounted for in the densities. However, MS confirmed the presence MSP7 p33 in the MSP1-FLAG$_{FL}$ sample; Alphafold predicts the region upstream of the p22 (Leu86 -> Ser177) forms a disordered loop (PF3D7_1335100, AF-Q8IDX8-F1). This may account for why this is not visible in the MSP1-FLAG$_{FL}$ map. Based on the EM density, MSP7 binds conserved regions of the p83. This may reflect the importance of this interaction in the erythrocytic cycle. MSP7 has been previously implicated in parasite growth and invasion (Kadekoppala et al., 2010). Although MSP6 and 9 were seen in high abundance in MS analysis of purified MSP1-FLAG$_{FL}$, no density was seen in the structure to account for this. Similarly, MSP3 could not be identified in the MSP1-FLAG$_{cleaved}$ map.

Further comparisons made between the 3D reconstructions of complexes indicated that there was density seen in the SUB1 cleaved complex that was not seen in the uncleaved reconstruction. This suggested that SUB1 cleavage is required for the recruitment of additional partner proteins to MSP1, which is likely related to MSP1 function in egress. The exact identity of the additional experimental densities is unclear due to low resolution and flexibility. However, the mass spectrometric analysis of the purified MSP1 complexes

allowed *in silico* screening of the predicted structures of hits using Alphafold3 multimer. SERA5 p47p18 was identified as a potential candidate for density seen at the top of the coiled-coil domain of MSP1-FLAG$_{cleaved}$, near the p38/42 SUB1 cleavage site. MSP6 was predicted to bind at the position of the additional density across the coiled-coil domain. A model of the MSP1/6/7 and SERA5 p47p18 complex fitted into the experimental density.

As described in the introduction (section 1.5.1), SERA5 is important for merozoite egress; in parasites lacking SERA5, merozoites do not egress normally (Collins et al., 2017). There is also evidence that SERA5 p47p18 is present on the merozoite surface (J. Li et al., 2002).The association of SERA5 to MSP1 may have a role in merozoite dispersion. Binding of SERA5 is predicted to present a negatively charged surface on SERA5 p47 and allow association and presentation of a negatively charged loop of MSP6, projecting from the PM, which may disfavour interaction between neighbouring daughter merozoites. SERA5 was predicted to bind via the loop between helices 34 and 35 of MSP1, where the 38/42 cleavage site lies. This provides a potential explanation of why cleavage at this site may be important for egress: to create a binding surface for SERA5.

The presence of other SERAs in the purified sample (MS analysis) is interesting and may need to be explored. Due to similarities in the predicted SUB1 processing pattern and structures of SERAs (Figure 5.15), it is plausible that other SERA N/C termini could bind cleaved MSP1. The EM density seen on the p34/42 coiled-coil may have been an average of different SERAs. This could have contributed to low resolution. An expansion of candidates for the *in silico* screen could help determine if other SERAs are predicted to bind at the same position.

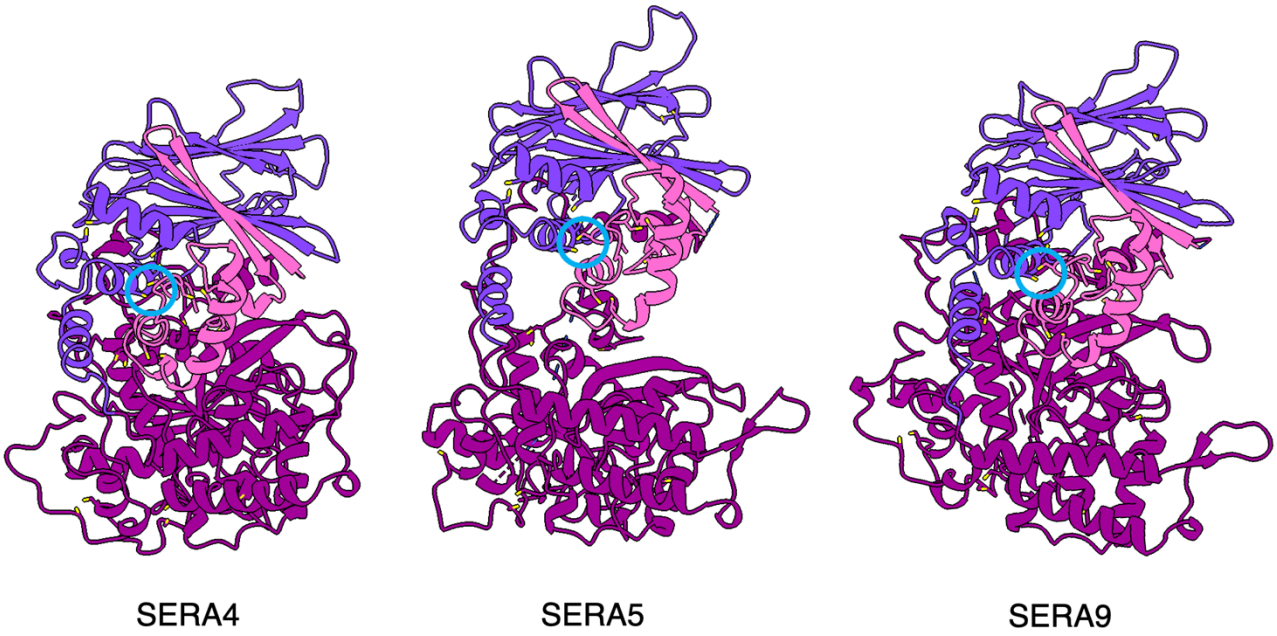

Figure 5.16 - Predicted structures of SERA4, 5 and 9 are homologous

Alphafold2 predictions of the structure of SERA4,5 and 9. Structures are coloured according to domains after SUB1 processing: purple: N-terminal domain, pink: C-terminal domain, magenta: papain-like domain. Cysteine residues are shown, demonstrating the potential of complex association by disulfide bond (blue ring suggests where this bond may be).

As mentioned in the introduction (Section 1.7) recent work has suggested that unprocessed MSP1 exists as a heterodimer, associating between p83 and p42 (Dijkman et al., 2021). This dimerization was shown to be hindered by β–spectrin, with the implication that the coiled-coil domain of MSP1 may be involved in the binding of β–spectrin to allow cytoskeleton remodelling. However, this 3D reconstruction is of recombinant MSP1 expressed in *E.coli* and lacks the partner proteins that would normally associate with MSP1. This may explain why dimers were seen in this data but not in single particle analysis of native MSP1.

Alternatively, it should also be noted that the purified native complex would be in a much lower concentration than in recombinant preparations of the complex. It may be that there is a critical concentration needed for dimerization which is reached at the merozoite surface and in the recombinant sample but not in our native sample.

As to whether β–spectrin is a binding partner of MSP1, our data is insufficient to answer this question. For this work MSP1 was expressed as a soluble FLAG-tagged protein, localised to the PV, potentially preventing endogenous interactions that occur at the merozoite membrane. Given that unprocessed MSP1 is purified from the soluble fraction of saponin lysis, and so should not include membrane associated binding partners, and that, after egress, β–spectrin would have been cleaved and may no longer associate with the MSP1 complex, it was thought unlikely that β–spectrin would be seen in 3D reconstructions. MS analysis of purified sample suggested β–spectrin was present in significantly greater amounts in the MSP1-FLAG$_{cleaved}$ complex, suggesting β–spectrin may bind to cleaved MSP1, which does not correlate with results of binding assays carried out on purified, recombinantly expressed MSP1 (Dijkman et al., 2021). However, density that could correspond to β–spectrin was not observed in the cryo-EM reconstruction.

Chapter 6 - Conclusions and future work

6.1 Invasion, development or egress?

Our work has refuted claims of MSP1 requirement for invasion and confirmed its requirement in egress. There have been conflicting hypothesis for the role of MSP1 in the malaria parasite erythrocytic cycle (Baldwin et al., 2015; Boyle et al., 2010; Das et al., 2015; Hanspal et al., 2002; Moss et al., 2012). Previous work suggesting a role for MSP1 in invasion was discussed in the introduction. Among other limitations, these studies characterised the interactions of MSP1 with GPA, Band 3 and heparin using recombinant MSP1 (Baldwin et al., 2015; Boyle et al., 2010; Hanspal et al., 2002). Recombinant protein lacks the partner proteins, so that observed interactions may be artefactual. We have shown RBC invasion can occur without MSP1 being present on the merozoite surface. When MSP1 is untethered to the merozoite surface or knocked out, merozoites released by mechanical rupture were able to invade RBCs. A study carried out by the Rayner group (Cambridge University, Cambridge Institute for Medical Research) using the 3D7MSP1KO:lox66/lox71rev line (Chapter 3) has confirmed MSP1 does not contribute to strong merozoite attachment to the RBCM. Optical tweezers were used to measure the force needed to dissociate merozoites from the erythrocyte surface (Emma Jones, unpublished). There was no significant difference seen between WT and MSP1-null merozoites for either the frequency or strength of attachment, supporting the conclusion that MSP1 is not required for invasion. It should be noted that the work described in this thesis and that carried out at the Cambridge Institute for Medical Research does not disprove a role for MSP1 in initial, weak attraction

to the RBCM, just prior to invasion. Video microscopy to quantify time taken to contact an erythrocyte and for the initiation of invasion for parasites lacking MSP1 would help to resolve if this protein plays any role in this process.

Antibodies to MSP1 have been shown to prevent parasite development (Moss et al., 2012; Woehlbier et al., 2010) but this is likely due to steric hinderance of SUB2 shedding of MSP1 before invasion (Collins et al., 2020). Although MSP1-null parasites showed some evidence of a segmentation defect, MSP1 cleavage mutants developed normally. Following development of MSP1-null merozoites after invasion would help clarify that MSP1 is not directly involved in development.

Recent work made clear that MSP1 must be tethered to the PM for merozoite egress to occur explosively (Das et al., 2015). We have confirmed MSP1 functions in egress, showing that MSP1-null schizonts have defective egress in which merozoites do not disperse as normal. Merozoites have a short invasive half-life in which to reach a host cell. Invasion and growth defects associated with MSP1 deletion could be due to stunted egress and defective merozoite dispersal. As stated above, further work studying invasion is needed to support this conclusion.

6.2 SUB1 cleavage 'activates' MSP1

As mentioned, MSP1 is cleaved by SUB1 at three sites and fragments remain non-covalently associated on the merozoite after proteolytic processing (Child et al., 2010; Das et al., 2015;

Kauth et al., 2003, 2006). The importance of this processing for MSP1 function, specifically at the p38/42 site, was implied by the inability to express a form uncleavable at this site. Cleavage at this site occurs last, indicative of a rate limiting step (Child et al., 2010). Additionally, the 38/42 site has three-fold redundancy and all three alternative SUB1 recognition motifs (alt1, alt2, can; see introduction section 1.5.2) must be mutated to block processing (Das et al., 2015). Here, we have simultaneously disrupted all three 38/42 SUB1 sites in a conditional mutant. Previous attempts to delete these sites were unsuccessful but semi-ablation was shown to have a temporal effect on egress. Upon complete prevention of cleavage, no temporal effect was observed but parasites were defective in egress and merozoites failed to disperse. This was akin to the egress phenotype seen in MSP1-null schizonts. This work has proven the necessity of SUB1 processing at the 38/42 site as an activation step for MSP1 function in egress.

There is extensive research demonstrating that MSP1 exists in a complex with other partner proteins (Kauth et al., 2006; Lin et al., 2014, 2016). Our work builds upon the published structures of recombinant MSP1, which lacks binding partners. We present the native (*ex vivo*) structures of the MSP1 complex before and after egress. We have confirmed the presence of MSP7 in both the full length and SUB1 cleaved complex (1:1). Previous work had suggested this interaction is mediated by p83, p30 and p38 of MSP1 (Kauth et al., 2006). We have demonstrated, using cryo-EM single particle analysis, that MSP7 binds a pocket on the p83 domain; interaction appears to be exclusively mediated by this fragment.

SUB1 cleavage of MSP1 and partner proteins just before egress has been shown to enable further interactions. SUB1 processed MSP6 p36 only associates with cleaved MSP1 (Kauth et

al., 2006) and there is evidence that cleavage of MSP3 must occur before it binds to the merozoite surface (Lin et al., 2016). Using structural and biochemical analysis, we have established that the MSP1 complex changes after SUB1 cleavage and shed light on a potential complex composed of cleaved MSP1, MSP6, MSP7 and SERA5 N and C termini (p47p18).

The C-terminus of MSP6 was predicted to bind MSP1 in the position of the α-helical domain observed in the cleaved MSP1 experimental density. MSP6 C-terminus has been shown to form tetramers, which were thought to bind MSP1. However, the experimental density only accounts for one molecule of MSP6. (Kauth et al., 2006). The density corresponding to SERA5, at the top of the coiled-coil domain of MSP1, is at low resolution in our EM map. Given the high similarity of these domains in the SERA family, it must be considered that this density could correspond to another SERA or indeed a combination of several. All *Plasmodium* species have several SERA genes encoded (Arisue et al., 2011). SERA1-8 are located on chromosome 2 and SERA9 on chromosome 9 of *P. falciparum;* SERA4-6 have been demonstrated to be important in blood stages (Miller et al., 2002). The reason for this duplication is largely unknown. Our results show SERA4-7 and 9 were pulled down with cleaved MSP1. To determine if a combination of these SERAs could interchangeably account for the additional density, an expanded *in silico* screen should be done. Experiments to demonstrate the presence of the N/C termini of these SERAs on the merozoite surface would be needed to further prove that alternate or multiple SERAs bind MSP1. Given that SERA5 is highly expressed in late schizogony (Collins et al., 2017), it is reasonable to assume most particles with this additional domain seen by cryo-EM are likely the MSP1-7-6-SERA5p47p18 complex.

Contrary to previous findings, we did not identify MSPDBL1/2 or MSP3 in either of our structures, despite these proteins being identified in MS analysis of the purified samples. MSP3 is predicted to be largely α-helical, based on biophysical data and Alphafold2 (AF-Q8IJ55-F1). Recombinantly expressed full length MSP3, as well as the C-terminal domain alone, form elongated oligomers (Gondeau et al., 2009). MSP6 and DBL1/2 are MSP3-like. DBL1/2 are much larger than MSP3, with an alpha helical core and subdomains making up the DBL domain (Hodder et al., 2012).

There is evidence that the MSP1 complex exists on the merozoite surface in multiple forms (Lin et al., 2016). Interactions between other MSPs and MSP1 may have been at low frequency, less stable or the bound protein too flexible to be observed in this work. Cryo-ET of FIB (focused ion beam) milled vitrified parasites might help elucidate diversity in the complex. Thin sections (<500 nm, known as lamella) of schizonts before SUB1 release (C2 treated) or just before egress (E64-d treated) can be produced and imaged to generate 3D views of MSP1 complexes on the merozoite surface *in situ*. Cryo-FIB and cryo-ET have already provided insights into merozoite invasion (Bisson et al., 2021) and allowed the visualisation of the Pf80S ribosome in 8 translation intermediate states over the intraerythrocytic lifecycle (Anton et al., 2023).

6.3 How does MSP1 function in egress: Cut or run?

Previously, SUB1 cleavage of MSP1 has been proposed to activate MSP1 to bind to β-spectrin and aid degradation of the RBC cytoskeleton, leading to RBCM rupture (Das et al., 2015). Other work suggests that MSP1 association with β-spectrin may contribute to PVM rupture. Here, we show that β-spectrin cleavage occurs normally in MSP1-null parasites and have demonstrated, through different imaging methods, that MSP1 is not required for PVM rupture or RBC rupture. β-spectrin and ankyrin cleavage that facilitates RBC rupture is known to be mediated by SERA6 and protein co-factor MSA180 (section 1.5.1) (Tan et al., 2021). Processes leading to PVM rupture are not fully determined. PVM poration, proposed to allow influx of water and solutes from the erythrocyte cytoplasm, and PV rounding occur before PKG-mediated degradation into multi-layered vesicles (Glushakova et al., 2018; Hale et al., 2017). Lipid changes during schizogony suggest alterations in PVM composition may either change membrane curvature or support vesicular transport of enzymes that promote vacuole rupture (Ramaprasad et al., 2023).

The exact mechanisms causing *P. falciparum* merozoite dispersal are not clear. Involvement of the merozoite actomyosin motor in this process has been excluded; knock-out of GAP45, a component of the glideosome, impacts invasion but not egress (Perrin et al., 2018). Though the gliding motility of merozoites at egress has recently been documented, it should be noted that this was seen only on certain substrates. This work indicates that the actomyosin motor is required for merozoite translocation across the host membrane prior to invasion or through tissues, but the motor is not responsible for the initial 'burst' from the RBC (Yahata et al., 2021).

Initially, RBCM rupture was hypothesised to cause release of osmotic pressure, aiding merozoite dispersal. Evidence for this is conflicting. In hypotonic conditions, schizonts have been shown to egress more readily (Glushakova et al., 2005). However, apparent swelling of schizonts before egress may be an artefact of light microscopy; parasites in protein free medium have also shown to balloon and egressed less frequently (Glushakova et al., 2007, 2018). The destabilisation of the RBCM is thought to allow breakage at a single point known as the lytic pore; this causes the membrane to curl, buckle and invert, which may aid diffusion of merozoites (Abkarian et al., 2011). Osmotic shock causes uninfected RBCs to behave similarly, forming inside-out vesicles. This suggests a host cell mediated process, manipulated by *P. falciparum* to allow explosive merozoite release (Abkarian et al., 2011; Lew et al., 1988). The egress phenotype we see for MSP1-null parasites and those with disrupted MSP1 processing shows that other factors are involved. MSP1 antibodies have shown previously to inhibit merozoite dispersion after egress (Lyon et al., 1989). Our findings together with this evidence indicates the MSP1 complex plays a role in merozoite dispersion post membrane rupture.

As discussed in the introduction (1.5.1) SERA5 has an unknown role in asexual blood stage egress. When SERA5 is absent, merozoite egress was accelerated but nonexplosive. It has been hypothesised that SERA5 acts as a negative kinetic regulator to slow rates of SUB1 activation of SERA6 and delay RBCM rupture (Collins et al., 2017). SERA5 acts as a protease when phosphorylated by PfCDPK1; blocking PfCDPK1 and thus preventing SERA5 phosphorylation inhibits egress (Iyer et al., 2018). Therefore, SERA5 may have multiple roles in egress. After SUB1 processing, SERA5 p47p18 has been found to localise to the merozoite

surface (J. Li et al., 2002; Tougan et al., 2018). Our results show that this is most likely caused by its association with cleaved MSP1 and we propose yet another role for SERA5 in egress. Description of SERA5 as a pseudoprotease explains premature RBCM rupture but fails to fully justify ineffective merozoite dispersal in ΔSERA5 parasites. Our model suggests that SERA5 p47p18 binding to cleaved MSP1 presents a negatively charged surface on SERA5 p47 and allows association and presentation of a negatively charged loop of MSP6, outward facing from the merozoite PM. This could disfavour interaction between daughter merozoite membranes or RBC and PV membrane remnants to aid dispersal at egress. This hypothesis requires further testing. Measurement of surface charge of merozoites has been done previously by atomic force microscopy, suggesting the PM is negatively charged other than at the apical end (Akaki et al., 2002). Charged fluorescent nanoparticles have enabled single cell mapping of surface charge, using light microscopy, of mammalian cells (Ouyang et al., 2021); this could be an alternative method to look at change in merozoite surface charge in parasites lacking MSP1 or in those expressing MSP1 38/42 mut.

Interestingly, our work predicts SERA5 to bind MSP1 near the SUB1 38/42 processing site, which fits with the importance of cleavage here for normal egress: to allow SERA5 association. Temporal analysis of RBCM dynamics in MSP1-null and cleavage mutant parasites is needed to determine if this function contributes to membrane buckling and inversion or is a separate mediator of dispersion.

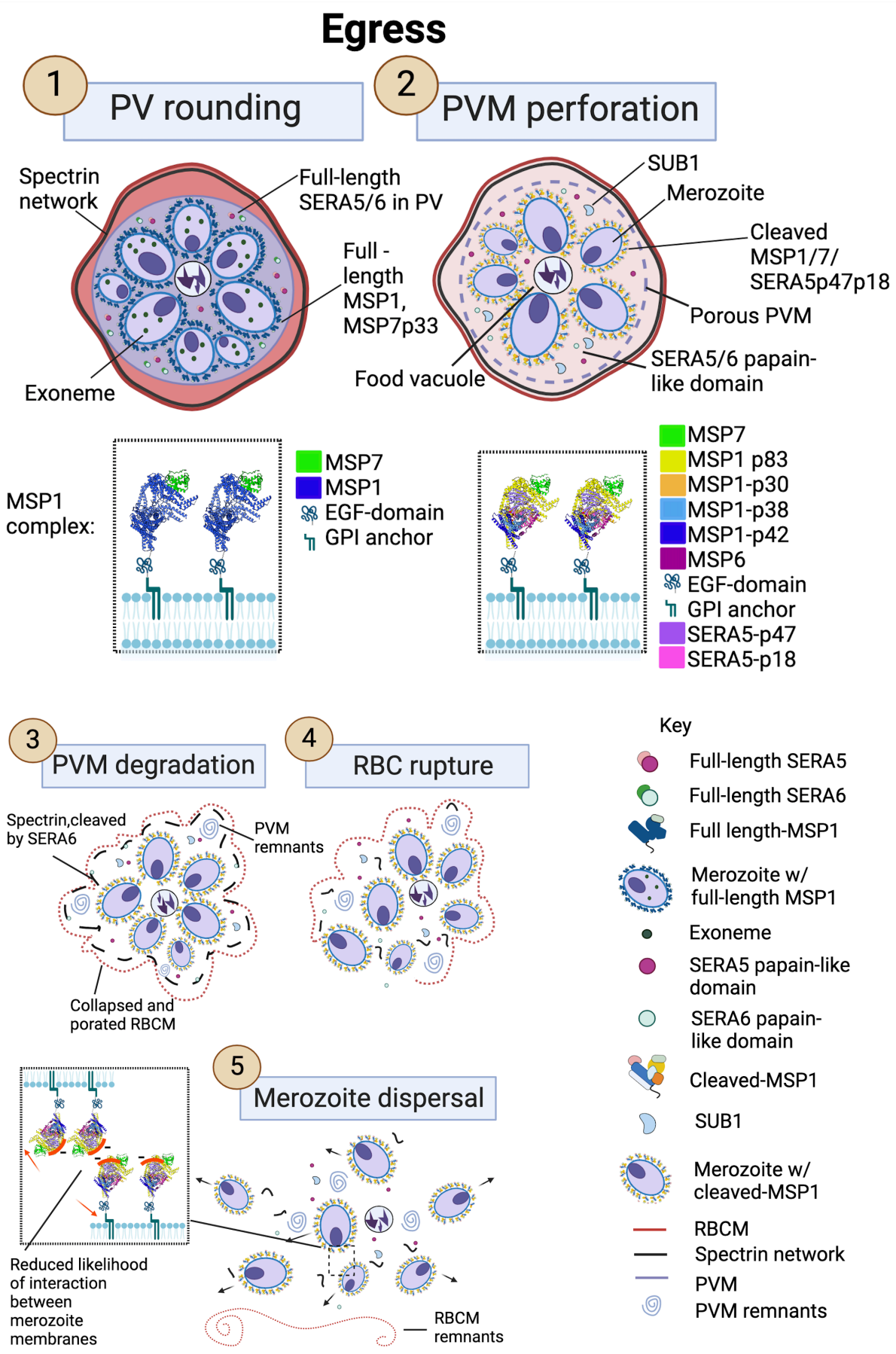
Egress
1
PV rounding
2
PVM perforation
Spectrin network
Full-length SERA5/6 in PV
Full - length MSP1, MSP7p33
Exoneme
SUB1
Merozoite
Cleaved MSP1/7/ SERA5p47p18
Porous PVM
Food vacuole
SERA5/6 papain-like domain
MSP1 complex:
MSP7
MSP1
EGF-domain
GPI anchor
MSP7
MSP1 p83
MSP1-p30
MSP1-p38
MSP1-p42
MSP6
EGF-domain
GPI anchor
SERA5-p47
SERA5-p18
3
PVM degradation
4
RBC rupture
Spectrin,cleaved by SERA6
PVM remnants
Collapsed and porated RBCM
5
Merozoite dispersal
Reduced likelihood of interaction between merozoite membranes
RBCM remnants
Key
Full-length SERA5
Full-length SERA6
Full length-MSP1
Merozoite w/ full-length MSP1
Exoneme
SERA5 papain-like domain
SERA6 papain-like domain
Cleaved-MSP1
SUB1
Merozoite w/ cleaved-MSP1
RBCM
Spectrin network
PVM
PVM remnants

Figure 6.1 - The MSP1-7-6-SERA5p47p18 complex could aid merozoite dispersion at egress. ***1)*** *Upon initiation of egress and PV rounding, SUB1 has not been released from merozoite exonemes. SERA5 and 6 are PV resident proteins, full-length MSP1, in complex with MSP7-p33, is tethered to the merozoite membrane.* ***2)*** *After PKG activation, SUB1 is released from exonemes into the PV and cleaves SERA5 and 6 to release the central papain-like domain, the N and C termini remain associated by a disulfide bond. This initiates SERA6 activation, SERA5 cleavage may regulate this process. MSP1-7 complex is also cleaved by SUB1, this creates a binding site for the N/C termini of SERA5. The PVM is perforated at this stage.* ***3)*** *The PVM degrades to form multilamellar vesicles and SERA6 cleaves β-spectrin, causing the RBCM to loose integrity. The RBCM also porates.* ***4)*** *The RBCM ruptures at a single point.* ***5)*** *The RBCM buckles and inverts, merozoites disperse from the residual body; the cleaved MSP1 complex presents a negatively charged surface of SERA5p47 and a negatively charged loop of MSP6. This is predicted to disfavour interaction between daughter merozoites PM or RBC/PV membrane remnants and aid dispersion.*

6.4 MSP1: A complex target?

The recent surge in cases of malaria highlights the need for continued ingenuity to eventually eradicate this disease (WHO, 2022). Though vaccines with modest efficacy are now available against liver stage, there are currently no vaccines targeting blood stage malaria (Datoo et al., 2021; Laurens, 2019). Due to growing resistance to anti-malarials, new drugs and indeed new targets are also needed (Hanboonkunupakarn et al., 2022).

MSP1 has long been considered a potential vaccine target. Fragments of MSP1 have largely been proven ineffective at providing protection in phase I clinical trials, despite antibodies inhibiting parasite growth in culture (Chitnis et al., 2015; Ogutu et al., 2009). Full-length MSP1 has more recently shown to have promising immunogenicity (Blank et al., 2020). It may be that the MSP1 complex could serve as an improved therapeutic target. In this vein, MSP3 has had moderate success as a vaccine candidate. Two MSP3 vaccines, GMZ2 and MSP3-LSP, have undergone some clinical testing. For these vaccines immunisation of MSP3 is in combination with a glutamine-rich protein or a long synthetic peptide respectively. Though immunogenic, protective capacity of these vaccines is low. (Alves et al., 2022) A vaccine based on a recombinant SERA5p47 antigen, which lacks polyserine repeats, is currently in development. This has had encouraging results in Phase I trials in Uganda and Burkina Faso. Studies have also indicated genetic variations in SERA5 do not impact vaccine effectiveness (Arisue et al., 2022). Could fragments of multiple components of the MSP1 complex be used simultaneously for immunisation? Would this improve efficacy of vaccines targeting MSP1?

References

Abkarian, M., Massiera, G., Berry, L., Roques, M., & Braun-Breton, C. (2011). A novel mechanism for egress of malarial parasites from red blood cells. *Blood*, *117*(15). https://doi.org/10.1182/blood-2010-08-299883

Abramson, J., Adler, J., Dunger, J., Evans, R., Green, T., Pritzel, A., Ronneberger, O., Willmore, L., Ballard, A. J., Bambrick, J., Bodenstein, S. W., Evans, D. A., Hung, C.-C., O'Neill, M., Reiman, D., Tunyasuvunakool, K., Wu, Z., Žemgulytė, A., Arvaniti, E., … Jumper, J. M. (2024). Accurate structure prediction of biomolecular interactions with AlphaFold 3. *Nature*. https://doi.org/10.1038/s41586-024-07487-w

Absalon, S., Blomqvist, K., Rudlaff, R. M., DeLano, T. J., Pollastri, M. P., & Dvorin, J. D. (2018). Calcium-dependent protein kinase 5 is required for release of egress-specific organelles in Plasmodium falciparum. *MBio*. https://doi.org/10.1128/mBio.00130-18

Absalon, S., Robbins, J. A., & Dvorin, J. D. (2016). An essential malaria protein defines the architecture of blood-stage and transmission-stage parasites. *Nature Communications*. https://doi.org/10.1038/ncomms11449

Adrian, M., Dubochet, J., Lepault, J., & McDowall, A. W. (1984). Cryo-electron microscopy of viruses. *Nature*, *308*(5954). https://doi.org/10.1038/308032a0

Akaki, M., Nagayasu, E., Nakano, Y., & Aikawa, M. (2002). Surface charge of Plasmodium falciparum merozoites as revealed by atomic force microscopy with surface potential spectroscopy. *Parasitology Research*, *88*(1). https://doi.org/10.1007/s004360100485

Al-Amoudi, A., Chang, J. J., Leforestier, A., McDowall, A., Salamin, L. M., Norlén, L. P. O., Richter, K., Blanc, N. S., Studer, D., & Dubochet, J. (2004). Cryo-electron microscopy of vitreous sections. In *EMBO Journal* (Vol. 23, Issue 18). https://doi.org/10.1038/sj.emboj.7600366

Alves, K. C. S., Guimarães, J. M., de Almeida, M. E. M., & Mariúba, L. A. M. (2022). Plasmodium falciparum merozoite surface protein 3 as a vaccine candidate: a brief review. In *Revista do Instituto de Medicina Tropical de Sao Paulo* (Vol. 64). https://doi.org/10.1590/S1678-9946202264023

Anton, L., Cheng, W., Haile, M. T., Cobb, D. W., Zhu, X., Han, L., Li, E., Nair, A., Lee, C. L., Ke, H., Zhang, G., Doud, E. H., & Ho, C.-M. (2023). Multiscale effects of perturbed translation dynamics inform antimalarial design. *BioRxiv*, 2023.09.03.556115. https://doi.org/10.1101/2023.09.03.556115

Arisue, N., Kawai, S., Hirai, M., Palacpac, N. M. Q., Jia, M., Kaneko, A., Tanabe, K., & Horii, T. (2011). Clues to evolution of the SERA multigene family in 18 Plasmodium species. *PLoS ONE*, *6*(3). https://doi.org/10.1371/journal.pone.0017775

Arisue, N., Palacpac, N. M. Q., Ntege, E. H., Yeka, A., Balikagala, B., Kanoi, B. N., Bougouma, E. C., Tiono, A. B., Nebie, I., Diarra, A., Houard, S., D'Alessio, F., Leroy, O., Sirima, S. B., Egwang, T. G., & Horii, T. (2022). African-specific polymorphisms in Plasmodium falciparum serine repeat antigen 5 in Uganda and Burkina Faso clinical samples do not interfere with antibody response to BK-SE36 vaccination. *Frontiers in Cellular and Infection Microbiology*, *12*. https://doi.org/10.3389/fcimb.2022.1058081

Baldwin, M. R., Li, X., Hanada, T., Liu, S. C., & Chishti, A. H. (2015). Merozoite surface protein 1 recognition of host glycophorin a mediates malaria parasite invasion of red blood cells. *Blood*. https://doi.org/10.1182/blood-2014-11-611707

Balestra, A. C., Koussis, K., Klages, N., Howell, S. A., Flynn, H. R., Bantscheff, M., Pasquarello, C., Perrin, A. J., Brusini, L., Arboit, P., Sanz, O., Castaño, L. P. B., Withers-Martinez, C., Hainard, A., Ghidelli-Disse, S., Snijders, A. P., Baker, D. A., Blackman, M. J., & Brochet, M. (2021). Ca2+ signals critical for egress and gametogenesis in malaria parasites depend on a multipass membrane protein that interacts with PKG. *Science Advances*, *7*(13). https://doi.org/10.1126/sciadv.abe5396

Beton, J. G., Mulvaney, T., Cragnolini, T., & Topf, M. (2024). Cryo-EM structure and B-factor refinement with ensemble representation. *Nature Communications*, *15*(1). https://doi.org/10.1038/s41467-023-44593-1

Bier, E. (2022). Gene drives gaining speed. In *Nature Reviews Genetics* (Vol. 23, Issue 1). https://doi.org/10.1038/s41576-021-00386-0

Birnbaum, J., Scharf, S., Schmidt, S., Jonscher, E., Maria Hoeijmakers, W. A., Flemming, S., Toenhake, C. G., Schmitt, M., Sabitzki, R., Bergmann, B., Fröhlke, U., Mesén-Ramírez, P., Soares, A. B., Herrmann, H., Bártfai, R., & Spielmann, T. (2020). A Kelch13-defined endocytosis pathway mediates artemisinin resistance in malaria parasites. *Science*, *367*(6473). https://doi.org/10.1126/science.aax4735

Bisson, C., Hecksel, C. W., Gilchrist, J. B., & Fleck, R. A. (2021). Preparing Lamellae from Vitreous Biological Samples using a Dual-Beam Scanning Electron Microscope for Cryo-Electron Tomography. *Journal of Visualized Experiments*, *2021*(174). https://doi.org/10.3791/62350

Blackman, M. J. (2008). Malarial proteases and host cell egress: An “emerging” cascade. In *Cellular Microbiology* (Vol. 10, Issue 10, pp. 1925–1934). Wiley-Blackwell. https://doi.org/10.1111/j.1462-5822.2008.01176.x

Blackman, M. J., & Carruthers, V. B. (2013). Recent insights into apicomplexan parasite egress provide new views to a kill. In *Current Opinion in Microbiology*. https://doi.org/10.1016/j.mib.2013.04.008

Blackman, M. J., Scott-Finnigan, T. J., Shai, S., & Holder, A. A. (1994). Antibodies inhibit the protease-mediated processing of a malaria merozoite surface protein. *Journal of Experimental Medicine*, *180*(1). https://doi.org/10.1084/jem.180.1.389

Blackman, M. J., Whittle, H., & Holder, A. A. (1991). Processing of the Plasmodium falciparum major merozoite surface protein-1: identification of a 33-kilodalton secondary processing product which is shed prior to erythrocyte invasion. *Molecular and Biochemical Parasitology*, *49*(1). https://doi.org/10.1016/0166-6851(91)90128-S

Blank, A., Fürle, K., Jäschke, A., Mikus, G., Lehmann, M., Hüsing, J., Heiss, K., Giese, T., Carter, D., Böhnlein, E., Lanzer, M., Haefeli, W. E., & Bujard, H. (2020). Immunization with full-length Plasmodium falciparum merozoite surface protein 1 is safe and elicits functional cytophilic antibodies in a randomized first-in-human trial. *Npj Vaccines*, *5*(1). https://doi.org/10.1038/s41541-020-0160-2

Boddey, J. A., & Cowman, A. F. (2013). Plasmodium nesting: Remaking the erythrocyte from the inside out. *Annual Review of Microbiology*. https://doi.org/10.1146/annurev-micro-092412-155730

Boyle, M. J., Richards, J. S., Gilson, P. R., Chai, W., & Beeson, J. G. (2010). Interactions with heparin-like molecules during erythrocyte invasion by Plasmodium falciparum merozoites. *Blood*. https://doi.org/10.1182/blood-2009-09-243725

Bridgford, J. L., Xie, S. C., Cobbold, S. A., Pasaje, C. F. A., Herrmann, S., Yang, T., Gillett, D. L., Dick, L. R., Ralph, S. A., Dogovski, C., Spillman, N. J., & Tilley, L. (2018). Artemisinin kills

malaria parasites by damaging proteins and inhibiting the proteasome. *Nature Communications*. https://doi.org/10.1038/s41467-018-06221-1

Bullen, A., Taylor, R. R., Kachar, B., Moores, C., Fleck, R. A., & Forge, A. (2014). Inner ear tissue preservation by rapid freezing: Improving fixation by high-pressure freezing and hybrid methods. *Hearing Research*, *315*. https://doi.org/10.1016/j.heares.2014.06.006

Callan-Jones, A., Albarran Arriagada, O. E., Massiera, G., Lorman, V., & Abkarian, M. (2012). Red blood cell membrane dynamics during malaria parasite egress. *Biophysical Journal*. https://doi.org/10.1016/j.bpj.2012.11.008

Carroni, M., & Saibil, H. R. (2016). Cryo electron microscopy to determine the structure of macromolecular complexes. In *Methods* (Vol. 95). https://doi.org/10.1016/j.ymeth.2015.11.023

Chaccour, C., Lines, J., & Whitty, C. J. M. (2010). Effect of ivermectin on Anopheles gambiae mosquitoes fed on humans: The potential of oral insecticides in malaria control. *Journal of Infectious Diseases*. https://doi.org/10.1086/653208

Chandramohanadas, R., Davis, P. H., Beiting, D. P., Harbut, M. B., Darling, C., Velmourougane, G., Lee, M. Y., Greer, P. A., Roos, D. S., & Greenbaum, D. C. (2009). Apicomplexan parasites co-opt host calpains to facilitate their escape from infected cells. *Science*. https://doi.org/10.1126/science.1171085

Child, M. A., Epp, C., Bujard, H., & Blackman, M. J. (2010). Regulated maturation of malaria merozoite surface protein-1 is essential for parasite growth. *Molecular Microbiology*. https://doi.org/10.1111/j.1365-2958.2010.07324.x

Chitnis, C. E., Mukherjee, P., Mehta, S., Yazdani, S. S., Dhawan, S., Shakri, A. R., Bharadwaj, R., Gupta, P. K., Hans, D., Mazumdar, S., Singh, B., Kumar, S., Pandey, G., Parulekar, V., Imbault, N., Shivyogi, P., Godbole, G., Mohan, K., Leroy, O., … Chauhan, V. S. (2015). Phase I clinical trial of a recombinant blood stage vaccine candidate for Plasmodium falciparum malaria based on MSP1 and EBA175. *PLoS ONE*, *10*(4). https://doi.org/10.1371/journal.pone.0117820

Collins, C. R., Das, S., Wong, E. H., Andenmatten, N., Stallmach, R., Hackett, F., Herman, J. P., Müller, S., Meissner, M., & Blackman, M. J. (2013). Robust inducible Cre recombinase activity in the human malaria parasite Plasmodium falciparum enables efficient gene deletion within a single asexual erythrocytic growth cycle. *Molecular Microbiology*, *88*(4). https://doi.org/10.1111/mmi.12206

Collins, C. R., Hackett, F., Atid, J., Tan, M. S. Y., & Blackman, M. J. (2017). The Plasmodium falciparum pseudoprotease SERA5 regulates the kinetics and efficiency of malaria parasite egress from host erythrocytes. *PLoS Pathogens*. https://doi.org/10.1371/journal.ppat.1006453

Collins, C. R., Hackett, F., Howell, S. A., Snijders, A. P., Russell, M. R., Collinson, L. M., & Blackman, M. J. (2020). The malaria parasite sheddase sub2 governs host red blood cell membrane sealing at invasion. *ELife*. https://doi.org/10.7554/ELIFE.61121

Collins, C. R., Hackett, F., Strath, M., Penzo, M., Withers-Martinez, C., Baker, D. A., & Blackman, M. J. (2013a). Malaria Parasite cGMP-dependent Protein Kinase Regulates Blood Stage Merozoite Secretory Organelle Discharge and Egress. *PLOS Pathogens*, *9*(5), e1003344. https://doi.org/10.1371/JOURNAL.PPAT.1003344

Cooper, R. A. (2002). SDS-PAGE and Western Blotting of Plasmodium falciparum Proteins. In *Malaria Methods and Protocols, Methods in Molecular Medicine™* (Vol. 72, pp. 177–188). Humana Press. https://doi.org/10.1385/1-59259-271-6:177

Cowman, A. F., Berry, D., & Baum, J. (2012). The cellular and molecular basis for malaria parasite invasion of the human red blood cell. *Journal of Cell Biology*. https://doi.org/10.1083/jcb.201206112

Cowman, A. F., & Crabb, B. S. (2006). Invasion of red blood cells by malaria parasites. In *Cell*. https://doi.org/10.1016/j.cell.2006.02.006

Cowman, A. F., Healer, J., Marapana, D., & Marsh, K. (2016). Malaria: Biology and Disease. In *Cell*. https://doi.org/10.1016/j.cell.2016.07.055

Cowman, A. F., Tonkin, C. J., Tham, W. H., & Duraisingh, M. T. (2017). The Molecular Basis of Erythrocyte Invasion by Malaria Parasites. In *Cell Host and Microbe*. https://doi.org/10.1016/j.chom.2017.07.003

Cox, J., & Mann, M. (2008). MaxQuant enables high peptide identification rates, individualized p.p.b.-range mass accuracies and proteome-wide protein quantification. *Nature Biotechnology*, *26*(12). https://doi.org/10.1038/nbt.1511

Croll, T. I. (2018). ISOLDE: A physically realistic environment for model building into low-resolution electron-density maps. *Acta Crystallographica Section D: Structural Biology*, *74*(6). https://doi.org/10.1107/S2059798318002425

Crosnier, C., Wanaguru, M., McDade, B., Osier, F. H., Marsh, K., Rayner, J. C., & Wright, G. J. (2013). A library of functional recombinant cell-surface and secreted p. Falciparum merozoite proteins. *Molecular and Cellular Proteomics*. https://doi.org/10.1074/mcp.O113.028357

Das, S., Hertrich, N., Perrin, A. J., Treeck, M., Epp, C., & Blackman, M. J. (2015). Processing of Plasmodium falciparum Merozoite Surface Protein MSP1 Activates a Spectrin-Binding Function Enabling Parasite Egress from RBCs. *Cell Host and Microbe*, *18*, 433–444. https://doi.org/10.1016/j.chom.2015.09.007

Das, S., Kar, A., Manna, S., Mandal, S., Mandal, S., Das, S., Saha, B., & Hati, A. K. (2021). Artemisinin combination therapy fails even in the absence of Plasmodium falciparum kelch13 gene polymorphism in Central India. *Scientific Reports*, *11*(1). https://doi.org/10.1038/s41598-021-89295-0

Dasgupta, S., Auth, T., Gov, N. S., Satchwell, T. J., Hanssen, E., Zuccala, E. S., Riglar, D. T., Toye, A. M., Betz, T., Baum, J., & Gompper, G. (2014). Membrane-wrapping contributions to malaria parasite invasion of the human erythrocyte. *Biophysical Journal*. https://doi.org/10.1016/j.bpj.2014.05.024

Datoo, M. S., Natama, M. H., Somé, A., Traoré, O., Rouamba, T., Bellamy, D., Yameogo, P., Valia, D., Tegneri, M., Ouedraogo, F., Soma, R., Sawadogo, S., Sorgho, F., Derra, K., Rouamba, E., Orindi, B., Ramos Lopez, F., Flaxman, A., Cappuccini, F., … Tinto, H. (2021). Efficacy of a low-dose candidate malaria vaccine, R21 in adjuvant Matrix-M, with seasonal administration to children in Burkina Faso: a randomised controlled trial. *The Lancet*, *397*(10287). https://doi.org/10.1016/S0140-6736(21)00943-0

Dawn, A., Singh, S., More, K. R., Siddiqui, F. A., Pachikara, N., Ramdani, G., Langsley, G., & Chitnis, C. E. (2014). The Central Role of cAMP in Regulating Plasmodium falciparum Merozoite Invasion of Human Erythrocytes. *PLoS Pathogens*, *10*(12). https://doi.org/10.1371/journal.ppat.1004520

De Monerri, N. C. S., Flynn, H. R., Campos, M. G., Hackett, F., Koussis, K., Withers-Martinez, C., Skehel, J. M., & Blackman, M. J. (2011). Global identification of multiple substrates for Plasmodium falciparum SUB1, an essential malarial processing protease. *Infection and Immunity*. https://doi.org/10.1128/IAI.00902-10

Demas, A. R., Sharma, A. I., Wong, W., Early, A. M., Redmond, S., Bopp, S., Neafsey, D. E., Volkman, S. K., Hartl, D. L., & Wirth, D. F. (2018). Mutations in plasmodium falciparum actin-binding protein coronin confer reduced artemisinin susceptibility. *Proceedings of the National Academy of Sciences of the United States of America*, *115*(50). https://doi.org/10.1073/pnas.1812317115

Dicko, A., Ouedraogo, J.-B., Zongo, I., Sagara, I., Cairns, M., Yerbanga, R. S., Issiaka, D., Zoungrana, C., Sidibe, Y., Tapily, A., Nikièma, F., Sompougdou, F., Sanogo, K., Kaya, M., Yalcouye, H., Dicko, O. M., Diarra, M., Diarra, K., Thera, I., … Greenwood, B. (2023). Seasonal vaccination with RTS,S/AS01E vaccine with or without seasonal malaria chemoprevention in children up to the age of 5 years in Burkina Faso and Mali: a double-blind, randomised, controlled, phase 3 trial. *The Lancet Infectious Diseases*. https://doi.org/10.1016/s1473-3099(23)00368-7

Dijkman, P. M., Marzluf, T., Zhang, Y., Chang, S. Y. S., Helm, D., Lanzer, M., Bujard, H., & Kudryashev, M. (2021b). Structure of the merozoite surface protein 1 from Plasmodium falciparum. *Science Advances*. https://doi.org/10.1126/sciadv.abg0465

Dvorin, J. D., Martyn, D. C., Patel, S. D., Grimley, J. S., Collins, C. R., Hopp, C. S., Bright, A. T., Westenberger, S., Winzeler, E., Blackman, M. J., Baker, D. A., Wandless, T. J., & Duraisingh, M. T. (2010). A plant-like kinase in plasmodium falciparum regulates parasite egress from erythrocytes. *Science*. https://doi.org/10.1126/science.1188191

Frénal, K., Polonais, V., Marq, J. B., Stratmann, R., Limenitakis, J., & Soldati-Favre, D. (2010). Functional dissection of the apicomplexan glideosome molecular architecture. *Cell Host and Microbe*. https://doi.org/10.1016/j.chom.2010.09.002

Garg, S., Agarwal, S., Kumar, S., Shams Yazdani, S., Chitnis, C. E., & Singh, S. (2013). Calcium-dependent permeabilization of erythrocytes by a perforin-like protein during egress of malaria parasites. *Nature Communications*. https://doi.org/10.1038/ncomms2725

Garg, S., Shivappagowdar, A., Hada, R. S., Ayana, R., Bathula, C., Sen, S., Kalia, I., Pati, S., Singh, A. P., & Singh, S. (2020). Plasmodium Perforin-Like Protein Pores on the Host Cell Membrane Contribute in Its Multistage Growth and Erythrocyte Senescence. *Frontiers in Cellular and Infection Microbiology*. https://doi.org/10.3389/fcimb.2020.00121

Ghorbal, M., Gorman, M., MacPherson, C. R., Martins, R. M., Scherf, A., & Lopez-Rubio, J. J. (2014). Genome editing in the human malaria parasite Plasmodium falciparum using the CRISPR-Cas9 system. *Nature Biotechnology*, *32*(8). https://doi.org/10.1038/nbt.2925

Glushakova, S., Beck, J. R., Garten, M., Busse, B. L., Nasamu, A. S., Tenkova-Heuser, T., Heuser, J., Goldberg, D. E., & Zimmerberg, J. (2018). Rounding precedes rupture and breakdown of vacuolar membranes minutes before malaria parasite egress from erythrocytes. *Cellular Microbiology*. https://doi.org/10.1111/cmi.12868

Glushakova, S., Lizunov, V., Blank, P. S., Melikov, K., Humphrey, G., & Zimmerberg, J. (2013). Cytoplasmic free Ca2+ is essential for multiple steps in malaria parasite egress from infected erythrocytes. *Malaria Journal*. https://doi.org/10.1186/1475-2875-12-41

Glushakova, S., Yin, D., Gartner, N., & Zimmerberg, J. (2007). Quantification of malaria parasite release from infected erythrocytes: Inhibition by protein-free media. *Malaria Journal*, *6*. https://doi.org/10.1186/1475-2875-6-61

Glushakova, S., Yin, D., Li, T., & Zimmerberg, J. (2005). Membrane transformation during malaria parasite release from human red blood cells. *Current Biology*, *15*(18). https://doi.org/10.1016/j.cub.2005.07.067

Gondeau, C., Corradin, G., Heitz, F., Le Peuch, C., Balbo, A., Schuck, P., & Kajava, A. V. (2009). The C-terminal domain of Plasmodium falciparum merozoite surface protein 3 self-assembles into α-helical coiled coil tetramer. *Molecular and Biochemical Parasitology*, *165*(2). https://doi.org/10.1016/j.molbiopara.2009.01.015

Hale, V. L., Watermeyer, J. M., Hackett, F., Vizcay-Barrena, G., Van Ooij, C., Thomas, J. A., Spink, M. C., Harkiolaki, M., Duke, E., Fleck, R. A., Blackman, M. J., & Saibil, H. R. (2017). Parasitophorous vacuole poration precedes its rupture and rapid host erythrocyte cytoskeleton collapse in Plasmodium falciparum egress. *Proceedings of the National Academy of Sciences of the United States of America*. https://doi.org/10.1073/pnas.1619441114

Hanboonkunupakarn, B., Tarning, J., Pukrittayakamee, S., & Chotivanich, K. (2022). Artemisinin resistance and malaria elimination: Where are we now? In *Frontiers in Pharmacology* (Vol. 13). https://doi.org/10.3389/fphar.2022.876282

Hanspal, M., Goel, V. K., Oh, S. S., & Chishti, A. H. (2002). Erythrocyte calpain is dispensable for malaria parasite invasion and growth. *Molecular and Biochemical Parasitology*. https://doi.org/10.1016/S0166-6851(02)00104-4

Harris, P. K., Yeoh, S., Dluzewski, A. R., O'Donnell, R. A., Withers-Martinez, C., Hackett, F., Bannister, L. H., Mitchell, G. H., & Blackman, M. J. (2005). Molecular identification of a malaria merozoite surface sheddase. *PLoS Pathogens*. https://doi.org/10.1371/journal.ppat.0010029

Hell, S. W., Sahl, S. J., Bates, M., & Levin, B. D. A. (2021). Direct detectors and their applications in electron microscopy for materials science. *J. Phys. Mater*, *4*, 42005. https://doi.org/10.1088/2515-7639/ac0ff9

Ho, C. M., Beck, J. R., Lai, M., Cui, Y., Goldberg, D. E., Egea, P. F., & Zhou, Z. H. (2018). Malaria parasite translocon structure and mechanism of effector export. *Nature*, *561*(7721). https://doi.org/10.1038/s41586-018-0469-4

Hodder, A. N., Czabotar, P. E., Uboldi, A. D., Clarke, O. B., Lin, C. S., Healer, J., Smith, B. J., & Cowman, A. F. (2012). Insights into duffy binding-like domains through the crystal structure and function of the merozoite surface protein MSPDBL2 from Plasmodium falciparum. *Journal of Biological Chemistry*, *287*(39). https://doi.org/10.1074/jbc.M112.350504

Hoermann, A., Habtewold, T., Selvaraj, P., Del Corsano, G., Capriotti, P., Inghilterra, M. G., Kebede, T. M., Christophides, G. K., & Windbichler, N. (2022). Gene drive mosquitoes can aid malaria elimination by retarding Plasmodium sporogonic development. *Science Advances*, *8*(38). https://doi.org/10.1126/sciadv.abo1733

Holder, A. A., & Freeman, R. R. (1982). Biosynthesis and processing of a Plasmodium Falciparum schizont antigen recognized by immune serum and a monoclonal antibody. *Journal of Experimental Medicine*, *156*(5). https://doi.org/10.1084/jem.156.5.1528

Holder, A. A., Lockyer, M. J., Odink, K. G., Sandhu, J. S., Riveros-Moreno, V., Nicholls, S. C., Hillman, Y., Davey, L. S., Tizard, M. L. V., Schwarz, R. T., & Freeman, R. R. (1985). Primary structure of the precursor to the three major surface antigens of Plasmodium falciparum merozoites. *Nature*, *317*(6034). https://doi.org/10.1038/317270a0

Iyer, G. R., Singh, S., Kaur, I., Agarwal, S., Siddiqui, M. A., Bansal, A., Kumar, G., Saini, E., Paul, G., Mohmmed, A., Chitnis, C. E., & Malhotra, P. (2018). Calcium-dependent phosphorylation of Plasmodium falciparum serine repeat antigen 5 triggers merozoite egress. *Journal of Biological Chemistry*. https://doi.org/10.1074/jbc.RA117.001540

Jumper, J., Evans, R., Pritzel, A., Green, T., Figurnov, M., Ronneberger, O., Tunyasuvunakool, K., Bates, R., Žídek, A., Potapenko, A., Bridgland, A., Meyer, C., Kohl, S. A. A., Ballard, A. J., Cowie, A., Romera-Paredes, B., Nikolov, S., Jain, R., Adler, J., … Hassabis, D. (2021). Highly accurate protein structure prediction with AlphaFold. *Nature*, *596*(7873). https://doi.org/10.1038/s41586-021-03819-2

Kadekoppala, M., & Holder, A. A. (2010). Merozoite surface proteins of the malaria parasite: The MSP1 complex and the MSP7 family. In *International Journal for Parasitology* (Vol. 40, Issue 10). https://doi.org/10.1016/j.ijpara.2010.04.008

Kadekoppala, M., O'Donnell, R. A., Grainger, M., Crabb, B. S., & Holder, A. A. (2008). Deletion of the Plasmodium falciparum merozoite surface protein 7 gene impairs parasite invasion of erythrocytes. *Eukaryotic Cell*, *7*(12). https://doi.org/10.1128/EC.00274-08

Kadekoppala, M., Ogun, S. A., Howell, S., Gunaratne, R. S., & Holder, A. A. (2010). Systematic genetic analysis of the Plasmodium falciparum MSP7-like family reveals differences in protein expression, location, and importance in asexual growth of the blood-stage parasite. *Eukaryotic Cell*, *9*(7). https://doi.org/10.1128/EC.00048-10

Karunamoorthi, K. (2011). Vector control: A cornerstone in the malaria elimination campaign. In *Clinical Microbiology and Infection*. https://doi.org/10.1111/j.1469-0691.2011.03664.x

Kauth, C. W., Epp, C., Bujard, H., & Lutz, R. (2003a). The merozoite surface protein 1 complex of human malaria parasite Plasmodium falciparum: Interactions and arrangements of subunits. *Journal of Biological Chemistry*. https://doi.org/10.1074/jbc.M302299200

Kauth, C. W., Epp, C., Bujard, H., & Lutz, R. (2003b). The merozoite surface protein 1 complex of human malaria parasite Plasmodium falciparum: Interactions and arrangements of subunits. *Journal of Biological Chemistry*. https://doi.org/10.1074/jbc.M302299200

Kauth, C. W., Woehlbier, U., Kern, M., Mekonnen, Z., Lutz, R., Mu¨cke, N., Langowski, J., & Bujard, H. (2006). Interactions between Merozoite Surface Proteins 1, 6, and 7 of the Malaria Parasite Plasmodium falciparum. *Journal of Biological Chemistry*, *281*(42), 31517–31527. https://doi.org/10.1016/S0021-9258(19)84065-6

Knuepfer, E., Napiorkowska, M., Van Ooij, C., & Holder, A. A. (2017). Generating conditional gene knockouts in Plasmodium - A toolkit to produce stable DiCre recombinase-expressing parasite lines using CRISPR/Cas9. *Scientific Reports*, *7*(1). https://doi.org/10.1038/s41598-017-03984-3

Koussis, K., Withers-Martinez, C., Baker, D. A., & Blackman, M. J. (2020). Simultaneous multiple allelic replacement in the malaria parasite enables dissection of PKG function. *Life Science Alliance*. https://doi.org/10.26508/LSA.201900626

Koussis, K., Withers-Martinez, C., Yeoh, S., Child, M., Hackett, F., Knuepfer, E., Juliano, L., Woehlbier, U., Bujard, H., & Blackman, M. J. (2009). A multifunctional serine protease primes the malaria parasite for red blood cell invasion. *The EMBO Journal*, *28*(6), 725. https://doi.org/10.1038/EMBOJ.2009.22

Laurens, M. B. (2019). RTS,S/AS01 vaccine (Mosquirix^{TM}): an overview. *Human Vaccines and Immunotherapeutics*. https://doi.org/10.1080/21645515.2019.1669415

Lew, V. L., Hockaday, A., Freeman, C. J., & Bookchin, R. M. (1988). Mechanism of spontaneous inside-out vesiculation of red cell membranes. *Journal of Cell Biology*, *106*(6). https://doi.org/10.1083/jcb.106.6.1893

Li, B., Zhu, D., Shi, H., & Zhang, X. (2021). Effect of charge on protein preferred orientation at the air–water interface in cryo-electron microscopy. *Journal of Structural Biology*, *213*(4). https://doi.org/10.1016/j.jsb.2021.107783

Li, J., Mitamura, T., Fox, B. A., Bzik, D. J., & Horii, T. (2002). Differential localization of processed fragments of Plasmodium falciparum serine repeat antigen and further processing of its N-terminal 47 kDa fragment. *Parasitology International*, *51*(4). https://doi.org/10.1016/S1383-5769(02)00042-9

Liebschner, D., Afonine, P. V., Baker, M. L., Bunkoczi, G., Chen, V. B., Croll, T. I., Hintze, B., Hung, L. W., Jain, S., McCoy, A. J., Moriarty, N. W., Oeffner, R. D., Poon, B. K., Prisant, M. G., Read, R. J., Richardson, J. S., Richardson, D. C., Sammito, M. D., Sobolev, O. V., … Adams, P. D. (2019). Macromolecular structure determination using X-rays, neutrons and electrons: recent developments in Phenix. *Acta Crystallographica. Section D, Structural Biology*, *75*(Pt 10), 861–877. https://doi.org/10.1107/S2059798319011471

Lin, C. S., Uboldi, A. D., Epp, C., Bujard, H., Tsuboi, T., Czabotar, P. E., & Cowman, X. A. F. (2016). Multiple plasmodium falciparum merozoite surface protein 1 complexes mediate merozoite binding to human erythrocytes. *Journal of Biological Chemistry*. https://doi.org/10.1074/jbc.M115.698282

Lin, C. S., Uboldi, A. D., Marapana, D., Czabotar, P. E., Epp, C., Bujard, H., Taylor, N. L., Perugini, M. A., Hodder, A. N., & Cowman, A. F. (2014). The merozoite surface protein 1 complex is a platform for binding to human erythrocytes by plasmodium falciparum. *Journal of Biological Chemistry*. https://doi.org/10.1074/jbc.M114.586495

Liu, N. (2015). Insecticide resistance in mosquitoes: Impact, mechanisms, and research directions. In *Annual Review of Entomology*. https://doi.org/10.1146/annurev-ento-010814-020828

Lyon, J. A., Thomas, A. W., Hall, T., & Chulay, J. D. (1989). Specificities of antibodies that inhibit merozoite dispersal from malaria-infected erythrocytes. *Molecular and Biochemical Parasitology*, *36*(1). https://doi.org/10.1016/0166-6851(89)90203-X

Matz, J. M., Beck, J. R., & Blackman, M. J. (2020). The parasitophorous vacuole of the blood-stage malaria parasite. In *Nature Reviews Microbiology*. https://doi.org/10.1038/s41579-019-0321-3

McHugh, E., Carmo, O. M. S., Blanch, A., Looker, O., Liu, B., Tiash, S., Andrew, D., Batinovic, S., Low, A. J. Y., Cho, H. J., McMillan, P., Tilley, L., & Dixon, M. W. A. (2020). Role of plasmodium falciparum protein GEXP07 in Maurer's Cleft morphology, Knob architecture, and P. Falciparum EMP1 trafficking. *MBio*, *11*(2). https://doi.org/10.1128/mBio.03320-19

Miller, S. K., Good, R. T., Drew, D. R., Delorenzi, M., Sanders, P. R., Hodder, A. N., Speed, T. P., Cowman, A. F., De Koning-Ward, T. F., & Crabb, B. S. (2002). A subset of Plasmodium falciparum SERA genes are expressed and appear to play an important role in the erythrocytic cycle. *Journal of Biological Chemistry*, *277*(49). https://doi.org/10.1074/jbc.M206974200

Mnzava, A., Monroe, A. C., & Okumu, F. (2022). Anopheles stephensi in Africa requires a more integrated response. In *Malaria Journal* (Vol. 21, Issue 1). https://doi.org/10.1186/s12936-022-04197-4

Morgan, W. D., Birdsall, B., Frenkiel, T. A., Gradwell, M. G., Burghaus, P. A., Syed, S. E. H., Uthaipibull, C., Holder, A. A., & Feeney, J. (1999). Solution structure of an EGF module pair from the Plasmodium falciparum merozoite surface protein 1. *Journal of Molecular Biology*. https://doi.org/10.1006/jmbi.1999.2753

Morotti, A. L. M., Martins-Teixeira, M. B., & Carvalho, I. (2017). Protozoan Parasites Glycosylphosphatidylinositol Anchors: Structures, Functions and Trends for Drug Discovery. *Current Medicinal Chemistry*, *26*(23). https://doi.org/10.2174/0929867324666170727110801

Moss, D. K., Remarque, E. J., Faber, B. W., Cavanagh, D. R., Arnot, D. E., Thomas, A. W., & Holder, A. A. (2012). Plasmodium falciparum 19-kilodalton merozoite surface protein 1 (MSP1)-specific antibodies that interfere with parasite growth In Vitro can inhibit MSP1 processing, merozoite invasion, and intracellular parasite development. *Infection and Immunity*. https://doi.org/10.1128/IAI.05887-11

Mukherjee, A., Bopp, S., Magistrado, P., Wong, W., Daniels, R., Demas, A., Schaffner, S., Amaratunga, C., Lim, P., Dhorda, M., Miotto, O., Woodrow, C., Ashley, E. A., Dondorp, A. M., White, N. J., Wirth, D., Fairhurst, R., & Volkman, S. K. (2017). Artemisinin resistance without pfkelch13 mutations in Plasmodium falciparum isolates from Cambodia. *Malaria Journal*, *16*(1). https://doi.org/10.1186/s12936-017-1845-5

Nasamu, A. S., Glushakova, S., Russo, I., Vaupel, B., Oksman, A., Kim, A. S., Fremont, D. H., Tolia, N., Beck, J. R., Meyers, M. J., Niles, J. C., Zimmerberg, J., & Goldberg, D. E. (2017). Plasmepsins IX and X are essential and druggable mediators of malaria parasite egress and invasion. *Science*. https://doi.org/10.1126/science.aan1478

Nofal, S. D., Patel, A., Blackman, M. J., Flueck, C., & Baker, D. A. (2021). Plasmodium falciparum guanylyl cyclase-alpha and the activity of its appended P4-ATPase domain are essential for cGMP synthesis and blood-stage egress. *MBio*. https://doi.org/10.1128/mBio.02694-20

Ogutu, B. R., Apollo, O. J., McKinney, D., Okoth, W., Siangla, J., Dubovsky, F., Tucker, K., Waitumbi, J. N., Diggs, C., Wittes, J., Malkin, E., Leach, A., Soisson, L. A., Milman, J. B., Otieno, L., Holland, C. A., Polhemus, M., Remich, S. A., Ockenhouse, C. F., … Withers, M. R. (2009). Blood stage malaria vaccine eliciting high antigen-specific antibody concentrations confers no protection to young children in Western Kenya. *PLoS ONE*, *4*(3). https://doi.org/10.1371/journal.pone.0004708

Orlova, E. V., & Saibil, H. R. (2011). Structural Analysis of Macromolecular Assemblies by Electron Microscopy. *Chemical Reviews*, *111*(12), 7710. https://doi.org/10.1021/CR100353T

Ouji, M., Augereau, J. M., Paloque, L., & Benoit-Vical, F. (2018). Plasmodium falciparum resistance to artemisinin-based combination therapies: A sword of Damocles in the path toward malaria elimination. In *Parasite*. https://doi.org/10.1051/parasite/2018021

Ouyang, L., Shaik, R., Xu, R., Zhang, G., & Zhe, J. (2021). Mapping surface charge distribution of single-cell via charged nanoparticle. *Cells*, *10*(6). https://doi.org/10.3390/cells10061519

Pachebat, J. A., Kadekoppala, M., Grainger, M., Dluzewski, A. R., Gunaratne, R. S., Scott-Finnigan, T. J., Ogun, S. A., Ling, I. T., Bannister, L. H., Taylor, H. M., Mitchell, G. H., & Holder, A. A. (2007). Extensive proteolytic processing of the malaria parasite merozoite surface protein 7 during biosynthesis and parasite release from erythrocytes. *Molecular and Biochemical Parasitology*, *151*(1). https://doi.org/10.1016/j.molbiopara.2006.10.006

Paul, A. S., Miliu, A., Paulo, J. A., Goldberg, J. M., Bonilla, A. M., Berry, L., Seveno, M., Braun-Breton, C., Kosber, A. L., Elsworth, B., Arriola, J. S. N., Lebrun, M., Gygi, S. P., Lamarque, M. H., & Duraisingh, M. T. (2020). Co-option of Plasmodium falciparum PP1 for egress

from host erythrocytes. *Nature Communications*. https://doi.org/10.1038/s41467-020-17306-1

Paul, A. S., Saha, S., Engelberg, K., Jiang, R. H. Y., Coleman, B. I., Kosber, A. L., Chen, C. T., Ganter, M., Espy, N., Gilberger, T. W., Gubbels, M. J., & Duraisingh, M. T. (2015). Parasite calcineurin regulates host cell recognition and attachment by apicomplexans. *Cell Host and Microbe*. https://doi.org/10.1016/j.chom.2015.06.003

Perrin, A. J., Bisson, C., Faull, P. A., Renshaw, M. J., Lees, R. A., Fleck, R. A., Saibil, H. R., Snijders, A. P., Baker, D. A., & Blackman, M. J. (2021). Malaria parasite schizont egress antigen-1 plays an essential role in nuclear segregation during schizogony. *MBio*, *12*(2). https://doi.org/10.1128/mBio.03377-20

Perrin, A. J., Collins, C. R., Russell, M. R. G., Collinson, L. M., Baker, D. A., & Blackman, M. J. (2018). The actinomyosin motor drives malaria parasite red blood cell invasion but not egress. *MBio*. https://doi.org/10.1128/mBio.00905-18

Pettersen, E. F., Goddard, T. D., Huang, C. C., Meng, E. C., Couch, G. S., Croll, T. I., Morris, J. H., & Ferrin, T. E. (2021). UCSF ChimeraX: Structure visualization for researchers, educators, and developers. *Protein Science*, *30*(1). https://doi.org/10.1002/pro.3943

Pino, P., Caldelari, R., Mukherjee, B., Vahokoski, J., Klages, N., Maco, B., Collins, C. R., Blackman, M. J., Kursula, I., Heussler, V., Brochet, M., & Soldati-Favre, D. (2017). A multistage antimalarial targets the plasmepsins IX and X essential for invasion and egress. *Science*. https://doi.org/10.1126/science.aaf8675

Pizarro, J. C., Chitarra, V., Verger, D., Holm, I., Pêtres, S., Dartevelle, S., Nato, F., Longacre, S., & Bentley, G. A. (2003). Crystal structure of a Fab complex formed with PfMSP1-19, the C-terminal fragment of merozoite surface protein 1 from Plasmodium falciparum: A malaria vaccine candidate. *Journal of Molecular Biology*. https://doi.org/10.1016/S0022-2836(03)00376-0

Punjani, A., Rubinstein, J. L., Fleet, D. J., & Brubaker, M. A. (2017). cryoSPARC: algorithms for rapid unsupervised cryo-EM structure determination. *Nature Methods 2017 14:3*, *14*(3), 290–296. https://doi.org/10.1038/nmeth.4169

Ramaprasad, A., Burda, P. C., Koussis, K., Thomas, J. A., Pietsch, E., Calvani, E., Howell, S. A., MacRae, J. I., Snijders, A. P., Gilberger, T. W., & Blackman, M. J. (2023). A malaria parasite phospholipase facilitates efficient asexual blood stage egress. *PLoS Pathogens*, *19*(6). https://doi.org/10.1371/journal.ppat.1011449

Rohou, A., & Grigorieff, N. (2015). CTFFIND4: Fast and accurate defocus estimation from electron micrographs. *Journal of Structural Biology*, *192*(2), 216–221. https://doi.org/10.1016/J.JSB.2015.08.008

Rosenthal, P. J. (2021). Has artemisinin resistance emerged in Africa? In *The Lancet Infectious Diseases* (Vol. 21, Issue 8). https://doi.org/10.1016/S1473-3099(21)00168-7

Rudlaff, R. M., Kraemer, S., Marshman, J., & Dvorin, J. D. (2020). Three-dimensional ultrastructure of Plasmodium falciparum throughout cytokinesis. *PLoS Pathogens*. https://doi.org/10.1371/journal.ppat.1008587

Rudlaff, R. M., Kraemer, S., Streva, V. A., & Dvorin, J. D. (2019). An essential contractile ring protein controls cell division in Plasmodium falciparum. *Nature Communications*. https://doi.org/10.1038/s41467-019-10214-z

Ruecker, A., Shea, M., Hackett, F., Suarez, C., Hirst, E. M. A., Milutinovic, K., Withers-Martinez, C., & Blackman, M. J. (2012). Proteolytic activation of the essential parasitophorous vacuole cysteine protease SERA6 accompanies malaria parasite egress

from its host erythrocyte. *Journal of Biological Chemistry*. https://doi.org/10.1074/jbc.M112.400820

Saini, E., Sheokand, P. K., Sharma, V., Agrawal, P., Kaur, I., Singh, S., Mohmmed, A., & Malhotra, P. (2021). Plasmodium falciparum PhIL1-associated complex plays an essential role in merozoite reorientation and invasion of host erythrocytes. In *PLoS Pathogens* (Vol. 17, Issue 7). https://doi.org/10.1371/journal.ppat.1009750

Sajid, M., Withers-Martinez, C., & Blackman, M. J. (2000). Maturation and specificity of Plasmodium falciparum subtilisin-like protease-1, a malaria merozoite subtilisin-like serine protease. *Journal of Biological Chemistry*. https://doi.org/10.1074/jbc.275.1.631

Srinivasan, P., Yasgar, A., Luci, D. K., Beatty, W. L., Hu, X., Andersen, J., Narum, D. L., Moch, J. K., Sun, H., Haynes, J. D., Maloney, D. J., Jadhav, A., Simeonov, A., & Miller, L. H. (2013). Disrupting malaria parasite AMA1-RON2 interaction with a small molecule prevents erythrocyte invasion. *Nature Communications*. https://doi.org/10.1038/ncomms3261

Stallmach, R., Kavishwar, M., Withers-Martinez, C., Hackett, F., Collins, C. R., Howell, S. A., Yeoh, S., Knuepfer, E., Atid, A. J., Holder, A. A., & Blackman, M. J. (2015). Plasmodium falciparum SERA5 plays a non-enzymatic role in the malarial asexual blood-stage lifecycle. *Molecular Microbiology*. https://doi.org/10.1111/mmi.12941

Tan, M. S. Y., Koussis, K., Withers-Martinez, C., Howell, S. A., Thomas, J. A., Hackett, F., Knuepfer, E., Shen, M., Hall, M. D., Snijders, A. P., & Blackman, M. J. (2021). Autocatalytic activation of a malarial egress protease is druggable and requires a protein cofactor. *The EMBO Journal*, *40*(11). https://doi.org/10.15252/embj.2020107226

Taylor, H. M., McRobert, L., Grainger, M., Sicard, A., Dluzewski, A. R., Hopp, C. S., Holder, A. A., & Baker, D. A. (2010). The malaria parasite cyclic GMP-dependent protein kinase plays a central role in blood-stage schizogony. *Eukaryotic Cell*. https://doi.org/10.1128/EC.00186-09

Thomas, J. A., Tan, M. S. Y., Bisson, C., Borg, A., Umrekar, T. R., Hackett, F., Hale, V. L., Vizcay-Barrena, G., Fleck, R. A., Snijders, A. P., Saibil, H. R., & Blackman, M. J. (2018). A protease cascade regulates release of the human malaria parasite Plasmodium falciparum from host red blood cells. *Nature Microbiology*. https://doi.org/10.1038/s41564-018-0111-0

Tilley, L., li, J., Shami, G., Cho, E., Liffner, B., Braet, F., Absalon, S., & Dixon, M. (2023). *Plasmodium falciparum kinetochore proteins stabilise a nexus between the mitotic apparatus and the apical complex*. https://doi.org/10.21203/rs.3.rs-3404985/v1

Tougan, T., Edula, J. R., Takashima, E., Morita, M., Shinohara, M., Shinohara, A., Tsuboi, T., & Horii, T. (2018). Molecular Camouflage of Plasmodium falciparum Merozoites by Binding of Host Vitronectin to P47 Fragment of SERA5. *Scientific Reports*, *8*(1). https://doi.org/10.1038/s41598-018-23194-9

Tukwasibwe, S., Mboowa, G., Sserwadda, I., Nankabirwa, J. I., Arinaitwe, E., Ssewanyana, I., Taremwa, Y., Tumusiime, G., Kamya, M. R., Jagannathan, P., & Nakimuli, A. (2023). Impact of high human genetic diversity in Africa on immunogenicity and efficacy of RTS,S/AS01 vaccine. In *Immunogenetics* (Vol. 75, Issue 3). https://doi.org/10.1007/s00251-023-01306-8

Tyanova, S., Temu, T., Sinitcyn, P., Carlson, A., Hein, M. Y., Geiger, T., Mann, M., & Cox, J. (2016). The Perseus computational platform for comprehensive analysis of (prote)omics data. In *Nature Methods* (Vol. 13, Issue 9). https://doi.org/10.1038/nmeth.3901

Wagner, T., Merino, F., Stabrin, M., Moriya, T., Antoni, C., Apelbaum, A., Hagel, P., Sitsel, O., Raisch, T., Prumbaum, D., Quentin, D., Roderer, D., Tacke, S., Siebolds, B., Schubert, E., Shaikh, T. R., Lill, P., Gatsogiannis, C., & Raunser, S. (2019). SPHIRE-crYOLO is a fast and accurate fully automated particle picker for cryo-EM. *Communications Biology 2019 2:1*, *2*(1), 1–13. https://doi.org/10.1038/s42003-019-0437-z

Wang, G. H., Gamez, S., Raban, R. R., Marshall, J. M., Alphey, L., Li, M., Rasgon, J. L., & Akbari, O. S. (2021). Combating mosquito-borne diseases using genetic control technologies. In *Nature Communications* (Vol. 12, Issue 1). https://doi.org/10.1038/s41467-021-24654-z

Wang, J., Zhang, C. J., Chia, W. N., Loh, C. C. Y., Li, Z., Lee, Y. M., He, Y., Yuan, L. X., Lim, T. K., Liu, M., Liew, C. X., Lee, Y. Q., Zhang, J., Lu, N., Lim, C. T., Hua, Z. C., Liu, B., Shen, H. M., Tan, K. S. W., & Lin, Q. (2015). Haem-activated promiscuous targeting of artemisinin in Plasmodium falciparum. *Nature Communications*, *6*. https://doi.org/10.1038/ncomms10111

Weiss, G. E., Gilson, P. R., Taechalertpaisarn, T., Tham, W. H., de Jong, N. W. M., Harvey, K. L., Fowkes, F. J. I., Barlow, P. N., Rayner, J. C., Wright, G. J., Cowman, A. F., & Crabb, B. S. (2015). Revealing the Sequence and Resulting Cellular Morphology of Receptor-Ligand Interactions during Plasmodium falciparum Invasion of Erythrocytes. *PLoS Pathogens*. https://doi.org/10.1371/journal.ppat.1004670

WHO. (2022). World Malaria Report 2022 - World | ReliefWeb. In *World Health Organization*.

Withers-Martinez, C., Strath, M., Hackett, F., Haire, L. F., Howell, S. A., Walker, P. A., Evangelos, C., Dodson, G. G., & Blackman, M. J. (2014). The malaria parasite egress protease SUB1 is a calcium-dependent redox switch subtilisin. *Nature Communications*, *5*. https://doi.org/10.1038/ncomms4726

Withers-Martinez, C., Suarez, C., Fulle, S., Kher, S., Penzo, M., Ebejer, J. P., Koussis, K., Hackett, F., Jirgensons, A., Finn, P., & Blackman, M. J. (2012). Plasmodium subtilisin-like protease 1 (SUB1): Insights into the active-site structure, specificity and function of a pan-malaria drug target. *International Journal for Parasitology*, *42*(6). https://doi.org/10.1016/j.ijpara.2012.04.005

Woehlbier, U., Epp, C., Hackett, F., Blackman, M. J., & Bujard, H. (2010). Antibodies against multiple merozoite surface antigens of the human malaria parasite Plasmodium falciparum inhibit parasite maturation and red blood cell invasion. *Malaria Journal*. https://doi.org/10.1186/1475-2875-9-77

Yahata, K., Hart, M. N., Davies, H., Asada, M., Wassmer, S. C., Templeton, T. J., Treeck, M., Moon, R. W., & Kaneko, O. (2021). Gliding motility of Plasmodium merozoites. *Proceedings of the National Academy of Sciences of the United States of America*, *118*(48). https://doi.org/10.1073/pnas.2114442118

Yang, A. S. P., O'Neill, M. T., Jennison, C., Lopaticki, S., Allison, C. C., Armistead, J. S., Erickson, S. M., Rogers, K. L., Ellisdon, A. M., Whisstock, J. C., Tweedell, R. E., Dinglasan, R. R., Douglas, D. N., Kneteman, N. M., & Boddey, J. A. (2017). Cell Traversal Activity Is Important for Plasmodium falciparum Liver Infection in Humanized Mice. *Cell Reports*. https://doi.org/10.1016/j.celrep.2017.03.017

Yeoh, S., O'Donnell, R. A., Koussis, K., Dluzewski, A. R., Ansell, K. H., Osborne, S. A., Hackett, F., Withers-Martinez, C., Mitchell, G. H., Bannister, L. H., Bryans, J. S., Kettleborough, C. A., & Blackman, M. J. (2007). Subcellular Discharge of a Serine Protease Mediates

Release of Invasive Malaria Parasites from Host Erythrocytes. *Cell*. https://doi.org/10.1016/j.cell.2007.10.049

Zhang, K. (2016). Gctf: Real-time CTF determination and correction. *Journal of Structural Biology*, *193*(1), 1–12. https://doi.org/10.1016/J.JSB.2015.11.003

Zheng, S. Q., Palovcak, E., Armache, J. P., Verba, K. A., Cheng, Y., & Agard, D. A. (2017). MotionCor2: anisotropic correction of beam-induced motion for improved cryo-electron microscopy. *Nature Methods*, *14*(4), 331–332. https://doi.org/10.1038/NMETH.4193

Zhu, L., van der Pluijm, R. W., Kucharski, M., Nayak, S., Tripathi, J., White, N. J., Day, N. P. J., Faiz, A., Phyo, A. P., Amaratunga, C., Lek, D., Ashley, E. A., Nosten, F., Smithuis, F., Ginsburg, H., von Seidlein, L., Lin, K., Imwong, M., Chotivanich, K., … Bozdech, Z. (2022). Artemisinin resistance in the malaria parasite, Plasmodium falciparum, originates from its initial transcriptional response. *Communications Biology*, *5*(1). https://doi.org/10.1038/s42003-022-03215-0

Zivanov, J., Nakane, T., Forsberg, B. O., Kimanius, D., Hagen, W. J. H., Lindahl, E., & Scheres, S. H. W. (2018). New tools for automated high-resolution cryo-EM structure determination in RELION-3. *ELife*, *7*. https://doi.org/10.7554/eLife.42166

Appendix

Appendix 1: Gating strategy for flow cytometry used to analyse parasitaemia in growth, invasion and development assays, screenshots are of FlowJo software.

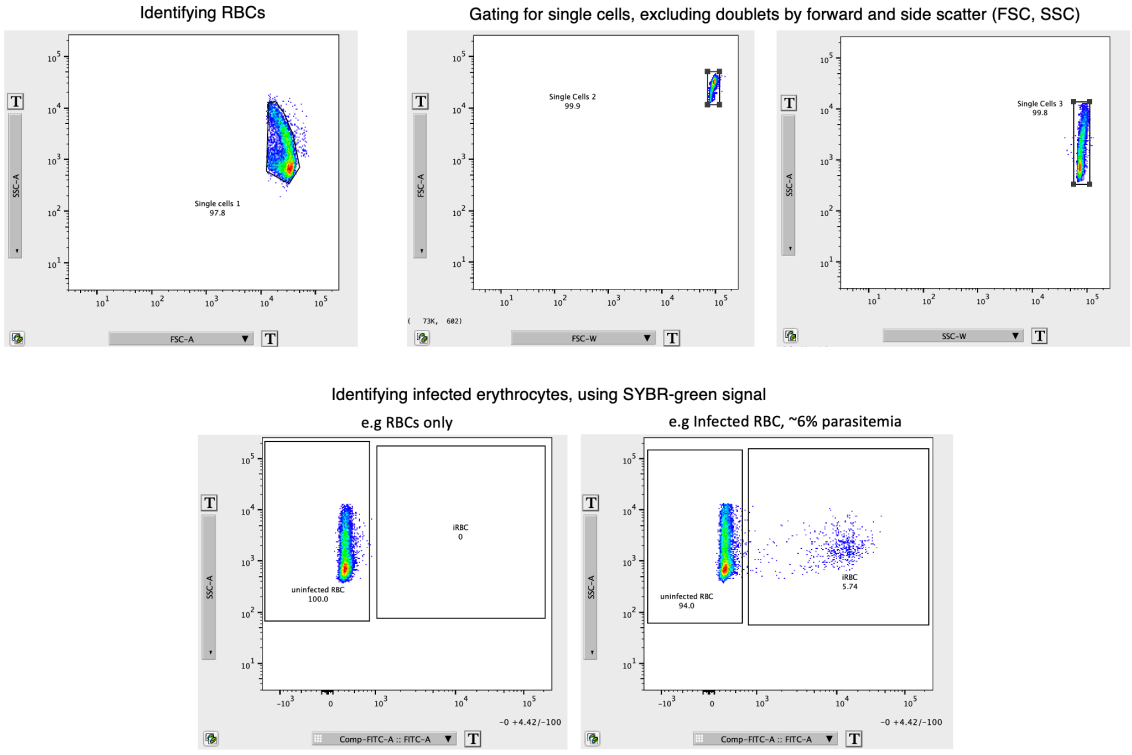

Appendix 2: Further detailed graphics of representatives of the models for A) $MSP1_{FL}$-7 and B) $MSP1_{cleaved}$-7-6-SERA5p47p18 complexes and associated EM densities after refinement and sharpening.

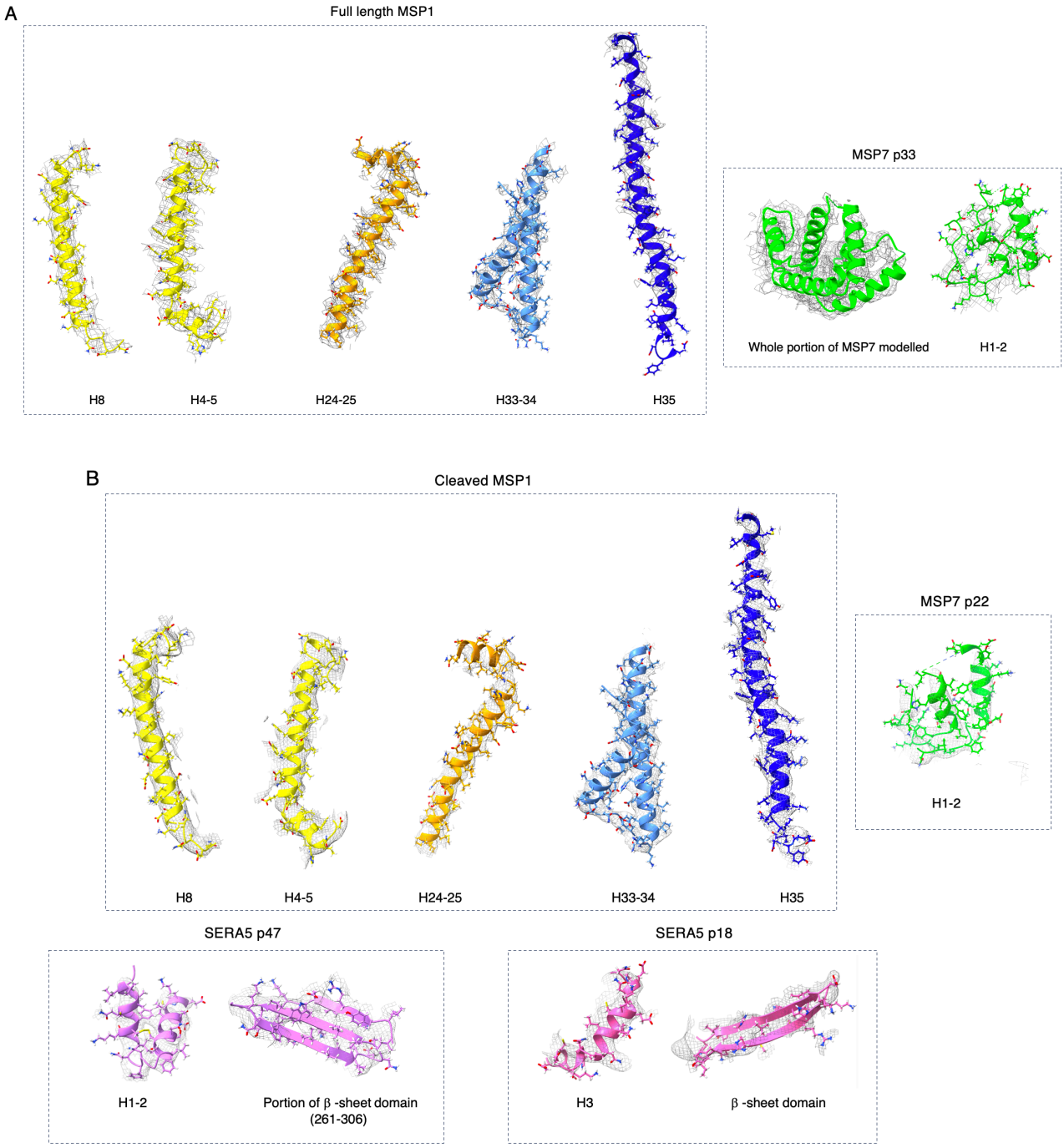

Appendix 3: Details of model refinement and validation obtained using Phenix

	$MSP1_{FL}$-MSP7	$MSP1_{cleaved}$ – MSP7-MSP6-SERA5p47p18
Residues modelled	1295	1658
B-factor mean, ($Å^2$)	172.15	256.88
Model vs map at 0.5 FSC	4.6	6.0
Model vs map CC(mask)	0.72	0.81
Ramachandran Plot		
Favoured (%)	97.71	97.15
Allowed (%)	2.29	2.85
Disallowed (%)	0	0
Molprobity score	0.99	1.27
Molprobity clashscore	1.74	3.28
Poor rotamers (%)	0.41	0.63
CaBLAM outliers (%)	0.8	1.14